Strong-field interactions in atoms and nanosystems: advances in fundamental science and technological capabilities of ultrafast sources

by

Adam M. Summers

B.S., Kansas State University, 2013

AN ABSTRACT OF A DISSERTATION

submitted in partial fulfillment of the
requirements for the degree

DOCTOR OF PHILOSOPHY

Department of Physics
College of Arts and Sciences

KANSAS STATE UNIVERSITY
Manhattan, Kansas

2019

Abstract

Modern laser sources can produce bursts of light that surpass even the fastest molecular vibrations. With durations this short even moderate pulse energies generate peak powers exceeding the average power output of the entire globe. When focused, this can result in an ultrafast electric field greater than the Coulomb potential that binds electrons to nuclei. This strong electric field strips electrons away from atoms in a process known as strong-field ionization. The first experimental realization of photoionization with intense laser pulses occurred only a few years after the invention of the laser. Yet, despite decades of intensive investigation, open questions remain. At the same time, the knowledge gained has led to the creation of multiple exciting fields such as attoscience, femtochemistry, and ultrafast nano-photonics.

In this thesis I present my work to advance the fundamental understanding of intense, ultrafast light-matter interactions as well as efforts to expand the technological capabilities of ultrafast light sources and measurement techniques. This includes the photoionization process of atoms and nanoparticles subject to intense, mid-infrared laser fields. The resulting photoelectron emission is measured, with high precision, in a velocity map imaging spectrometer. Other parts of this thesis detail my work on the generation and characterization of non-Gaussian optical pulses. Femtosecond Bessel beams are used to drive and study high harmonic generation with the ultimate goal of creating a compact, high-flux XUV source. Further studies include few-cycle pulses and the carrier-envelope phase, specifically methods of locking and tagging the carrier-envelope phase. A single-shot, all optical tagging method is developed and directly compared to the standard tagging method, the carrier-envelope phase meter. Finally, both experimental and computational studies are presented investigating the ultrafast thermal response cycle of nanowires undergoing femtosecond heating.

Strong-field interactions in atoms and nanosystems: advances in fundamental science and technological capabilities of ultrafast sources

by

Adam M. Summers

B.S., Kansas State University, 2013

A DISSERTATION

submitted in partial fulfillment of the
requirements for the degree

DOCTOR OF PHILOSOPHY

Department of Physics
College of Arts and Sciences

KANSAS STATE UNIVERSITY
Manhattan, Kansas

2019

Approved by:

Major Professor
Daniel Rolles

Copyright

© Adam Summers 2019.

Abstract

Modern laser sources can produce bursts of light that surpass even the fastest molecular vibrations. With durations this short even moderate pulse energies generate peak powers exceeding the average power output of the entire globe. When focused, this can result in an ultrafast electric field greater than the Coulomb potential that binds electrons to nuclei. This strong electric field strips electrons away from atoms in a process known as strong-field ionization. The first experimental realization of photoionization with intense laser pulses occurred only a few years after the invention of the laser. Yet, despite decades of intensive investigation, open questions remain. At the same time, the knowledge gained has led to the creation of multiple exciting fields such as attoscience, femtochemistry, and ultrafast nano-photonics.

In this thesis I present my work to advance the fundamental understanding of intense, ultrafast light-matter interactions as well as efforts to expand the technological capabilities of ultrafast light sources and measurement techniques. This includes the photoionization process of atoms and nanoparticles subject to intense, mid-infrared laser fields. The resulting photoelectron emission is measured, with high precision, in a velocity map imaging spectrometer. Other parts of this thesis detail my work on the generation and characterization of non-Gaussian optical pulses. Femtosecond Bessel beams are used to drive and study high harmonic generation with the ultimate goal of creating a compact, high-flux XUV source. Further studies include few-cycle pulses and the carrier-envelope phase, specifically methods of locking and tagging the carrier-envelope phase. A single-shot, all optical tagging method is developed and directly compared to the standard tagging method, the carrier-envelope phase meter. Finally, both experimental and computational studies are presented investigating the ultrafast thermal response cycle of nanowires undergoing femtosecond heating.

Table of Contents

List of Figures ix

List of Tables xiii

Acknowledgements xiv

Dedication xvi

1 Introduction 1

2 Generation of Ultrafast Pulses 5

2.1 Mathematical Representation of Ultrafast Optical Pulses 5

2.2 Generation of Ultrafast Pulses Directly from a Laser Cavity 11

2.2.1 Mode-Locking 13

2.2.2 Chirped Pulse Amplification 15

2.3 Generation of New Frequency Components Through Non-linear Optical Interactions 17

2.3.1 Optical Parametric Amplification 20

2.3.2 Few-Cycle Pulse Generation 22

2.4 High Harmonic Generation and Attosecond Pulses 24

3 Wavelength Scaling of Strong-Field Ionization 27

3.1 Photoionization 28

3.2 Theory of Strong-Field Ionization 29

3.2.1 Multiphoton Ionization 30

3.2.2 Tunnel Ionization . . . 31
3.2.3 The Simple Man Model and Classical Propagation in the Electric Field 34
3.2.4 Strong-Field Approximation Ionization Theories . . . 37
3.2.5 Time-Dependent Schrödinger Equation . . . 42
3.3 Experiment and Results . . . 43
3.4 Interpretation and Discussion . . . 61
3.4.1 Direct Ionization . . . 62
3.4.2 Photoelectron Rescattering . . . 66
3.5 Conclusion . . . 71

4 Controlling and Measuring the Carrier-Envelope Phase for Strong-Field Science Studies . . . 72
4.1 The Carrier-Envelope Phase . . . 73
4.2 Methods of Measuring the Carrier-Envelope Phase . . . 78
4.3 Long-Term Stabilization of the Carrier-Envelope Phase in a Terawatt-Class Laser System . . . 85
4.4 Single-Shot Carrier-Envelope-Phase Tagging Using an f-2f Interferometer and a Phase Meter: A Comparison . . . 87

5 Ultrafast Non-Gaussian Optics, Characterization and Applications of Femtosecond Bessel Beams . . . 94
5.1 Propagation of Electromagnetic Energy . . . 96
5.2 Spatial Characterization of Bessel-Like Beams for Strong-Field Physics . . . 107
5.2.1 Optical Setup and Beam Characterization . . . 108
5.2.2 Results and Discussion . . . 111
5.3 High Harmonic Generation from Bessel Beams . . . 115
5.3.1 High Harmonic Phase Matching with Bessel Beams . . . 117

5.3.2 Experimental Realization of High Harmonic Generation with Bessel Beams . . . 121
5.4 Conclusions and Future Work . . . 133

6 Strong-Field Interactions in Nanosystems . . . 135
6.1 Thermal Dynamics in Nanowires Exposed to Intense, Ultrafast Pulses . . . 136
6.1.1 Measurement of the Optical Damage Threshold of Gold Nanowires . 137
6.2 Numerical Simulation of Ultrafast Laser Heating in Gold Nanowires . . . 142
6.2.1 Thermal Response of Gold Nanowires to a Single Femosecond Laser Pulse . . . 144
6.2.2 Thermal Response and Effects of Gold Nanowires to a Train of Femtosecond Pulses . . . 153
6.3 Wavelength Scaling of Photoionization of Dielectric Nanoparticles . . . 159
6.3.1 Size Dependent Electron Emission from Laser-Driven SiO_2 Nanoparicles 160
6.3.2 Experimental Setup . . . 164
6.3.3 Results and Discussion . . . 165
6.3.4 Conclusion and Future Work . . . 171

7 Conclusion . . . 173

Bibliography . . . 176

List of Figures

2.1 Effects of second and third order dispersion 10

2.2 Coherent addition of frequency components to create an ultrafast pulse . . . 12

2.3 Ti:Sapphire Kerr lens oscillator schematic 15

2.4 CPA pulse compressor 16

2.5 Depiction of second order non-linear frequency mixing 19

2.6 Layout of high energy OPA 21

2.7 Generation of few-cycle pulses 23

2.8 The three-step model of HHG 25

3.1 Regimes of photoionization 29

3.2 Experimental setup for studying photoelectron momentum distributions . . 46

3.3 Sample of the acquired raw PMD images and the states of postprocessing and inversion 47

3.4 On-axis energy spectra for 5, 785nm measurements with successively increasing input pulse energy 50

3.5 High repeller voltage on-axis energy spectra 51

3.6 Results from intensity and wavelength dependent study of strong-field ionization in Xe 60

3.7 Evolution of the photoelectron spectrum from the multiphoton to tunneling regime 63

3.8 Photoelectron distributions exhibiting a quantum carpet pattern 67

3.9 Sketch of the typically energy spectrum of photoelectrons from ionization in the tunneling regime 68

3.10 Photoelectron distribution illustrating "spider" patterns 70

4.1 Explanation and origin of the carrier-envelope phase 76
4.2 Layout for an f-2f interferometer designed to stabilize Ti:Sapphire oscillator CEP 81
4.3 All optical f-2f interferometer for measuring the CEP 82
4.4 Optical interference pattern in f-2f interferometer for measuring the CEP . . 83
4.5 Depiction of carrier-envelope phase meter 84
4.6 Schematic of f-2f interferometer for stabilizing the CEP in an amplifier . . . 87
4.7 Layout of the HITS laser and long-term stabilization of the CEP 88
4.8 Few-cycle pulse generation system 90
4.9 Experimental setup and timing synchronization logic for generating few-cycle pulses and measuring the CEP with both the f-2f interferometer and Stereo-ATI Phase Meter simultaneously 90
4.10 Correlation of the single-shot CEP measured by the CEPM and HCF-based f-2f interferometer 92

5.1 Gaussian beam propagation 102
5.2 Propagation of plane-waves through and axicon and the formation of a Bessel beam 107
5.3 Experimental setup for the characterization of Bessel beam focal profile . . . 109
5.4 HDR image analysis technique for characterization of Bessel beams 110
5.5 Bessel-like beams observed at various distances from the axicon 112
5.6 Longitudinal sections of femtosecond Bessel-like beams generated at various lens-axicon distances 113
5.7 Bessel beam spot size measurments 114
5.8 Bessel beam focal profiles 116
5.9 Experimental setup for HHG with femtosecond Bessel beams 122

5.10 Ionization of air from focused Bessel beam 123
5.11 Argon ionization yield as function of position from axicon 124
5.12 Tipblock effects on the ionization yield of argon 124
5.13 MCP images for the HHG spectrum generated with Gaussian beam and Bessel beam 125
5.14 Ionization yield along with the accompanying HHG yields as a function of position within the Bessel profile 127
5.15 Ionization and HHG yields from Bessel beam 128
5.16 Ionization trace plotted with the spectral map of HHG yield 129
5.17 2D map of HHG yield spectrum as function of distance from the axicon tip (i) 130
5.18 2D map of HHG yield spectrum as function of distance from the axicon tip (ii) 131
5.19 2D map of HHG yield spectrum as function of distance from the axicon tip (iii) 132

6.1 Experimental setup for measuring the optical damage threshold of single-crystalline gold nanowires 138
6.2 Nanowire SEM and optical microscope images 140
6.3 Measured optical damage threshold distribution as a function of intensity . . 141
6.4 Simulated fast time-scale thermal response of nanowire to ultrafast pulse . . 146
6.5 Initial heat profile of the lattice temperature in a 100 nm thick nanowire after exposure to a 25 fs, 800 nm laser pulse 147
6.6 Heat diffusion through the depth of a nanowire after exposure to a 25 fs, 800 nm laser pulse (i) 149
6.7 Heat diffusion through the depth of a nanowire after exposure to a 25 fs, 800 nm laser pulse (ii) 150
6.8 Peak temperature of the nanowire after heat diffusion in the z-dimension . . 151
6.9 Gold nanowire cooling profile from an initial heat distribution after exposure to a 25 fs, 800 nm laser pulse 152
6.10 Schematic of how multi-pulse heating simulations 155

6.11 Asymptotic final peak temperature of a 100 nm gold nanowire as a function of laser intensity and repetition rate 157
6.12 Temperature profiles showing the asymptotic final peak temperature of a 100 nm gold nanowire as a function of laser intensity and repetition rate 158
6.13 Photoelectron momentum distribution for Xe and 120 nm SiO_2 nanopartices 161
6.14 High energy velocity map imaging (VMI) spectrometer with nanoparticle source 165
6.15 Photoelectron cutoff energies as a function of nanoparticle diameter 166
6.16 Size dependent photoelectron cutoff energy values in units of ponderomotive potential 167
6.17 Squared maximum field enhancement as a function of nanoparticle diameter 168
6.18 Size dependent photoelectron cutoff energy values scaled by ponderomotive potential and squared field enhancement 169
6.19 SiO_2 field enhancement along the polarization axis as a function of distance from the nanoparticle surface 170

List of Tables

2.1 Common pulse envelope functions 8

Acknowledgments

Throughout this thesis I comment on how this document represents my contributions to the overall scientific community. While certainly true, this is also somewhat of a misnomer. The work presented here is the shared product of many other individuals as well. Obtaining my Ph.D. has been a long process throughout which I have been supported by many friends, family members and colleagues. My deepest gratitude goes out to all those who have helped, encouraged, occasionally cajoled and stood by me. Without you, my journey to this point would have been impossible.

To my parents, who have always believed in me, been my biggest fans, and pushed me to reach my fullest potential not just as a scientist but also as a person.

To my wife, for her support, understanding, and love throughout this journey.

To Jeff Powell and Derrek Wilson, my lab partners and more importantly friends. You have made graduate school not just endurable but enjoyable. Hopefully we also accomplished some science along the way as well.

To Travis Severt, my longtime friend, occasional lab partner, and colleague through both the toughest and finest grad school had to offer.

To Itzik Ben-Itzhak and Matthias Kling, my advisors as I started my scientific career during my undergraduate studies. Through you I learned how to be a scientist and researcher. For this I will be eternally grateful. Thank you also for the continued guidance through my graduate career.

To current and past members of the extended Itzik Ben-Itzhak group, Kevin Carnes, Nora Kling, Kelsie Betsch, Ben Berry, Bethany Jochim, and Bishwanath Gaire. You all played an integral role in my scientific development for which I will always appreciate.

To the other members of the James R. Macdonald lab and physics department machine shop, Chris Aikens, Justin Millette, Al Rankin, Mike Wells, Charles Fehrenbach, Scott Chainey, Vince Needham, and Andy Thurlow. Thank you for all your help, putting up with

my crazy requests, and always being patient when explaining what I was asking for just is not possible. Your support will be sorely missed.

To Carlos Trallero, my first advisor in graduate school and continued mentor. Your passion and excitement for science has been truly infectious. You taught me the value of analyzing problems from a top down view, focusing on the issues that matter most, and to always keep moving forward. Thank you for seeing my potential, even when I may have not. You have always pushed me to be a better scientist, in all senses of the word.

To other members of the Carlos Trallero group: Stefan Zigo, Jan Tross, Georgios Kolliopoulos, Pratap Timilsina, Josh Nelson, Daniel Todd and Lindsay Hutcherson. It takes a team to keep a lab running and working with each of you throughout the years was a pleasure

To Daniel Rolles, my advisor and guide through the later stages of my Ph.D. Thank you for agreeing to take me on, always holding me and my research to a high standard and imparting many elements of wisdom.

To Artem Rudenko, who has continued to be a strong mentor and teacher throughout my Ph.D. What I have learned from your approach to problem solving and scientific reasoning will continue to be one of the most valuable skills I have learned in graduate school.

To several other professors in the KSU physics department: Brian Washburn, Vinod Kumarappan, Chris Sorensen and Larry Weaver. You were all always willing to drop what you were doing and answer whatever insistent questions I happened to drop by with. Your enthusiasm for both teaching and science will always be remembered.

To Shuting Lei and members of his group, Xiaoming Yu and Xinya Wang. I always enjoyed working alongside you and learning from you.

Finally, to all the members of the Ph.D. committee: Daniel Rolles, Carlos Trallero, Artem Rudenko, Uwe Thumm, and Shuting Lei. You all served as my teachers and mentors.

Dedication

To those around the world who continue the quest for truth, to those who pursue knowledge in its pure form, to those who seek to impart objectivity, to those to who devote their lives in the fight against ignorance and to those who relentlessly pursue progress and exploration of the unknown.

Truth cares neither for our beliefs nor for our desires. For truth it matters not our politics nor our dogmas. Truth exists above us, not through us; in spite of us, not because of us.

In a time where humanity's understanding of the universe has never been greater nor has ever grown faster, it also is a time where willful ignorance seeks to destroy these gains and alternative facts go unquestioned. Here, the role of the philosopher, the role of the educator, the role of the thinker, the role of scientist has never been more vital.

"There is only one good, knowledge, and one evil, ignorance"

- Socrates

Chapter 1

Introduction

The history of science is also the history of measurement. Indeed, measurement is the final step in the scientific method, testing a hypothesis. As measurement technologies have advanced, so too has science and our understanding of the universe we live in. The research presented in this thesis is tied together with the common theme of observing, describing and ultimately predicting how the physical world evolves on its fastest timescales. Working with incomprehensibly short optical pulses, ultrafast science focuses on measuring some of the fastest processes known in nature. Examples of ultrafast processes include the rotations and vibrations of molecules, the motion of bound electrons, the formation of electronic bonds, and the electronic properties of condensed matter systems. These processes represent the most fundamental, dynamic building blocks of our natural world. Understanding these dynamics is essential for the continued advancement of critical technologies in medicine, computation, and material sciences.

An essential tenant of measuring a dynamic process lies in the fact that a measurement technique must be faster than the dynamics being measured. Thus, ultrafast science is an inherently technology driven field. As faster measurement methods become available, new areas of science open up for investigation. Historical examples of novel 'ultrafast' measurements include the often referenced works of Muybridge, investigating the hoofs of a galloping horse in 1878 and Edgerton with the microsecond resolution flash lamp photo of a bullet

passing through an apple in 1964. Despite these early, iconic examples, ultrafast science did not become a field of its own until after the invention of the laser in 1960 [1]. Just two years after, the first Q-switched laser was demonstrated with a pulse duration of 100 nanoseconds [2]. The pursuit of even shorter pulses has continued and currently, attosecond optical pulses, produced utilizing the process of high harmonic generation, represent the state of the art in ultrafast measurement techniques. Using high harmonic generation, it is now possible to produce X-ray pulses of light shorter than 100 attoseconds (ten millionths of a billionth of a second, 100×10^{-18} seconds), unlocking the ability to study processes such as the motion of electrons around nuclei.

This decrease in pulse duration has also been accompanied with the complementary increase in peak-power. Since the demonstration of the first laser in 1960, the peak-power obtainable with pulsed laser radiation has increased by a factor of roughly 1,000 every ten years [3]. The peak-power achievable with modern laser sources is truly unfathomable. The HITS laser, used for many of the studies here, produces 20 mJ laser pulses with a pulse duration of 25fs, giving a peak power of almost a terawatt. For reference, it would take almost 500 Hoover Dams, operating at full capacity, to generate this much average power. These ultrafast pulses can be focused down to produce similarly incredible peak electric fields (exceeding an exawatt per square centimeter for the HITS laser). Thus, the fields of ultrafast science and strong-field science are inexorably linked.

The electric field strength in the focus of high-energy, ultrafast pulses can approach or exceed the binding Coulomb potential of atoms, molecules, and solids. This gives rise to a phenomenon known as strong-field ionization, where an intense electric field rips electrons off of the target. The exact dynamics that occur in this ionization process are complicated, intricate and at times counterintuitive. The first experimental observation of strong-field ionization also occurred only a few years after the invention of the laser [4; 5]. Yet, despite more than 50 years of intensive investigation, open questions remain.

However, the knowledge gained about strong-field ionization has also proved extremely powerful and has lead to the creation of entire fields and sub-fields. Chief among these is high harmonic generation and the field of attoscience [6; 7]. Without a detailed understanding

of strong-field ionization, the control necessary to produce isolated attosecond pulses would not be possible. Progress in ultrafast and strong-field science has also enabled the field of femtochemistry and the ability to track molecular reactions on their natural timescales [8–10].

Many of the same concepts developed in atomic and molecular ultrafast and strong-field studies can be directly adapted for understanding physics at the nanoscale. However, a number of significant differences and deviations also exist. These include processes such as near-field enhancement, collective electron motion and the possibility for an individual electron to continue to gain energy through many, sequential rescattering events. Photoelectron spectroscopy has shown that these effects give rise to numerous exciting and potentially highly-impactful physical phenomena. A strong material dependency has also been observed with large differences between metallic and dielectric samples. Thermal effects also arise at the nanoscale and present a set of their own unique challenges [11; 12].

This thesis documents and explains several of my contributions to the fields of strong-field and ultrafast science. Some of these contributions are aimed at increasing fundamental understanding of strong-field, light-matter interactions. This includes the photoionization process of atoms and nanoparticles subject to intense mid-infrared laser fields as well as the ultrafast thermal response cycle of nanowires undergoing femtosecond heating. Other parts of this thesis detail my efforts to improve the technological capabilities of ultrafast measurement techniques and light sources. Within this context, is my work on non-Gaussian optical pulses along with my work in both locking and tagging of the carrier-envelope phase of few-cycle pulses.

Thesis Layout and Organization

During my PhD I have been fortunate enough to be involved in a wide range of studies and experimental efforts. This thesis presents a subset of those and the progress made within each. Four primary studies are included, each organized into their own chapter. Each chapter is written to largely stand alone in its own right, but the overall thesis is organized in

a manner such that, where possible, concepts presented in the earlier chapters will be useful in understanding subsequent chapters. As ultrafast methods represent the core thread tying this thesis together, chapter 2 presents the basics of ultrafast fields, including how ultrafast pulses are produced and amplified as well as the important points of describing ultrafast pulses mathematically.

Chapter 3 begins the main body of research and focuses on furthering the fundamental understanding of strong-field ionization of atoms, particularly as a function of wavelength through the near to mid-infrared. Chapter 4 concentrates on few-cycle pulses and methods for locking and tagging the carrier-envelope phase. A single-shot all-optical tagging method is presented and compared to the standard tagging method using a carrier-envelope phase meter. The potential applications and benefits of non-Gaussian ultrafast optics are explored in chapter 5. The generation and optical characterization of femtosecond Bessel beams is presented along with the application in driving high harmonic generation. Finally, chapter 6 turns to ultrafast nanophotonics. Two distinct topics are covered: the thermal response and damage of gold nanowires under exposure to intense laser radiation and the wavelength scaling of photoionization in dielectric nanoparticles.

To facilitate easier reading, particularly for those reading only an isolated chapter, abbreviations are generally redefined within each chapter. An effort has been made to standardize notation wherever possible but in some cases, standard conventions within the different subfields make this difficult. In all cases, new notations abbreviations are defined or redefined as introduced.

Chapter 2

Generation of Ultrafast Pulses

While a number of different and somewhat distinctive topics are presented in the following chapters, ultrafast laser pulses denote the common theme tying all of them together. These incomprehensibly short bursts of radiation serve as the predominate tool in investigating the fundamental dynamics of the fastest events in our natural world. To repeat a key phrase from the previous chapter, the fundamental tenant of measuring a dynamical process lies in the fact that the measurement technique must be faster than the process being measured.

This chapter serves to introduce the technical aspects of ultrafast pulses, both the basics of their mathematical description as well as the how they are created. It is certainly not the goal to give an extensive and fully rigorous treatment. Rather, the goal is to provide a reasonable summary and background, sufficient for understanding the work presented in the later chapters.

2.1 Mathematical Representation of Ultrafast Optical Pulses

It is fairly easy to write out a mathematical equation for an optical pulse which, according to Maxwell's equations, can be expressed as an electromagnetic wave. For a single point in space, with the pulse traveling in the positive z-direction and linearly polarized along the

x-axis, the electric field as a function of time is

$$\mathbf{E}(t) = G(t)cos(\omega_c t + \phi(t))\hat{\mathbf{x}}, \tag{2.1}$$

where $G(t)$ is a temporal envelope function, ω_c is the carrier frequency and $\phi(t)$ is the time dependent phase.

The magnetic component will then be

$$\mathbf{B}(t) = \frac{G(t)}{c}cos(\omega_c t + \phi(t))\hat{\mathbf{y}}, \tag{2.2}$$

where c is the speed of light.

The fact that the magnitude of the magnetic field is scaled by the speed of light means that its effect on any system being studied is usually completely negligible. Thus, the magnetic component of the pulsed EM-wave is typically ignored and only the electric field is considered when considering ultrafast light-matter interactions. The exception to this is for pulses that generate high intensities to require a relativistic treatment where the magnetic field can become quite important.

Numerous functionalities can be adopted for $G(t)$. The most typical is a Gaussian envelope but others, including squared hyperbolic secant, Lorentzian or even flat top are commonly used. A truncated, squared cosine envelope is a favorite of theorists due to the fact that it drops to zero much faster at the edges, speeding up computational studies. Table 2.1 gives the intensity profile for a few of these envelope functions.

The duration of a pulse is usually defined and reported at the full-width-half-maximum (FWHM) of the intensity (not the field). There is a lot of confusion in the literature about this, and at times care is needed to identify the exact definition of pulse duration that is being used.

No matter what specific mathematical description for the envelope function is used, the following must be true:

$$\int_{-\infty}^{\infty} \mathbf{E}(t)dt = 0. \tag{2.3}$$

Constructing a pulse where the full temporal integral of the electric field is not identically zero requires negative frequency components and thus is not a physical solution to the wave equation.

While the temporal domain may seem the natural choice for working with ultrafast pulses, in many cases the frequency domain is more useful.

The frequency and temporal domains are linked through the Fourier transform of each other

$$E(t) = \mathcal{F}[E(\omega)] = \frac{1}{\sqrt{2\pi}} \int_{-\infty}^{\infty} E(\omega) e^{i\omega t} d\omega, \tag{2.4}$$

$$E(\omega) = \mathcal{F}^{-1}[E(t)] = \frac{1}{\sqrt{2\pi}} \int_{-\infty}^{\infty} E(t) e^{-i\omega t} dt. \tag{2.5}$$

This can be used to find a relation between the width in the frequency domain [13], $\Delta\omega$, to the pulse duration, τ

$$\tau \Delta\omega = \sigma_{TBP}, \tag{2.6}$$

where σ_{TBP} is a constant known as the time-bandwidth-product and depends on the envelope function. Table 2.1 lists σ_{TBP} for the common pulse envelopes.

It is often useful to have this expression in terms of wavelength

$$\tau \Delta\lambda \frac{c}{\lambda_0^2} = \sigma_{TBP}, \tag{2.7}$$

where λ_0 is the central wavelength.

For those working with Ti:Sapphire lasers, a particularly useful output of this expression is that, for a bandwidth of 30 nm, at a central wavelength of 800nm, thus pulse duration is approximately 30 fs (31.38 fs to be exact).

There is an extremely notable exception to equations 2.6 and 2.7 that originates from the time dependent phase, $\phi(t)$, in equation 2.1.

Table 2.1: *Pulse information for common pulse envelope functions. τ represents the FWHM for all cases*

Pulse Type	Intensity Envelope Function	σ_{TBP}
Gaussian	$\exp[-4ln(2)\frac{t^2}{\tau^2}]$	0.441
Hyperbolic Secant	$\text{sech}^2[2ln(1+\sqrt{(2)})\frac{t}{\tau}]$	0.315
Lorentzian	$\left(1+4(\sqrt{2}-1)\frac{t^2}{\tau^2}\right)^{-2}$	0.142
Flat Top	$\lvert t/\tau\rvert \leq 1$; 0 elseware	0.443

The fixed relationship between the bandwidth and pulse duration is only true when

$$\frac{\partial}{\partial t}\phi(t) = c. \tag{2.8}$$

Where c is an arbitrary constant.

When this is the case, the pulse is said to be Fourier transform limited (FTL) or transform limited (TL). This is the shortest pulse duration possible for a given bandwidth.

Any non-constant phase will add dispersion to the pulse and lengthen the pulse duration. In the temporal domain, this dispersion manifests as a delay between different frequency components where the instantaneous frequency will either increase or decrease as a function of time. This phenomenon is also known as "chirp" in reference to the frequency evolution in the sound made by many birds.

Dispersion is imparted onto an optical pulse as the pulse travels through a system with a frequency dependent index of refraction, $n(\omega)$. As the speed light travels through a medium is given as the (vacuum) speed of light divided by the index of refraction, it is easy to see how a frequency dependent index of refraction will cause dispersion for a pulse with any amount of bandwidth. The larger the bandwidth, the more susceptible the pulse will be to dispersion. It is frequently convenient to define a propagation constant, β, for a material or optical system

$$\beta(\omega) = \frac{n(\omega)\omega}{c}. \tag{2.9}$$

This is often expressed as a power series

$$\beta(\omega) = \beta(\omega_c) + \beta'(\omega - \omega_c) + \frac{1}{2}\beta''(\omega - \omega_c)^2 + ... \tag{2.10}$$

where $\beta' \equiv d\beta/d\omega$ and $\beta'' \equiv d^2\beta/d\omega^2$ evaluated at $\omega = \omega_c$, with ω_c defined as the carrier frequency. The carrier frequency is calculated as the centriod frequency

These coefficients can then be used to express the following

$$\beta = \frac{1}{\text{phase velocity}} \tag{2.11}$$

$$\beta' = \frac{1}{\text{group velocity}} \tag{2.12}$$

and

$$\beta'' = \text{group velocity dispersion.} \tag{2.13}$$

The first two terms in equation 2.10 do not change the shape of a pulse envelope but all higher order terms, starting with the group velocity dispersion (GVD) can. A pulse entering a material that has second order dispersion with an pulse duration, τ_{in} will leave the system with a output duration, τ_{out} given by [13]

$$\tau_{out} = \tau_{in}\sqrt{1 + \left(\frac{4ln(2)\beta''}{\tau_{in}^2}\right)^2} \tag{2.14}$$

The sign of β'' does not matter for the effect on pulse duration for an isolated system but in optical systems with multiple elements the total dispersion does depend on the magnitude and sign of the individual elements. While not explicitly expressed in equation 2.10 higher order dispersive terms also exist. Figure 2.1 shows the effects of negative second order (GVD) and negative third order dispersion (TOD).

Equation 2.6 also shows that the only way to make a pulse shorter is to increase the bandwidth. This is true for all Fourier conjugate variables, if something is narrow in one domain it is necessarily broad in the other. So, in a very real sense, ultrafast optics is all about generating as much coherent bandwidth as possible. This can be quite a challenge as

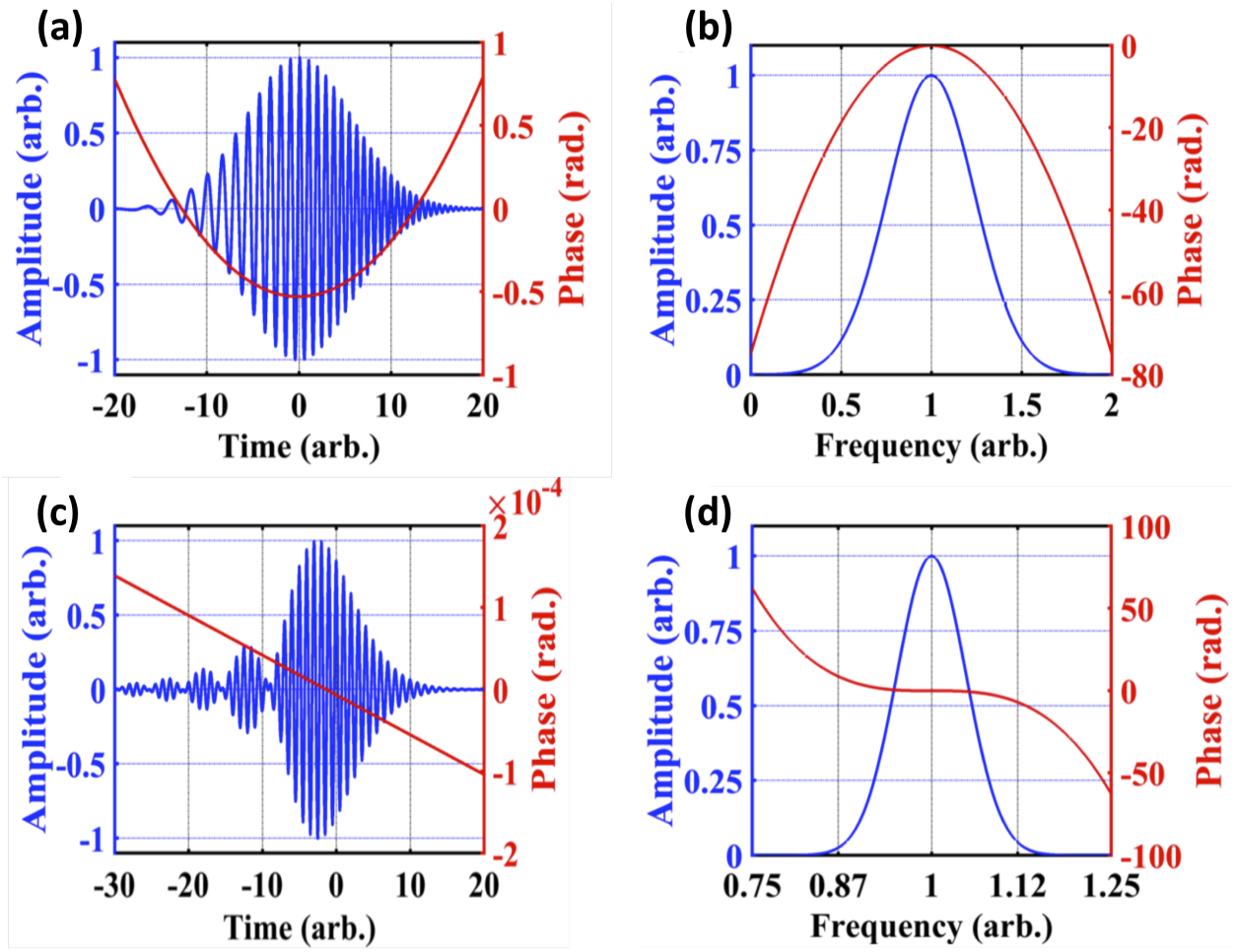

Figure 2.1: *Effects of second and third order dispersion. (a) Time domain electric field with negative group delay dispersion (GDD), (b) Spectrum for (a). (c)Time domain electric field with negative TOD, (d) Spectrum for (c). Adapted from [14].*

most laser systems tend to prefer to lase in only a narrow bandwidth window. To generate the bandwidth needed to make an ultrafast pulse, elaborate schemes, typically exploiting non-linear optical properties, are needed to "trick" a system into producing more bandwidth. These schemes can be broken roughly into two categories. The first uses intra-cavity setups to increase the bandwidth directly in the lasing process. There are several ways of doing this, but this section will limit the discussion to a technique known a passive mode-locking, which has emerged as the predominate method for generating ultrafast pulses directly from a laser cavity. The second method for obtaining the bandwidth needed for ultrafast pulses relies on any number of non-linear optical processes to generate new frequency components after the output of a laser. In many cases, both methods are used in conjunction to produce the desired pulse.

2.2 Generation of Ultrafast Pulses Directly from a Laser Cavity

Almost all lasers have three common components: a cavity, a gain medium, and a pump source. The gain medium provides a system where population inversion can be established so that stimulated emission can be used to amplify the light. The pump source couples energy into the gain medium to invert the population. Depending on the nature of the gain medium this is typically done either electrically or optically. Ti:Sapphire, for example, cannot be pumped electrically so a second laser is used as the pump source. This second laser is typically a neodymium-doped solid-state diode laser which is pumped electrically. The cavity contains the emited radiation so that it can pass through the gain medium, hundreds, thousands or even millions of times (depending on the Q-factor of the cavity) to be amplified before outcoupling.

The laser cavity establishes the allowed frequency domain modes for lasing. This is discussed in greater detail in section 4.1 but essentially a (longitudinal) mode is only allowed if it is comprised of an integer number of wavelengths that fit in the cavity with nodes at

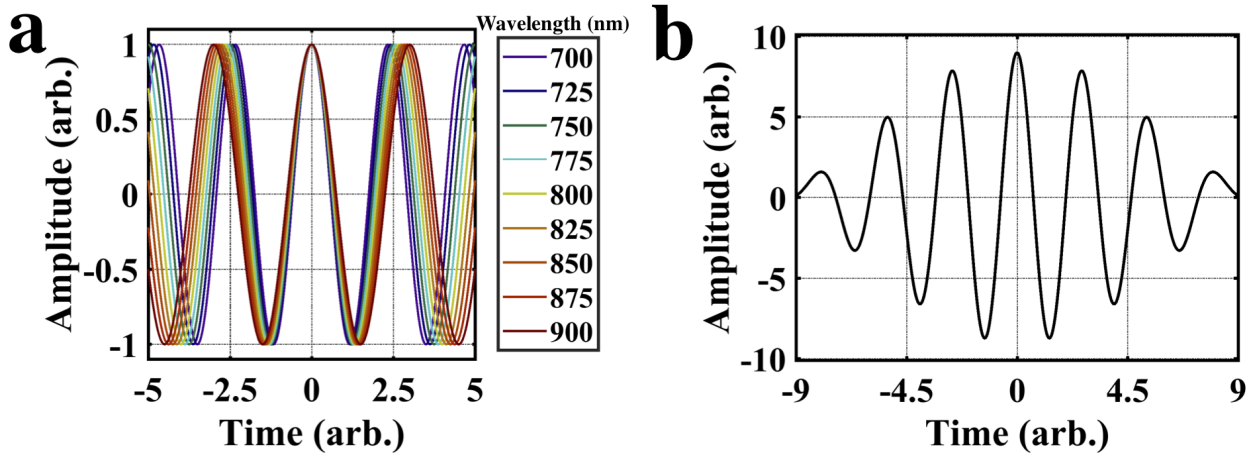

Figure 2.2: *(a) Frequencies of light from 700 nm - 900 nm where all frequencies have a peak amplitude at t = 0 fs. (b) Coherent addition of the frequency components from (a). Adapted from [14].*

the cavity mirrors. The cavity can lase on one of these modes or any combination of modes. The output is the superposition of the lasing modes. Which exact modes contain energy, and their relative strengths, depends on the gain medium. This is part of what makes Ti:Sapphire such an excellent crystal for ultrafast pulse generation. Ti:Sapphire supports gain on a large number of longitudinal cavity modes (on the order of one million) spread over tens to hundreds of nanometers in the near infrared.

These laser modes can be construed to interfere such that they only add constructively for a short period of time resulting in a train of pulses. The mode-locking process establishes this condition. In the temporal domain, a mode-locked laser can be thought of as a single pulse traveling around the cavity. When this pulse is reflected by the out-coupling end mirror, a small percentage of the pulse is transmitted. The output of a mode-locked laser is thus a pulse train with a spacing between each pulse equal to the round-trip time of the cavity. Figure 2.2 depicts how a number of different frequency components can be added to produce a pulse.

2.2.1 Mode-Locking

In most lasers, the phase of the individual modes, ϕ_m, undergoes random fluctuations. In order to get a laser to produce a pulse train through the interference of cavity modes, all of the modes must have a fixed phase relation. This is instituted through the mode-locking process. For Ti:Sapphire based lasers, the mode-locking is done through a passive amplitude modulation in time.

The electric field of the mth cavity mode can be expresses as

$$E_m(z,t) = A_m sin(k_m z) sin(\omega_m t + \phi_m), \tag{2.15}$$

where A_m is the amplitude, k_m is the wavenumber, ω_m is the angular frequency and ϕ_m is the phase of the mth mode respectively

Now, suppose that A_m is modulated at a fixed frequency defined by

$$A_m(z,t) = A_0(1 + \epsilon cos(\Omega t)), \tag{2.16}$$

where A_0 and ϵ are constants and Ω sets the modulation frequency.

Then $E_m(z,t)$ can be expressed as

$$E_m(z,t) = A_0[sin(\omega_m t + \phi_m) + \frac{\epsilon}{2} sin((\omega_m \pm \Omega)t + \phi_m)] sin(k_m z). \tag{2.17}$$

From this expression, it can be seen that the amplitude modulation creates new, sideband frequency components at $\omega_m \pm \Omega$. If Ω is set to be exactly at the frequency corresponding to the round-trip time of the cavity, then the sidebands will occur on top of the adjacent cavity modes. When this happens, the cavity modes become strongly coupled and adopt a fixed phase across the entire gain bandwidth. The result is a laser cavity that "oscillates" with a frequency equal to the round-trip time and outputs a train of ultrafast pulses, spaced by the same time constant. For this reason, many mode-locked laser cavities are referred to as oscillators.

The amplitude modulation at a frequency defined by the spacing of the cavity modes is

accomplished by inserting a saturable absorber into the laser cavity. A saturable absorber is a material that exhibits higher transmission for higher incident intensities than for lower intensities. The random noise in a laser cavity creates small, but important, ripples in the lasing amplitude of each mode, A_m. When these ripples pass though the saturable absorber the peaks of the ripples experience a higher transmission than the valleys. This naturally causes an amplitude modulation exactly at the correct frequency for mode-locking and is referred to as passive mode-locking. In the temporal domain, this process can be viewed as the higher intensity ripples traveling around the cavity, undergoing continued amplification, while the lower intensity ripples experience increased loss and quickly die out. In a way, the high intensity parts "steal" energy from the low intensity parts and quickly form into pulses.

Any form of passive mode-locking is an inherently non-linear process. In a Ti:Sapphire laser, the amplitude modulation is accomplished through a very ingenious exploitation of a non-linear optical process known as the Kerr effect. In the Kerr effect, a material's index of refraction becomes intensity dependent, typically becoming larger as a function of intensity. This, coupled with the spatial profile of the TEM_{00} mode most lasers are designed to lase on, creates a lens. The higher intensity at the center of the mode as compared to the wings induces an index of refraction the decreases radially, from the center out, for materials that exhibit an intensity dependent index of refraction. This creates the exact same condition as a positive lens which focuses light due to the increased amount of material at the center of the lens.

The strength of the lens, setup by the Kerr effect, depends on the incident intensity. If a second element, or set of elements, are used in conjunction with the Kerr lens such that the transmission function increases with the stronger lens effect, then a saturable absorber is created. This if often done by placing an iris after the Kerr lens element so only light that is focused tighter can pass through, while the more loosely focused components are blocked. The overall result is known a Kerr lens mode-locking (KLM).

The truly amazing part of Ti:Sapphire gain crystals is that not only do they support gain over an enormous bandwidth, the Ti:Sapphire crystal also has a highly intensity dependent index of refraction. So, the same element serves as both the gain medium and establishes

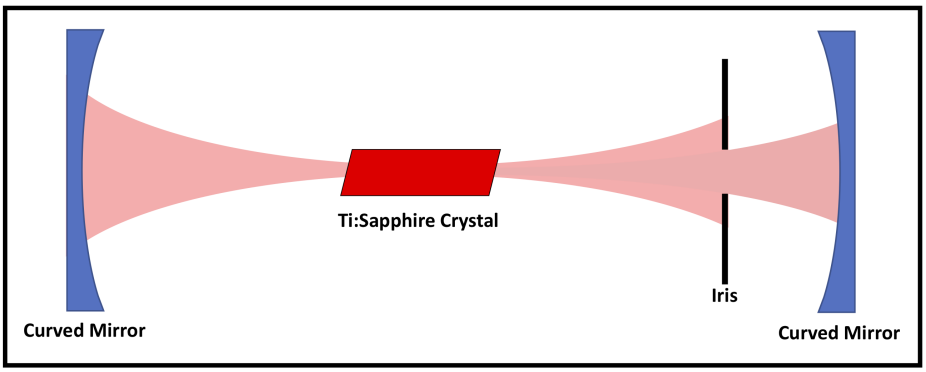

Figure 2.3: *Ti:Sapphire oscillator schematic for using the Kerr effect in the gain crystal to create a saturable absorber.*

KLM. As such, Ti:Sapphire has become the main workhorse material for ultrafast pulse generation. A typical oscillator produces 10-15 fs pulses with a few nanojoules of energy each at a repetition rate of around 80 MHz. Figure 2.3 depicts a typical setup for KLM with Ti:Sapphire.

The extremely short pulses produced by a Ti:Sapphire oscillator can be focused down to produce relatively high peak intensities. For example, a 1 nj pulse with a pulse duration of 10 fs focused down to the diffraction limit, can generate an intensity exceeding 10TW/cm^2. However, for many applications, significantly higher intensities or pulse energies are desired. To do this, the output from the oscillator needs to be amplified. This rapidly presents a problem. Even an extremely small amount of energy, contained within 10fs will produce a peak power above the damage threshold of most optical elements, including the gain crystal.

2.2.2 Chirped Pulse Amplification

Equation 2.14 typically presents a problem for researchers attempting to generate high peak intensity. For short pulses with a large bandwidth, even very thin optical elements have enough dispersion to significantly broaden the pulse and reduce the maximum achievable intensity accordingly. However, in the 1980s several researchers figured out how to circumvent the damage threshold problem for ultrafast pulse amplification using dispersion.

This solution, known as chirped pulse amplification (CPA), uses dispersion to significantly

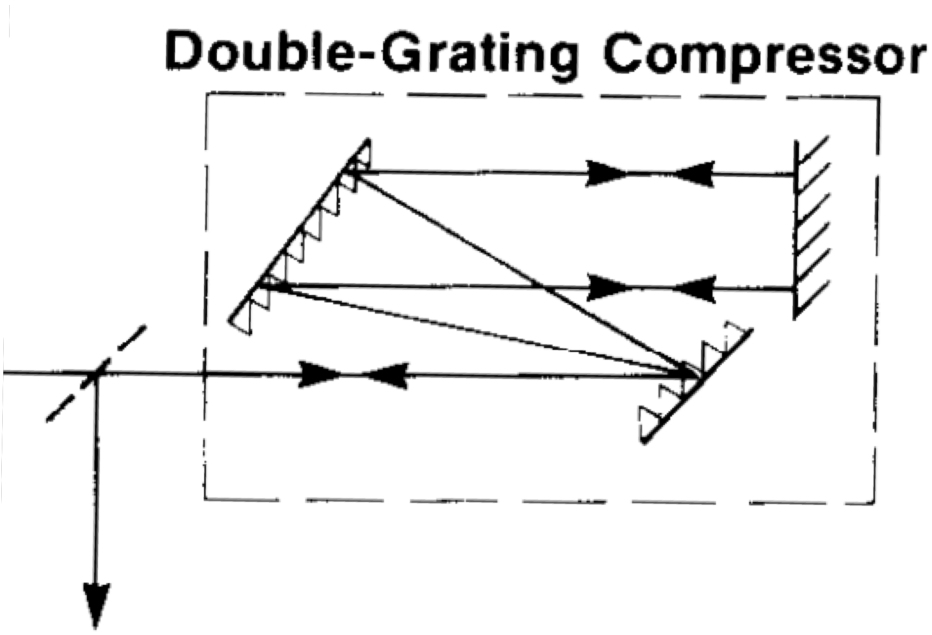

Figure 2.4: *Compressor used to compression pulse after amplification. Adapted from [15].*

temporally stretch the output pulse of an oscillator. The stretched pulse can then be safely amplified to high pulse energies without reaching peak powers that damage the amplifier system. Then after amplification, the opposite sign dispersion can be applied to shrink pulse back down to a transform limited or near transform limited pulse duration. This new laser technology lead to the development of laser system capable of generating peak focal intensities millions or even billions of time larger than possible with mode-locked oscillators. Two of the pioneering researchers in developing chirped pulse amplification, Gerard Mourou and Donna Strickland, were awarded the 2018 Nobel Prize for their "groundbreaking inventions in the field of laser physics".

In the first reported CPA system by Strickland and Mourou [15], the pulse was initially stretched using a highly dispersive, single-mode optical fiber. The pulse was then amplified and subsequently compressed using a double grating compressor [16]. Figure 2.4 is taken from the original CPA paper [15] and shows the design of the compressor used by Strickland and Moruou. This design is still the typical way of compressing pulses after amplification. However, most modern CPA systems now use a grating-based stretcher as well, instead of an optical fiber.

In a typical Ti:Sapphire CPA, the pulse is stretched to around 100 ps prior to amplification. The compressor is then able to decrease the pulse duration down somewhere between 20-50 fs, depending on the amplifier design. In addition to stretching the pulse duration, the number of pulses in the pulse train must be reduced prior to amplification. It is not possible to significantly amplify the full 80 MHz train. To do this, a Pockels cell down-samples the number of pulses to the desired repetition rate for amplification. This repetition rate is largely dictated by the desired output pulse energy, with higher energies requiring a lower repetition rate. As a rough rule of thumb [17], it is very difficult get more than 20W average power out of a Ti:Sapphire system. So, if a pulse energy of 20 mJ is required, then the max repetition rate would be 1 kHz. This is the case for the HITS laser used for many of the studies presented in this thesis. This HITS laser has a repetition rate of 1 kHz with a pulse energy of 20 mJ giving a total output of 20 W.

2.3 Generation of New Frequency Components Through Non-linear Optical Interactions

Up to this point in the chapter, the bandwidth and frequency components necessary for creating an ultrafast pulse have been generated by stimulated emission. Thus, the excited level structure of the gain medium dictates the output spectrum. As previously mentioned, one of the main characteristics of Ti:Sapphire that makes it so well-suited for ultrafast pulse generation is its incredibly large gain bandwidth. While gain materials suitable for mode-locked lasers, other than Ti:Sapphire, certainly exist, they are few and far between. This significantly limits the available frequencies for ultrafast pulses from mode-locked lasers. To produce ultrafast pulse at difference frequencies, a different approach is required.

A process that is directly proportional to the strength of the laser field is referred to as a linear process. Using a more formal definition, the induced polarization of the material, $P(t)$, contains only a linear dependence on the field

$$P(t) = \epsilon_0 \chi^{(1)} E(t), \tag{2.18}$$

where ϵ_0 is the vacuum permittivity and $\chi^{(1)}$ is a materiel dependent property known as the linear susceptibility.

However, the induced polarization can also depend non-linearly on the electric field. Ignoring any spatial dependencies and expressing this as a power series gives

$$P(t) = \epsilon_0(\chi^{(1)} E(t) + \chi^{(2)} E^2(t) + \chi^{(3)} E^3(t) + ...), \tag{2.19}$$

where $\chi^{(2)}$ and $\chi^{(3)}$ are the second and third order susceptibilities respectively.

Grouping all higher order components into the non-linear polarization term, P^{NL}, and inserting the induced polarization into the electromagnetic wave equation gives

$$\nabla^2 E(t) - \frac{n^2}{c^2} \frac{\partial^2 E(t)}{\partial t^2} = \frac{1}{\epsilon_0 c^2} \frac{\partial^2 P^{NL}}{\partial t^2}. \tag{2.20}$$

When $P^{NL} = 0$ then this becomes a homogeneous equation, with no source term, and thus the frequencies present in the field are only those that already exist in $E(t)$, from when it was created. However, when $P^{NL} \neq 0$ then a source term is present that generates new frequencies. $\partial^2 P^{NL}/\partial t^2$ describes the acceleration of the charge in the material and, according to the Larmor formula, an accelerating charge will radiate. The exact frequencies that are generated depend on the fundamental frequencies (already contained in the electric field) and which order of susceptibilities participate in the process. In general, the second or third order susceptibility typically dominate the non-linear response and because of symmetry conditions of the material, rarely participate together[18].

Non-linear interactions that are dominated by the second order non-linear susceptibility are denoted to as two-photon processes. This refers to the fact that, in these interactions, two frequencies components combine to produce a new, third component. The two input frequencies can either sum together to generate a new component in sum-frequency generation (SFG) or the new component can be produced at a frequency equal to the difference of

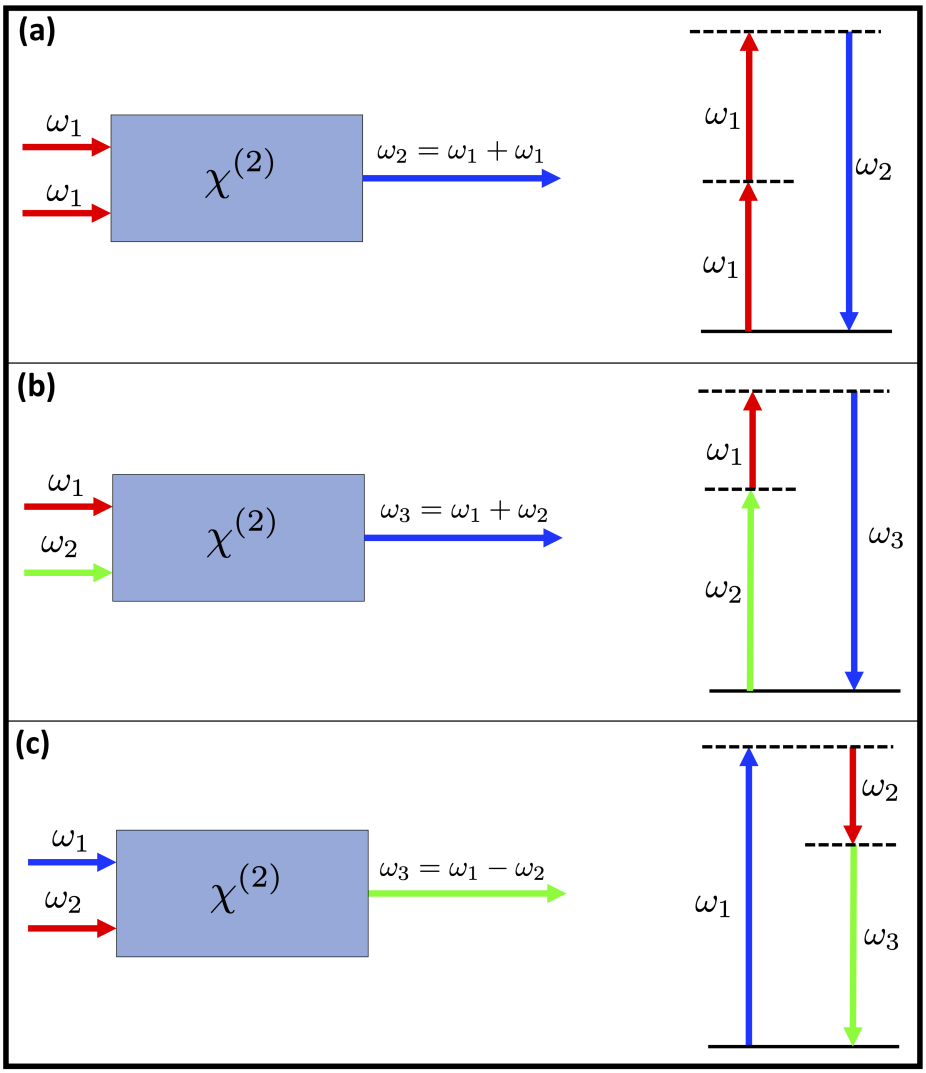

Figure 2.5: *Non-linear frequency mixing with a $\chi^{(2)}$ non-linear crystal. (a) Second harmonic generation. (b) Sum-frequency generation. (c) Difference-frequency generation.*

the input frequencies in the process of difference-frequency generation (DFG). In the degenerate case where two frequencies of the same energy sum together, the process is known as second-harmonic generation (SHG). Figure 2.5 depicts these various cases schematically.

Third order non-linear processes depend on the interaction of three input frequencies. This can be significantly more complicated, with three input frequencies mixing to produce as many as 44 frequency components [18]. Third order non-linearities can also result in a contribution to the induced polarization at the input frequency. This gives rise to the intensity dependent index of refraction responsible for the previously mentioned Kerr effect.

Non-linear optical systems continue to advance in sophistication and capability. The amount of tunability and flexibility researchers now have in generating ultrafast pulses across a wide range of wavelengths is truly amazing. Using the 800 nm output from a CPA based Ti:Sapphire system, it is possible to produce high power pulses from the extreme ultraviolet (XUV) to the long-wave infrared (LWIR). Several of the specific non-linear techniques used in the research presented in this thesis are described in more detail in the next sections.

2.3.1 Optical Parametric Amplification

Several of the studies presented in the upcoming chapters investigate the wavelength scaling of strong-field processes from the near infrared (NIR) regime into the mid infrared (MIR) regime. An optical parametric amplifier (OPA), pumped with the output of a CPA Ti:Sapphire is used to generate these pulses. The OPA uses difference frequency generation to convert the 800 nm Ti:Sapphire pulses into two, longer wavelength pulses. In this process the higher frequency input is referred to as the pump and the output beams are referred to as the signal and idler, with the lower frequency (longer wavelength) being the idler. In a zeroth order sense, the OPA can be viewed as a "photon splitter" where the energy of the input pump photon is split into two lower energy output photons. The energy of the output photons can be tuned continuously but the sum of their individual energies must add up to the energy of the pump photon. Tuning the energy of the signal and idler beams starts with the generation of a seed pulse which is then amplified through the optical parametric amplification process. Selecting the frequency of the seed pulses establishes the output signal and idler frequencies. The OPA used for the work in this thesis (Light Conversion HE-TOPAS prime) is pumped with 18 mJ of 800 nm radiation at a repetition rate of 1 kHz. The amplification is done in three subsequent stages. The conversion efficiency is approximately 30% with a total output pulse energy (combined signal and idler) of 5.5 to 6.0 mJ depending on the wavelength selection. Figure 2.6 shows a schematic of the layout.

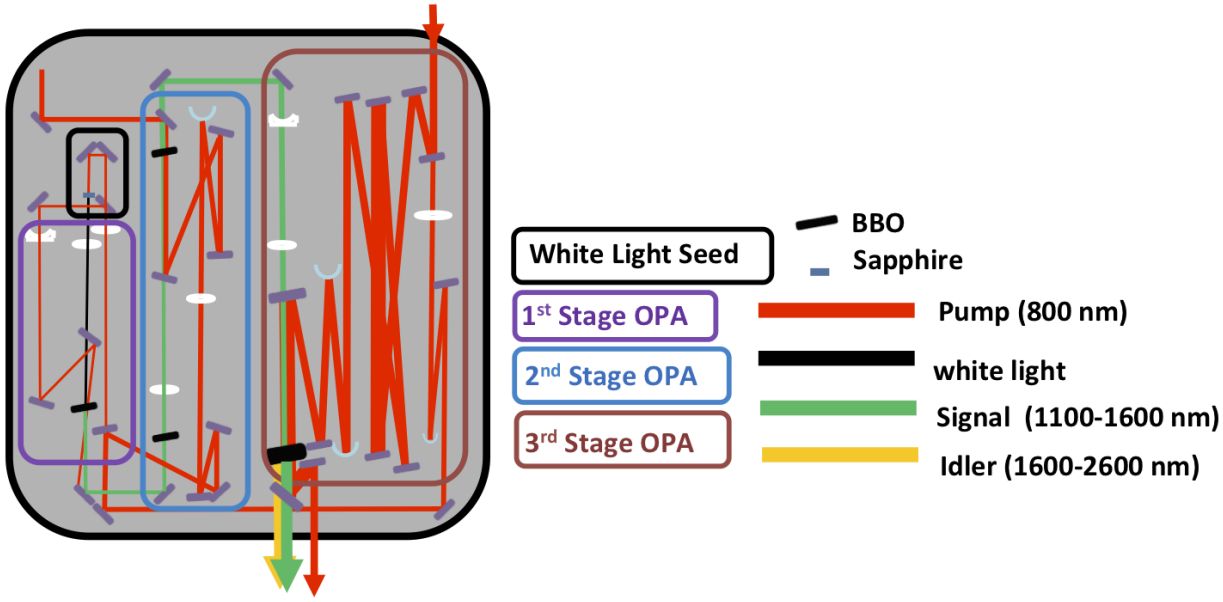

Figure 2.6: *Layout of the high energy OPA used in this thesis. 18 mJ enters the setup from the top right of the figure and is split into four different arms using a series of beam splitters. A few μJ are used to generate a white light signal via self-phase modulation in a sapphire plate in the area circled in black. This produces a weak signal in the NIR (1100-1600 nm) which is then amplified to the 1 μJ level in the first stage, circled in purple, using a BBO crystal. A second amplification stage, circled in blue, amplifies the signal to the 100 μJ level with another BBO. The final amplification stage, circled in red, pumps the resulting signal with approximately 16 mJ of energy, scaling the signal to the millijoule level while simultaneously producing an idler field the milijoule level. Figure and caption adapted from [14].*

2.3.2 Few-Cycle Pulse Generation

Chapter 4 makes extensive use of few-cycle pulses. A pulse is defined as a few-cycle pulse if the pulse duration is short enough that the electric field only undergoes approximately 2-3 optical cycles underneath the envelope. For NIR wavelengths this corresponds to a pulse duration of approximately 5 fs. This is far below the shortest pulse an oscillator can produce, let alone a CPA system. Despite its many wonders, Ti:Sapphire simply cannot support the bandwidth needed to produce pulse durations this short. Instead, a non-linear process must be used to broaden the spectral content of a pulse by generating new frequencies.

This spectral broadening occurs via self-phase modulation (SPM), a nonlinear process also caused by an intensity dependent index of refraction [19]. To achieve this broadening, 1-2 mJ pulses from a Ti:Sapphire amplifier are focused into a hollow-core-capillary, filled with either argon or neon. The pulse is then guided in a gas-filled capillary where the high intensity interaction with the gas, over a long relatively long distance (approximately 1 m), results in an intensity dependent, temporally evolving phase shift on spectral components of the pulse. The overall result is that the pulse spectrum can be significantly broadened. After exiting the fiber, the beam is collimated and sent through a series of anomalous dispersion chirped-mirrors to compensate for the dispersion acquired in the process. The result is a spectrum spanning hundreds of nanometers in the visible and NIR that supports few-cycle pulses. Figure 2.7 shows the layout for producing few cycle pulses.

Ultimately all of these nonlinear frequency conversion techniques are limited in the amount of new frequencies they can be employed to generate. Figure 2.5 shows the degenerate SFG case. A single frequency pumps a $\chi^{(2)}$ medium and resultant frequency output is twice that input, otherwise known as the second harmonic. In a $\chi^{(2)}$ material, no more than two frequencies can mix, so it is not possible to produce higher harmonics in a single stage. The degenerate process also exists for a $\chi^{(3)}$ material, where three photons of the same frequency combine to produce a third harmonic photon. However, this process typically has very low efficiency. It is also possible to use successive $\chi^{(2)}$ materials where the second harmonic produced in the first stage is combined with the fundamental in a second

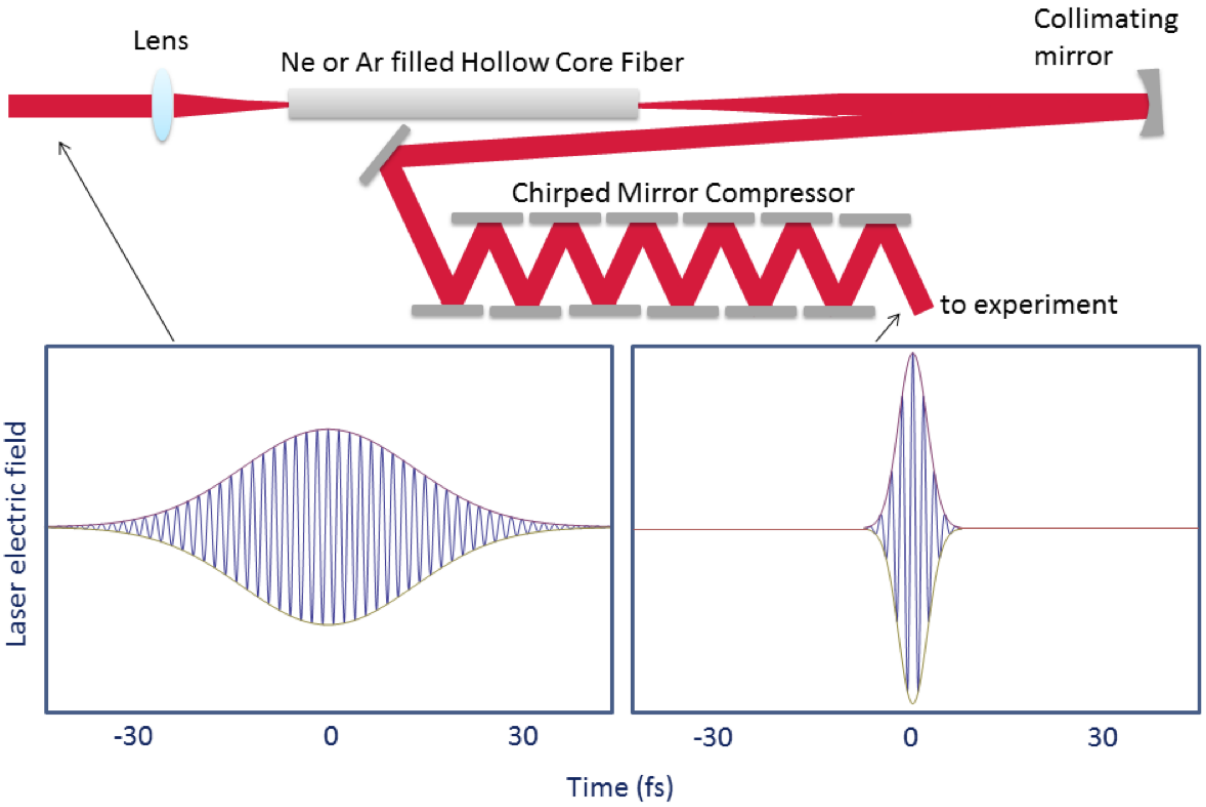

Figure 2.7: *Schematic for generation of few-cycle pulses through self-phase modulation in a hollow-core capillary. Adapted from [20].*

stage to produce the third harmonic. This is a common technique but conversion efficiencies into the third harmonic are typically limited to less than 10%. Additional conversion stages can be used to continue to increase the frequency of the fundamental but the total efficiency of the output plummets. Up to a certain extent the drop in efficiency can be combated by increasing the driving intensity but eventually this will damage the material. Also, finding suitable $\chi^{(2)}$ materials becomes increasingly difficult as the frequency moves into the XUV regime. This is the limit of perturbative non-liner optics and going further requires a different process.

2.4 High Harmonic Generation and Attosecond Pulses

High Harmonic Generation (HHG) is a highly non-linear process that can produce photons with a frequency more than a thousand times the fundamental frequency [21]. The HHG process is also highly non-perturbative, in that the strong driving laser field cannot be treated as a perturbation to the field-free state and the amplitude of the harmonics does not follow perturbative scaling. HHG is best understood with the semi-classical, three-step model [22].

The first step of the three-step model is tunnel ionization. Tunnel ionization is described in greater detail in chapter 3. Briefly, it occurs when the laser field is strong enough to significantly bend the atomic Coulomb potential. This results in a finite barrier between the bound state and the continuum. The electron can then tunnel through this barrier into the continuum. Once in the continuum, the electron feels the full electric field of the laser and is accelerated away from the atomic core. When the laser field changes sign, the electron experiences a force back towards the parent ion. The photoelectron gains kinetic energy during this acceleration in the laser field. This is the second step of the three-step model. When the electron reencounters the ion core there is a possibility for it to undergo photorecombination and return to the ground atomic state. All of the energy the electron gained during ionization and field acceleration is then released in a single, high-energy photon. The maximum energy of this photon is $3.17U_p + I_p$ where U_p is the ponderomotive potential of the laser field and I_p is the ionization potential. Figure 2.8

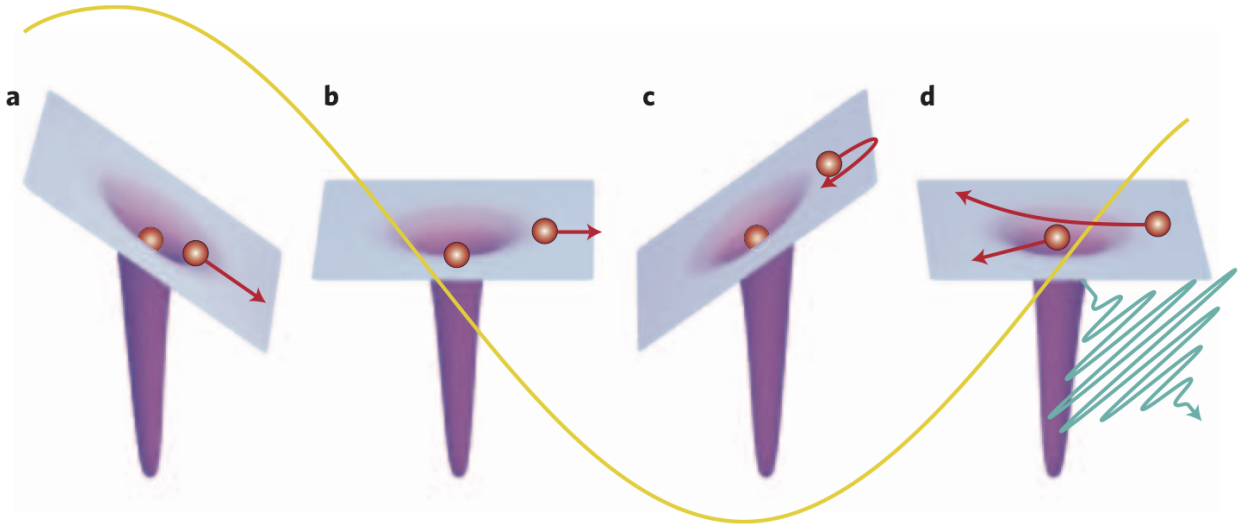

Figure 2.8: *The three-step model of HHG. a-d, An intense femtosecond near-infrared or visible pulse (yellow) extracts an electron wave packet from an atom or molecule. First, the electron is pulled away from the atom near the peak of optical field (a) and accelerated (b). When the optical field reverses, the electron is driven back (c) where it can 'recollide' during a small fraction of the laser oscillation cycle (d). This way the parent ion sees an attosecond electron pulse that can be used directly, or its kinetic energy, amplitude and phase can be converted to high harmonics on recollision. Figure and caption adapted from [23].*

shows a cartoon of the three-step model.

According to the three-step model, electrons emitted into the laser field at different times recollide and recombine with the parent ion after different times. This different amount of time spent in the field results in different electron kinetic energies, which in turn produce different energy photons. The important parameter is when the ionization event occurs with respect to the laser cycle (ionization phase). A specific ionization phase maps to the same recombination energies. This happens twice per laser cycle (both the positive and negative field values) and repeats identically for every cycle where the intensity is high enough to drive ionization. Accordingly, there is a burst of photons twice per laser cycle. This twice per cycle radiation burst gives, through Fourier transform theory, distribution of radiated photon energies over the odd harmonics of the fundamental driving frequency. Using this process researchers have been able to produce harmonic photons with energies extending 1.5 keV [21].

When HHG is driven with a many-cycle pulse, the result is a train of pulses separated

in time by half the cycle time, as described above. However, if the ionization (or more specifically the recombination) can be constrained to a single half-cycle event then only one burst of radiation will occur. Due to the very short window over which both ionization and recombination occur, this pulse can have a duration of less than a femtosecond leading to an attosecond pulse. The first isolated attosecond pulse was demonstrated in 2001 [24]. Isolated attosecond pulses represent the absolute state-of-the-art in ultrafast science. Recently researchers have created isolated attosecond pulses with spectral components spanning the entire water window [25] and with pulse durations of less than two atomic units of time (less than 50 attoseconds) [26].

Chapter 3

Wavelength Scaling of Strong-Field Ionization

After the preceding introductory chapters, this chapter starts the new research portion of the thesis. The following presents an experimental investigation of the photoelectron momentum distribution (PMD) of xenon over a range of wavelengths and intensities. Published, intensity dependent data is very common, particularly for on-axis spectra. Full angular data as a function of intensity is less common and only a few studies have been published that track the full PMD over both wavelength and intensity [27–29]. Even more rare is data using mid-infrared wavelengths. Thus, the significant goal of these measurements is to provide a consistent, self-contained, high-quality dataset that spans a reasonably large range of intensities and driving wavelengths in the near-infrared and mid-infrared regime.

Prior to the experimental details and results, an explanation of strong-field ionization is given along with an introduction to the numerous theoretical approaches currently in use throughout the field. The merits of these theories are discussed in context with their ability to describe the assorted dynamics that occur during photoionization from an intense driving field. Various features within the experiment are identified and interpreted within the framework of presented theoretical models.

3.1 Photoionization

Photoionization is one of the most fundamental physical process to emerge from the study of the interaction of light and matter. In 1921 Albert Einstein famously won the Nobel Prize, not for his theories of relativity, but for his description of the photoelectric effect [30]. Einstein's 1905 paper proposed a solution to resolve the paradox that classical electromagnetic theory could not explain earlier experiments performed by Heinrich Hertz [31] and others, such as Philipp Lenard, just before the turn of the century. These experiments observed that electrical discharges could be initiated by shining light on a metal surface. However, the energy of the electrons ionized from the metal was not proportional to the intensity of the light, as classical electromagnetic theory would suggest, but instead on the frequency of the incident radiation. In his solution to this enigma, Einstein formalized Max Plank's earlier, heuristic formula for black body radiation and proposed that, not only is the energy of light proportional to frequency, but that this energy is carried by discrete packets. We now term these discrete packets of light photons. This quantization of light simultaneously provided the theoretical underpinnings not to just explain the photoelectric effect but also to understanding fundamental physics of blackbody radiation. It would also prove one of the most important stepping stones in the full development of quantum mechanics.

Within the description of the photoelectric effect, the kinetic energy of an electron ionized from a material by light (photoelectron) is given by

$$E_{kin} = \hbar\omega - \phi, \tag{3.1}$$

where $\hbar$ is Plank's reduced constant, ω is the angular frequency of light and ϕ is the work function of the material. The work function is replaced with the ionization potential, I_p, if the target of study is a gas instead of a solid.

This formula suggests that if the photon energy is less than the work function, then photoionization would be energetically forbidden and not occur. This is consistent with the observations Einstein originally sought to explain and would remain the case for much of the 20th century. However, with the invention of the laser, and the ability to generate

optical intensities approaching one Terawatt per square centimeter, this was shown not to strictly be the case. Subsequently, several new regimes of photoionization have since been discovered [32]. A schematic picture of these regimes is shown in figure 3.1. At high enough intensities, it is possible for a material to simultaneously absorb multiple photons, providing the necessary energy to overcome the work function (or ionization potential (I_p) for atoms and molecules) and produce a photoelectron even though the individual photon energy is below the threshold.

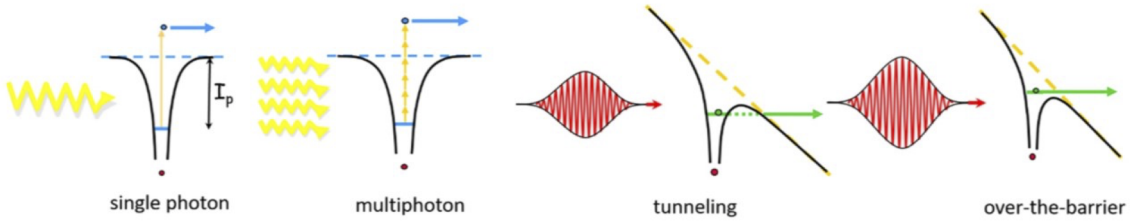

Figure 3.1: *Four regimes of photoionization arranged in order of increasing optical intensity from the left to the right.*

3.2 Theory of Strong-Field Ionization

Multiphoton ionization was first reported experimentally in 1963 when the breakdown of a gas sample was observed in the focus of a pulsed ruby laser [4; 5]. In 1965 Keldysh published his now famous paper [33] laying out the theory of ionization by a strong laser field. In this paper, Keldysh clearly lays out two separate regimes, multiphoton ionization and tunnel ionization. These regimes depend on the strength and frequency of the laser field as well as the ionization potential of the target. This is expressed in terms of the dimensionless adiabaticity parameter, γ, now referred to as the Keldysh parameter:

$$\gamma = \omega \frac{\sqrt{2I_p}}{F}, \tag{3.2}$$

where F is the electric field.

This can also be expressed in terms of the ponderomotive potential, U_p, the cycle averaged energy of an electron oscillating in an electric field.

$$\gamma = \sqrt{\frac{I_p}{2U_p}}, \tag{3.3}$$

where,

$$U_p(eV) = \frac{e^2F^2}{4m_e\omega^2} \approx 9.34 \times 10^{-20} \times \lambda(nm)^2 \times I_0(Wcm^{-2}), \tag{3.4}$$

where e is the electron charge, m_e is the electron mass, I_0 is the intensity of the laser, and λ is the laser wavelength.

When γ is much greater than unity ($\gamma >> 1$) the system is said to be in the multiphoton regime and when γ is much less than unity ($\gamma << 1$) the system is in the tunneling regime.

3.2.1 Multiphoton Ionization

In the multiphoton ionization regime, the laser intensity becomes high enough such that a non-zero probability develops for multiple photons to be absorbed during the laser pulse. However, the intensity is not so strong as to significantly distort the binding potential of the target, as described in the next section. An additional, and perhaps unexpected effect of multiphoton ionization is that nothing a prori prohibits the target from absorbing more than the required minimum number of photons to overcome the ionization potential. This leads to a photoelectron energy spectrum comprised of a series of discrete values, each separated by the photon energy. Photoionization that produces photoelectrons with kinetic energies above the minimum amount required to overcome the ionization potential is collectively known as above threshold ionization (ATI).

For multiphoton ionization in a short, intense laser pulse, the energy of the photoelectron is given by [34]

$$E_n = n\hbar\omega - U_p - I_p, \tag{3.5}$$

where n is the number of photons absorbed.

Two significant deviations from equation 3.1 are present here. The first is of course the multiphoton absorption and the ability to have above threshold ionization. The second is the

inclusion of the ponderomotive potential. This is required, from energy conservation * as the multiphoton ionization occurs under the presence of a strong laser field. A free electron in a laser field necessarily oscillates with a kinetic energy equal to U_p. As such, the photoelectron must gain this extra energy to be present in the field-dressed continuum during the ionization process. The ponderomotive energy essentially raises the ionization potential of the atom. U_p increases linearly with intensity, so not only does the photoelectron energy spectrum consist of a series of peaks, these peaks also shift with changes in the laser intensity.

While the experiments performed 1963 did observe ionization with frequencies below the ionization potential, they did not measure the discrete peaks predicted by equation 3.5. The first measurement of a photoionization energy spectrum showing discrete peaks, separated by one phonon energy, was done in 1979 by Agostini and colleagues [35]. This work is often, referenced as the discovery of above threshold ionization.

For above threshold ionization, the ionization rate has a highly nonlinear dependence on the field strength [32]. This fixes the condition that the majority of ionization occurs very near the peak of the oscillating laser field. This, of course, occurs twice per cycle, but with an opposite sign. Thus, an ionization burst in a given direction occurs once per laser cycle. Fourier transform theory then gives that discrete peaks (spectral components) should be present in the conjugate Fourier domain, which in this case is energy. These spectral peaks are the ATI spectrum. Several studies have shown that if the laser pulse is short enough to limit the ionization burst to a single cycle then there are no ATI peaks present in the spectrum [36]. So, the ATI spectrum can also be viewed as the coherent interference of wave packets originating at subsequent field cycles.

3.2.2 Tunnel Ionization

Tunnel ionization is a general process that occurs when any strong electric field (not just an optical field) significantly bends the binding Coulomb potential of an atom, such that a finite

*If the pulse duration is longer than it takes the electrons to escape the laser focus (typically longer than 1 ps) then photoelectron peaks are not shifted by the ponderomotive potential as they move out of the field-dressed continuum while the laser is still present.

barrier (classically forbidden region) exists between the bound state and the continuum. This is depicted schematically in figure 3.1. The potential of a single electron atom in the presence of a static electric field oriented along the z-direction is given as:

$$V(\mathbf{r}) = -\frac{Z}{r} + Fz, \tag{3.6}$$

where, Z is the nuclear charge. (In general, atomic units, $\hbar = e = m = 1$, are used in this chapter unless otherwise indicated)

With this potential, the time independent Schrödinger equation is separable in parabolic coordinates and the tunnel ionization rate can be calculated. The tunnel ionization rate of a ground state hydrogen atom in a static electric field was originally derived by Landau and Lifshitz [37] and then later extended to a generalized asymptotic Coulomb potential [38]. A nicely explained, full derivation of the generalized static field ionization rate is presented by Bisgaard and Madsen [39]. This rate, w_{stat}, is given as [40]

$$w_{stat} = C_l^2 \frac{\frac{(2l+1)(l+|m|)!}{2(l-|m|)}}{2^{|m|}|m|!} \frac{1}{\kappa^{2Z/\kappa-1}} \left(\frac{2\kappa^3}{F}\right)^{2Z/\kappa-|m|-1} e^{-2\kappa^3/3F}, \tag{3.7}$$

where l is the orbital quantum number, m is the magnetic quantum number, κ is given by $I_p = \kappa^2/2$, and C_l is a target specific coefficient. C_l can only be calculated analytically for the hydrogen atom but tabulated values for some atomic targets can be found in Tong et. al. [41].

Neglecting all of the prefactors, it can be seen that the ionization rate in a static electric field grows exponentially with the strength of the electric field. This is a general characteristic of tunnel ionization as the width of the barrier is inversely proportional to the strength of the electric field (a stronger field bends the Coulomb potential more) and the probability distribution of a wavefunction decays exponentially through a classically forbidden region.

The Keldysh parameter fundamentally represents the ratio of the "time" it takes the electron to quantum mechanically tunnel out of the bound state, to the period of the laser field. Rigorously, this time is an ill-defined quantity for the quantum mechanical process of tunneling. However, the tunneling time can be calculated as the time it would take a

classical electron to traverse the barrier assuming that the motion is classically allowed [42]. The tunneling time can also be defined as the inverse of the tunneling rate

When γ is much less than unity ($\gamma << 1$) the tunneling process is rapid compared to the laser period. When this is the case, the tunnel ionization rate adiabatically follows the laser field in time and the total ionization rate can be calculated by inserting the time varying laser field directly for the static field in equation 3.7. This can then be integrated over an optical cycle to compute the cycle averaged ionization rate. The result is known as the ADK rate or the ADK model after Ammosov, Delone, and Krainov [43]. The ADK rate is

$$w_{ADK} = |C_{n^*l^*}|^2 G_{lm} I_p \Big(\frac{2(2I_p)^{2/3}}{F} \Big)^{2n^* - |m| - 1} e^{-\frac{2(2I_p)^{2/3}}{3F}}, \tag{3.8}$$

where the effective principle quantum number, $n^* = Z/\sqrt{2I_p}$, the effective orbital quantum number, $l^* = n^* - 1$, and the coefficients are:

$$|C_{n^*l^*}|^2 = \frac{2^{2n^*}}{n^* \Gamma(n^* + l^* + 1)\Gamma(n^* - l^*)}, \tag{3.9}$$

and

$$G_{lm} = \frac{(2l+1)(l+|m|)!}{2^{|m|}|m|!(l-|m|)!}. \tag{3.10}$$

The total ionization probability, P_{ion}, by a laser pulse with a temporal dependence given by $F(t)$ is

$$P_{ion} = 1 - exp\Big[\int_{-\infty}^{\infty} w(|F(t)|) \Big]. \tag{3.11}$$

This begins to fail with increasing optical frequencies as the tunneling time becomes comparable to the optical period. However, it has been shown that even when γ is slightly more than one, tunneling is still the dominate ionization mechanism [44].

3.2.3 The Simple Man Model and Classical Propagation in the Electric Field

The ionization rate in equation 3.8 only refers to the process of the electron leaving the bound state. It says nothing about the kinetic energy the electron will possess in the continuum after the laser pulse. Just as the presence of the strong field shifts the energy of the multiphoton peaks in equation 3.5 the laser field has a strong effect on the photoelectron's kinetic energy after tunneling. Decades of research have been put into better understanding this intricate and complicated process.

One of the most important concepts, or parameters, in strong-field ionization is the birth time (or birth phase) of the photoelectron. Different birth times, with respect to the laser field, lead to dramatically different processes. An electron born into the laser field will initially be accelerated away from the parent ion. However, when the field switches sign, the electron then experiences a force and can accelerate back towards the ionic core. The exact dynamics of this process depend strongly on the birth time.

As a simple model, take the case of a monochromatic, CW laser field given by $F(t) = Fcos(\omega t)$. If the electron tunnel-ionizes sufficiently far away from the core, such that the Coulomb potential can be neglected, then the classical equations of motion for the electron are given by [40]

$$\ddot{z} = -Fcos(\omega t), \tag{3.12}$$

$$\dot{z} = -\frac{F}{\omega}sin(\omega t) + v_0, \tag{3.13}$$

and

$$z = \frac{F}{\omega^2}cos(\omega t) + v_0 t + z_0. \tag{3.14}$$

If the electron is born at $z = 0$ with a birth time $t = t_0$ and no initial velocity $\dot{z} = 0$ then

the equations of motion becomes

$$\dot{z}(t) = \frac{F}{\omega}(sin(\omega t_0) - sin(\omega t)), \tag{3.15}$$

and

$$z(t) = \frac{F}{\omega^2}(cos(\omega t) - cos(\omega t_0)) + \frac{F}{\omega}(t - t_0)sin(\omega t_0). \tag{3.16}$$

The kinetic energy of the electron is given by its velocity. If the electron is born at the peak of field ($t_0 = 0$) and goes directly to the detector, it will have zero kinetic energy. If the other extreme occurs, and the electron is ionized at or near the zero of the field ($t_0 = \pi/2\omega$) and goes directly to the detector, it will have a velocity of $\dot{z} = F_0/\omega$. This gives a kinetic energy of

$$E_{kin} = \frac{1}{2}\left(\frac{F}{\omega}\right)^2 = 2U_p. \tag{3.17}$$

Evidently, the maximum energy a direct photoelectron can have is twice the ponderomotive energy. As shown by equation 3.8 the ionization rate depends exponentially on the strength of the field. So, one would expect exponentially more electrons to be ionized near or at the peak of the field than near the zero of the field. This would predict an energy spectrum containing many low energy electrons with decreasing yield down to electrons with a maximum energy of $2\,U_p$. It turns out this is consistent with experimental observations.

If this was the complete story, then strong-field physics would be quite boring and most likely would have been left behind decades ago in physicist's pursuits of more exciting areas. Luckily, this is not the case. Equation 3.16 also predicts an additional possibility, one that has had profound implications not just for strong-field physics but also for the entire field of ultrafast science.

After tunnel ionization and initial acceleration by the laser field, the electron need not leave the field. It can in fact be driven back towards the parent ion as the field switches sign, accelerating and gaining energy along the way. If the photoelectron returns to the origin at

a time t_r then equation 3.16 gives

$$cos(\omega t_r) - cos(\omega t_0) + \omega(t_r - t_0)sin(\omega t_0) = 0, \tag{3.18}$$

providing a relation for the return time in terms of the birth time.

The kinetic energy of the electron, at the time of return, given by equation 3.15, is

$$E_{kin} = \frac{1}{2}(\dot{z}(t_r))^2 = 2U_p(sin(\omega t_0) - sin(\omega t_r))^2. \tag{3.19}$$

Using equations 3.18 and 3.19 together it can be found that the electron returns with a maximum energy of $3.17U_p$ when it is born with $\omega t_0 = 17^\circ$ (with respect to the peak of the laser field).

When the electron returns to the ion core, there are several distinct possibilities that can occur. The electron can recombine with the ion, releasing its kinetic energy (as well as the binding energy of the atom) in the form of a single, high-energy photon. This is the process that the whole field of high harmonic generation is based on. The maximum emitted photon energy is $3.17U_p + I_p$. This has long been known to be the cutoff energy for high harmonic generation. The recolliding electron can also inelastically rescatter and further ionize the core. This process is known as non-sequential double ionization (NSDI) or non-sequential multiple ionization (NSMI) and is the dominate mechanism for multiple ionization in intense, infrared laser fields [45; 46]. The final possibility is that the returning electron can elastically rescatter at an angle θ_r.

After elastic rescattering, the velocity components parallel($\hat{z}$) and perpendicular ($\hat{y}$) to the polarization are

$$\dot{z}(t) = -\frac{F}{\omega}[sin(\omega t) - sin(\omega t_r + cos(\theta_r)(sin(\omega t_r) - sin(\omega t_0))], \tag{3.20}$$

and

$$\dot{y}(t) = -\frac{F}{\omega}sin(\theta_r)(sin(\omega t_r) - sin(\omega t_0)). \tag{3.21}$$

The averaged kinetic energy of the rescattered electron is

$$E_{kin} = 2U_p[sin^2(\omega t_0) + 2sin(\omega t_r)(1 - cos(\theta_r))(sin(\omega t_r) - sin(\omega t_0))]. \quad (3.22)$$

Again, equation 3.18 can be used to find the birth time corresponding to the maximum energy. In this case, $\omega t_0 = 14°$ gives a maximum kinetic energy of $10\,U_p$ for direct backscattering ($\theta_r = 180°$). As a note, U_p must be subtracted from the calculation to give the correct final energy for eleastic backscattered photoelectrons [40] Electrons that are rescattered in the forward direction will have a final energy at the detector of less than $2\,U_p$.

3.2.4 Strong-Field Approximation Ionization Theories

These simple calculations reproduce three of the most important results in strong-field science, the $2\,U_p$ cutoff energy for direct ionization, the $10\,U_p$ cutoff energy for directly backscattered photoelections and the HHG cutoff of $3.17\,U_p + I_p$. Despite this, it still took decades and hundreds of experiments for the field to arrive at a consensus as to full picture (for a recent review see [47]). In this model, all that was assumed was that the electron tunnel ionized with zero initial velocity and then was classically propagated under the influence of the only the laser field. This is often referred to as the simple man model (SMM), although that term in general is often extended to any calculation where the electron dynamics are treated purely classically and propagated using Newtons equations, no matter the local potential.

The above calculations proved adequate in reproducing the cutoff laws. They did however neglect several major (and a whole host of minor) effects important to photoelectron rescattering. In many ways, it is either a miracle or perhaps even a concerning happenstance that a calculation that neglects so many aspects (finite tunneling distance and the Coulomb potential of the parent ion to name two) is able to predict anything with quantitate accuracy. One of the other aspects specifically excluded so far is multiple rescattering events. This classical calculation also expressly excluded the possibility for the interference of different electron trajectories. Both the possibility of multiple rescattering events as well

as the coherent interference between trajectories lead to incredibly detailed photoelectron distributions.

While certainly insightful and to some extent quantitatively accurate, these simple theories, the ADK tunneling rate and the SMM photoelectron cutoff energies, do not describe the entire strong-field ionization process. Neither give both the rate and the resultant spectrum. (Although, in some cases, they can be bootstrapped together to produce reasonably accurate results.) The first "full" theory of photoionization in a strong field was laid out by Keldysh (in the same paper where the Keldysh parameter originates). In this paper Keldysh uses what is now referred to as the Keldysh ionization ansatz [48]. Theories that use this type of approach are often referred to as non-perturbative theories. This is not to suggest that the laser field does perturb the quantum system. In fact, it is quite the opposite, the laser disturbs the system so strongly that treating the laser interaction using perturbation theory around the original state would be highly inaccurate.

The Keldysh ionization ansatz states the probability, $M(\mathbf{p})$ that a photoelectron is measured with a given momentum ($\mathbf{p}$) is [48]

$$M(\mathbf{p}) = -\frac{i}{\hbar}\int_{\infty}^{\infty} \langle \Psi_{\mathbf{p}} | \, V_{int}(t) \, | \Psi_0 \rangle \, dt, \tag{3.23}$$

where Ψ_p is the final state wavefunction, $V_{int}(t)$ is the electron field interaction operator, and Ψ_0 is the bound state wave function unperturbed by the laser field. In the Keldysh model

$$\Psi_0 = \psi(r) e^{iI_p t/\hbar}, \tag{3.24}$$

with

$$\psi(r) = \sqrt{\frac{\kappa}{2\pi}} \frac{e^{-\kappa r}}{r}, \tag{3.25}$$

and

$$\kappa = \sqrt{2I_p}. \tag{3.26}$$

V_{int} is expressed in the velocity gauge as

$$V_{int}(\mathbf{r},t) = -i\mathbf{A}(t)\nabla + \mathbf{A}^2(t), \tag{3.27}$$

where $\mathbf{A}(t)$ is the vector potential defined by $\mathbf{E}(t) = -\dot{\mathbf{A}}(t))$, with $\mathbf{E}(t)$ being the electric field strength of the laser.

The final state wavefunction, $\Psi_{\mathbf{p}}$, is the Volkov wavefunction, also expressed in the velocity gauge

$$\Psi_{\mathbf{p}}(\mathbf{r},t) = \frac{1}{(2\pi)^{3/2}} exp\Big[i\Big(\mathbf{v}_{\mathbf{p}}(t)(r) - \frac{1}{2}\int_{-\infty}^{t} \mathbf{v}_{\mathbf{p}}^2(t^{'})dt^{'}\Big)\Big], \tag{3.28}$$

where, in the dipole approximation, $\mathbf{v}_p$ is

$$\mathbf{v}_{\mathbf{p}}(t) = (\mathbf{p} + \mathbf{A}(\mathbf{t})). \tag{3.29}$$

The total probability of ionization, W, can then be calculated by integrating over all momentum space

$$W = \int |M(\mathbf{p})|^2 d^3p. \tag{3.30}$$

The concept of expressing the final state wavefunction as a Volkov wavefunction was first proposed by Reiss in 1962 [49]. The Volkov wavefunction describes a free electron in the presence of a laser field. As such, it contains no functionality from the Coulomb potential. Thus, equation 3.23 approximates strong-field ionization using an initial bound state wavefunction (that completely ignores effects from the laser field) and a final state wavefunction (that completely ignores the coulomb potential). This is the essential tenant of the strong-field approximation (SFA) and the SFA theory, which is sometimes referred to as KFR theory for Keldysh [33], Faisal [50], and Reiss [51]. In practice these are three distinct theories, but all are based on the foundation of the strong-field approximation.

Strong-field approximation theories can also be constructed in terms of what are referred to as "quantum trajectories" [52]. These formulations follow the same logic originally proposed by Feynman in his path integral treatment of quantum mechanics. This states that

a quantum mechanical process can be described by the superposition of all paths that connect the initial and final state of the system. Each path carries a complex weight with the phase equal to the classical action acquired along the path. In the process of evaluating the integrals that arise from equation 3.23, the method of stationary phase or the saddle point approximation (SPM) is commonly applied. This is mathematically equivalent to treating the ionization process with Feynman path integrals. An important distinction however, is that the trajectories calculated using the SPM, within the strong-field approximation, follow classical trajectories (while acquiring a complex phase), while in general, Feynman path integrals have no such restriction. The classical trajectory is given by the path that minimizes the action acquired during the path from initial to final state. The quantum trajectory approach to strong-field ionization is formalized by the imaginary time method (ITM) [53].

As SFA completely neglects the Coulomb potential, it only produces results describing direct ionization and is incapable of describing the high energy photoelectrons that are produced by direct back scattering with the ion core.

It turns out that leaving out the Coulomb potential also has a large effect on the total ionization yield [45]. Perelomov-Popov-Teren'ev addressed this shortly after Kelydsh published his original results. In this work, Perelomov-Popov-Teren'ev derive a generalized analytical rate equation [38], (PPT) rate, that is quite capable of predicting ionization rates over a wide range of wavelength and intensities, making up both the tunneling and multiphoton regimes [54]. In the limit of zero frequency (long wavelength) the PPT rate reduces to the ADK rate given by equation 3.8.

There have been multiple approaches to modifying SFA to include the Coulomb potential [48]. In the simplest form, this can be done by adding a perturbative term to the field interaction operator in equation 3.23 that considers rescattering as a first order correction to the zeroth order direct electrons. This amounts to making the first Born approximation. This is known as the improved Keldysh approximation or the improved SFA (ISFA) or sometimes as SFA2. More detailed explanations can be found in publications by Lohr et al. [55] and in a review article on SFA by Becker and colleagues [56].

Other approaches have also been developed that treat the Coulomb potential. The two

most common in use are the Coulomb Corrected Strong-Field Approximation (CCSFA) [57] and the classical trajectory Monte Carlo (CTMC) method [58]. In CCSFA the Coulomb field is added in as perturbation to the quantum trajectory originally calculated using SFA with the ITM. An interesting effect of this is the emergence of two new trajectories not originally present in non-Coulomb corrected ITM calculations [57]. These Coulomb-induced trajectories are responsible for producing the highly studied low energy structure [59] and the off-axis side lobes, also referred to as "spiders" [27], which are interpreted as the inference of these new trajectories with the original trajectories from non-Coulomb corrected SFA [59; 60].

One very important aspect not accounted for in any of the theories and models presented is the excited bound state of the target atom. Ionization is far from the only channel possible under exposure to a strong laser field. Multiphoton absorption can also occur to one or more excited states. Unlike the continuum, these bound states have a strict resonant condition with the number of photons absorbed. In general, this condition means that it is unlikely that an integer number of photons will add up exactly to the energy needed to transition to the excited state, making that transition unlikely. However, the high lying states can be significantly Stark-shifted by the strong laser field. As these states lie very near the continuum, they are also shifted down by the ponderomotive energy. When this shift brings a state into resonance with an integer number of photons it becomes what is known as a Freeman resonance [61]. The resonant condition makes the transition probability from the bound state to the excited state much higher than ionization to the continuum. Once the atom has been promoted to the excited state it can then be photoionized, often with only a single or a few photons. The overall cross section for multiphoton ionization by this mechanism can be much, much larger than straight multiphoton ionization [29]. The energy of the photoelectron from the Freeman resonance channel is given by

$$E_{kin} = n\hbar\omega - E_b, \tag{3.31}$$

where E_b is the binding energy of the excited state and n is number of photons absorbed to

ionize from the excited state.

Since both the high-lying excited state energy and the continuum shift by U_p, the energy of the photoelectron does not depend on U_p and thus will not shift with laser intensity. This is often the condition used experimentally to separate photoelectron peaks from resonant ionization from those generated by standard multiphoton ionization.

3.2.5 Time-Dependent Schrödinger Equation

To date, no successful modification of the SFA has emerged that incorporates atomic structure. As such, theoretical approaches that include atomic structure are largely limited to solving the time-dependent Schrödinger equation. With all of the models, pictures, approximations and methods introduced here to represent strong-field ionization, it is important to remember that solving the time-dependent Schrödinger equation (TDSE) is the only calculation that truly represents the fundamental physics. This seems like an obvious statement but with the sheer volume of work and publications devoted specifically to arguing the merits of various methods it is very easy to forget that everything else is just a model. That is not to say that models such as SFA or SMM do not have value. Quiet the opposite is true and many of these models offer a clear picture of what the important aspects of the underlying physics are.

To ultimately test the validity of an approximation, it must be compared against the TDSE. Of course, comparison to experiment is the ultimate goal of any physical theory but the extreme difficultly of matching the exact conditions present in an experiment make the TDSE a more ideal benchmark. In this sense the TDSE, is often viewed as a "numerical experiment". If no approximations are made in solving the TDSE this is accurate up to the precision of the numerical calculation.

However, only in very specific cases is it tractable to solve the TDSE exactly. Several approximations are almost always required. The most common of these is the single active electron (SAE) approximation. For most strong-field atomic processes this approximation remains quite accurate. Still, even with the SAE, full TDSE calculations can be extremely

numerically expensive. A second disadvantage, aside from the computational resources required, is the somewhat paradoxical fact that it is often difficult extract the exact origin of effects given by the TDSE solution. Nevertheless, it still represents the most complete description.

3.3 Experiment and Results

To study how the various aspects of strong-field ionization evolve as a function of, intensity, wavelength, ponderomotive energy, and Keldysh parameter we employ ultrafast pulses produced using a chirped pulse amplified (CPA) Ti:Sapphire laser system as well as an optical parametric amplifier (OPA) pumped using the same laser. With these systems, we are able to generate ultrafast pulses over a wide range of the mid-infrared (MIR) regime. Four specific wavelengths are used for this study, 785 nm, 1410 nm, 1825 nm and 2025 nm. Full photoelectron momentum distributions were collected using a velocity map imaging (VMI) spectrometer.

The Ti:Sapphire laser system is described in greater detail in section 4.3 and in reference [62]. Briefly, it's consists of a mode-locked oscillator running at 80MHz that seeds a two-state, multipass amplifier system (KM Labs Red Dragon Class). The total output is 20 W consisting of a 1 kHz, 20 mJ pulse train with a pulse duration of 25 fs. 18 mJ of this output are used to pump a high-energy OPA (Light Conversion HE-TOPAS prime). The OPA is a three stage, white-light seeded, OPA based on beta-barium-borate (BBO) conversion crystals. The signal can be tuned from 1100 nm to approximately 1550 nm while the idler can reach up to approximately 2400 nm. The signal and idler beams are separated in the far field by tuning the OPA for a very slight, non-colinear overlap in the final amplification crystal. This is done to avoid the need for transmissive beam separators which add dispersion and degrade the mode quality. Additional information about the OPA can be found in [14].

For the photoionization studies, each beam is individually coupled into the setup depicted in figure 3.2. A half waveplate rotates the polarization into a polarizer used for attenuation of the beam. The polarizer consists of two germanium plates set at Brewester's angle. Each

reflection off the germanium plate reflects approximately 80 % s-polarization and 0.1% p-polarization. Two reflections give an extinction ratio of better than 1/1000 for the output s-polarized beam. A second waveplate is then used to rotate the beam back to p-polarization before being focused into the chamber with an uncoated, plano-convex, CaF2 lens. A 500 mm lens is used for the 1410 nm, 1825 nm and 2025 nm beams while a 1000 mm lens is used for the 785 nm beam. An uncoated, 1 mm thick, UV fused-silica plate is used as an entrance window into the chamber for all wavelenghts.

The pulse duration for each individual wavelength is measured using a second-harmonic generation (SHG) frequency resolved optical gating (FROG) device prior to the focusing lens. Compensation glass is placed in the beam path prior to the FROG to match the dispersion from the focusing optic and the entrance window. The FROG, also shown schematically in figure 3.2, is based on an all-reflecting, split d-mirror design to allow for use with all wavelengths. A 10 μm thick BBO is used for doubling. The SHG spectrum is measured using a fiber-coupled spectrometer (Stellarnet Bluewave). The FROG v3.2.2 (Femtosoft Technologies) program is used to evaluate the measured spectrogram and recover the pulse duration. The durations are 28 fs, 40 fs, 60 fs, and 85 fs for the 785 nm, 1410 nm, 1825 nm and 2025 nm beams respectively.

The VMI spectrometer is based on a high-voltage, thick-lens design. More details about the design can be found in [63] and [64]. By adjusting the voltage on the repeller plate, the maximum transverse photoelectron collection energy can be tuned from 10 eV to 1000 eV. This allows the spectrometer to be adjusted to provide maximum resolution for the individual process being investigated. For the results reported here, repeller voltages of -250 V, -500 V and -4,000 V are used, giving a maximum transverse photoelectron collection energy of approximately 12 eV, 25 eV and 175 eV respectively. The full, 4π solid angle of electron emission is collected up to these energies. The spectrometer rings are surrounded by a μ-metal shield to reduce stray magnetic fields. The photoelectrons are accelerated onto an 80 mm micro-channel-plate (MCP) in a chevron configuration (Hammamatsu F2226-24P218) with a P47-type phosphor screen at the output. The front MCP plate is grounded while the voltage across the MCP stack and is gated by adding a -700 V gating pulse to a base

voltage of -1200 V for a 400 ns window around the arrival time of the electron burst. This dramatically reduces the background signal of the measurements. The phosphor screen is capacitively coupled to, and floated -3500 V from the back MCP plate. A low noise, 12-bit camera (PCO-Sensicam QE) is used to collect images from the phosphor. Depending on the strength of the signal, between 100 and 1,000 laser shots are collected per camera exposure. For most experimental parameter sets approximately 3 million laser shots are acquired, but this is varied throughout the experiment to maximize the number of runs that can be taken while acquiring adequate statistics. For very low intensities, as many as approximately 30 million laser shots are collected.

Xenon is used at the target gas for these studies. The gas is inserted into the interaction chamber using an effusive gas jet through a small hole in the center of the repeller plate. The chamber pressure is adjusted based on the count rate to maximize the amount of data collected while also avoiding detector saturation and space charge effects. For lower intensities, the xenon pressure is raised to as high as 5×10^{-6} torr while for high intensities, it is decreased to as low 1×10^{-8} torr. The background chamber pressure is below 4×10^{-9} torr. Varying the backing pressure allows the highest statistics to be collected in an experimentally realistic time. This makes ionization yield comparisons between the various intensities difficult to impossible. However, as the predominate goal of the experiment is high-quality PMDs this is not a major concern.

After the raw image was collected, several post processing steps are performed. First, the image is rotated and centered so that the laser polarization lies vertically in the plane of the image and the center of the distribution falls directly in the center of the image. Then to overcome several low efficiency spots in the detector and to increase overall statistics, the four quadrants are averaged together. After averaging, the distributions are inverted using an iterative Abel transform to reconstruct the 3D velocity and angular distribution of the photoelectrons and therefore obtain photoelectron momentum maps [65]. Figure 3.3 shows the raw, quadrant averaged, and inverted image for several representative PMDs.

The focusing condition of the VMI spectrometer maps velocities to a specific point onto the detector. To convert this velocity distribution into an energy spectrum, a transfer func-

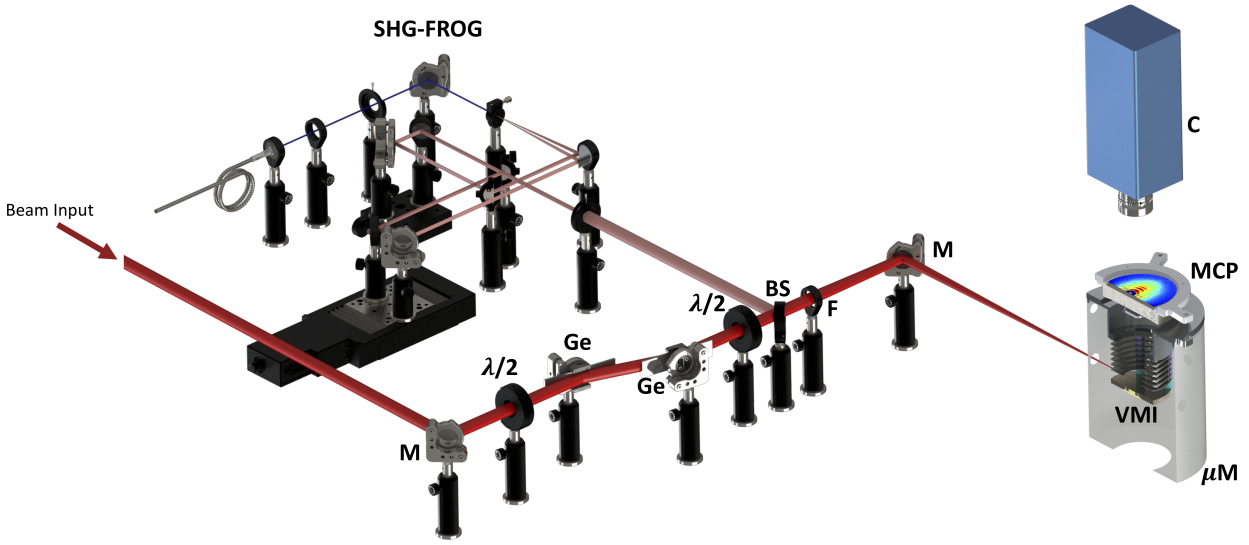

Figure 3.2: *Experimental setup for studying photoelectron momentum distributions with various IR wavelengths. M-silver mirror, λ/2 -zero order air-spaced half waveplate, Ge-germanium plate, BS-removable beamsplitter, F-focusing lens, SHG-FROG- homebuilt second harmonic frequency resolved optical gating (FROG) device for pulse duration characterization, μM- μ metal shield, VMI- velocity map imaging spectrometer, MCP- microchannel plate and phosphor detector, C-camera*

tion is needed. While it is theoretically possible to calculate this transfer function by simulating the electrostatic fields in the spectrometer, it is typically much more accurate to build this map from the measurement of known velocities. The ATI spectrum itself can provide this reference. For the work presented here, the calibration is done using the spacing of the ATI peaks from the 785 nm pulses. Additional information can be found in [64; 66].

Accurately calibrating the intensity is a critical yet often extremely difficult process in many strong-field ionization experiments. In this study, two independent methods are used, sometimes in combination, depending on the wavelength. The first method is based on ponderomotive shift of the ATI photoelectron energy with intensity, as given in equation 3.5. A series of ATI spectra are taken with several known input pulse energies. A single, multiphoton ATI order is identified in each of these spectra and the absolute shift in photoelectron energy of the ATI peak is extracted. The ratio of shift in ATI energy to the difference in pulse energy is then used calculate a constant that links the pulse energy to the peak focal intensity.

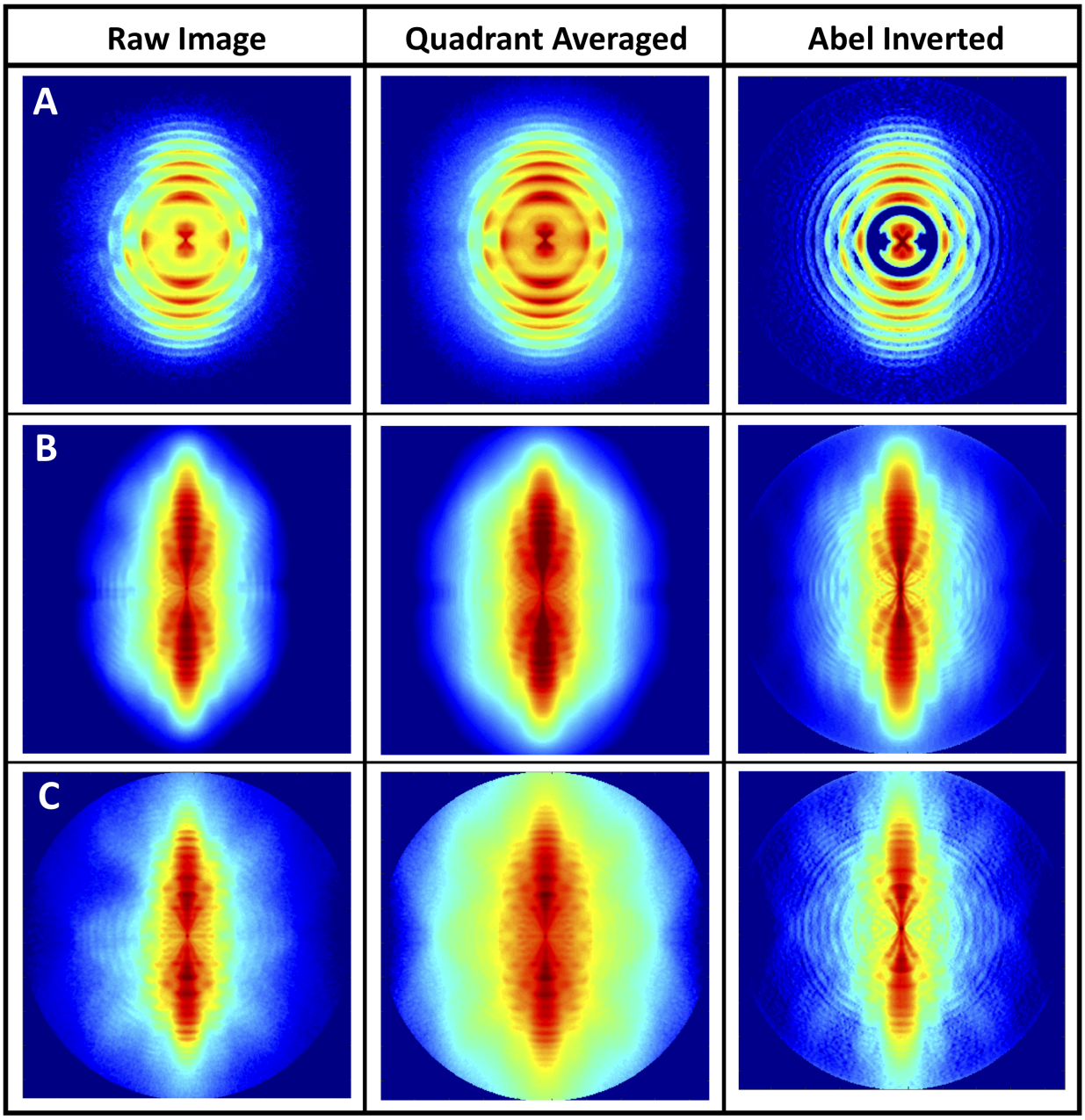

Figure 3.3: *Sample of the acquired raw PMD images and the stages of postprocessing and inversion. The columns are labeled and show, left to right, the raw image, the image after the quadrant averaging procedure, and the image after inverse Able inversion. The rows represent three different experimental conditions, A-785nm* 1×10^{13} *W/cm*^{2}*, B- 1825nm* 4.9×10^{13} *W/cm*^{2}*, C- 2025nm* 1.5×10^{13} *W/cm*^{2}

To prove this mathematically, let the peak intensity, for given pulse energy be expressed as

$$I_0 = \alpha E_p, \tag{3.32}$$

where α is the yet as undetermined calibration constant and E_p is the measured pulse energy.

The ponderomotive potential is linear with intensity giving

$$U_p = \beta I_0 = \alpha\beta E_p, \tag{3.33}$$

where β is the appropriate, wavelength dependent, scaling constant.

Inserting this into equation 3.5 gives

$$E_n = n\hbar\omega - \alpha\beta E_p - I_p, \tag{3.34}$$

where again, E_n is the energy of the ATI peak corresponding to n-photon absorption.

Using this expression, the shift in energy for the n-photon absorption peak (ΔE_n) is

$$\Delta E_n = -\alpha\beta\Delta E_p, \tag{3.35}$$

where ΔE_p is the corresponding difference in pulse energies. The negative sign indicates that ATI peaks shift to lower values for increasing pulse energy (intensity).

Comparing equation 3.33 to equation 3.4 and solving for α gives the final expression for the calibration constant between pulse energy and peak focal intensity

$$\alpha = -9.34 \times 10^{-20}\lambda^2(nm)\frac{\Delta E_n}{\Delta E_p}. \tag{3.36}$$

If the shift of the ATI peak can be cleanly measured, then this method can give very accurate intensity calibrations, typically on the order of 10 % or better, if the position to energy calibration of the VMI is performed accurately and all other sources of error are low. This level of accuracy is possible because this method can be performed over a series of

pulse energies and photon orders, providing higher statistics than other intensity calibration methods.

However, for longer wavelengths, this method can be challenging as the absolute ponderomotive shift in photoelectron energy grows quadratically while the spacing between photon peaks decreases. This has the effect that even a small change in pulse energy can cause the ATI peak to jump multiple photon orders. An additional complication arises from the fact that Freeman resonance peaks play a larger role in the photoelectron spectra for ionization with longer wavelengths. When this is the case, the ponderomotive shift intensity calibration procedure can still be used but great care needs to be taken to correctly select the ATI peaks.

For this study, the ponderomotive shift method was found to work successfully for all wavelengths but was quite difficult at 1825 nm and 2025 nm, resulting in a larger estimated error bar of 25%. This number is conservatively adopted as the estimated error for all wavelengths. Figure 3.4 shows the on-axis, photoelectron energy spectrum for five increasing pulse energies at 785 nm. Three ATI peaks are identified and the ponderomotive shift is clear.

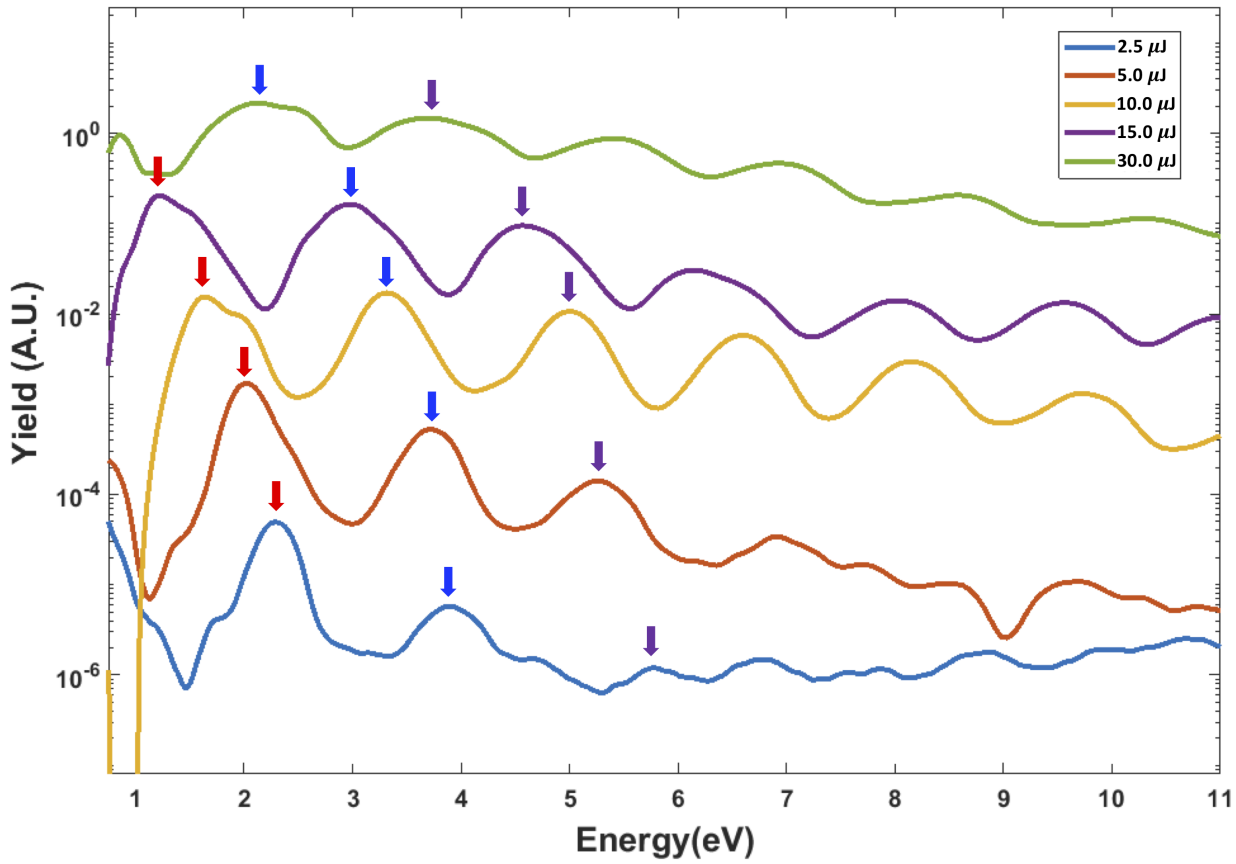

Figure 3.4: *On-axis energy spectra for 5, 785nm measurements with successively increasing input pulse energy. A vertical constant offset has been applied to some of the lines to make the peak shift easier to visualize. Solid color arrows mark the peak of single ATI order. These peaks shift to lower energy with increasing pulse energy which is used to calibrate the intensity.*

The intensity calibrations at 1410 nm and 1825 nm are also checked to be consistent with the $2U_p$ and $10U_p$ cutoffs. Figure 3.5 shows the corresponding spectra for this. The $2U_p$ is primarily selected and the $10U_p$ is examined for consistency. In both cases, the indicated $2U_p$ cutoffs agree to within 20% of the intensity retrieved with the ponderomotive shift calibration method.

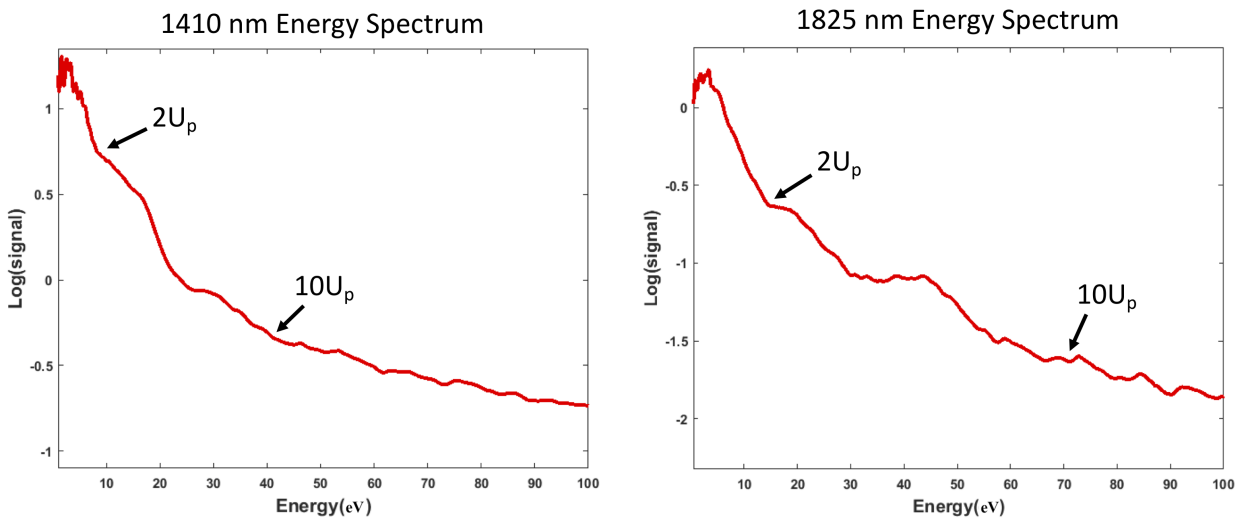

Figure 3.5: *On-axis energy spectra taken with a VMI repeller voltage of -4 kV. The $2U_p$ and $10U_p$ cutoffs are used to verify the calibrate intensities. For both plots, the $2U_p$ was selected first and the $10U_p$ point was found and evaluated for consistency. $10U_p$ cutoffs are often very difficult to cleanly identify.*

Figure 3.6 (multipage) shows plots of the photoelectron momentum distribution, on-axis energy spectrum and angular integration for the range of laser wavelengths and intensities studied. The log of the yield is plotted, and the color scale is adjusted individually for each PMD to maximize visibility of all of the various features. For each set of plots the wavelength, peak intensity, ponderomotive potential energy, and Keldysh parameter are listed. Additionally, a series of dotted arcs in the bottom right quadrant indicate the position of the $0.2U_p$, $2U_p$ and $10U_p$ values to the extent that they fall on the detector. The evolution and nature of the various features present in the data set are discussed in more detail in the following section.

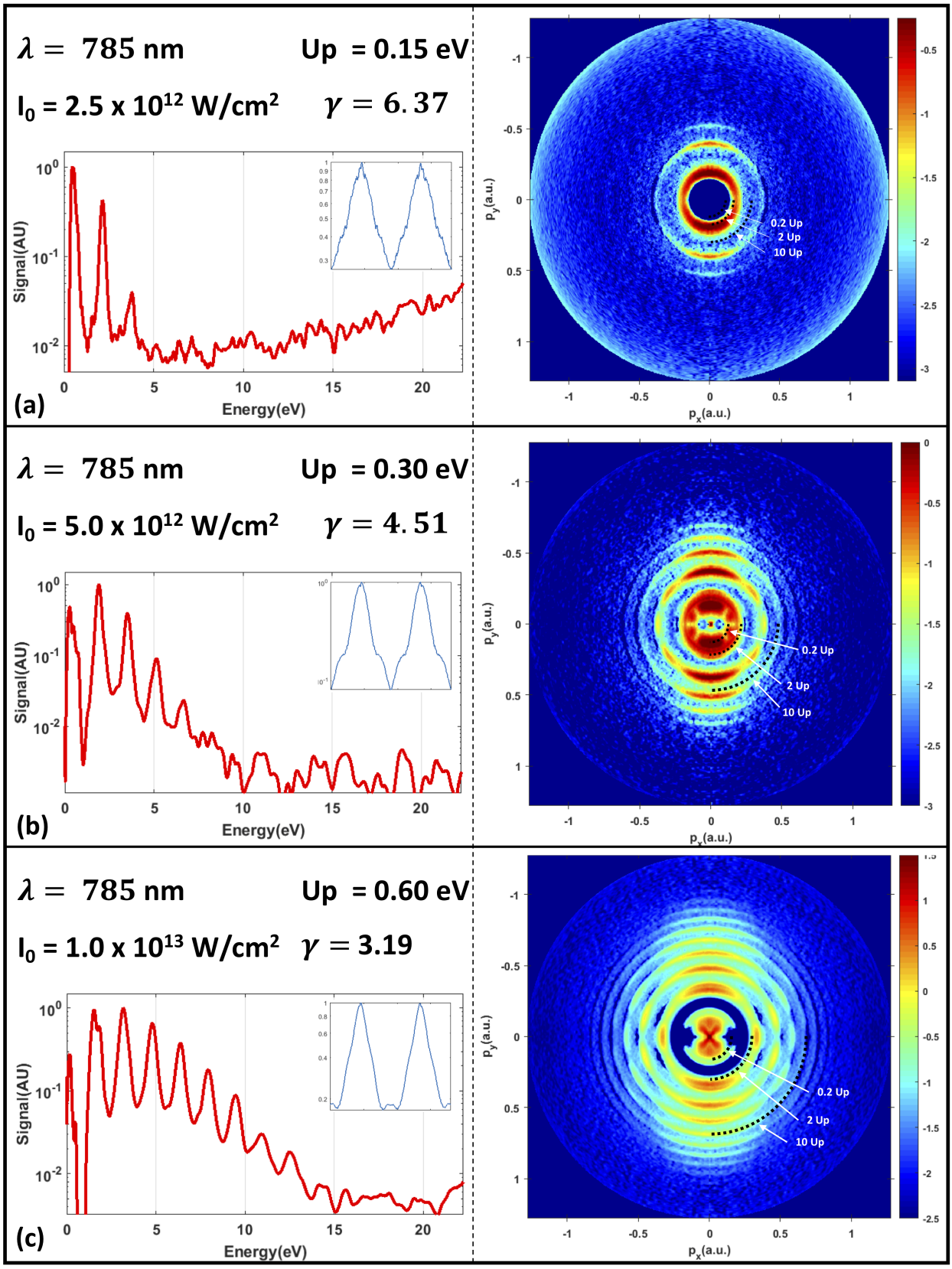
λ = 785 nm
Up = 0.15 eV
I0 = 2.5 x 10^12 W/cm^2
γ = 6.37
Signal(AU)
Energy(eV)
(a)
0.2 Up
2 Up
10 Up
py(a.u.)
px(a.u.)
λ = 785 nm
Up = 0.30 eV
I0 = 5.0 x 10^12 W/cm^2
γ = 4.51
Signal(AU)
Energy(eV)
(b)
0.2 Up
2 Up
10 Up
py(a.u.)
px(a.u.)
λ = 785 nm
Up = 0.60 eV
I0 = 1.0 x 10^13 W/cm^2
γ = 3.19
Signal(AU)
Energy(eV)
(c)
0.2 Up
2 Up
10 Up
py(a.u.)
px(a.u.)

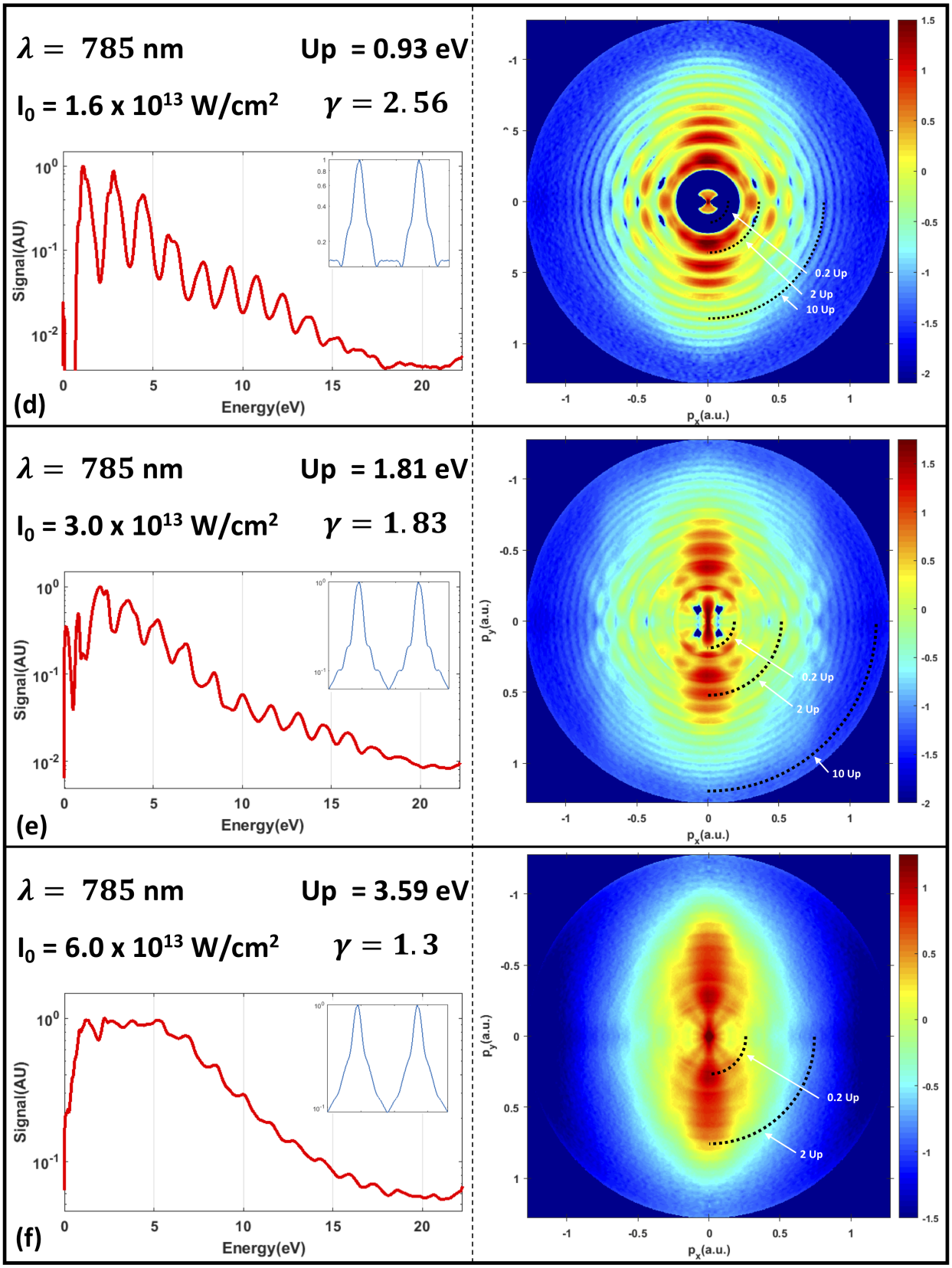
λ = 785 nm
Up = 0.93 eV
I0 = 1.6 x 10^13 W/cm^2
γ = 2.56
Signal(AU)
Energy(eV)
(d)
0.2 Up
2 Up
10 Up
px(a.u.)
λ = 785 nm
Up = 1.81 eV
I0 = 3.0 x 10^13 W/cm^2
γ = 1.83
Signal(AU)
Energy(eV)
(e)
0.2 Up
2 Up
10 Up
py(a.u.)
px(a.u.)
λ = 785 nm
Up = 3.59 eV
I0 = 6.0 x 10^13 W/cm^2
γ = 1.3
Signal(AU)
Energy(eV)
(f)
0.2 Up
2 Up
py(a.u.)
px(a.u.)

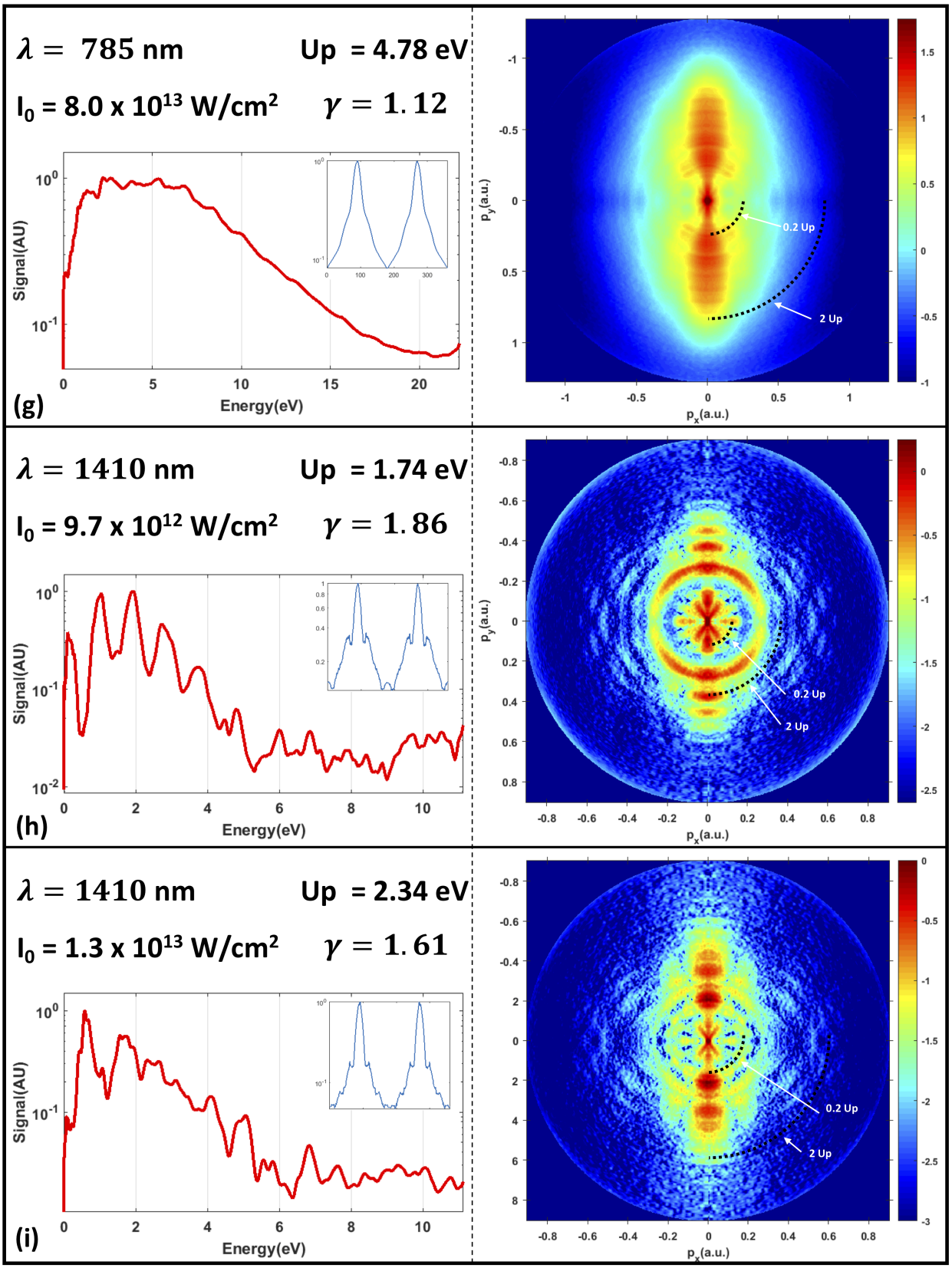
λ = 785 nm
Up = 4.78 eV
I0 = 8.0 x 10^13 W/cm^2
γ = 1.12
Signal(AU)
Energy(eV)
(g)
0.2 Up
2 Up
py(a.u.)
px(a.u.)
λ = 1410 nm
Up = 1.74 eV
I0 = 9.7 x 10^12 W/cm^2
γ = 1.86
Signal(AU)
Energy(eV)
(h)
0.2 Up
2 Up
py(a.u.)
px(a.u.)
λ = 1410 nm
Up = 2.34 eV
I0 = 1.3 x 10^13 W/cm^2
γ = 1.61
Signal(AU)
Energy(eV)
(i)
0.2 Up
2 Up
py(a.u.)
px(a.u.)

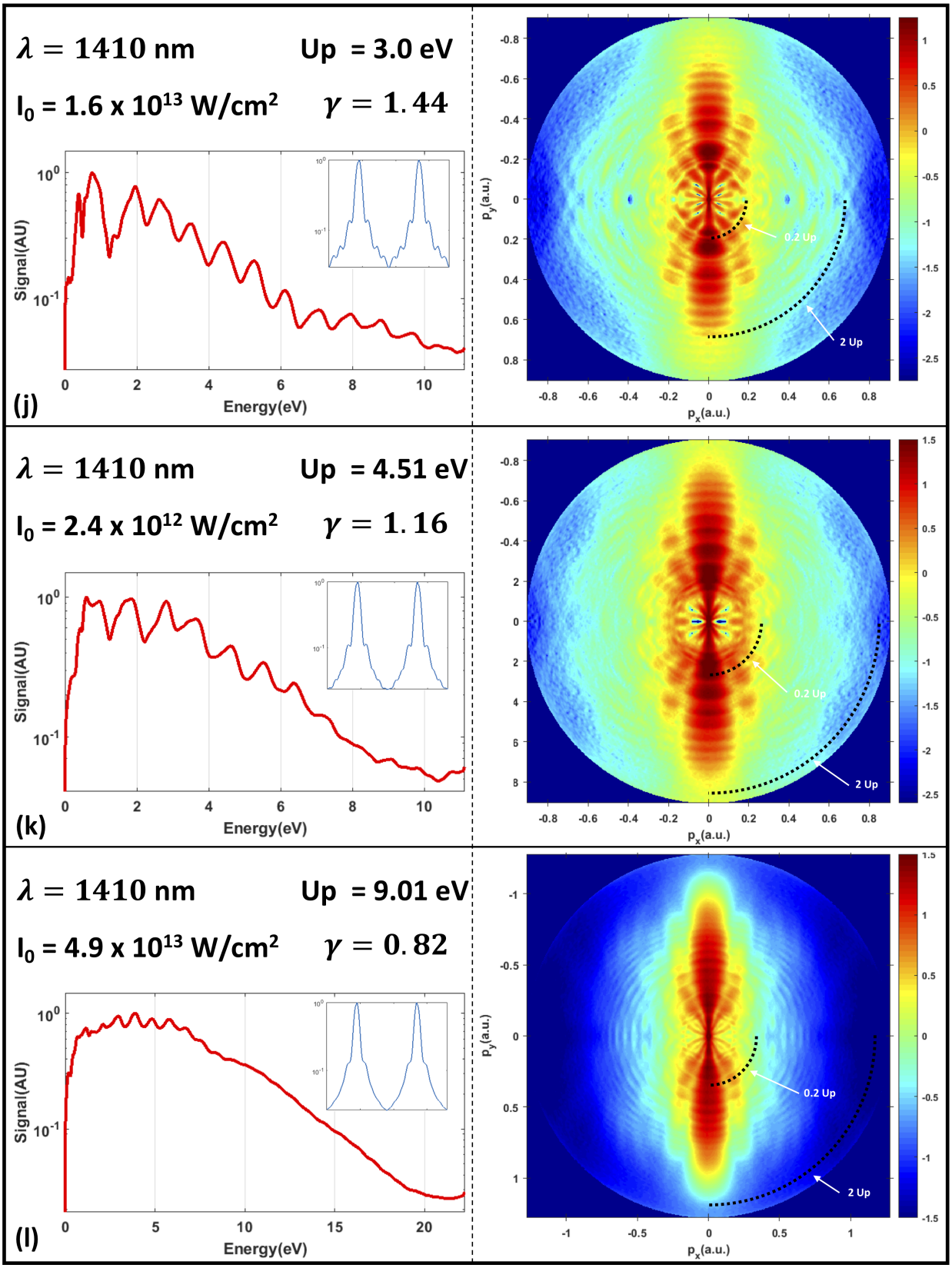
λ = 1410 nm
Up = 3.0 eV
I0 = 1.6 x 10^13 W/cm^2
γ = 1.44
Signal(AU)
Energy(eV)
(j)
py(a.u.)
px(a.u.)
0.2 Up
2 Up
λ = 1410 nm
Up = 4.51 eV
I0 = 2.4 x 10^12 W/cm^2
γ = 1.16
Signal(AU)
Energy(eV)
(k)
py(a.u.)
px(a.u.)
0.2 Up
2 Up
λ = 1410 nm
Up = 9.01 eV
I0 = 4.9 x 10^13 W/cm^2
γ = 0.82
Signal(AU)
Energy(eV)
(l)
py(a.u.)
px(a.u.)
0.2 Up
2 Up

$\lambda = 1825$ nm Up = 3.55 eV

$I_0 = 1.1 \times 10^{13}$ W/cm^2 $\gamma = 1.3$

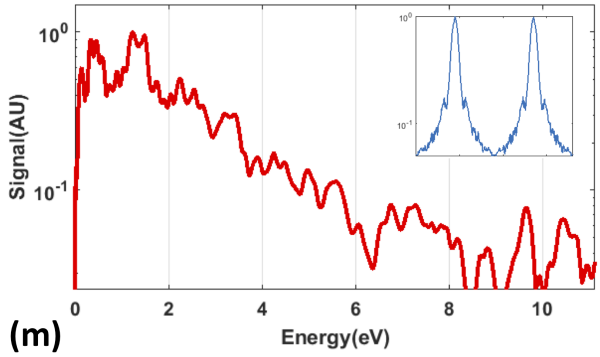

(m)

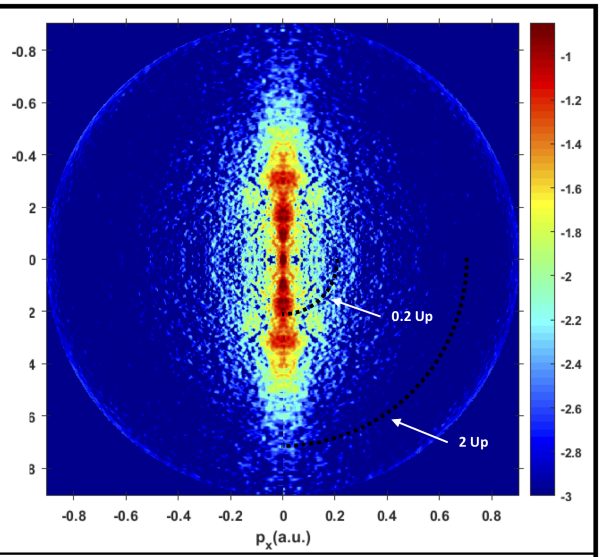

$\lambda = 1825$ nm Up = 3.87 eV

$I_0 = 1.2 \times 10^{13}$ W/cm^2 $\gamma = 1.25$

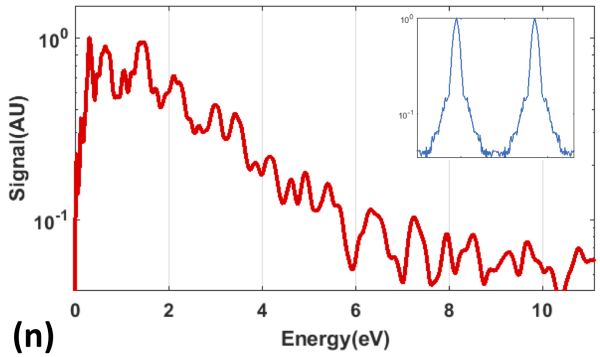

(n)

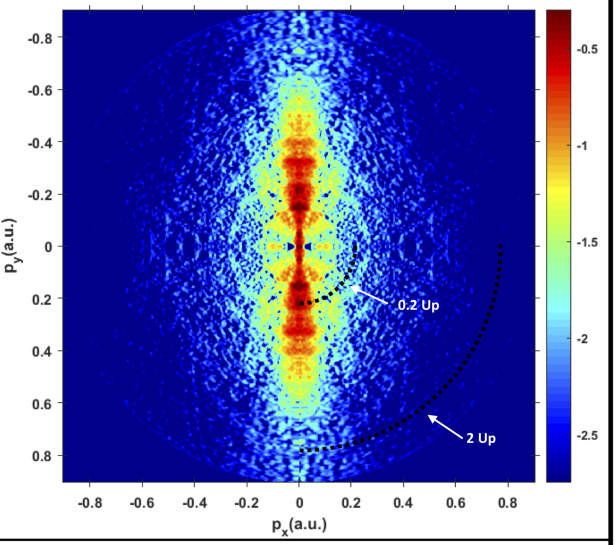

$\lambda = 1825$ nm Up = 4.09 eV

$I_0 = 1.3 \times 10^{13}$ W/cm^2 $\gamma = 1.22$

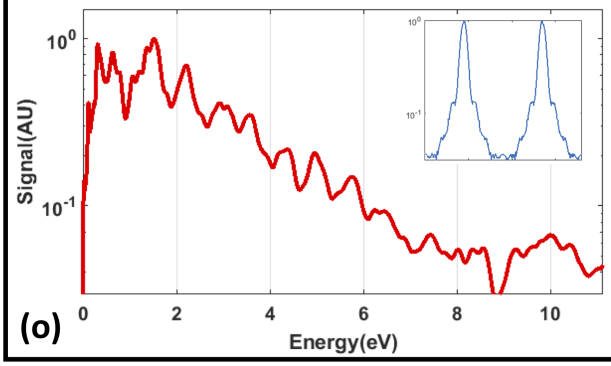

(o)

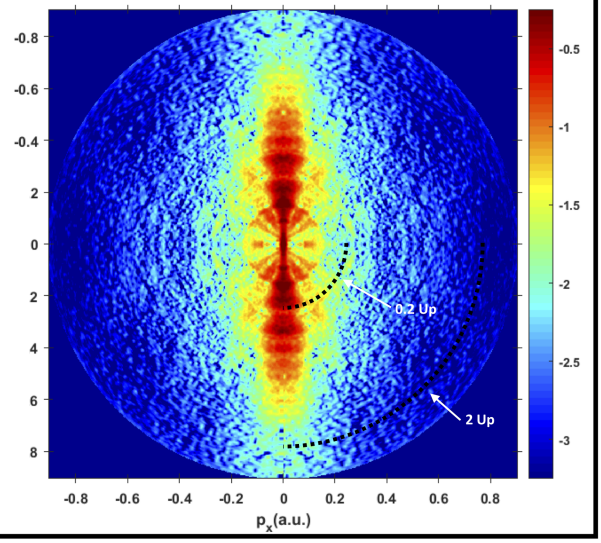

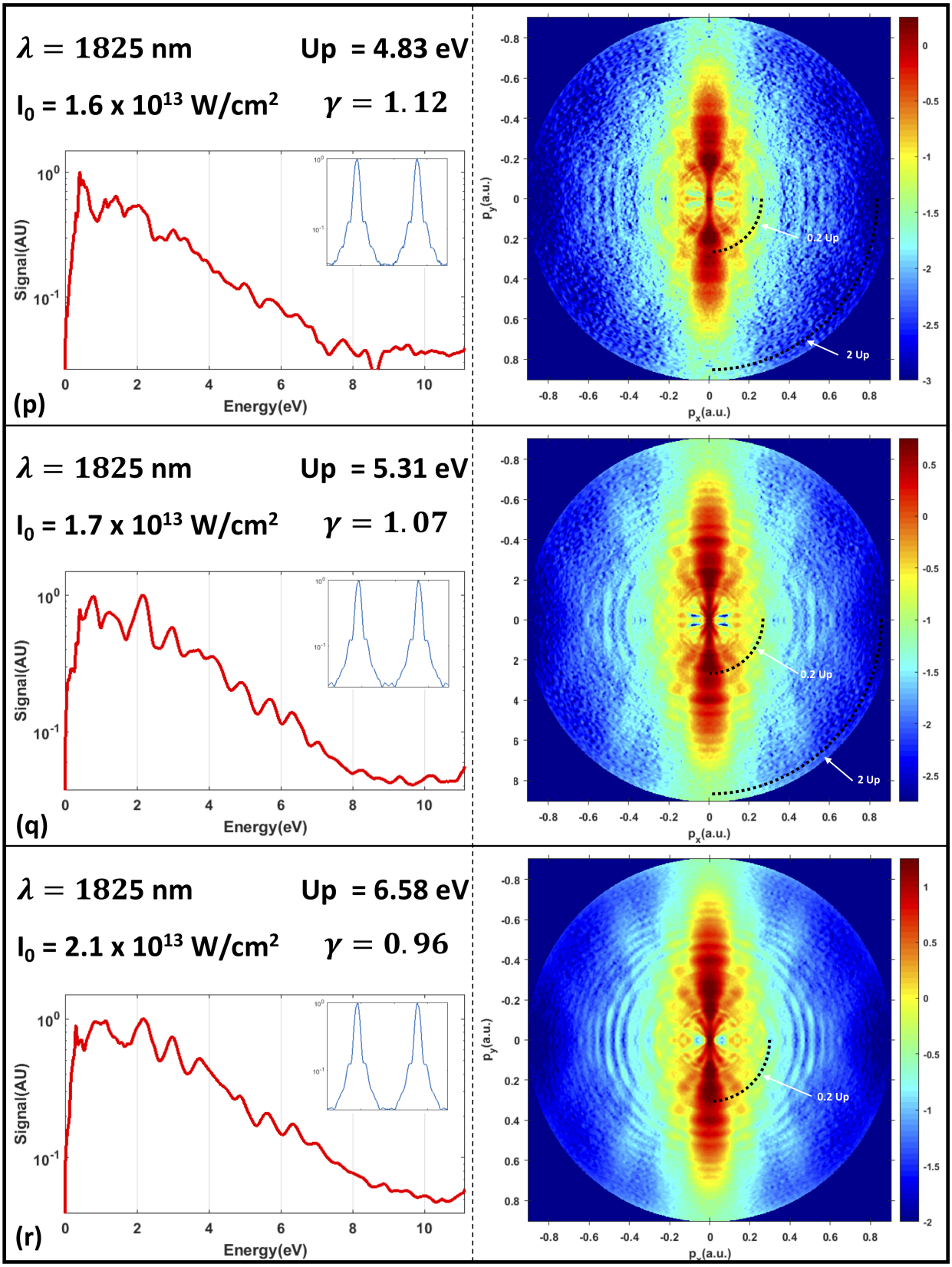
λ = 1825 nm
Up = 4.83 eV
I0 = 1.6 x 10^13 W/cm^2
γ = 1.12
Signal(AU)
Energy(eV)
(p)
py(a.u.)
px(a.u.)
0.2 Up
2 Up
λ = 1825 nm
Up = 5.31 eV
I0 = 1.7 x 10^13 W/cm^2
γ = 1.07
Signal(AU)
Energy(eV)
(q)
py(a.u.)
px(a.u.)
0.2 Up
2 Up
λ = 1825 nm
Up = 6.58 eV
I0 = 2.1 x 10^13 W/cm^2
γ = 0.96
Signal(AU)
Energy(eV)
(r)
py(a.u.)
px(a.u.)
0.2 Up

$\lambda = 1825$ nm Up = 7.96 eV

$I_0 = 2.5 \times 10^{13}$ W/cm^2 $\gamma = 0.87$

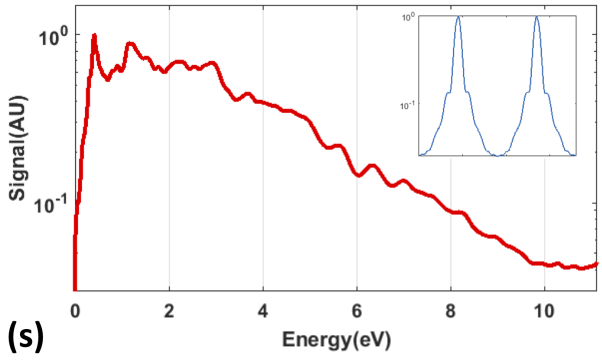

(s)

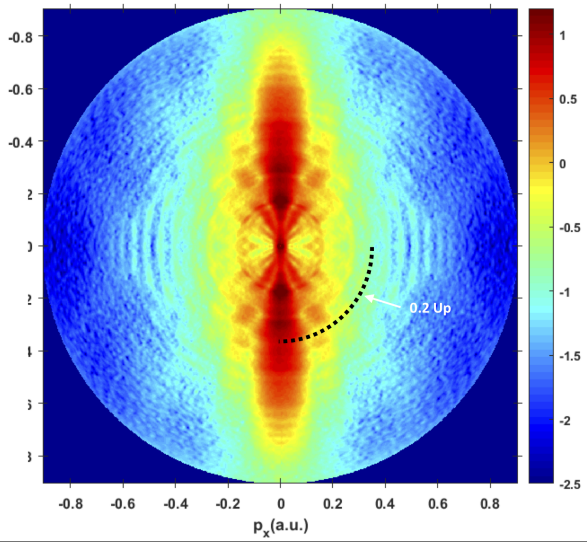

$\lambda = 1825$ nm Up = 10.6 eV

$I_0 = 3.4 \times 10^{13}$ W/cm^2 γ 0.76

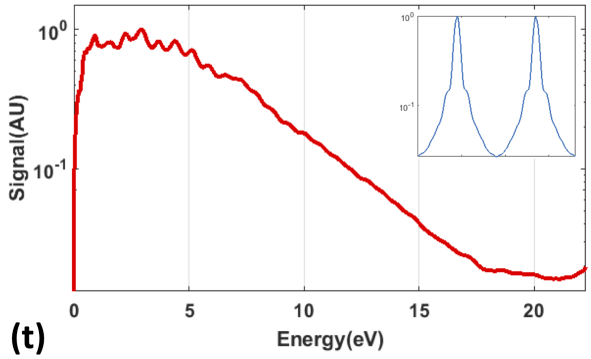

(t)

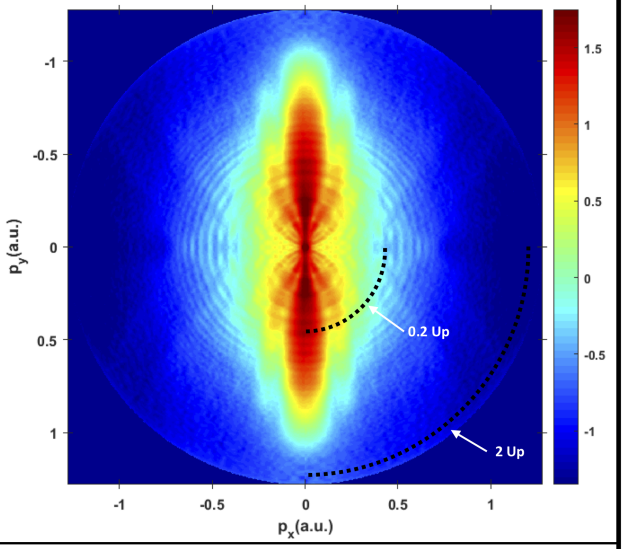

$\lambda = 2025$ nm Up = 4.12 eV

$I_0 = 1.1 \times 10^{13}$ W/cm^2 $\gamma = 1.21$

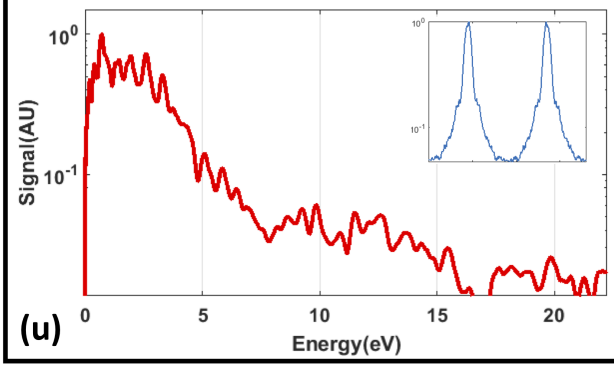

(u)

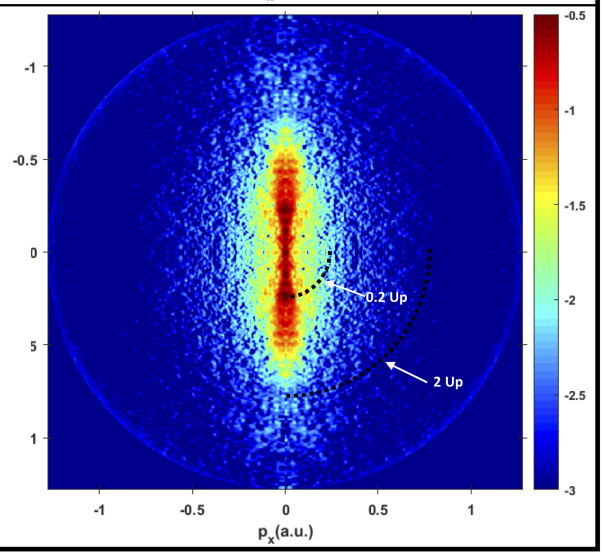

$\lambda = 2025$ nm Up = 4.68 eV

$I_0 = 1.2 \times 10^{13}$ W/cm^2 $\gamma = 1.13$

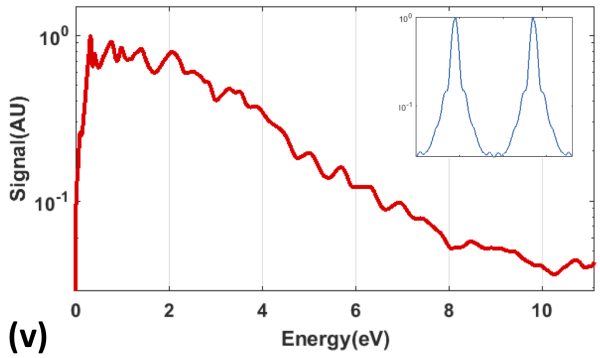

(v)

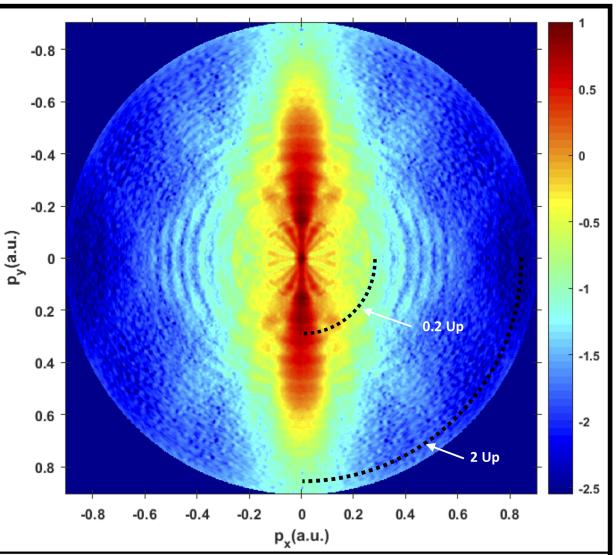

$\lambda = 2025$ nm Up = 5.28 eV

$I_0 = 1.4 \times 10^{13}$ W/cm^2 $\gamma = 1.07$

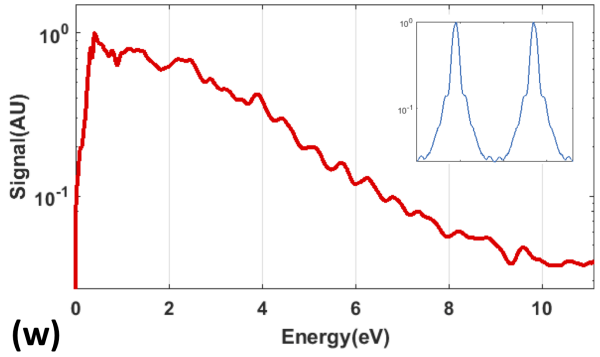

(w)

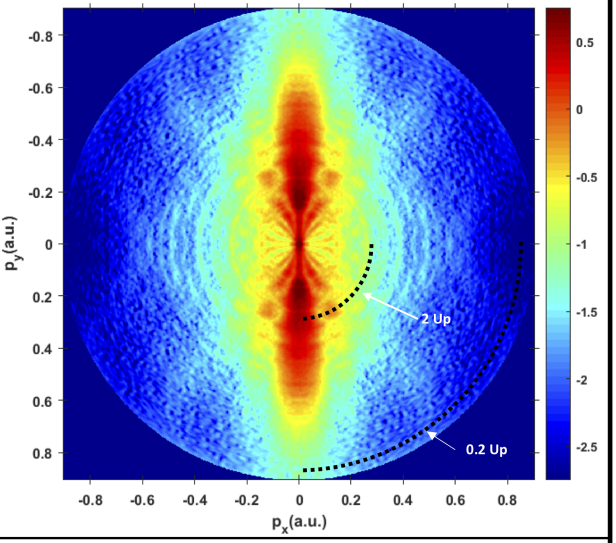

$\lambda = 2025$ nm Up = 5.80 eV

$I_0 = 1.5 \times 10^{13}$ W/cm^2 $\gamma = 1.02$

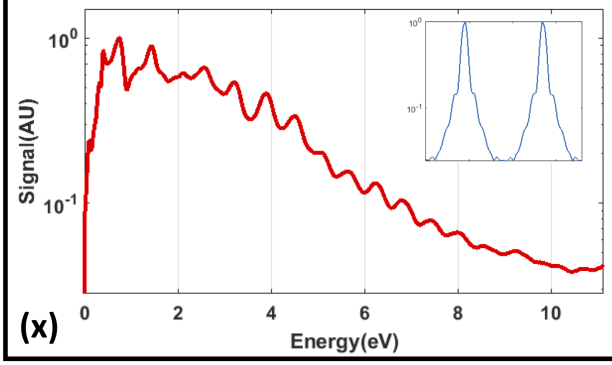

(x)

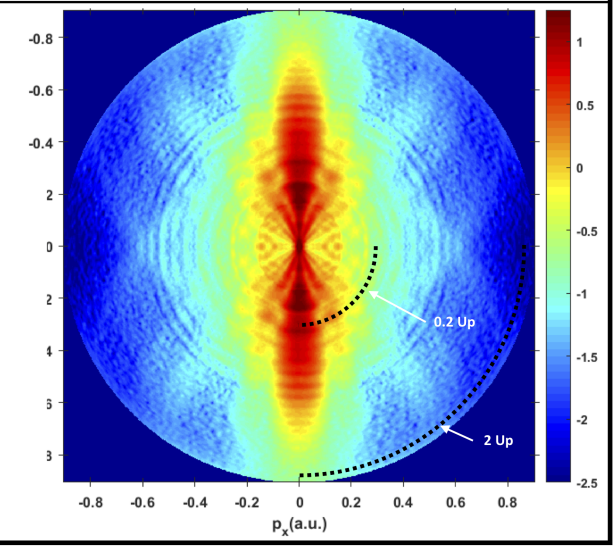

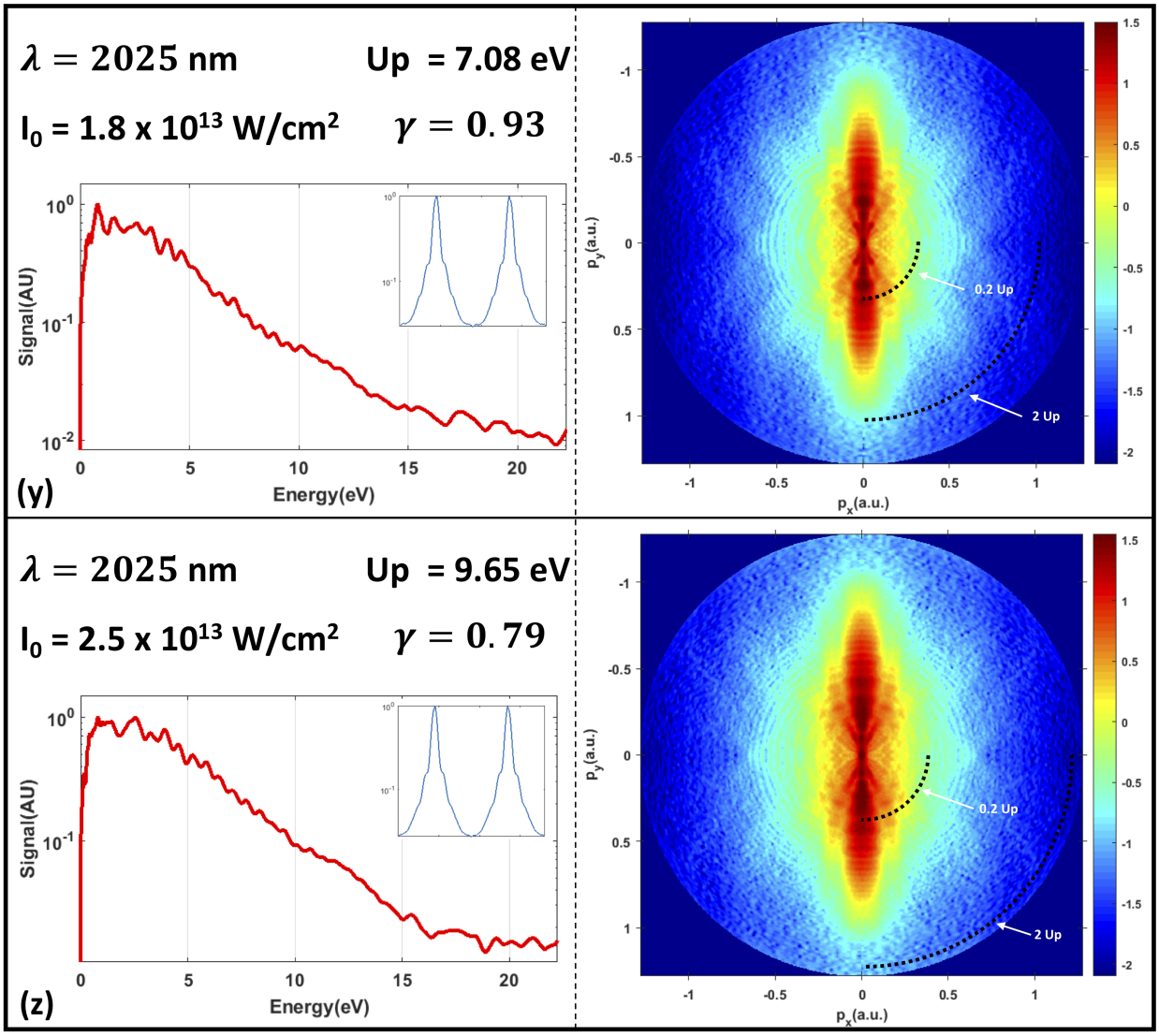

Figure 3.6: *Results from intensity and wavelength dependent study of strong-field ionization in Xe. Each panel shows the results for a single laser wavelength and peak intensity. On the right side of each, the photoelectron momentum distribution is plotted for the log of the yield, with a color scale selected to increase the visibility of the various features present in each PMD. To the extent that they fall on each image, the $0.2U_p$, $2U_p$ and $10U_p$ points are denoted by a black, dashed arc in the bottom right corner of each image. The left side shows the on-axis energy spectra extracted from the PMD. Inset into each of these is the momentum integration of the full distribution (all energies), providing the photoelectron angular distribution. The x-axis limits range from 0 to 360 degrees, the polarization is at 90 and 180 degrees. The yield is plotted in log scale. For each case, the driving wavelength (λ), ponderomotive energy (U_p), peak intensity (I_0) and Keldysh parameter (γ) are given.*

3.4 Interpretation and Discussion

Since the original experimental demonstration of non-perturbative, above threshold ionization in 1979 by Agostini and colleagues [35] hundreds to thousands of experimental results, along with an impressively similar number of theoretical investigations, have been published. Despite this intensive 40-year quest to better understand the interaction between atoms and intense, ultrafast laser pulses, new understanding is still developing. Many new discoveries have largely been driven by developments in ultrafast laser technology. These include breakthroughs such as the carrier-envelope-phase dependence of ATI for few-cycles pulses [67], the identification of the spider like side lobes that originate from interference of multiple types of photoelectron orbits [60] and the first observation of the low energy structure (LES) for mid-infrared driving pulses [68]. Other features, such as the directly off-axis quantum carpet pattern [69] largely escaped notice until recently, despite being, to some extent, present in earlier data.

This section is dedicated to identifying, interpreting, and discussing various "features" and observables present in the strong-field ionization dataset presented in the previous section. The photoelectron momentum distributions in figure 3.6 show the intricacy and richness, as well as the complexity, present in strong-field ionization. Here, the various features are presented and categorized by the degree the photoelectrons that make them up interact with the parent ion core. As a final note, much of the literature is highly focused on identifying a specific feature, or set of features, and attempting to explain it in terms of various models or pictures. The rest of this chapter takes a similar approach. However, it is important to remember that, while it can be insightful and highly useful to apply various models to different parts of the PMD, these are all just approximations and simplifications. Ultimately, the fundamental physics is just the propagation of the electron wavefunction under the various forces present. The difficulty in solving the TDSE (particularly at longer wavelengths) necessitates the development of simpler pictures. Care should be taken however, not to extend the predictions of the given model past what is justified.

3.4.1 Direct Ionization

As originally introduced in section 3.2.2, direct photoelectrons are defined as those that do not rescatter during the ionization process. The ATI peaks, spaced by one photon energy, are a clear example of direct ionization. These ATI peaks are most easily identified when the ionization process is in the multiphoton limit ($\gamma >> 1$). Figure 3.6 (a-e) clearly exhibit this behavior. For panel (a) $\gamma = 6.37$, which is decidedly in the multiphoton limit. Multiphoton peaks described by equation 3.5 are also present to varying strengths in figure 3.6 panels (f, h-k, m-r, & u-x). As seen in figure 3.4, the multiphoton peaks do shift with the ponderomotive potential as expected.

While the number of visible peaks generally grows with intensity, the contrast between peaks is reduced. This is due to the combination of the ponderomotive shift in coordination with volume averaging effects.

So far, all discussions have more or less tacitly assumed that only a single peak intensity drives the ionization or rescattering process. While the dream of many experimentalists and theorists alike, performing a measurement with a single intensity (or even a narrow range of intensities) is largely an experimental impossibility. To generate the high peak intensities for non-linear ionization, laser radiation must be tightly focused. This necessarily creates a distribution of intensities with only a very small percentage of the interaction region being at the peak intensity [70]. The measured PMD is the sum of all the electrons produced in this extended region. The summation across this distribution of intensities has a blurring effect for many measured parameters, including the multiphoton peaks, in this case due to the different ponderomotive shift at each local intensity. This effect is very clear in the 785 nm data. Figure 3.7 (a) plots the on-axis energy line outs for a series of results from figure 3.6 where the decreasing contrast in ATI peaks is evident.

Freeman resonances also produce peaks in the photoelectron energy spectrum. The resonant nature makes the cross section much higher and results in an increase in yield at that energy. As given by equation 3.31, the kinetic energy of the photoelectron ionized through a Freeman channel does not depend on U_p as the excited bound state energy also Stark

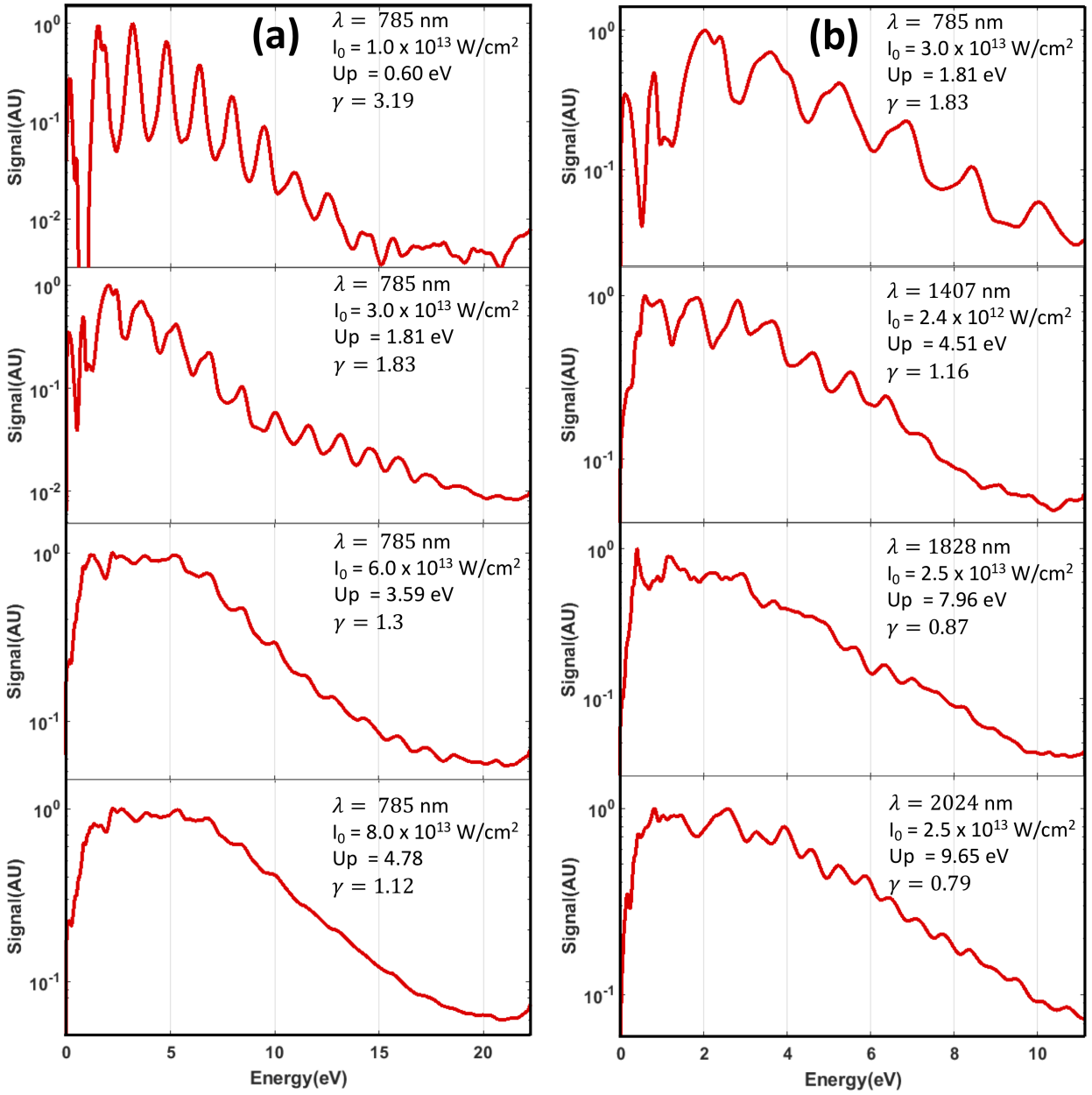

Figure 3.7: *Evolution of the photoelectron spectrum from the multiphoton to tunneling regime. (a) Fixed wavelength of 785nm with increasing intensity. (b) Approximately fixed intensity of* $2.5 \times 10^{13} W/cm^2$ *with increasing wavelengths.*

shifts by U_p. Volume effects play a strong role in the observation of Freeman resonances. The resonance condition, for a given state, is only satisfied once the driving intensity is strong enough to Stark shift the binding energy of the high-lying state into resonance with an integer number of photons. However, once that intensity has been reached (first at the peak of the intensity distribution) the requisite intensity will continue to be present at some point in the focal volume as the intensity is further increased. As such, it is characteristic of a Freeman resonance photoelectron energy to remain visible in the spectrum even when the intensity is high enough to put the ionization conditions deep into the tunneling regime. Freeman resonances can only currently be reproduced using the TDSE. All SFA models ignore any atomic structure other than the ionization potential. Even many TDSE solutions can struggle to calculate the Freeman peaks with quantitatively accuracy due to necessary approximations such as the single active electron approximation.

Off-axis, a different and interesting direct ionization mechanism is present. Originally discussed and explained by Korneev and coworkers [69] in 2012, this feature is often described as a strong-field ionization version of the quantum carpet [71]. The quantum carpet takes the form of a grid-like interference pattern of maxima and minima, perpendicular to, or almost perpendicular to, the polarization axis. The most interesting part of the carpet pattern is that the peaks are spaced by two photons as opposed to the one photon spacing of the on-axis ATI. Recall that the one photon spacing originates from interference, at a given final momentum, from ionization bursts occurring once per laser cycle. Two photon spacing would then suggest interference from events that occur twice per cycle. This can be interpreted using the SMM which gives that the electron will acquire no drift velocity when ionized directly at the field extremal point. This happens twice per cycle and since the electrons do not gain any momentum along the direction of the laser polarization, emission from one half cycle to the next is indistinguishable. Essentially, emission directly at the peak of the field has an increased degeneracy that is broken for all other cases when the photoelectron has a momentum component along the laser polarization.

Quantum carpet patterns are easily visible in panels (b-e) of figure 3.6 for 785 nm data and (h-j) of figure 3.6 for 1410 nm data. Low-order carpet-like patterns are visible in both

the 1825 nm data and the 2025nm data but separating these features from the other off-axis structures at low energies for long wavelengths is difficult.

Figure 3.8 (a & c) show the PMD's for two cases, one at 785 nm and the other at 1410 nm, with the color scale adjusted to enhance the visibility of the carpet pattern (marked on the right side of each PMD with a white dotted box). Three white dashed arcs on each PMD delimit two subsequent orders, the inner of which has a maximum on axis and the outer of which has a minimum. The angular integration for the regions within these arcs is plotted in 3.8 (b & d) for the 785 nm and 1410 nm case respectively. To the best of our knowledge the carpet pattern at 1410 nm represents the longest wavelength at which the feature has been seen for ionization from the neutral ground state. There is also very little, to no currently published, data tracking the emergence and decay of the carpet as a function of wavelength as seen for both the 785 nm runs as well as the 1410 nm runs.

In several pervious experiments these off-axis carpet patterns have been linked to ionization pathways involving Freeman resonances [72; 73]. In this mechanism, as described above, a high-lying state is shifted in resonance with an integer number of photons which are absorbed to transition the atom into to the excited state. From there, ionization can occur via single photon absorption. The full photoelectron angular distribution of a given final energy is then determined by the angular momentum symmetry of the high-lying state [73]. As described in section 3.2.4, since the binding energy of the high-lying state is shifted in the laser field by a value equal to (or almost equal to) U_p the energy of a photoelectron created through this pathway does not shift with U_p and is thus independent of the driving intensity. This can be used to determine if the observed quantum carpet patterns we observe arise though resonate multiphoton ionization as in [72; 73] or from non-resonate multiphoton ionization as described and observed in [69]. For the carpet patterns referenced above and shown in figure 3.8 the directly off-axis peaks do shift with intensity indicating that quantum carpet patterns we observe do not emerge though a resonant ionization pathway. It should be noted that in the studies measuring and attributing the carpet pattern to resonance ionization were performed at 800 nm with pulse durations of 100 fs, approximately four times longer than ours. So, it is possible that the pulse duration plays an important

role in determining the dominate ionization pathway.

3.4.2 Photoelectron Rescattering

By far the most discussed subset of strong-field ionization processes over the last several decades has been field-driven rescattering. A large part of the development has been arriving at a consistent understanding of the processes at play and establishing the relevance and limitations of the purely classical simple man model. The SSM has long been known for describing the most important components of HHG [22] but its full applicability, and limits, to the photoelectron spectrum took longer to establish [47].

The SMM correctly predicts that the maximum kinetic energy a direct photoelectron can acquire from propagation in the laser field is $2\,U_p$. It also correctly gives that the maximum rescattered energy is $10\,U_p$, originating from elastic backscattering. The $2\,U_p$ is evident in the data plotted in figure 3.5 but the $10\,U_p$ is much harder to see due to the decreased signal to noise ratio at higher photoelectron energies.

However, the cutoff picture can be too simplistic and has led to the often-misconstrued idea that all electrons between $2\,U_p$ and $10\,U_p$ are rescattered electrons. Plots similar to the sketch shown in figure 3.9 are quiet prevalent in literature while also being quite misleading.

In reality, direct ionization can readily produce photoelectrons with energy greater than $2\,U_p$. This is quite apparent in figure 3.6 (a-d) where the ATI peaks extend past $10\,U_p$. In all of these cases U_p is less than one photon energy and the Keldysh parameter is greater than one. Figure 3.7 shows the transition from the multiphoton regime into the tunneling regime through two different ways. Column (a) shows the case for when the wavelength is fixed and the intensity is increased. Column (b) shows four spectra for approximately equal intensity but with increasing wavelength.

It is also an incorrect statement that all electrons with a final kinetic energy below $2\,U_p$ are due to direct ionization. In fact, a series of investigations over the past decade, into the low energy structure (LES) [68], have shown that in many cases the opposite is more correct [40].

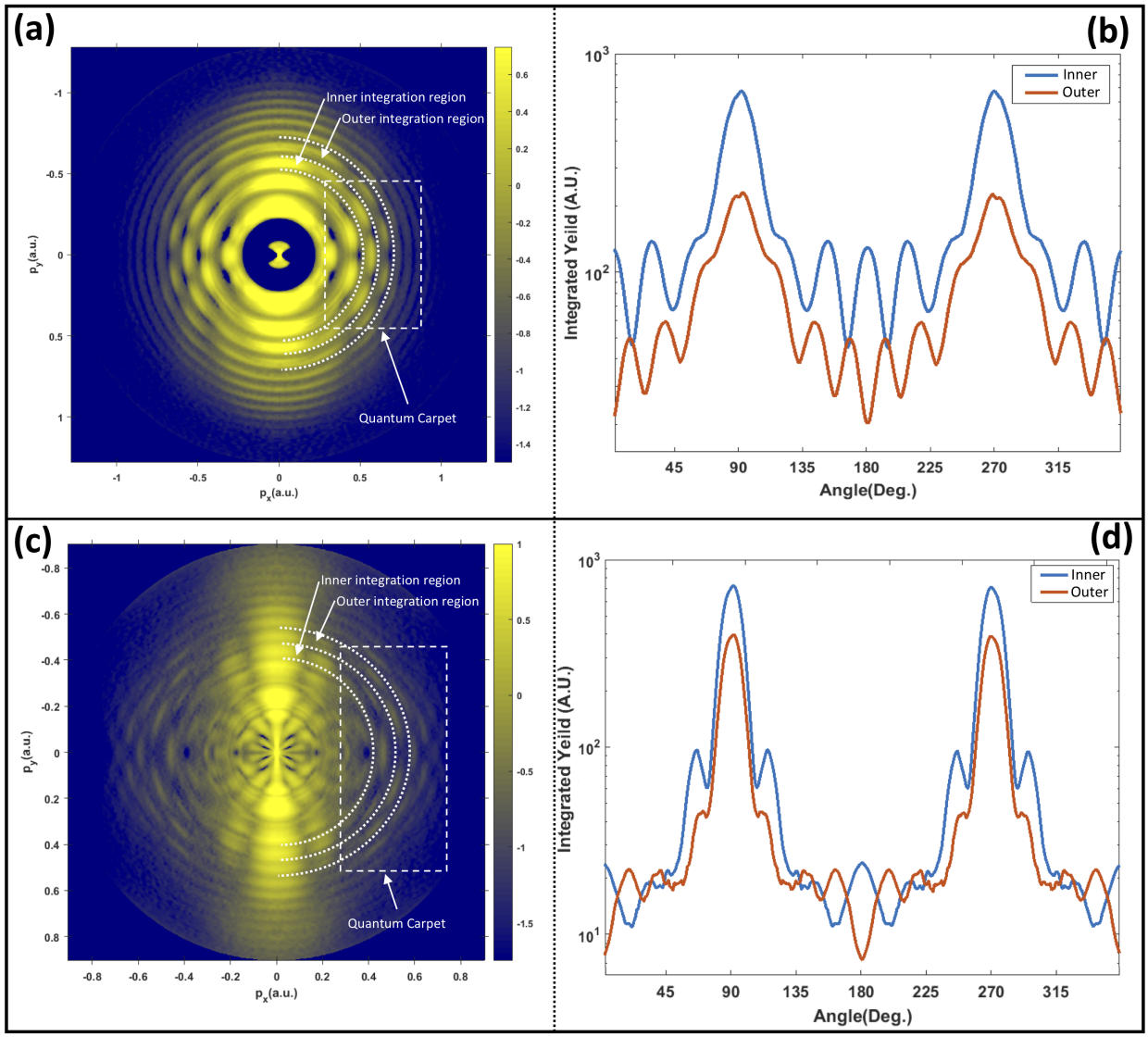

Figure 3.8: *Photoelectron distributions exhibiting a quantum carpet pattern. For both PMD's ((a) & (c)) a dashed white box indicates the quantum carpet area. Additionally, three dashed arcs are shown on each distribution. These denote the inner and outer regions for the angular integration plots ((b) & (d). ((a) & (b) 785nm* $1.6 \times 10^{13}\, W/cm^2$*; ((c) & (d)) 1410nm* $1.6 \times 10^{13}\, W/cm^2$*)*

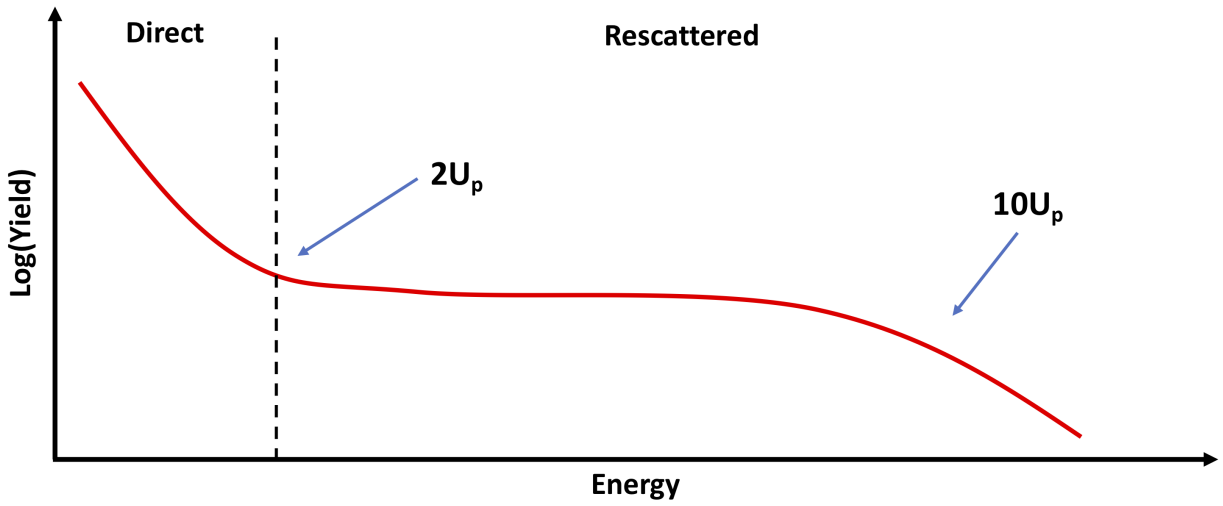

Figure 3.9: *Sketch of the typically energy spectrum of photoelectrons from ionization in the tunneling regime. The $2U_p$ cutoff is used to separate the Direct and Resattered regimes. See text for more commentary.*

The LES is a dramatic enhancement in the on-axis photoelectron yield at energies of less than $0.1\,U_p$ [74]. It also only appears at longer wavelengths an in the tunneling regime. This feature is completely absent in all first order SFA theories that do not include interactions of the returning electrons with the ion core (as well as of course the SMM). It is now established that the LES originates from forward scattered electrons that interact with the long-range Coulomb potential. The LES is largely target independent and is nearly universal for driving wavelengths longer than 1,000 nm [40]. Due to the fact that the LES originates from the long-range Coulomb potential most theoretical approaches that include rescattering in any form reproduce LES effects.

The LES is visible in several of the longer wavelength measurements shown in figure 3.6. However, VMI measurements are not ideal for resolving these peaks that occur at very low energies.

Aside from the highly visible ATI rings, in the multiphoton regime, the other predominate feature observable in the data shown in figure 3.6 is the off-axis, extended side-lobes in the tunneling regime. A number of studies have examined these structures, under various conditions, both experimentally and theoretically [27; 60]. Due to their resemblance to spider

legs, these patterns are often referred to as spiders or spider-like patterns. Like the LES, the spider pattern is not reproduced by any theory that does not include the interaction of the returning electrons with the ion core. It has also been established the long-range potential has the predominate effect in producing "the spider" [27; 40].

As mentioned in section 3.2.2 the Coulomb potential produced two additional trajectories not originally present for pure laser field-dressed trajectories. The spider fringes can be interpreted as the interference between electron wave packets from these new trajectories with the direct ionization trajectories. As such, the fringes die off prior to, or at, the $2\,U_p$ cutoff. This interference between two competing pathways to the same final momentum has been interpreted at something akin to "photoelectron holography". Within this language, the wave packet from the direction ionization channel becomes the reference wave and the rescattering wave packet becomes the signal wave. The signal wave acquires additional phase as it samples the Coulomb potential of the ion during the rescattering process, which produces the holographic pattern. Quantum trajectory models can be quite effective and are often employed to simulate the spider pattens. These models also offer the easiest to interpret results as the exact sets of trajectories that form the patterns can be extracted.

Both the direct and rescatering trajectories leading to the spider pattern originate from the same quarter laser cycle. In addition to the primary spider legs, that can extend out to $2\,U_p$, lower energy, inner spider patterns also exist. The inner patters are due to rescattering electrons that undergo two (or more) returns before finally scattering. As with the LES, this results in a lower final photoelectron momentum. Figure 3.10 shows two PMD's for 1410 nm (a &b) and 1825nm (c&d) with intensities $4.9 \times 10^{13} W/cm^2$ and $2.5 \times 10^{13} W/cm^2$ respectively. Panels (a &c) show the full PMD while (b &d) are zoomed in to show the inner structures better. The color scale for each plot is chosen to enhance the spider interference pattern. On the bottom half of each image white lines are places to better indicated the patterns.

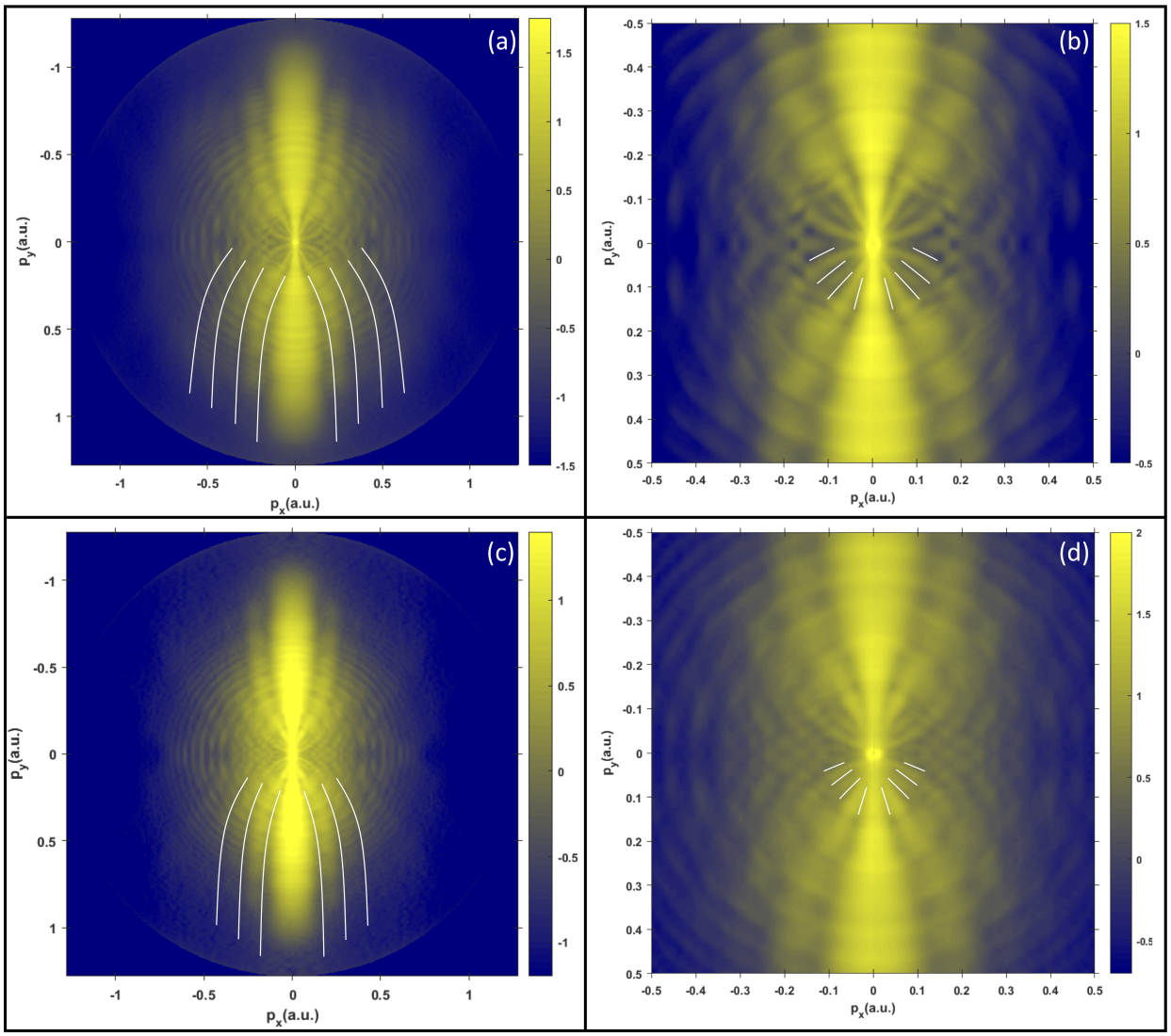

Figure 3.10: *Photoelectron distribution illustrating the "spider" patterns. Color scale is chosen to enhance the visibility of the fringes. White lines have been added on the bottom half of the image to indicate the patterns. The full distribution is plotted ((a) & (c)) as well as zoomed in ((b) & (d)) to show the inner patterns. ((a) & (b) 1410nm* $4.9 \times 10^{13}\, W/cm^2$*; ((c) & (d)) 1825nm* $2.5 \times 10^{13}\, W/cm^2$*)*

3.5 Conclusion

This chapter presents our work to better understand the intricate process of strong-field ionization by measuring the photoelectron momentum distribution of xenon as a function of both driving wavelength and intensity. These high-quality measurements allow for the simultaneous observation multiple features and structures that originate during the ionization and rescattering dynamics. Signatures of direct above threshold ionization, Freeman resonances, direct backscattering, and the interference between direct electrons and low-energy rescattered electrons were tracked from the near-infrared regime through the mid-infrared regime. They are interpreted with comparisons to the current state-of-the-art understanding and theoretical models.

Detailed understanding of and the ability to model with true quantitative accuracy, strong-field ionization dynamics in the MIR regime has ever increasing significance. This is motivated largely by quadratic wavelength scaling of the ponderomotive potential and its implications for the continued development of techniques such as high harmonic generation and laser induced electron diffraction. Here we showed data that tracked evolution the photoelectron momentum distribution from the multiphoton regime into the tunneling regime at a range of mid-infrared diving wavelengths. This provides insight into the strong-field ionization process in a wavelength regime were multiphoton ionization spectra is rare.

Future work is planed to try to match this data set with TDSE calculations with the ultimate goal of achieving substantial quantitate agreement between theory and experiment over a range of intensities and wavelengths. TDSE calculations become increasingly expensive with longer wavelengths, even when performed using the single active electron approximation. This data set will allow for validation of such calculations and is important for understanding topics such as multi-electron effects in strong-field ionization at longer wavelengths.

Chapter 4

Controlling and Measuring the Carrier-Envelope Phase for Strong-Field Science Studies

As ultrafast science moves towards shorter and shorter time scales, laser sources with pulse durations in the few to sub-femtosecond regime become more desirable [75]. For Ti:Sapphire lasers, which are commonly used nowadays, the bandwidth of the laser pulses can be broadened by self-phase-modulation (SPM) through propagation in a hollow-core fiber (HCF) filled with a noble gas [76]. By properly compensating for the dispersion with chirped mirrors, pulse durations as short as 3 fs can be achieved [77]. For a center wavelength of 800 nm, this is close to one optical cycle. Optical synthesizers are being used to push this even further. State of the art techniques can now produce pulses less than a single femtosecond, as measured by the FWHM of the intensity [78]. In this regime, it is no longer appropriate just to use the envelope to describe the shape of the laser pulse. For few-cycle pulses, the actual shape of the laser electric field plays an important role in strong-field processes [79]. Therefore, the carrier-envelope phase (CEP), the offset between the peak of the electric field and the peak of the envelope, is a crucial aspect of ultrafast pulses. For example, photoelectron momentum distributions, like those shown in the previous chapter have a strong dependence

on the value for the carrier-envelope phase [79; 80]. Numerous studies have demonstrated carrier envelope phase effects in atoms [81–83], molecules [84; 85], nanosytems [86–90], and solids [91–94].

4.1 The Carrier-Envelope Phase

As originally introduced by 2.1, the temporal description of the electric field from an ultrafast laser pulse is given by:

$$E(t) = A(t)cos(\omega_c t + \phi_{CE}), \tag{4.1}$$

where $A(t)$ is the envelope (usually given as one of the pulse shapes listed in table 2.1), ω_c is the carrier frequency and ϕ_{CE} is the carrier-envelope phase. Figure 4.1 shows various physical aspects of the carrier-envelope phase. Figure 4.1 (a) depicts a series of 800 nm pulses, all with an envelope of 4 fs, with different CEP values. As can be seen by comparing the various pulses, the actual peak intensity varies for different CEP values, which can be somewhat non-intuitive since each pulse contains the same energy. This difference in intensity distribution is what gives rise to CEP effects in many CEP sensitive systems. It should be noted that the CEP is a quantity present for all laser pulses, not just for few-cycles pulses. However, as the number of cycles within the envelope increases the effects of different CEPs are dramatically reduced.

Figure 4.1 (b) more clearly demonstrates that the CEP is defined as the offset between the peaks of carrier and the envelope respectively. As a pulse propagates, the CEP can evolve due to the difference between phase velocity and group (or envelope) velocity. This change is given by [95]

$$\Delta\phi_{CE}(z) = \omega_c\Big(\frac{1}{v_g} - \frac{1}{v_p}\Big)z, \tag{4.2}$$

where v_g and v_p are the group and phase velocity respectively. This difference in phase and group velocity is a result of the fact that index of refraction, n, is always a function of

frequency (or, of course wavelength). Using this $\Delta\phi_{CE}(z)$ can be written as

$$\Delta\phi_{CE}(z) = -2\pi z\Big(\frac{dn}{d\lambda}\Big)|_{\lambda_0}, \tag{4.3}$$

where $dn/d\lambda$ is evaluated at the central frequency, λ_0.

In the discussion of the origin of the carrier-envelope phase it is helpful to review a few basics of laser cavities as the CEP is directly related to the dispersion in a laser cavity. A laser cavity can only support integer multiples of the cavity frequencies due to the boundary condition that the field go to zero at the end mirrors. This essentially requires that the mode must "fit" in the cavity with nodes at the end mirrors and an integer number of wavelengths in between. Mathematically this is

$$f_m = \frac{mc}{2nL} + f_0, \tag{4.4}$$

where f_m is the frequency of the mth mode, c is the speed of light, n is the effective index of refraction of the cavity (which is frequency dependent) L is the length of the cavity and f_0 is the frequency of the first mode. The quantity nL is the optical path length of the cavity.

The frequency difference between two modes (comb teeth) is

$$f_{m+1} - f_m = f_{rep} = \frac{c}{2nL}. \tag{4.5}$$

Right away we can see this quantity is actually just m times the inverse of the round-trip time for light in the cavity. Most Ti:Sapphire laser oscillators operate with the spacing between modes of around $f_{rep} = 80\,\text{MHz}$ or a round trip time of 12 ns. Since a laser cavity is constructed with one end-mirror as a partial reflector, so that light can be outcoupled, this also implies that the output pulse train is spaced by $1/f_{rep}$.

If you take the frame of reference of a single pulse traveling around the cavity, the CEP

will change by a fixed amount per round trip given by equation 4.3 to be

$$\Delta\phi_{CE} = -4\pi L\Big(\frac{dn}{d\lambda}\Big)|_{\lambda_0}. \tag{4.6}$$

This also of course gives the CEP change from one output pulse to the next in the pulse train emitted from a mode locked oscillator.

It can be shown from a Fourier transform of the laser gain bandwidth, which gives the temporal description of the pulse, that [96]:

$$f_0 = \Delta\phi_{CE}\frac{f_{rep}}{2\pi}. \tag{4.7}$$

So, the dispersion in a mode locked laser cavity results in an offset frequency that has the effect of shifting the carrier-envelope phase by a fixed amount from pulse to pulse. The frequency comb representation of a ultrafast pulse is shown by 4.1 (c).

Now, the real problem arises from just how sensitive f_0, and thus the CEP, is on dispersion for real world uses. As an example, for fused silica at 800 nm, $dn/d\lambda$ has a value of -0.017288 μm^{-1} [96]. Inserting this into equation 4.3 gives that a single micron of glass will change the CEP by more than 100 mrads. The constant fluctuations in a laser (temperature, air, vibration, etc.) mean that in practice $\Delta\phi_{CE}$ is effectively random over time. There are two strategies for dealing with this when the actual value of the CEP matters. This first method is to lock $\Delta\phi_{CE}$ using feedback loops. The second is to tag the CEP along with whatever data is being taken and the sort in post analysis. Each have their own advantages and disadvantages.

Propelled by the need for precision in laser frequency metrology [97], methods for the stabilization of the CEP developed rapidly for Ti:sapphire oscillators [98] and amplifiers [99; 100]. In 2005, T. W. Hänsch and J. L. Hall won the physics Nobel Prize for their contributions to this field [98; 101]. The ability to lock the CEP with high fidelity has enabled numerous seminal efforts such as single isolated attosecond pulse generation [102]and multi-octave waveform synthesis [78; 103]. Nowadays, oscillator technology and stability have

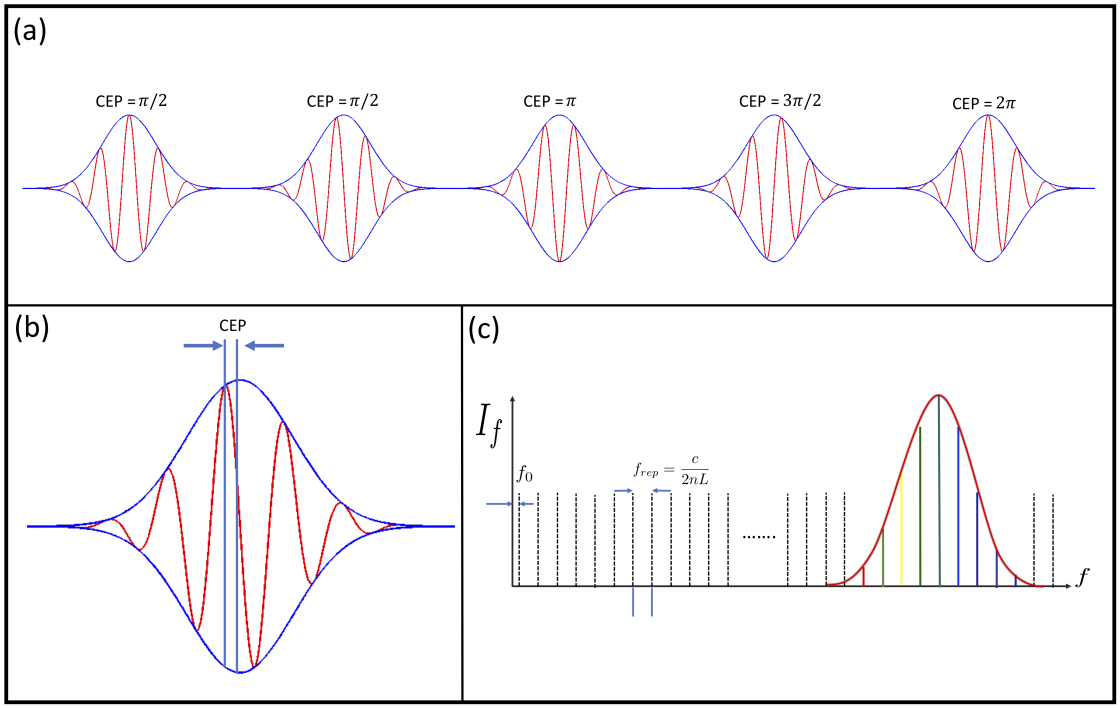

Figure 4.1: *Carrier-Envelope Phase, (a) 800nm, 4fs FWHM pulses plotted for varying values of CEP. The red line is the carrier and the blue line represents the pulse envelope. The CEP is defined as peak value of the carrier with respect to the envelope, which is illustrated by (b). CEP is defined as the offset between the peak of the envelope and the peak of the carrier wave. The offset frequency f_0 is shown in (c) along with the frequency comb representation of a laser pulse. The dashed lines represent the natural frequencies of the laser cavity. The gain bandwidth of a laser is represented by the red Gaussian line while the different frequency components within this are color-coded from red to blue. (c) Adapted from [96].*

evolved to the point where it is possible to lock the CEP for long periods of time utilizing f-2f [98] interferometry. Amplifier systems, especially with high pulse energies, are more difficult. The large scale of the systems and CEP jitter through grating-based stretchers and compressors [104; 105] introduces a significant amount of CEP noise. Even so, it is possible to lock the CEP to within 140 mrad (root mean square error) for short time periods (minutes) [106] or 300 mrad for longer time periods (hours) [62] using a feedback signal from an f-2f interferometer, a stereo above-threshold-ionization carrier-envelope phase meter (CEPM) [107], or feed forward methods [106; 108]. Designing laser systems with more and more robust CEP locking is still an active area of research, particularly for use in high-flux attosecond sources.

An alternate way of studying CEP-dependent processes is to record the CEP value for each pulse. This measurement can then be synchronized with the observable data. This technique is known as CEP tagging and does not require the laser pulses to be CEP locked. However, several other conditions need to be satisfied. First, CEP values need to be measured on a single-shot basis. Additionally, the acquisition rate of the single-shot CEP should ideally be at the level of the laser repetition rate (now typically several kHz) to allow enough statistics for reconstructing the CEP dependence. These conditions are readily satisfied by the carrier-envelope phase meter [109]. As such, the CEPM has emerged as a standard method for CEP tagging experiments [83; 85; 88; 110–112]. Single-shot CEP measurements for milijoule amplified systems have also been performed using an f-2f interferometer in the past [110; 113–116]. Later in this chapter, I present our results showing the first single-shot, direct comparison of a CEPM and an f-2f interferometer. These results demonstrate that f-2f interferometry is an accurate and robust way to tag CEP values and provide an all optical alternative for CEP tagged experiments.

In either case, locking the CEP or tagging the CEP, methods are needed to accurately measure its value. The next section focuses on this measurement process.

4.2 Methods of Measuring the Carrier-Envelope Phase

The motivation for measuring the carrier-envelope phase from a mode-locked oscillator comes from multiple fronts. In strong-field science, this motivation originates from the sensitivity of tunnel ionization to the exact conditions of the laser pulse. In particular, as tunnel ionization is the first of step of the three-step model of high harmonic generation, CEP effects become imprinted in the output HHG radiation. This is acutely true for producing isolated attosecond pulses, which can only be created for certain CEP values [102]. However, the field of optical metrology also has a strong interest in the CEP of mode locked lasers. As shown above, a change in CEP also corresponds to a change in the offset frequency. Stabilizing this offset frequency is critical for high precision frequency measurements. Control of the carrier-envelope phase is equivalent to control of the absolute optical frequencies components in an ultrafast pulse [98].

On the surface, measuring the offset frequency (and thus the CEP) seems like a simple problem. Just use an optical spectrometer to measure the spectrum of the pulse, then compare the spectral components (comb teeth) to the natural frequencies of the cavity, the difference will be the offset frequency. In practice of course, this is completely untenable. No spectrometer is even close to the level of resolution needed to do that. Here I explain two different CEP measurement techniques. One uses optical self-referencing to measure f_0, while the other uses the sensitivity of strong-field ionization to recover a CEP value. Section 4.4 presents our work directly comparing these techniques.

The process of f-2f interferometry uses a series of non-linear optical process to compare the frequency of comb lines on the low-frequency side of the optical spectrum to those on the high-frequency side. As shown in equation 4.11, this directly gives f_0. However, as demonstrated below, the spectrum of the ultrafast pulse must be greater than an optical octave. That is, f_{max} must be greater than or equal to $2f_{min}$ where f_{min} is amongst the lowest frequency in the pulse and f_{max} is amongst the highest. Once this condition is established, then second harmonic generation (SHG) can be used to double f_{min} for comparison in f-2f interferometry.

The absolute frequencies of f_{max} and f_{min} are

$$f_{min} = mf_{rep} + f_0, \tag{4.8}$$

and

$$f_{max} = 2mf_{rep} + f_0, \tag{4.9}$$

respectively.

If f_{min} is doubled though SHG then:

$$2f_{min} = 2(mf_{rep} + f_0). \tag{4.10}$$

Now, if two frequencies combined together, in a technique known as heterodyning [117] the result will be a beat note, δ, with a frequency equal to the difference between the two fundamental frequencies. If this is done with f_{max} and the doubled f_{min} then we would have

$$\delta = |2f_{min} - f_{max}| = |2(mf_{rep} + f_0) - 2mf_{rep} - f_0| \tag{4.11}$$

$$\delta = f_0 \tag{4.12}$$

So evidently, heterodyning frequency components on the blue side of an octave spanning pulse with the optically doubled red components will produce a direct measurement of the offset frequency. This process is what is known as f-2f interferometry. The offset frequency can either be recorded to tag the CEP, as presented in section 4.4 or used in a feedback loop to stabilize a laser system, as shown in section 4.3.

Now, the question is how an optical f-2f interferometer is actually constructed. First, an octave spanning pulse is required. This can be accomplished in one of several ways. The most common way, for pulses directly out of an oscillator, is to use a photonic crystal fiber (PCF) specifically constructed to have its zero dispersion point in the near infrared [118]. Another common method is to focus the laser into a sapphire plate at sufficiently high

intensities so that self-phase modulation occurs, broadening the spectrum. It is also now possible to construct Ti:Saphhire oscillators that directly produce a pulse with an octave spanning spectrum.

Figure 4.2(a) shows a schematic of a typical f-2f interferometer using a PCF for spectral broadening. A beamsplitter reflects the high frequency side of the spectrum while transmitting the low frequency components. The low frequencies are then passed through a doubling crystal (in this case periodically-poled potassium titanyl phosphate PPKTP) (shown in 4.2(b)) before being recombined with the low frequencies with a polarizing beam cube. Both beams are then dispersed with a reflection grating before transmitting through a narrow line width filter and finally a slit. This ensures only the desired frequency components are allowed onto an avalanche photo diode (APD). The APD records the time dependent intensity fluctuations corresponding to the beat note $\delta = f_0$. The APD signal can then be sent into a PID loop for stabilization. Figure 4.2(c) shows a typical output spectrum from an APD used for f-2f interferometry. A well-presented and detailed explanation of CEP stabilization in ultrafast oscillators can be found in [96].

Figure 4.3 shows an alternative design of an f-2f interferometer, after the pulse broadening step. This f-2f is designed to use a camera in the frequency plane to measure the CEP instead of an APD measuring f_0 temporally. In this setup, the entire pulse is sent though a Beta-Barium Borate (BBO) crystal for doubling. The BBO is optimized for SHG on the red side of the pulse. The pulse is then dispersed with a transmission grating on to a camera sensor. The doubled frequency interferes with the blue end (500 nm) of the original spectrum and produces an interference pattern in the spectral domain after a transmission grating.

Figure 4.4 (a) shows both the raw spectrum and line-out, obtained by integrating in the vertical direction, for one laser shot recorded with the f-2f depicted in Figure 4.3. The interference fringes can be mathematically expressed as

$$I(\omega) \propto I_{WL}(\omega) + I_{SH}(\omega) + 2\sqrt{I_{WL}(\omega)I_{SH}(\omega)}cos(\omega\tau + \phi_{SH}(\omega) - \phi_{WL}(\omega) + \phi_{CE}), \quad (4.13)$$

where $I_{WL}(\omega)$ and $I_{SH}(\omega)$ represent the intensites of the blue-end spectrum directly from

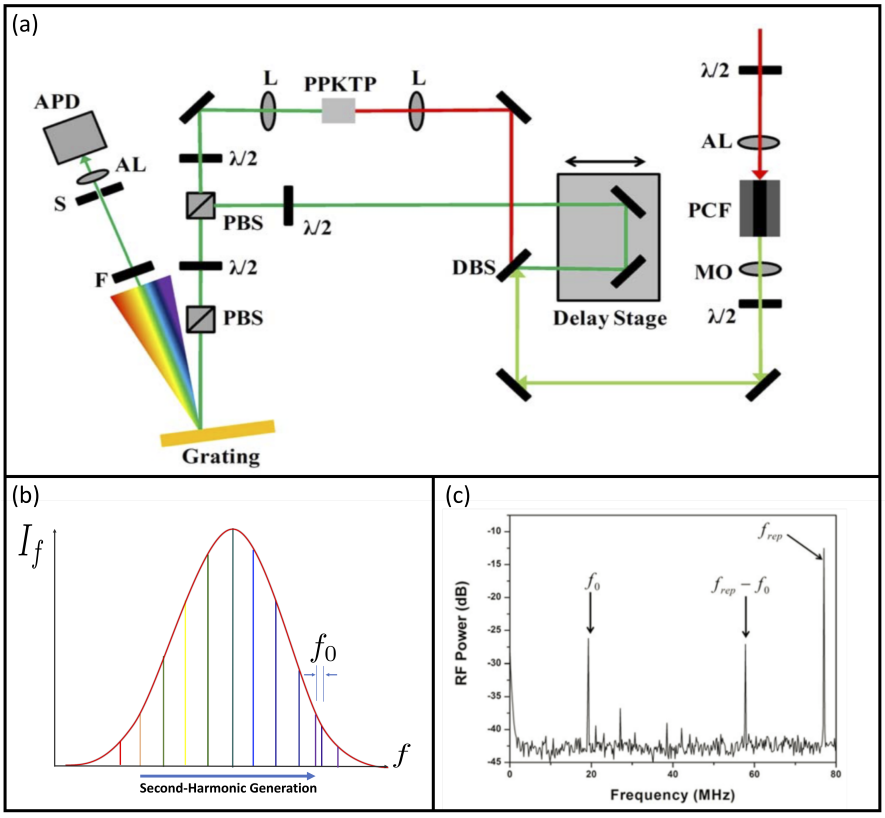

Figure 4.2: *(a) Layout for an f-2f interferometer designed to stabilize f_0. $\lambda/2$- half-wave plate, AL - aspheric lens, PCF- photonics crystal fiber, MO- microscope objective, DBS- dichoric beam splitter, L- lens, PPKTP- periodically-poled potassium titanyl phosphate, PBS- polarization beamcube splitter, F- narrow linewidth filter, S- slit, APD- avalanche photodiode. (b) Second-harmonic generation of frequency comb to measure f_0. (c) RF power spectrum from avalanche photodiode. Adapted from [96].*

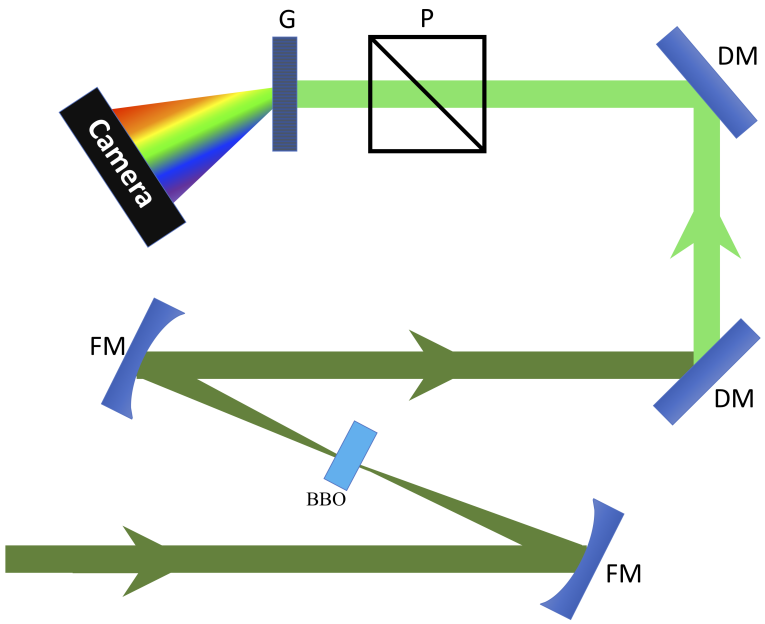

Figure 4.3: *f-2f interferometer. FM: focusing mirror; DM: dichroic mirror; P: polarizer; G: grating*

the few-cycle pulse and the frequency-doubled from the red end of the pulse respectively. τ is the delay between these two pulses, $\phi_{SH}(\omega)$ and $\phi_{WL}(\omega)$ denote the spectral phases of the frequency doubled portion and original portion respectively and ϕ_{CE} is the CEP. It is reasonable to assume that $\omega\tau + \phi_{SH}(\omega) - \phi_{WL}(\omega)$ stays constant for one particular frequency as the component, and thus the phase of $I(\omega)$ can be retrieved as the CEP plus a constant offset.

The spectrum is recorded by the camera sensor, integrated vertically, then filtered through a Hanning window to reduce high frequency noise and padded with zeros to reduce low frequency noise. The spectrum is then Fourier transformed (FFT), and a phase associated with the CEP is extracted as the phase of the first, non-dc peak in the time domain, shown in Figure 4.4 (b). It has been shown previously that a fast camera or spectrometer with sufficiently low exposure time is able to measure a single-shot interference pattern at high speed [104]. A Camera Link interface can be used to transfer the images at kHz rates if the image size is small enough. Further, the FFT is carried out online and only the phase of each shot is saved at a CEP measurement rate of 600 Hz. Several of the acquisition electronics implemented this upper limit of 600 Hz. In practice, this number could be made

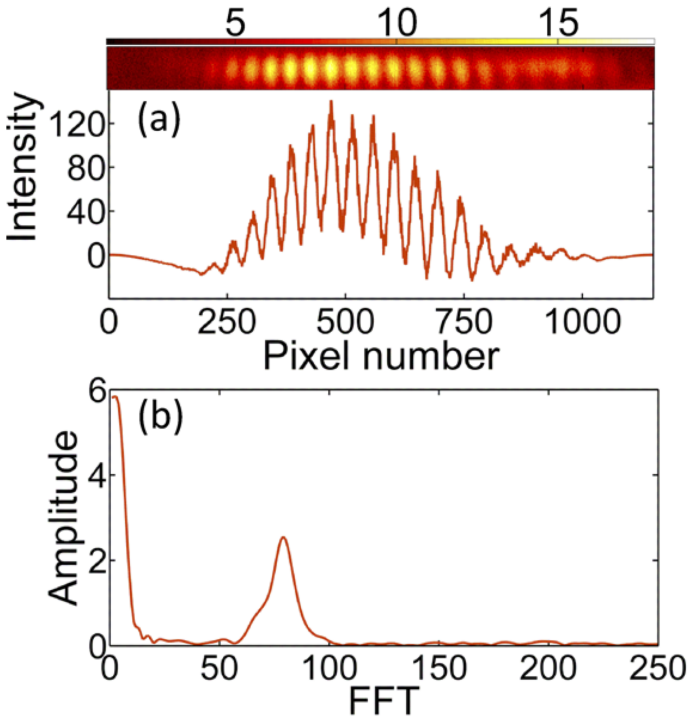

Figure 4.4: *(a) Interference pattern for one laser shot. Fringes are obtained after integrating along the height of the image and applying a Hanning filter. (b) Amplitude of the FFT of the fringes. The relevant component is the peak shown around index 75 from which the phase is extracted.*

much higher by using more efficient acquisition electronics, specifically dedicated 'on-chip' processing schemes such as field-programable gate arrays (FPGAs).

In general, f-f2 interferometry is used more extensively for locking the CEP rather than tagging. However, as presented in section 4.4 the technique is perfectly capable of single shot CEP tagging.

The second method for measuring the CEP presented here is based on strong-field ionization, in particular above threshold ionization (ATI). A few-cycle will inherently have a spatial asymmetry in the optical field. That is, for a given CEP, the pulse will necessarily have a higher intensity in either the positive or negative direction. A stereographic above threshold ionization (ATI) phase meter (CEPM) uses two back-to-back electron time-of-flight spectrometers to measure this effect on the ATI spectrum and extract a CEP value. Figure 4.5 shows a schematic of the CEPM. The concept for the phase meter was first developed by Paulus and co-workers [79; 119]. More detailed explanations can be found in

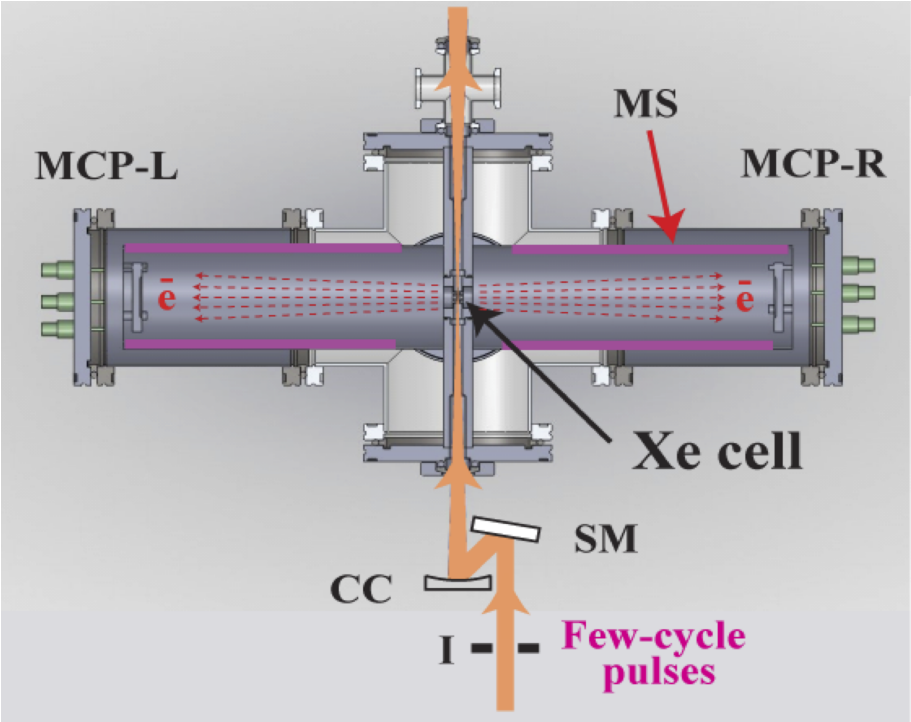

Figure 4.5: *(c) CEPM (described in detail in [20]). I: iris; SM: silver mirror; CC: concave mirror; MS: m-metal shield; MCP: micro channel plate; Xe cell: xenon gas cell.*

[20; 83; 109; 111]

For use, a few tens of microjoules are focused using an f = 25 cm spherical mirror into the phase meter. The few-cycle pulses ionize the target gas at the focus, located inside a gas cell filled with Xe at $\sim 1.3 \times 10^{-6}$ bar. The generated direct (low energy) and backscattered (high energy) electrons are detected using two microchannel plate detectors (Photonis, APD 2 MA25/12/10/12 D 60:1) on both sides of the phase meter (MCP-L & MCP-R). The laser polarization is aligned along the time-of-flight axis, normal to the MCPs. A thin μ-metal sheet shields the electron path from external magnetic field influences. The electron time-of-flight signals from each of the detectors are processed by dedicated electronics [20], and the resulting parametric asymmetry plot (PAP) provides the carrier envelope phase information shot-by-shot [20; 109; 111; 112]. From the PAP, a one-to-one mapping of the polar angle of each individual hit and the single-shot CEP value can be established.

This stereo-ATI phase meter has proven to be a very capable instrument for real-time, single shot CEP tagging. They have also been successfully used across a range of wavelengths

[120]. To date, almost all single-shot CEP tagging studies have been performed using these types of instruments. In some cases, phase meters have also been used to lock the CEP of a laser [107], although f-2f interferometry still remains the dominate technique used for feedback schemes.

4.3 Long-Term Stabilization of the Carrier-Envelope Phase in a Terawatt-Class Laser System

Stabilizing the carrier-envelope phase of a mode locked oscillator is by now a common and robust technique [97]. Excellent commercial CEP stabilization systems exist [121], making it relatively easy to produce few-cycle pulse trains with highly stabilized CEP values. However, this is not the case with amplified laser systems. The chirped-pulse amplification process introduces a large amount of noise into a CEP stabilized pulse train. Mechanical vibrations in the stretcher and compressor are particularly disruptive [105]. This chapter briefly presents work done to produce a 20 mJ laser system with a high degree of long-term CEP stability. This laser is known as the high intensity tunable source or HITS laser.

This HITS laser has two separate amplification stages. The first stage is a 14-pass ring amplifier pumped with a 35 W, Q-switched, DPSS pump laser (Photonics Industries DM35). The second stage consists of a five-pass amplifier in a "bow tie" configuration optically pumped by two frequency doubled, 50 W, Q-switched, DPSS pump lasers (Photonics Industries DM50). The Ti:Sapphire crystals in both stages are cooled to below -200 °C with a cold helium cryogenic cooling system (CryoMech) to avoid thermal lensing. Figure 4.7 (a) shows a layout of the respective components of the laser.

When locking the CEP of an amplified system, it is not actually necessary to fix the CEP of every pulse in the mode locked pulse train seeding the amplifier. Instead, it is only required to lock the CEP change, $\Delta\phi_{CE}$, to a rational fraction of π. For example, if the pulse-to-pulse CEP change of the oscillator is stabilized so that $\Delta\phi_{CE} = \pi/2$, then every fourth pulse will have an identical CEP value since a 2π shift in the CEP constitutes a return

to the original value. Then care just needs to be taken when down-sampling the repetition rate of the pulse train for amplification to select pulses with the same CEP. Locking to a constant phase change is much easier than locking every single pulse because it amounts to locking f_0 to a fixed value instead of zero, as would be required to fix the carrier-envelope phase of every pulse. For the HITS laser, f_0 is locked to $f_{rep}/4$ since a 20 MHz signal is easy to measure and control. This gives $\Delta\phi_{CE} = \pi/2$ as described above, and when the repetition rate is reduced to 1 kHz for amplification, every pulse has the same CEP.

To stabilize the HITS oscillator, a portion of the output is sent into a Menlo Systems XPS800 f-2f interferometer with the SYNCRO electronics package. The CEP noise correction is provided by moving the high reflector in the dispersed arm of the oscillator. Every fourth pulse of the resulting pulse train typically carries CEP noise of 110 mrad in the integration range from 1 MHz to 2 MHz.

The CEP noise accumulated in the CPA process is measured by a sapphire crystal-based f-2f interferometer [113]. A portion of the interferometric signal is split off for single-shot spectral fringe detection using a spectrometer with 1 ms integration time. The rest is sent to a quadrant position sensitive photodiode to measure the "jitter" of a single-shot fringe pattern. This f-2f interferer is shown in figure 4.6. The photodiode signal is integrated to give an analog error signal with a bandwidth up to the repetition rate of the amplifier. This analog error signal is then processed in a proportional-integral-derivative (PID) controller and used as feedback to both the oscillator and compressor gratings. The feedback to the oscillator is termed fast-loop. It pre-compensates the fast drifts of the CEP by modulating the same high reflector used for oscillator CEP locking. The feedback to the compressor grating is termed the slow-loop. It drives the piezo stage under one of the gratings using a PID program to correct for long-term CEP drifts.

A sophisticated mounting system that "floated" both the stretcher and compressor was developed to isolate vibration in each. This proved critical to achieving the final, high degree of CEP stability. More details about the vibration dampening mounts can be found in [62] and [122]. The final carrier-envelope stabilization results are shown in figure 4.7 (b) and (c). The CEP was locked to a value of 300 mrad, single-shot, for a 9-hour period. Figure 4.7 (b)

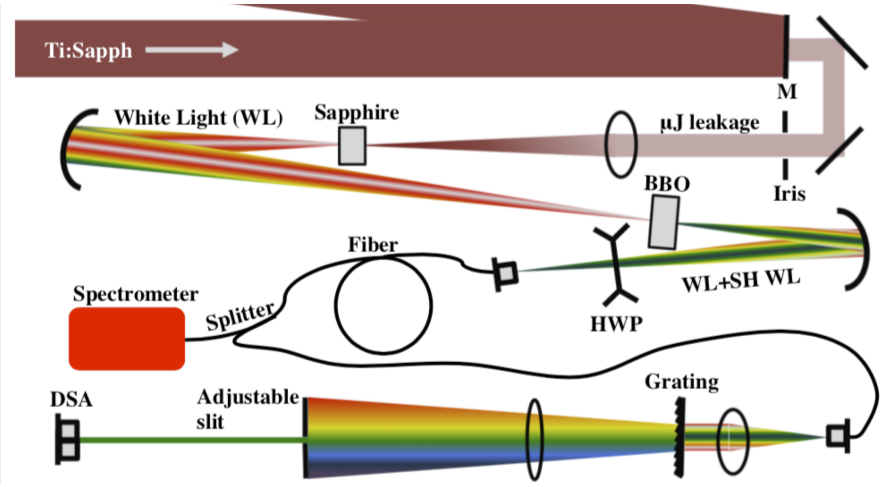

Figure 4.6: *Amplifier CEP locking f-2f interferometer. Adapted from [14]*

shows the CEP value as a function of time. The spike around 250 minutes occurred when the fast-loop PID reached the locking limit, but it was driven back by the slow-loop. Figure 4.7 (c) shows the corresponding spectral fringe pattern. A temperature fluctuation caused the slightly dimmer spectral fringe at around 300 and 500 minutes but did not seem to affect the CEP locking.

4.4 Single-Shot Carrier-Envelope-Phase Tagging Using an f-2f Interferometer and a Phase Meter: A Comparison

This section presents work to directly compare and correlate single-shot carrier-envelope phase tagging with the all optical method of f-2f interferometry and a stereo-above threshold ionization carrier-envelope phase meter. This study uses the PULSAR Ti:Sapphire laser which produces 21 fs, 2 mJ pulses at a repetition rate of 10 kHz. The goal here is to measure the CEP of the pulses simultaneously and synchronously with both methods to allow for a direct comparison. In this study, the PULSAR laser is running without CEP locking, which is the typical operational mode in CEP tagged experiments. Our results demonstrate

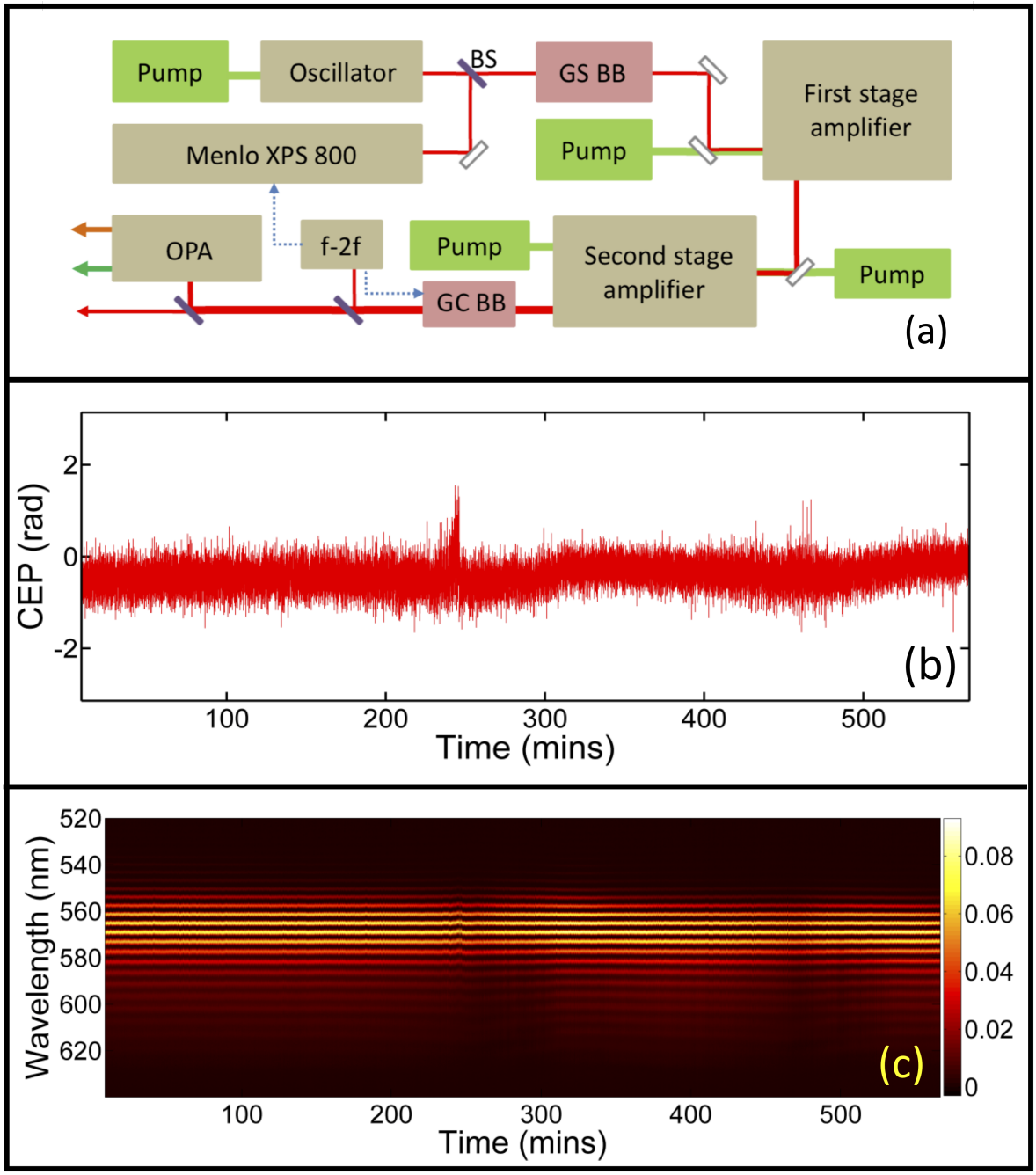

Figure 4.7: *(a) Layout of the 1 kHz, 20 mJ, 26 fs HITS laser system. BS: beam splitter; GS BB: grating stretcher breadboard; GC BB: grating compressor breadboard. (b) Long-term single shot CEP error with the "floated" stretcher and compressor. (c) The spectral fringes for the long-term CEP stabilization using the floating and compressor and stretcher. All measurements performed with an f-2f interferometer.*

that f-2f interferometry is an accurate and robust way to tag CEP values with comparable accuracy to that of the CEMP.

Unlike an f-2f interferometer, the CEPM only operates with few-cycle pulses as the pulse must be short enough to have CEP effects on strong-field ionization due to the spatial intensity asymmetry. In order to produce few-cycle pulses [123], we couple ∼0.9 mJ, 21 fs pulses from the PULSAR laser system into an inert-gas-filled HCF as shown in Figure 4.8. A 1.5 m focal length plano-convex lens is used to focus the laser beam into a 1 m long hollow-core fiber (HCF) with 250 μm inner diameter filled with ∼2.4 bar of Ne gas. The HCF system generates an octave- spanning spectrum from 500 to 1000 nm through self-phase modulation (Figure 4.8 inset). A small portion of the PULSAR beam, split off before the HCF, is used for beam pointing stabilization. The output of the HCF goes through a set of ultra-broadband chirped mirrors (UltraFast Innovations, PC70; -50 fs^2 per reflection at 800 nm) to compensate the positive dispersion due to propagation through the fiber. A pair of fused-silica wedges (LENS-Optics) is used to control the small residual dispersion. Ultimately, this allows for the generation of 5 fs pulses with 0.4 mJ of energy at 10 kHz repetition rate. The pulse duration was estimated from the radius of the parametric asymmetry plot (PAP), as described in [124], as well as from results in previous studies using the same setup [85].

After broadening and re-compression, the pulse is split in two, with one arm sent to the f-2f interferometer and the other into the CEPM. Since the spectrum out of the HCF is already greater than an octave, no pulse broadening is needed to operate the f-2f interferometer. The overall setup is depicted in figure 4.9. The f-2f interferometer and the CEPM were described in section 4.2 and shown in figures 4.3 and 4.5 respectively.

In order to compare the single-shot CEP measured by the f-2f and the CEPM, the timing of the acquisition needs to be precisely controlled. A flow chart of the timing logic is shown in figure 4.9. The camera in the f-2f interferometer is triggered from a delayed photodiode signal and is exposed for a 50 μs window to allow for single-shot detection. At the same time, the frame grabber (NI PCIe-1433) sends a trigger to a National Instrument Data Acquisition (NI-DAQ) card inside the computer. The output signals from the CEPM processing electronics are then recorded by the DAQ card for the same laser shot that produced the f-2f interference

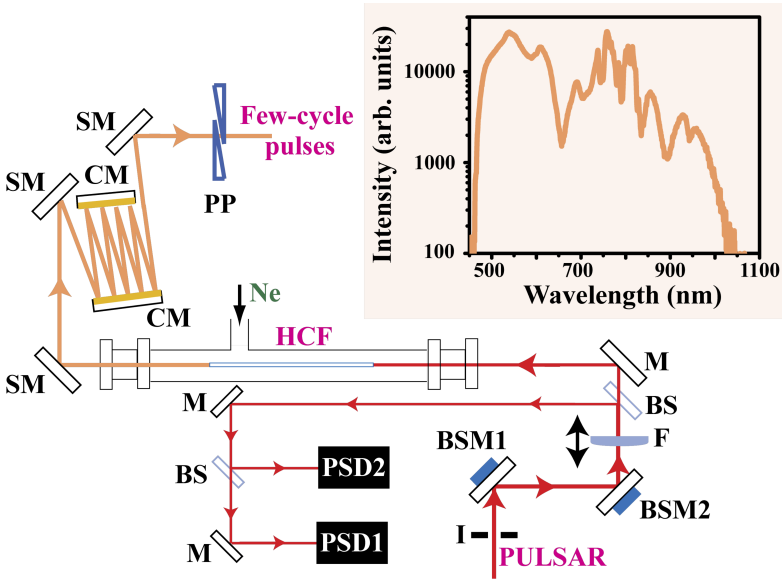

Figure 4.8: *Few-cycle pulse generation system. I: Iris; BSM: beam stabilization mirror; F: lens; BS: beam splitter; M: mirror; PSD: position sensitive detector; HCF: hollow-core fiber; SM: low-dispersive broadband silver mirror; CM: chirped mirror; PP: prism pair. Inset shows octave-spanning spectrum generated through this process.*

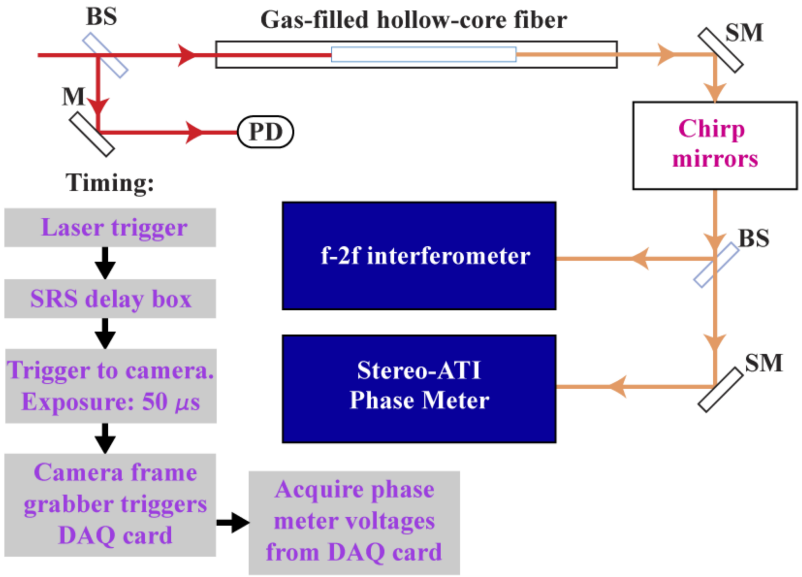

Figure 4.9: *Experimental setup and timing synchronization logic for generating few-cycle pulses and measuring the CEP with both the f-2f interferometer and Stereo-ATI Phase Meter simultaneously.*

pattern.

The results are shown in figure 4.10 panels (a) and (b). Specifically, panel (a) shows a shot-to-shot mapping of the CEP measured by the two methods for 6 million laser shots. Two narrow bands at 45 degrees are clearly observed, suggesting that the CEP measurements from the two are very well correlated with a constant phase difference of 2.24 rad. This constant phase offset depends on the beam path in each measurement arm. Figure 4.10 panel (b) shows the distribution of the shot-to-shot difference between the two measured CEP values. A standard deviation of 220 mrad is calculated from this difference. Möller et al. [125] suggested that, for a 5 fs pulse, CEPM has a CEP measurement uncertainty of about 120 mrad. Using this value, the uncertainty for the f- 2f can then be estimated to be about 184 mrad. However, there is no guarantee that our CEPM has such a low uncertainty, suggesting that 184 mrad might be a high estimate for the CEP uncertainty for the f-2f interferometer. Thus, we can conclude that both methods produce comparable accuracies for CEP tagging.

To check the generality of this conclusion, we performe a further comparison of the CEP measured using the CEPM and a commonly used sapphire-based f-2f interferometer. A small portion of the laser is picked off before the HCF and sent into this second f-2f. The CEP values are then detected and analyzed as described before. The results are shown in figure 4.10 panels (c) and (d). Comparing with figure 4.10 panels (a) and (b), we can see that the correlation between the CEP measurements is much worse than with the f-2f interferometer after the HCF. We measure a standard derivation of 1.25 rad in this case. It has been shown previously that the change of the CEP during the SPM process in the sapphire crystal [115; 126] has a stronger dependence on laser energy fluctuation than the one in the HCF [106; 115]. As such, the relation between carrier-envelope phase measured in the f-2f interferometer and carrier-envelope phase measured in the CEPM are not well correlated. In addition to the increased sensitivity of the self-phase-modulation process, the poor correlation is also compounded from the long optical path difference between the two CEP measurements. Any small laser pointing differences will cause the CEP measured by the two to be very different. This issue is also present for any experiment seeking to make use of the tagged CEP value measures prior to few-cycle pulse generation. However, for the

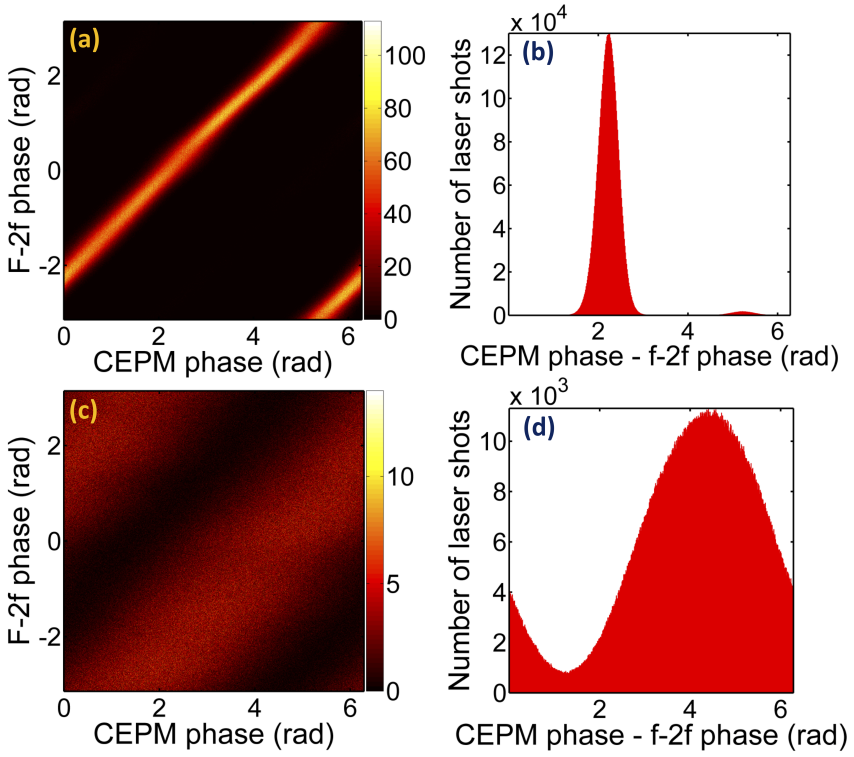

Figure 4.10: *(a) Correlation of the single-shot CEP measured by the CEPM and HCF-based f-2f interferometer. (b) Histogram of the difference between the two phases; phases have been converted to within 0 to 2π (c) and (d) are same as (a) and (b), respectively, but for the CEPM and the sapphire-based f-2f.*

case of the f-2f measurement performed after broadening in the hollow-core-fiber the f-2f and the CEPM share common optical path before being split for CEP detection, making the correlation less susceptible to laser energy and pointing fluctuations.

We have presented a method, based on f-2f interferometry, for single-shot CEP tagging with an estimated 184 mrad uncertainty and shown evidence that CEP-tagged experiments can be performed using an f-2f interferometer. This all-optical method is simpler and easier to operate than the carrier-envelope phase meter. We also note that the f-2f interferometer does not provide the absolute CEP while the CEPM in principle can [109]. However, since the CEP needs to be calibrated at the experiment in both cases, this is not a significant disadvantage.

Chapter 5

Ultrafast Non-Gaussian Optics, Characterization and Applications of Femtosecond Bessel Beams

The simplest method of determining the behavior of an optical element is ray optics. A few simple equations and methods provide a way to estimate how a beam of light will propagate through an optical system. A great deal of sophisticated optical engineering is performed using nothing more than Snell's Law and ray propagation. However, ray optics can produce non-physical behavior, such as focusing light to an infinite point, and it completely ignores diffraction.

Gaussian optics, derived as a solution to the Helmholtz wave equation, provides a much more rigorous method of calculating beam propagation behavior. Within this framework, the transverse profile of a laser beam is described by a Gaussian distribution. As shown in the following section only two independent parameters are needed to fully classify a Gaussian beam, the waist size (or alternatively the confocal parameter) and the optical wavelength. Additionally, as most laser cavities are constructed to lase on the TEM00 mode, which is nearly Gaussian, the equations of Gaussian optics provide a relatively accurate and simple way to calculate the response of most optical systems. In fact, even when used with beam

profiles that are decidedly non-Gaussian (such as the output of a strongly pumped Optical Parametric Amplifier), the equations of Gaussian optics can provide a reasonable estimate (within a factor of two) for quantities such as the minimum spot size and far field divergence.

However, it is also possible to have optical beams that do not, in any form, follow Gaussian beam propagation. Of course, these beams must still satisfy Maxwell's equations (from which the Helmholtz wave equation is derived). Perhaps the most famous class of these non-Gaussian optical beams are Bessel Beams. As the name implies, the transverse profile of a Bessel Beam is mapped out with Bessel functions (for almost all circumstances a zero order Bessel function of the first kind). This has dramatic effects on their propagation dynamics. An "ideal" Bessel beam, one that is exactly described by a Bessel function, propagates with no diffraction at all. As seen in the next section, this seemingly unphysical behavior comes straight out of the wave equation, solved in vacuum with cylindrical coordinates. This isn't a trick of the coordinates though, in Cartesian coordinates a plane wave is a non-diffracting solution. However, the Bessel solution has one major and fundamental difference from a plane wave, the localization of optical energy into finite area. For a J_0 Bessel beam, the peak intensity comes at the central maximum. Each of the subsequent local radial maximum also contain energy. This is where the concept of an ideal Bessel beam ends. The intensity in each of these rings falls of radially as 1/r and as such a Bessel function is not square integrable. Thus, a true Bessel beam would require an infinite amount of optical energy to support.

What really makes Bessel beams an interesting area of experimental research, and not just a mathematical trick, is the ability to generate or engineer quasi-Bessel or Bessel-like beams. These are mathematically described by a Bessel distribution but convolved with an additional profile, such as a Gaussian or flat-top, to localize the beam. These Bessel-like beams still contain, in some form, properties of the ideal Bessel beam. For example, while not perfectly diffractionless Bessel-like beams can be used to contain optical energy to incredibly small areas and propagate with negligible spreading. This difference, when compared to Gaussian beams, can be dramatic. Bessel-Gauss beams or Bessel-like beams have a series of enticing and desirable properties [127; 128]. Among the most notable is

the ability to overcome limitations of the Rayleigh range [129; 130]. Bessel beams maintain focused, on-axis peak intensity for much longer distances than focused Gaussian beams [131].

In the following, I will derive some of the basic formulas for the electromagnetic propagation Bessel beams (Section 5.1), describe development and characterization of an optical setup for the generation of tunable femtosecond Bessel beams (Section 5.2), and present our application of this setup to drive high harmonic generation (Section 5.3).

5.1 Propagation of Electromagnetic Energy

This section derives and presents the equations that govern the spatial propagation of optical beams. These equations are applied to two particular cases, Gaussian beams and Bessel beams. All classical Electrodynamics is, of course, governed by Maxwell's equations (expressed here in vacuum and the absence of free charge)

$$\nabla \cdot \mathbf{E} = 0, \tag{5.1}$$

$$\nabla \cdot \mathbf{B} = 0, \tag{5.2}$$

$$\nabla \times \mathbf{E} = -\frac{\partial \mathbf{B}}{\partial t}, \tag{5.3}$$

$$\nabla \times \mathbf{B} = \mu_0 \epsilon_0 \frac{\partial \mathbf{E}}{\partial t}. \tag{5.4}$$

Maxwell's equations can be re-expressed in the form of the electromagnetic wave equation in vacuum

$$\boxed{\nabla^2 \mathbf{E} - \mu_0 \epsilon_0 \frac{\partial^2 \mathbf{E}}{\partial^2 t} = 0}, \tag{5.5}$$

with

$$\frac{1}{\sqrt{\epsilon_0 \mu_0}} = c \tag{5.6}$$

where c is the speed of light.

Now we use separation of variables for the temporal and spatial part of E.

$$E(\mathbf{r}, t) = R(\mathbf{r})T(t) \tag{5.7}$$

The temporal equation has the simple solution of

$$T(t) = e^{i\omega t}. \tag{5.8}$$

The spatial part can be rearranged as

$$(\nabla^2 - k^2)R = 0 \tag{5.9}$$

otherwise known as the Helmholtz equation where

$$k = \frac{\omega}{c}. \tag{5.10}$$

The solutions to the Helmholtz equation will give the spatial dependence of an electromagnetic wave. One approximation/assumption in this was that R is a scalar or that the direction of the Electric field can be described using only one spatial variable. For linearly polarized beams this is the case and more complex beams can always be constructed as a superposition of linearly polarized waves.

When solving the Helmholtz equation for an electromagnetic wave, it is usually convenient to orient the propagation direction along the z-axis and separate out the primary propagation factor such that spatial portion of the electric field is expressed as

$$R(\mathbf{r}) \equiv \widetilde{u}(x, y, z)e^{-ikz}. \tag{5.11}$$

Where u is a complex scalar that describes the profile of the beam. Inserting this into 5.9 and differentiating by parts gives

$$\nabla_t^2 \widetilde{u}(\mathbf{s}, z) + \frac{\partial^2 \widetilde{u}}{\partial z^2} - 2ik\frac{\widetilde{u}}{\partial z} = 0, \tag{5.12}$$

where s is the radial coordinate which can be either $s(x, y)$ or $s(r, \theta)$.

At this point everything so far has been exact. But it is now very helpful to make the paraxial approximation which essentially says the rate of change along z is small compared to that along the radial coordinate. Mathematically, this lets us set $\frac{\partial^2 \widetilde{u}}{\partial z^2} \approx 0$ and gives the paraxial wave equation.

$$\boxed{\nabla_t^2 \widetilde{u}(\mathbf{s}, z) - 2ik\frac{\widetilde{u}}{\partial z} = 0}, \tag{5.13}$$

where

$$\nabla_t^2 \widetilde{u}(\mathbf{s}, z), \tag{5.14}$$

is the Laplacian operating on the transfers coordinates. The paraxial wave approximation is equivalent to making the small angle approximation and is generally valid as long as beams are traveling at a reasonably small angle (less than 30 degrees [13]) to the z-axis.

Now, let's propose a solution to the paraxial wave equation of the form:

$$\widetilde{u}(x, y, z) = A(z)\exp\Big[-ik\frac{x^2 + y^2}{2\widetilde{q}(z)}\Big], \tag{5.15}$$

where both $A(z)$ and $\widetilde{q}(z)$ are as yet undetermined and Cartesian coordinates have obviously been chosen.

Plugging this into the paraxial wave equation gives

$$\Big[\Big(\frac{k}{2}\Big)^2\Big(\frac{d\widetilde{q}}{dz} - 1\Big)(x^2 + y^2) - \frac{2ik}{\widetilde{q}}\Big(\frac{\widetilde{q}}{A}\frac{dA}{dz} + 1\Big)\Big]A(z) = 0. \tag{5.16}$$

For this equation to be valid for all sets of transverse coordinates, both terms in the large

brackets must be identically zero, leading too:

$$\frac{d\widetilde{q}(z)}{dz} = 1, \tag{5.17}$$

and

$$\frac{dA(z)}{dZ} = -\frac{A(z)}{\widetilde{q}z} \tag{5.18}$$

Which have the respective solutions of

$$\widetilde{q}(z) = \widetilde{q}_0 + z - z_0, \tag{5.19}$$

and

$$A(z) = \frac{A_0\widetilde{q}_0}{\widetilde{q}(z)} \tag{5.20}$$

Inserting $\widetilde{q}(z)$ into 5.15 gives

$$\widetilde{u}(x,y,z) = A(z)\exp\Big[-ik\frac{x^2+y^2}{2(\widetilde{q}_0 + z - z_0)}\Big]. \tag{5.21}$$

Split $\widetilde{q}_0$ into its imaginary and real components

$$\widetilde{q}_0 \equiv q_{oR} + iq_{0I}. \tag{5.22}$$

Which gives:

$$\widetilde{u}(x,y,z) = A(z)\exp\Big[-\frac{ik}{2}(x^2+y^2)\Big(\frac{1}{q_{0R} + z - z_0 + iq_{0I}}\Big)\Big]. \tag{5.23}$$

Partial fraction decomposition gives the following relation,

$$\frac{1}{\alpha + i\beta} = \frac{\alpha}{\alpha^2+\beta^2} - i\frac{\beta}{\alpha^2+\beta^2}. \tag{5.24}$$

Which allows 5.24 to be split as

$$\widetilde{u}(x,y,z) = A(z)\exp\Big[-\frac{ik}{2}(x^2+y^2)\Big(\frac{q_{0R}+z+z_0}{(q_{0R}+z-z_0)^2+q_{0I}^2} - i\frac{q_{0I}}{(q_{0R}+z-z_0)^2+q_{0I}^2}\Big)\Big]. \quad (5.25)$$

Writing this in a more convenient way gives

$$\widetilde{u}(x,y,z) = A(z)\exp\Big[\frac{-ik(x^2+y^2)}{2R(z)} - \frac{k(x^2+y^2)}{\omega^2(z)}\Big], \quad (5.26)$$

where we will see that $R(z)$ and $\omega^2(z)$ are the radius of curvature and waist size of a gaussian beam respectively, as shown in figure 5.1 with

$$R(z) = \frac{(q_{0R}+z+z_0)^2+q_{0I}^2}{q_{0R}+z-z_0}, \quad (5.27)$$

and

$$\omega^2(z) = -2\frac{(q_{0R}+z+z_0)^2+q_{0I}^2}{q_{0I}}. \quad (5.28)$$

The actual value of q_{0R}, and q_{0I} are in practice almost never actually used, as beams are defined in terms of the "lab based" quantities $R(z)$ and $\omega(z)$. Mathematically, q_{0R}, and q_{0I} represent the real and imaginary initial coordinates of a spherical wave propagating outwards with a complex radius of curvature given by $\widetilde{q}(z)$. Evidently, a Gaussian beam is mathematically equivalent to a spherical wave propagation from a complex source point and a complex radius of curvature. A discussion and derivation of this is nicely presented in chapter 16 of [13].

The complex radius of curvature is related to $R(z)$ and $\omega(z)$ by

$$\widetilde{q}(z) = \Big[\frac{1}{R(z)} - i\frac{\lambda}{\pi\omega^2(z)}\Big]^{-1} \quad (5.29)$$

The final step of this solution is to write $A(z)$ in terms of $R(z)$ and $\omega(z)$. Using equations 5.27, 5.28 and 5.29, along with a hefty amount of algebra and remembering that a complex

number can be expressed an exponential, we get:

$$\frac{\widetilde{q_0}}{q_(z)} = \omega_0 \frac{exp\big[i\psi(z) - \psi_0\big]}{\omega(z)}, \tag{5.30}$$

where ω_0 is the initial beam waist, ψ_0 a term known as the initial phase angle (an often not relevant for most calculations) and $\psi(z)$ is the phase angle defined by:

$$\psi(z) = arctan\Big(\frac{\pi\omega^2(z)}{R(z)\lambda}\Big). \tag{5.31}$$

Finally, all of these expressions can be plugged back in to give the paraxial solution to the Helmholtz equation for a Gaussian beam defined in terms of the radius of curvature and the beam waist.

$$\boxed{\widetilde{u}(x,y,z) = \Big(\frac{1}{\pi}\Big)^{1/2} \frac{exp(-ikz + i\psi(z))}{\omega(z)} exp\Big[-\frac{x^2+y^2}{\omega^2(z)} - ik\frac{x^2+y^2}{2R(z)}\Big]} \tag{5.32}$$

Now, after all of the math, let us take a look a what the exact physics behind this are. First, it is important to remember that this is just *a* solution to the Helmholtz's equation not *the* solution. The form we chose in equation 5.15 has no special meaning, at least not mathematically speaking. It is however, a very physically relevant solution. As mentioned previously, most lasers are constructed to lase on the TEM00 mode which is almost Gaussian. So, this expression should do a good job of calculating the behavior of most laser beams propagating through an optical system. These would typically be quantities such as the minimum spot size after a focusing optic (necessary to calculate the peak laser intensity) or the far-field divergence of a beam. To completely characterize a Gaussian beam, only two quantities are needed, the wavelength and the minimum spot size, or beam waist. All of the relevant parameters are related by the following equations [13]. The complex radius of curvature is related to $R(z)$ and $\omega(z)$ by

$$\omega(z) = \omega_0 \sqrt{1 + \Big(\frac{z}{z_r}\Big)^2}, \tag{5.33}$$

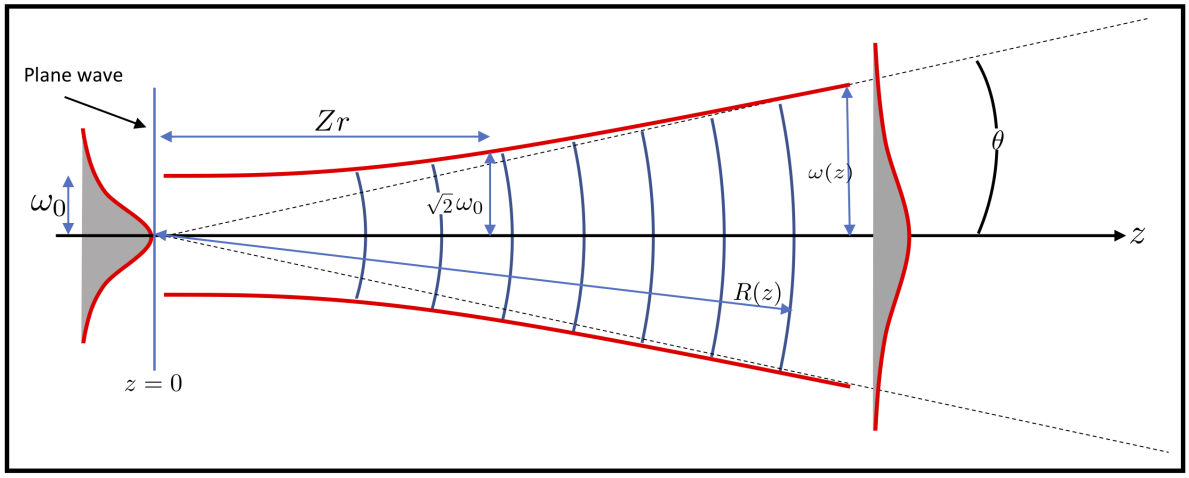

Figure 5.1: *Propagation of a Gaussian beam from a minimum spot-size outward.*

$$R(z) = z + \frac{z_R^2}{z}, \tag{5.34}$$

and

$$\psi(z) = arctan\left(\frac{z}{z_r}\right), \tag{5.35}$$

where z_r is a particularly useful quantity known as the Rayleigh range,

$$z_r \equiv \sqrt{2}\omega_0 = \frac{2\pi\omega_0^2}{\lambda}. \tag{5.36}$$

The Rayleigh range gives a way of quantifying the depth of field of a focus. After a beam has propagated one Rayleigh range away from the focal plane, $\omega(z)$ has grown by $\sqrt{2}$ and the overall peak amplitude falls by a factor of two.

As a final consideration, let's examine how a Gaussian beam is focused, namely what the focal spot size and Rayleigh range are as a function of the focal length of the focusing optic and input beam size to that optic. In equation 5.33 ω_0 is the beam waist with $\omega(z)$ expanding from there. Of course, this could be reversed and we could alternately think of $\omega(z)$ as the input parameter which propagates down to a focus.

As such, we can write

$$\omega(f) = \omega_0\sqrt{1 + \left(\frac{f}{z_r}\right)^2}, \tag{5.37}$$

where f is the focal length and $\omega(f)$ is the size of the beam at that position of the focusing optic.

If f is much larger than z_R as it is for almost all cases, then we can write

$$\omega(f) \approx \omega_0 \frac{f}{z_r} = \frac{\lambda f}{\pi \omega_0} \tag{5.38}$$

Which gives:

$$\omega_0 = \frac{\lambda f}{\pi \omega(f)}. \tag{5.39}$$

The focal spot size scales linearly with wavelength and focal length while scaling inversely with the input spot size. So, for a given laser source, the only things that can be adjusted to change the spot size are the beam size or focal length. The behavior is very rigid for Gaussian beams.

This hard link between the input spot-size, wavelength and Gaussian focal profile is the primary reason that motivates the use of non-Gaussian beams in strong-field physics.

Now we will consider Bessel-type beams. The full derivation of a Bessel beam is many times more involved than a Gaussian beam, so I will only present a few qualitative derivations and cite the final results from other works. However, the formal method is the same as for a Gaussian beam, start with Helmholtz equation, or the paraxial wave equation, propose a solution of the desired form and turn the crank to get the full solution and relevant relations.

In cylindrical coordinates, the wave equation from 5.5 can be expressed as

$$\frac{1}{r}\frac{\partial}{\partial s}\left(r\frac{\partial \overrightarrow{E}}{\partial r}\right) + \frac{1}{r^2}\frac{\partial^2 \overrightarrow{E}}{\partial \phi^2} + \frac{\partial^2 \overrightarrow{E}}{\partial z^2} - \mu_0 \epsilon_0 \frac{\partial^2 \overrightarrow{E}}{\partial^2 t} = 0. \tag{5.40}$$

An exact, scalar solution for this equation is

$$E(r,t) = exp(i(\beta z - \omega t))J_0(\alpha r), \tag{5.41}$$

where J_0 is the zero-order Bessel function and α and β are defined by $\beta^2 + \alpha^2 = (\omega/c)^2$.

This solution clearly has no radial dependence on z. That is to say that the radial

profile does not change with propagation. This is distinctly different than what we saw for Gaussians beams and is known as a diffraction free beam. As mentioned above, this solution has the incredibly interesting fact that it also has localized features (unlike a plane wave). Note that when $\alpha = 0$ this solution reduces to a plane wave. The first zero of a zero-order Bessel function is at 2.4048. So, the Bessel beam above will have a central spot size of

$$r\alpha = 2.4048 \Rightarrow r_0 = \frac{2.4048}{\alpha} \tag{5.42}$$

As depicted in figure 5.2, the J_0 beam can be constructed by a superposition of plane waves traveling on a cone with an angle β with respect to the z-axis defined by [132]

$$\alpha = \frac{2\pi}{\lambda} sin(\beta) \tag{5.43}$$

An important note is that β in equation 5.43 is not the same as the one in equation 5.41. It is an unfortunate limit of notation but in almost all literature β is used to describe the angle of a plane wave (or optical ray) with respect to the optical axis. All further uses of β will refer to this and equation 5.43.

By expressing the Bessel beam as a superposition of plane waves, we can get a better feel for the physics of a Bessel beam. For example, if we set the radius of the central maxima to be $100\,\mu$m, then we can calculate the angle at which the plane wave would travel to be:

$$\beta = arcsin\left(\frac{2.4048}{\frac{2\pi}{\lambda} r_0}\right) = 0.13^\circ, \tag{5.44}$$

with a wavelength of 500 nm.

So, if we could construct a cone of perfect plane waves traveling at 0.13 degrees, then we could produce a spot $200\,\mu$m in diameter with no spreading as it propagates. Of course, it is vital to remember that this type of beam would require an infinite amount of energy to support. Durnin addresses this by simulating the propagation after an aperture is used to truncate an ideal Bessel beam such that the energy to form the beam would be finite [133].

He finds that, for a zero-order Bessel beam with the same central maximum spot size of 200 μm as above, truncated by an aperture with a radius of 2 mm, the central maxima propagates with near constant intensity (neglecting some fast oscillators) for almost a meter. It would take a focal length of almost 5 meters to get a Rayleigh range that long with the same input size. Additionally, the focal waist ω_0 would be 5 times larger than the Bessel central maximum. If the aperture radius is increased to 1 cm, then the central spot stretches out to more the 5 meters. Clearly, even quasi-Bessel beams are extremely resistant to diffractive spreading.

The question is how to generate a Bessel or quasi-Bessel beam. There are quite a few methods including ring-apertures [134], Fresnel zone plates [135], Air-spaced doublet lens systems [136], spatial light modulators [137] and axicon lens [138]. Each of these have their own advantages and disadvantages. Ring-apatures can generate high-quality beams but, by design, only transmit a small fraction of the incident radiation. Zone-plates can be very expensive and often require custom fabrication. Doublet lens systems can be quite limited in the properties of beam they can be used to produce. Spatial light modulators can be used very effectively and offer a large degree of tunablity. However, they are expensive, limited to certain wavelengths, and cannot be used for high-power beams. Axicons are relatively inexpensive, easy to use and can be used with a wide range of wavelengths. The rest of this chapter will focus solely on axicons.

The conical lens axicon was originally introduced and used by McLeod [138]. Shown in figure 5.2, an axicon is typically made of glass, and defined by a base angle γ. Axicons have several major advantages over the other methods. The first is that unlike ring apertures, axicons convert all of the input optical energy into the Bessel beam. They are also relatively inexpensive (at least compared to many of the other options) and since they are constructed with glass, they work over a large frequency range.

An axicon produces a Bessel beam by tilting the wave front onto the cone of propagation described by equation 5.43. Using Snell's law, it is relatively easy to calculate the outgoing

angle of propagation (with respect to the optical axis)

$$\beta = arcsin[nsin(\gamma)] - \gamma, \tag{5.45}$$

in terms of the base angle, γ and the index of refraction, n, of the axicon.

As long as the incoming beam to the axicon can be reasonably approximated as a set of plane waves, then an axicon will produce a Bessel beam and these results remain at least good estimates of the behavior. A full treatment using Huygens phase integrals can be found in [132].

However, the input beam into an optical system is rarely approximated well by plane waves. As mentioned above, a Gaussian beam is a much more realistic input. The theory and results for this case are worked out in [139; 140]. In the paraxial approximation the solution of the the Bessel-Gauss electric field ($E_{BG}(r,z)$) takes the form [141]:

$$E_{BG}(r,z) = \frac{E_f}{\sqrt{1+(2z/b_{BG})^2}} J_0\Big(\frac{krsin(\gamma)}{1+(2z/B_{BG})}\Big) \times \exp\Big[-\frac{k(r^2+z^2sin^2(\gamma))/b_{BG}}{1+(2z/b_{BG})^2}\Big] \times$$
$$\exp\Big[i\Big(kzcos(\gamma) - arctan\Big(\frac{2z}{b_{BG}}\Big)\Big)\Big] \times \exp\Big[i\frac{2z}{b_{BG}}\Big(\frac{k(r^2+z^2sin^2(\gamma))/b_{BG}}{1+(2z/b_{BG})^2}\Big)\Big]. \tag{5.46}$$

The full (non-paraxial) solution is worked out in [142].

In practice, these expressions are not particularly useful for most experimental cases, but it is nice to see that an analytic expression is obtainable. Most of the insight comes from the simpler equations and the concept that a Bessel beam can be constructed as a cone of plane waves.

A final discussion on the properties of Bessel beams is the far-field behavior. The finite size of the axicon, along with the angle of propagation for the wavevectors means that at some point, the on-axis intensity will completely fall off (infinite energy is required to permanently support the Bessel beam on-axes intensity). After this, the mode transforms into a "donut mode" where all of the energy is concentrated into a single, expanding ring. A wide verity of experiments use this behavior feature of Bessel beams. The work presented

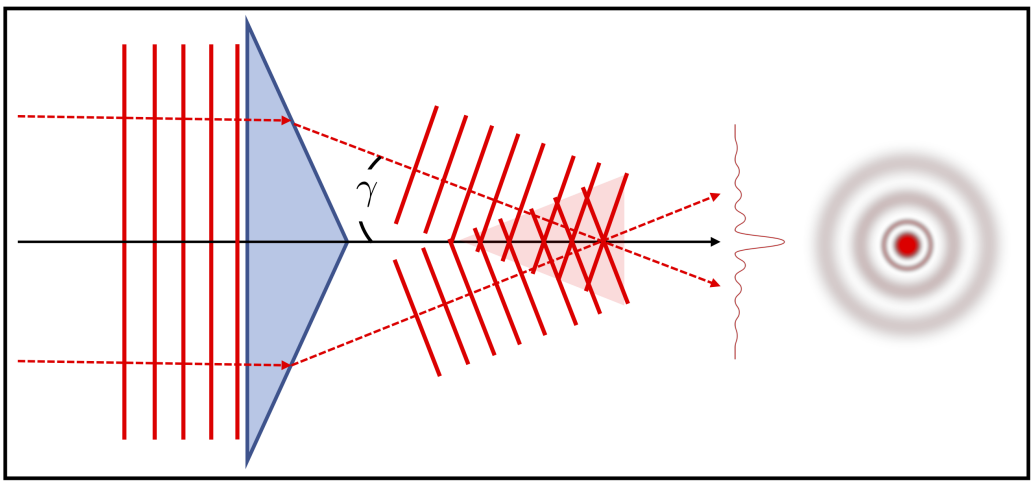

Figure 5.2: *Propagation of plane-waves through and axicon and the formation of a Bessel beam.*

later in this chapter, with high harmonic generation, exploits both the extremely long on-axis peak intensity of a Bessel beam and the transition into the donut mode to increase the flux of deliverable HHG radiation.

All of the tunability of a Bessel beam generated from an axicon comes from the angle of the axicon, γ. This obviously means that a new axicon would be needed to adjust the properties of the beam.

In the next section, a design of an optical system that uses a focusing lens in combination with an axicon is presented. A great deal of tunability in the focal profile can be achieved by varying the distance between the lens and axicon.

5.2 Spatial Characterization of Bessel-Like Beams for Strong-Field Physics

The use of high-power Bessel beams has several large technical challenges. Most notably, as a large number of experiments using ultrafast lasers are performed in vacuum chambers, the laser light needs to be coupled into the system through a window. The fluence on such windows needs to be kept low to avoid damage and undesired nonlinear effects. In conventional setups, using Gaussian focusing optics, this is frequently overcome using long

focal length optics with the window placed far away from the focus. This is difficult to do using just an axicon as shallow axicons produce a very large "focal waist". This limits the maximum achievable intensity to prohibitively low values. Sharp-angle axicons can produce very tight foci but also have extremely short working distance, unsuitable for coupling into vacuum.

This section focuses on designing and characterizing a simple, compact and flexible setup for generating relatively tight focusing Bessel-like beams with long effective working distances. By placing a positive, spherical lens before a shallow-angle axicon, it is possible to produce tight focal spot sizes while keeping the working distance long enough to allow for high-energy laser pulses to be coupled into vacuum. Additionally, by adjusting the ratio of the spherical lens focal length to the distance between the two optics, a very large array of spot sizes can be produced using a single axicon. This adds a great deal of tunability to the setup and dramatically increases the usability. We present detailed characterization measurements for a variety of spherical lens focal lengths and distances between the axicon and focusing lens using both pulsed and continuous-wave lasers.

These measurements use a form of high dynamic range (HDR) imaging to accurately measure the intensity profile of focused Bessel beams over a large scanning range. Both the ability to generate tight foci with long effective working distances and the extreme tunability of our setup are promising for using Bessel beams in strong-field science.

5.2.1 Optical Setup and Beam Characterization

A schematic of the experimental setup is shown in figure 5.3 For comparison purposes, we use two laser sources, a continuous-wave HeNe laser with 633 nm wavelength and a femtosecond laser delivering 35 fs pulses with a center wavelength of 795 nm and a repetition rate of 2 kHz. Three neutral density (ND) filters are used to attenuate the beam to different levels for our high-dynamic-range (HDR) imaging scheme. The ND filters are individually calibrated for each of the two laser sources and their values are reported in terms of optical density. Three positive spherical lenses with focal lengths of 100, 200 and 300 mm are placed in front

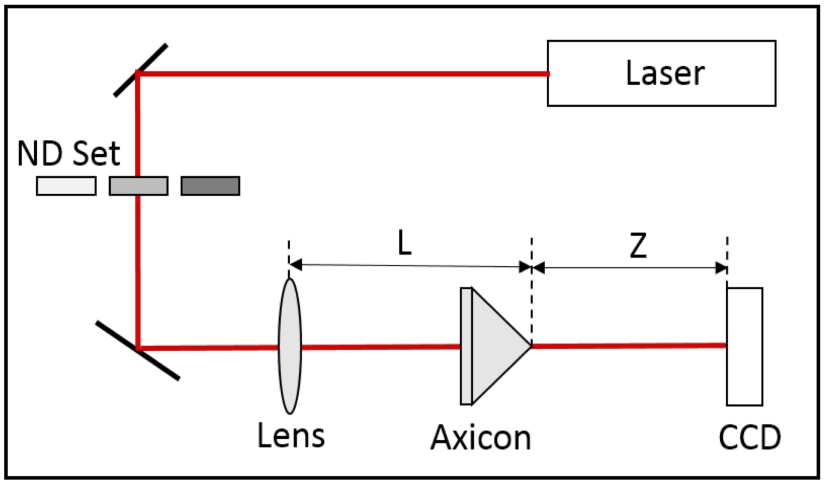

Figure 5.3: *Experimental setup*

of the axicon (Edmund Optics), which has a base angle of 1 degree and diameter of 25.4 mm. The distance (L) between the lens and the axicon is changed in order to tune the focal spot size and the axial depth of field of the Bessel-like beam. A camera (Mightex, SME-B050-U B/W) is used to record beam profiles at various axial (Z) positions (Z=0 is defined at the axicon tip). For some measurements, a circular piece of aluminum foil of 2 mm in diameter is placed directly in front of the axicon to block the central portion of the laser in order to reduce intensity modulation caused by the blunt axicon tip [136].

One key issue in the focal profile analysis is the accurate determination of intensity distribution. This issue becomes more difficult for analyzing laser beams with large intensity variations. Bessel-like beams are an extreme example of such a case. Due to the fact that each of the outer rings in an ideal Bessel beam contains the same amount of energy [143], the intensity of each ring falls off as a function of radius. Imaging with high bit-depth is required to capture both the outer rings and the minima in between rings. In this work, we use the technique of high-dynamic-range imaging to extend the image bit-depth. This process is shown in figure 5.4. At each axial (Z) position, three distinct images (Figure 5.4 (a)-(c)) are captured, each using a separate ND filter. Due to the limited, 8-bit depth of the camera, either high intensity regions are saturated (Figure 5.4 (b) and (c)), or low intensity regions are not visible (Figure 5.4 (a)). The HDR image is generated algorithmically by replacing saturated pixels of the middle image (ND2) with the corresponding, unsaturated, pixels in

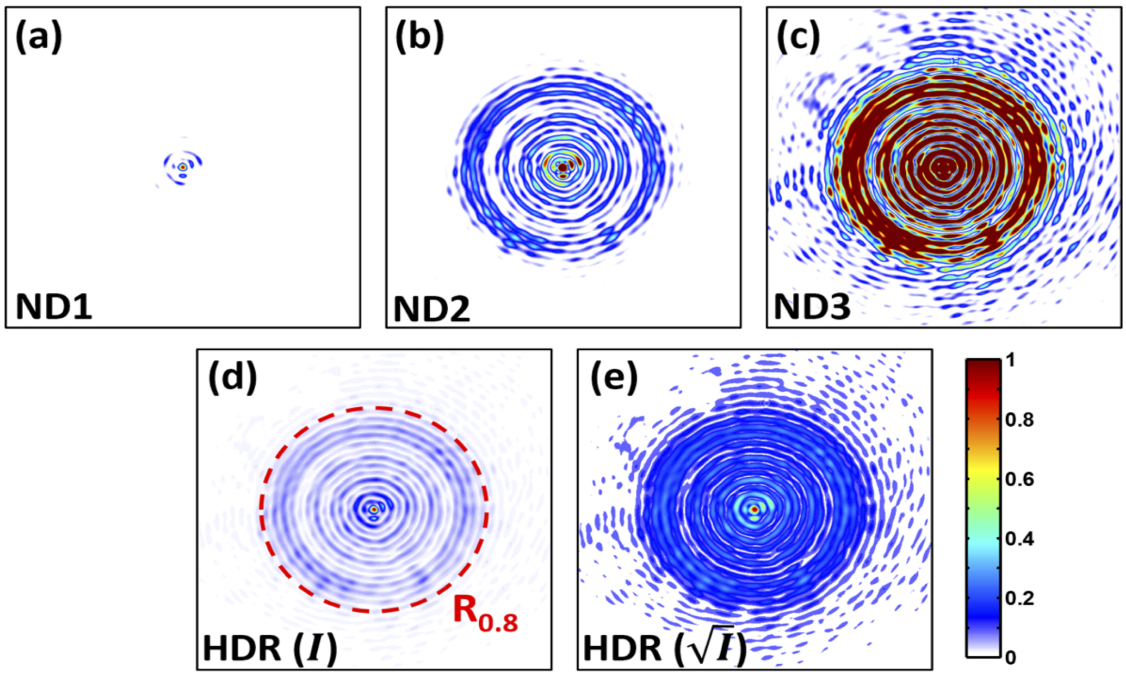

Figure 5.4: *An example showing HDR image processing. Images (a)-(c) are obtained using three ND filters with the femtosecond laser. Combined high dynamic range (HDR) images are shown in (d) with linear intensity (I) and in (e) with square root I. 80% of the total energy falls within the red circle in (d) with a radius of* $R_{0.8}$.

the highly attenuated image (ND1). Similarly, pixels with a low value in the middle image are replaced with the corresponding pixels in the least attenuated image (ND3). Before combination, the raw pixel values of all images are multiplied by the corresponding optical density values. The result is a combined image where both high and low intensity regions are present, as shown in Figure 5.4 (d). The low-intensity, outer rings are emphasized in Figure 5.4 (e) by plotting the square root of the intensity.

This technique can significantly increase the effective bit depth of the camera. As such, detailed and accurate measurements can be performed without the need for prohibitively expensive, high-bit-depth cameras. The effective bit-depth of the combined images is approximately 14-bits, representing a 64-fold increase in detection range over a single 8-bit image.

The intensity of focused Bessel-like beams does not decrease monotonically as a function of radial distance away from the center beam. As such, standard parameters such as the

full-width-at-half-maximum (FWHM) and $1/e^2$ beam waist do not accurately describe the focal profile. For this study, we use a more suitable parameter, the radius at which 80% of the beam energy falls within, $R_{0.8}$. Shown as the dotted red line in figure 5.4 (d), this parameter captures the most usable part of the mode but was admittedly chosen, to some degree, arbitrarily.

5.2.2 Results and Discussion

We examine the profiles of Bessel-like beams generated with the combination of a lens and an axicon. As stated above, we use two laser sources, a continuous-wave (CW) HeNe laser and a femtosecond laser delivering 35 fs FWHM pulses. Figure 5.5 shows the beam shape on the transverse plane (figure 5.5 a) and (b)) and the longitudinal sections (figure 5.5 (c) and (d)), for the two laser types. These measurements were taken using a lens with a focal length of 200 mm and a distance L of 10 mm.

We observe similarities between the two cases. Bright cores start to form at around Z=85 mm, where Z is the distance between the axicon and the observation plane. Concentric rings appear at a further distance (Z=90-100 mm), resembling those of Bessel and Bessel-Gauss beams [134; 143]. However, a few key differences are observed compared to the ideal Bessel and Bessel-Gauss beams. We attribute most these differences to the imperfect axicon tip. First, as L changes, the central cores vary in intensity, which is more noticeable on the longitudinal profiles (figure 5.5). This has been linked in previous work [136] to an imperfect axicon tip. We show later that it can be suppressed by blocking the central part of the input beam.

Second, we observe reduced intensity for the inner rings at Z 100 mm. For instance, on the Z=110 mm images in Figure 5.5 (a) and (b), one can see that some inner rings have lower intensity (in whiter color) compared to the outer rings. This intensity modulation is more apparent in figure 5.5 (c) and (d), where one can see discrete, symmetric structures around the cores at Z>100 mm. At first glance, such modulation is similar to the diffraction pattern of a circular aperture. However, in our experimental setup no aperture is used to truncate

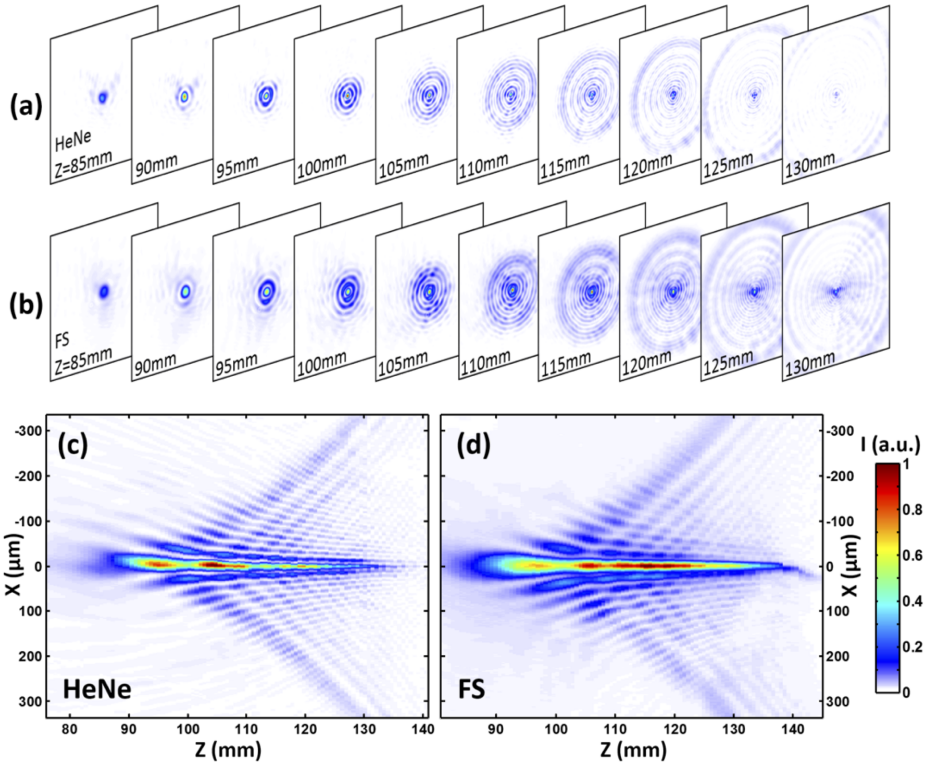

Figure 5.5: *(a, b) Bessel-like beams observed at various distances (Z) from the axicon for (a) HeNe and (b) femtosecond (FS) lasers. (c, d) Longitudinal profiles of laser beams for (c) HeNe and (d) femtosecond lasers. Intensities are normalized to the peak values in the two cases.*

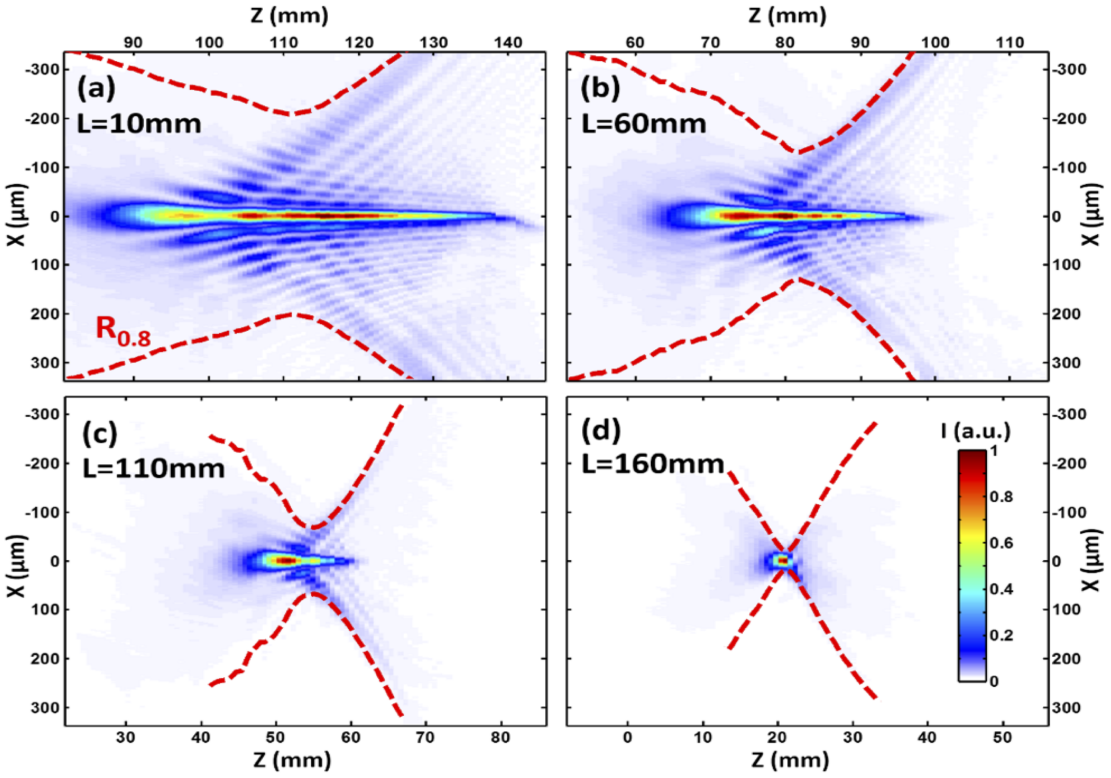

Figure 5.6: *Longitudinal sections of femtosecond Bessel-like beams generated at various lens-axicon distances (L) as a function of distance from the axicon tip. The focal length of the lens is 200 mm. Red dashed lines mark the boundary of 80% energy beam size ($R_{0.8}$).*

the beam.

We also observe differences between the HeNe and pulsed laser. The HeNe beam shape is smaller than the pulsed beam, in both transverse and axial dimension. This is due to the fact the HeNe wavelength (633 nm) and input beam size (7.4 mm, $1/e^2$ size) are both smaller than those of the pulsed laser (790 nm and 9.8 mm, respectively). One difference of particular interest is the reduced fidelity of outer rings for the pulsed laser, which is more noticeable by comparing figure 5.5 (d) with figure 5.5 (c). As has been pointed out by others [144; 145], the temporal aspect of the pulsed laser can alter the spatial aspect. We speculate that the difference is due to the bandwidth content in a femstosecond pulse compared to CW lasers. This is an important effect to keep in mind when generating Bessel-like beams with pulsed lasers.

Next, we investigate the beam profiles for various lens-to-axicon distances, L. The results

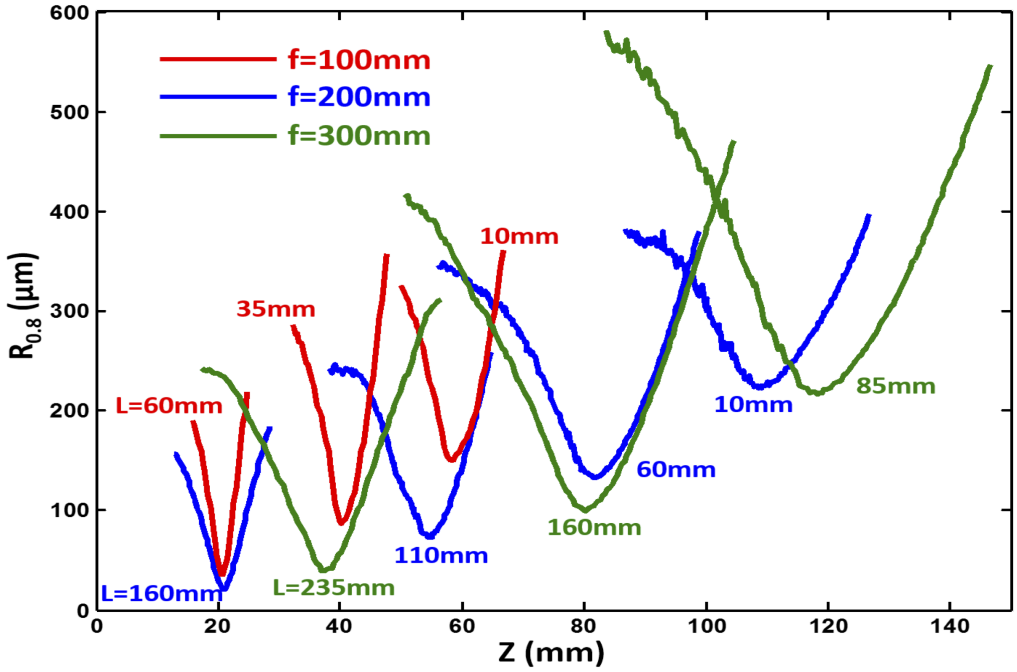

Figure 5.7: *The 80%-energy beam size measured for three focal lengths (f) and various distances from the axicon (L). Axicon is at Z=0.*

are shown in figure 5.6 for L=10, 60, 110 and 160 mm. The focal length of the lens is f=200 mm. We can see that as L increases, the depth of field decreases along with the focal spot size. This is expected, because as the lens moves away from the axicon, the beam size on the axicon aperture reduces, resulting in a shortened focal range. Even though the axial length is reduced, the beam shape maintains similar characteristics, e.g., bright cores and modulated ring structures, between L=10 mm to L= 110 mm. At L=160 mm, for which the axicon is placed close to the focal plane of the lens (f=200 mm), the ring structures disappear. This, again, is attributed to the blunt axicon tip. These figures illustrate the large degree of tunability achievable through changing the distance between the lens and axicon. It is possible to change the 80% minimum spot size by over a factor of two through this simple parameter.

Figure 5.7 demonstrates the flexibility of tuning the axial length of the generated Bessel-like beams by changing the lens-axicon distance L and the focal length of the lens. To this end, we choose three focal lengths, f=100, 200 and 300 mm, and record beam profile for various L distances. Figure 5.7 shows the 80% energy radii $R_{0.8}$ calculated for each data

set. We can see that for each focal length, the $R_{0.8}$ curves move closer to the axicon when L increases. The minima of the curves point to the Z-position where laser energy is most concentrated, and their values are the corresponding smallest spot size of 80% total energy. While the three sets of curves from three focal lengths have similar shape, longer focal lengths lead to a longer axial extent and thus wider curves. This can be seen by comparing f=200 mm, L=160 mm and f=300 mm, L=160 mm curves with the f=100 mm, L=60 mm and f=200 mm, L= 60 mm curves, respectively.

The on-axis intensity variation can be suppressed by blocking the central part of the beam, as has been demonstrated in a previous study with a HeNe laser [136]. To demonstrate that this method applies also to femtosecond laser, we cut a circular piece of aluminum foil with 2 mm diameter and attach it to a glass microscope slide. We then place the assembly before the lens so that the foil blocks the central portion of the beam. All other optics are unaltered. The Bessel-like beam generated in this way is shown in figure 5.8 in comparison with the original beam (5.8 (a)). Red curves are the on-axis intensity averaged around X=0 with a width of 30 μm. This width is approximately the size of the cores. The suppression of intensity variation can be seen, especially in the front part (L<110 mm) of the beam. Besides, the modulation in the rings, while not completely removed, is also suppressed. One should also note that the laser power/energy used in this study is low ($<$ 1 mW for the HeNe laser and $<$ 1 μJ for the femtosecond laser), and therefore the generated Bessel-like beams are all observed in the linear regime, without any nonlinear effect such as plasma generation in air [146]. Since many strong-field studies, such as high harmonic generation, are conducted in vacuum, our results can provide adequate assessment of beam profiles when used for those experiments.

5.3 High Harmonic Generation from Bessel Beams

Since the first demonstration high harmonic generation in the late 1980's an enormous amount of research has been put into generating pulses with increasingly shorter wavelengths and higher photon flux. The payoff for creating a high-flux HHG source is huge, not

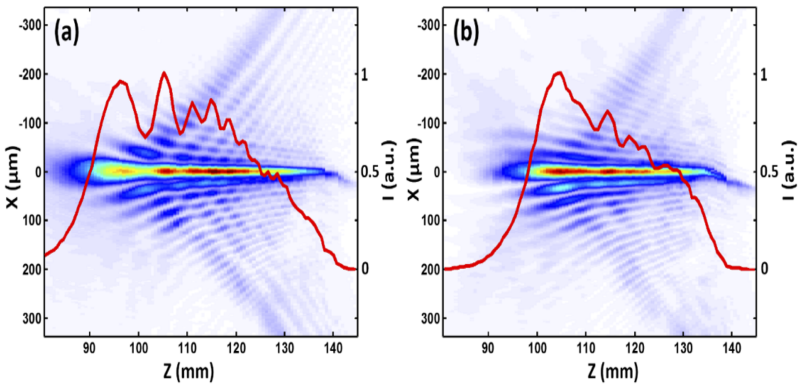

Figure 5.8: *Beam profiles for (a) original and (b) center-blocked input beam as a function of distance from the axicon. Red curves are intensity profiles averaged around the cores (X=0, average width 30μm). f=200mm, L=10mm.*

just scientifically but also industrially. The only other viable sources of coherent XUV and X-ray radiation are synchrotrons and free-electron lasers (FELs). While most HHG sources are not exactly cheap from a conventional stand point (order $1 million), they are dramatically less expensive than a synchrotron (order $10 million to $100 million) or free-electrons laser (order $100million to $1 billion). In some circumstances, the latest generation of HHG sources produce usable pulses that are on par with synchrotron radiation while maintaining much shorter pulse durations. In terms of continuous bandwidth and pulse duration, no other sources come close to high harmonic generation.

In this work, we explore using Bessel beams, in particular those generated using the lens-axicon combination from the previous section, to more efficiently generate and deliver XUV radiation. Bessel beams have several notable theoretical advantages to Gaussian beams for high harmonic generation. The most noteworthy of these are:

1. Favorable phase matching conditions for large interaction regions
2. Self-filtering of the fundamental radiation
3. Extended region for of high-intensity, on-axis fields
4. More compact geometry than conventional setups.

5.3.1 High Harmonic Phase Matching with Bessel Beams

Let's start with the phase matching for Bessel beams. The process of creating high harmonic photons can fairly accurately be described by the three-step model [22]. A laser ionizes a target atom or molecule (neglecting more complicated or solid-state systems) through either multiphoton or tunnel ionization. The photoelectron gains energy from the oscillating vector potential of the laser field before being driven back and undergoing photorecombination with the parent ion. This produces a single, high-energy photon. To produce an actual appreciable amount of flux, this process must be repeated simultaneously in billions of atoms (or molecules). This is typically not an issue, even with the relatively low combined cross section for photorecombination. What is very difficult however, is to get all of these high harmonic photons to add constructively in the far field. Achieving this condition is known as phase matching.

A condition must be established such that photons generated at a position z+dz in the laser focus are in phase with those generated a time-step earlier, at a position z. This amounts to a requirement that all frequencies (both fundamental and generated) propagate with the same phase through the target medium. This is not an easy task considering the immense number of frequencies (bandwidth) ranging from the fundamental (typically in the near to mid infrared) though the XUV to soft X-ray regime. Finding and establishing the best conditions for phase matching has been one of the most active areas of high harmonic and attosecond science [40]. Achieving good phase matching is basically a study in balancing numerous, competing elements.

The four main terms that affect phase matching are material dispersion (of the target gas), plasma dispersion (of the ionized target gas), a geometric term from the geometry of the laser focus, and a term originating from the rather inconveniently named "atomic phase".

For propagation directly on-axis, the phase mismatch is given by [147; 148]

$$\Delta k = q k_{laser} - k_q = \Delta k_{disp} + \Delta k_{plasma} + \Delta k_{geom} + \Delta_{atomic}, \tag{5.47}$$

where the terms refer to the previously mentioned contributions respectively and q is the harmonic order.

Putting this into more explicit terms gives

$$\Delta k = \frac{q2\pi(1-\eta)}{\lambda}\Delta n + P\eta N_{atm} r_e\left(\frac{\lambda}{q} - q\lambda\right) + \Delta k_{gemo} + \Delta k_{atomic} \tag{5.48}$$

where λ is the laser wavelength, P, η, N_{atm}, r_e are the gas pressure in atmospheres, the ionization fraction, the gas density at 1 atm, and the classical electron radius, respectively, and $\Delta_n = n_{laser} - n_k$ with n_{laser} the refractive index for the laser and n_q for the qth harmonic.

Perfect phase matching is achieved when $\Delta k = 0$, so all of the respective terms need to be balanced. For all practical situations, Δk_{disp} is always positive because the index of refraction is greater than one in the infrared/visible and less than one in the XUV and X-ray regimes. The dispersion from plasma is necessary to correctly account for the ionized target gas. Only a very small fraction (approximately one in a million [149]) of the ionized atoms undergo photorecombination, but a significant number of the atoms are ionized by the laser field and contribute to the total ionization fraction. The plasma dispersion term is always negative and its magnitude depends on the target (ionization potential), driving wavelength, and intensity.

Δk_{atomic} arises from the propagation of the photoelectron in the laser field prior to recombination. It can be quite complicated, but it is typically proportional, macroscopically, to the gradient of the intensity along the axis of propagation dI/dZ [150]. This term plays a part in the phase matching conditions for Bessel beams, namely in that it is small due to the quasi-diffraction-free beam and the long length of on-axis high intensity. This results in a propagation with a smooth intensity and phase evolution that keeps Δk_{atomic} small relative to the other phase mismatch terms [151].

The geometric phase mismatch comes from focusing a laser beam to achieve high intensities. A plane wave would have no geometric mismatch. For a focused Gaussian beam, the

phase mismatch is due to the Gouy phase and will always be positive with a value of [147].

$$\Delta k_{geom} = \frac{d}{dz}\Big[arctan\Big(\frac{z}{Z_r}\Big)\Big](q-1) = \frac{Z_r(q-1)}{Z_r^2+z^2} \tag{5.49}$$

where Z_r is the Rayleigh range and $z = 0$ at the focal plane.

The positive contributions of the material dispersion and geometric phase mismatch necessitate compensation with the negative plasma dispersion. This is primarily controlled with laser intensity, which also changes the harmonic cutoff, or by varying the density of the gas jet.

It should be noted that a full discussion of high harmonic generation in gas-filled capillaries has been intentionally excluded for the sake of brevity. The geometric phase matching term for this geometry is negative with a magnitude inversely proportional to the size of the capillary channel [152].

The majority of the benefits of using Bessel beams for high harmonic generation come out of the geometric term, Δk_{geom}. This is, of course, expected since this term arises from the geometry of the beam focus. As developed in [133], a Bessel beam can be described as a superposition of plane waves propagating on a cone with an angle γ relative to the optical axis. The overall phase velocity of the pulse can be controlled by varying this angle. This allows for a degree of tunability not present with Gaussian beams. When a Bessel beam is generated using an axion, the base angle of the axicon controls γ. The wave vector of a Bessel beam will always be shortened as compared to a plain wave propagating directly along the optical axis. That is, the phase velocity will be slower than for a plain wave. Thus, the geometric phase mismatch term for a Bessel beam will always be negative and have a magnitude of [148]:

$$\Delta k_{Bessel} = qk_0(1 - cos(\gamma)). \tag{5.50}$$

Thus, Bessel beams provide an interesting candidate for increasing the flux of HHG sources, particularly in the regime below the critical ionization limit where the material dispersion phase mismatch term is greater in magnitude than the plasma dispersion.

With correct phase matching established, the extended axial focal area, provided by a Bessel beam, would allow for high harmonic generation in a large target area. This large target is typically experimentally realized in a gas cell geometry. The longer the cell, the more HHG light that can be generated, at least up to the point where reabsorption in the target gas beings to dominate. All or almost all current high-flux HHG sources employ a gas cell in one geometry or another. When using conventional Gaussian pulses to drive HHG in gas cells, the long Rayleigh range required is achieved with extremely long focal lengths. For example, an attosecond beamline at ELI ALPS uses a 50 meter focal length! This makes high-flux HHG sources quite large, particularly for lab-based experiments. As seen in figure 5.7 an axicon-lens combination can be used to produce a long, peak-intensity region with a short working distance. An HHG source, designed with this focusing geometry, would be much more compact than one that utilizes a shallow, Gaussian beam.

The final major advantage of Bessel beams for high harmonic generation is self-filtering. In most cases, using the radiation produced with HHG requires the elimination of the fundamental beam. This is typically accomplished by employing a series of very thin filters. While these filters block significantly more IR than XUV or X-ray radiation, they still reduce the total flux of the HHG beam. After all the work and expense of making these photons, a majority of them are just "thrown away". However, a Bessel beam will form into a donut mode in the far field, where the on-axis intensity goes to zero. This allows for a simple filtering scheme where an iris is used to block the IR fundamental radiation while the HHG beam passes though untouched.

While most previous investigations into HHG with Bessel beams have been theoretical, preliminary experimental studies have been performed by Dinh et al. [153]. This work employed a lens-axicon combination, similar to that described in section 5.2.2, coupled into a semi-infinite gas cell filed with argon. An enhancement in the HHG flux was observed in the cuttoff harmonics when using the lens-axicon combination as opposed to just a focusing spherical lens. Additionally, Dinh and coworkers observed an improvement in the spatial coherence of the HHG beam. Both of these were attributed to the improved phase matching conditions of Bessel beams, as described above.

5.3.2 Experimental Realization of High Harmonic Generation with Bessel Beams

The goal of this study is to map out the harmonic generation at various places in the Bessel beam focal profile. This is different than the study by Dihn [153] in that the goal is not to measure the total increase in flux from a gas cell but instead to acquire a better overall understanding of the relative ionization and phase matching conditions throughout the Bessel focal profile. So instead of using a gas cell, we employ a thin gas jet produced using a hollow core capillary. The jet diverges quickly so the fundamental beam is focused very close to the output ($\sim$ 1 mm). Additionally, the ionization yield is measured in conjunction with the HHG signal to provide information into the local intensity and at the interaction. This allows any increases in HHG flux to be investigated not just as a function of higher intensity but also local phase matching conditions, deconvoluting the two competing effects.

A schematic of the experimental setup is shown in figure 5.9. We use the same optical setup (lens and axicon combination) described in 5.2.1. A 300 mm lens is placed a distance L behind the axicon (1 degree base angle). L is varied from 10.7 cm to 13 cm to tune the Bessel focusing conditions and explore the effects of different focal profiles on high harmonic generation. Both the lens and the axicon sit on a computer-controlled stage to allow the focal profile to be scanned through the gas jet. The stage is set to have a total travel distance of 30 mm allowing a minimum distance from the tip of the axicon to the gas jet of 95 mm and a maximum distance of 125 mm. For the larger values of L, the usable range is more limited as the beam on the entrance window became too small and intense. Prior to the positive lens, the incoming beam is telescoped down to approximately 20 mm. The laser pulse energy is 2 mJ with a duration of 30 fs FWHM and a central wavelength of 795 nm.

The gas jet is approximately 5 cm after the entrance window of the source chamber. The capillary used to produce the gas jet has an inner core diameter of 250 μm and is 10 mm in length. Approximately 30-40 psi of argon gas is placed behind a needle valve that limits the gas flow through the capillary to approximately 200 mbar l/sec. To measure the ionization yield simultaneously to the HHG, a channeltron is placed several centimeters

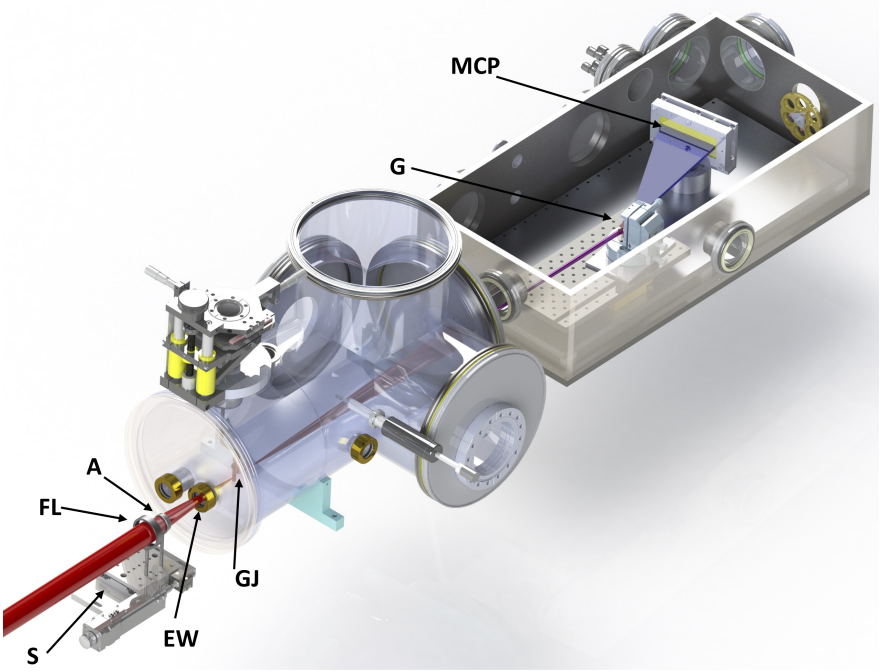

Figure 5.9: *Experimental setup for HHG with femtosecond Bessel beams. S-motorized state, FL- focusing lens, A- axicon, EW- Entrance window, GJ- Gas jet, G- Grating, MCP- Micro Channel Plate.*

behind the gas jet and slightly off axis so as to not block the harmonics. A 2000 l/sec magnetic levitation turbo pump keeps the source chamber at a vacuum of approximately 5×10^{-5} torr during operation. An HHG spectrometer is placed approximately 1 meter behind the generation region. Differential pumping tubes between the source chamber and the spectrometer chamber keeps the pressure in the spectrometer chamber a 1×10^{-7} torr during operation. The HHG spectrometer consists of a curved, variable-spacing, holographic, grating, with a groove density of 1,200 grooves/mm, that disperses the generated harmonics across a Z-stack, 105 mm by 35 mm MCP (Photonis) with a P46 phosphor plate on the output. A Hamamatsu Orca Flash 2.8, low-noise, 12-bit resolution camera is used to capture the harmonic spectrum.

Figure 5.10 shows photo taken of the HHG source chamber with the entrance flange removed. The gas capillary is glued to a SwageLok s-bend tube, which is attached to a 3D manipulator. Below the capillary, a strip of ionization can been seen from focusing the laser though the axicon lens setup. This strip of ionization is more the 4 cm in length, illustrating

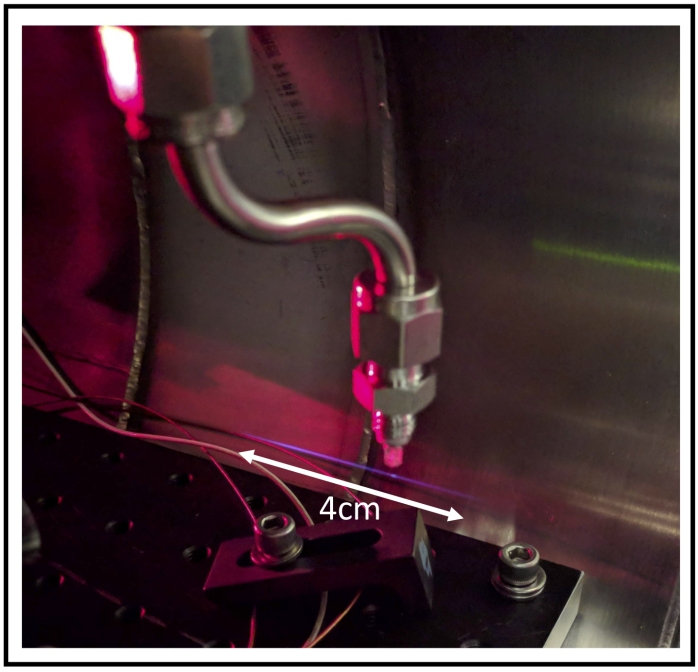

Figure 5.10: *Ionization of air from 2 mJ, 30 fs, 795 nm pulse focused by the axicon lens setup. The ionization strip is the "electric blue" line and extends for more than 4 cm. Increased ionization can be seen directly below the glass capillary from a Kr gas jet.*

the extremely long area of high intensity produced by a focused Bessel beam. Directly below the capillary, a small section of increased ionization is present. This is due to krypton gas coming from the capillary. Since the ionization potential of Kr is lower than air, it is more easily ionized leading to increased ionization where the gas jet is present. This gives an idea of how much of the Bessel profile the gas jet samples at a given position.

Before looking at the high harmonic yield results, let us first examine just the ionization yields. Figure 5.11 shows the recorded ionization yield as a function of distance from the axicon to the gas jet for several different values of L. Several striking features are immediately visible. The first is the extremely long range over which strong-field ionization takes place. The second major feature is the strong oscillations in yield as the beam is scanned through the jet. Both the extended ionization range and the oscillations are features absent from strong-field ionization using Gaussian beam. However, in light of the results of section 5.2.2, neither of these observations are surprising. In fact, the strong-field ionization measurements are refreshingly consistent with the HDR imaging results.

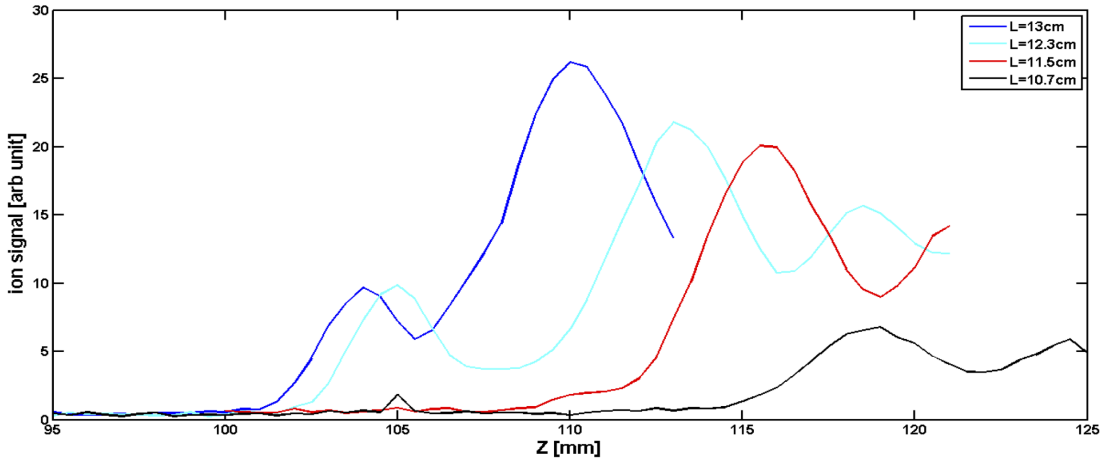

Figure 5.11: *Ionization yield as function of position from the axicon, for four different distances between the positive lens and axicon.*

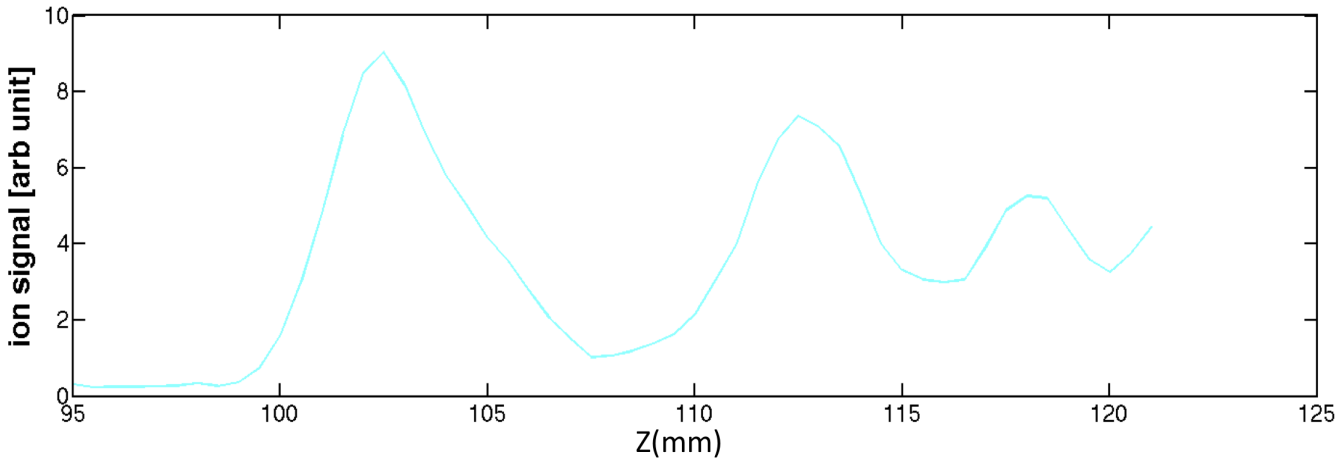

Figure 5.12: *Ionization yield as function of position from the axicon, for L=12.3mm with the 2mm tipblock inserted.*

All traces in figure 5.11 were taken with the tip block discussed in 5.2.2 inserted. As seen in figure 5.8 the effects of this tip block are dramatic. Figure 5.12 shows the results without the tip block.

Figure 5.12 shows the ionization yield with a value of L = 12.3 mm with and without the tip block. When the tip block is removed, the position of peak ionization yield shifts by approximately 10 mm and increases by more than a factor of two. Three local ionization maximuma are still observed but their relative values are extremely different than when the tip block is used. These scans were taken a short time apart and no difference exists other

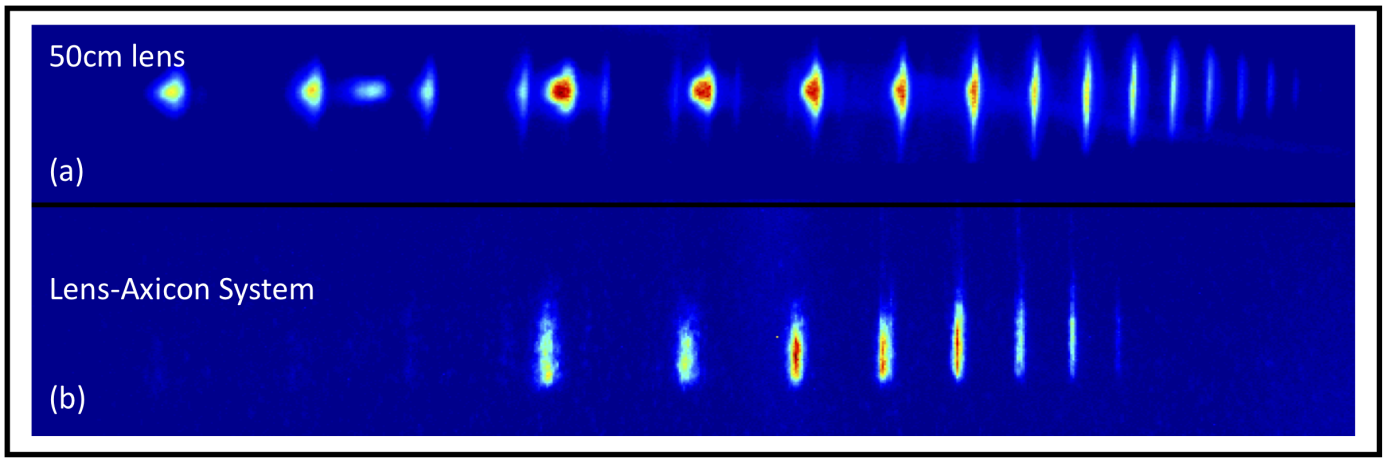

Figure 5.13: *MCP images for the HHG spectrum generated with (a) a normal Gaussian beam using a 50 cm positive lens and (b) with the axicon-lens combonation. Harmonic order increases from left to right.*

than the presence (or absence) of the tip block.

Clearly, femtosecond Bessel beams are capable of strong-field ionization. This is no surprise as the only requirement is high peak intensity. High harmonic generation, however is a much more sensitive process. As developed in section 5.3.1, pulsed Bessel beams can "theoretically" produce harmonics. This is also supported experimentally by the early work of Dinh citeDinh2012Thesis in a semi-infinite gas cell. However, the complexity of high harmonic phase matching and the non-standard profile of Bessel beams makes demonstrating HHG with our setup and experimental conditions far from guaranteed. The first step our investigation into studying HHG through the focal profile of a Bessel beam is to confirm our ability to produce harmonics from the lens-axicon combination with a gas jet. Figure 5.13 (a) shows the HHG spectrum generated with a conventional focusing geometry using a 50 cm lens. Figure 5.13 (b) shows the same, but instead generated with the lens-axicon combination.

Next, we can look at exactly where in the focal profile harmonics are generated and how that relates to the corresponding ionization rate. We will also look at the effects of changing the distance between the lens and axicon. Figure 5.14 (a) shows the same ionization data as figure 5.11. Figure 5.14 (b)-(e) gives a line-out of the yield for harmonic 11 though 17 respectively. To allow for better overall comparison of the profiles, the vertical axis of each

plot is adjusted individually. A dashed line is drawn through all fames to depict the position of peak ionization for each value of L. The overall shape of each harmonic is largely similar for each respective value of L, indicating similar phase matching for all harmonics in the regions studied. We can also see that the peak harmonic yield corresponds almost exactly with the peak ionization for all cases. As ionization maps out the peak intensity, we can clearly see that local intensity plays the largest role on harmonic generation. Also evident from caparison to ionization yield data is the fact that the overall length of harmonic generation is shorter than the length of ionization. This is possibly from decreased phase matching, but it is difficult conclude without more extended scans which are prevented by prohibitively high fluence on the input window.

In the beam profiling study, it was seen that the tip block had a large effect on the overall on-axis intensity. How does this translate to HHG? Figure 5.15(a) shows the yield of harmonic 17 with L = 12.3 mm, both with and without the tip block inserted. Figure 5.15 (b) shows the associated ionization rates. The first thing that is apparent is that the effects of the tip block are even more dramatic than in the ionization data. The peak yield is shifted by more than 10 mm. Also, without the tipblock, there are two clear maxima while only one is present when the block is inserted. This is despite the fact that the ionization yield (and thus the intensity) is relatively similar from the first maxima to the second. Evidently, the phase matching conditions are very different even for nearly constant intensities.

The next interesting feature is the relative maximum of the harmonics compared to the relative maximum of the ionization. With the tip block inserted, the peak ionization yield is reduced by more than a factor of two. However, the peak harmonic actually increases slightly. In the absence of other effects, this change can be attributed to phase matching. This is actually quite an important point for the overall scaling of HHG with the axicon lens system. Typically, the ultimate limit of HHG flux is due to target depletion and ionization when the driving field becomes too strong. Above this value, adding more pump intensity energy will actually drive the amount of harmonic light generated down due to the plasma dispersion effect on the phase matching. The fact that more harmonic flux is produced with less ionization indicates that the system can easily be scaled to higher pump energy with

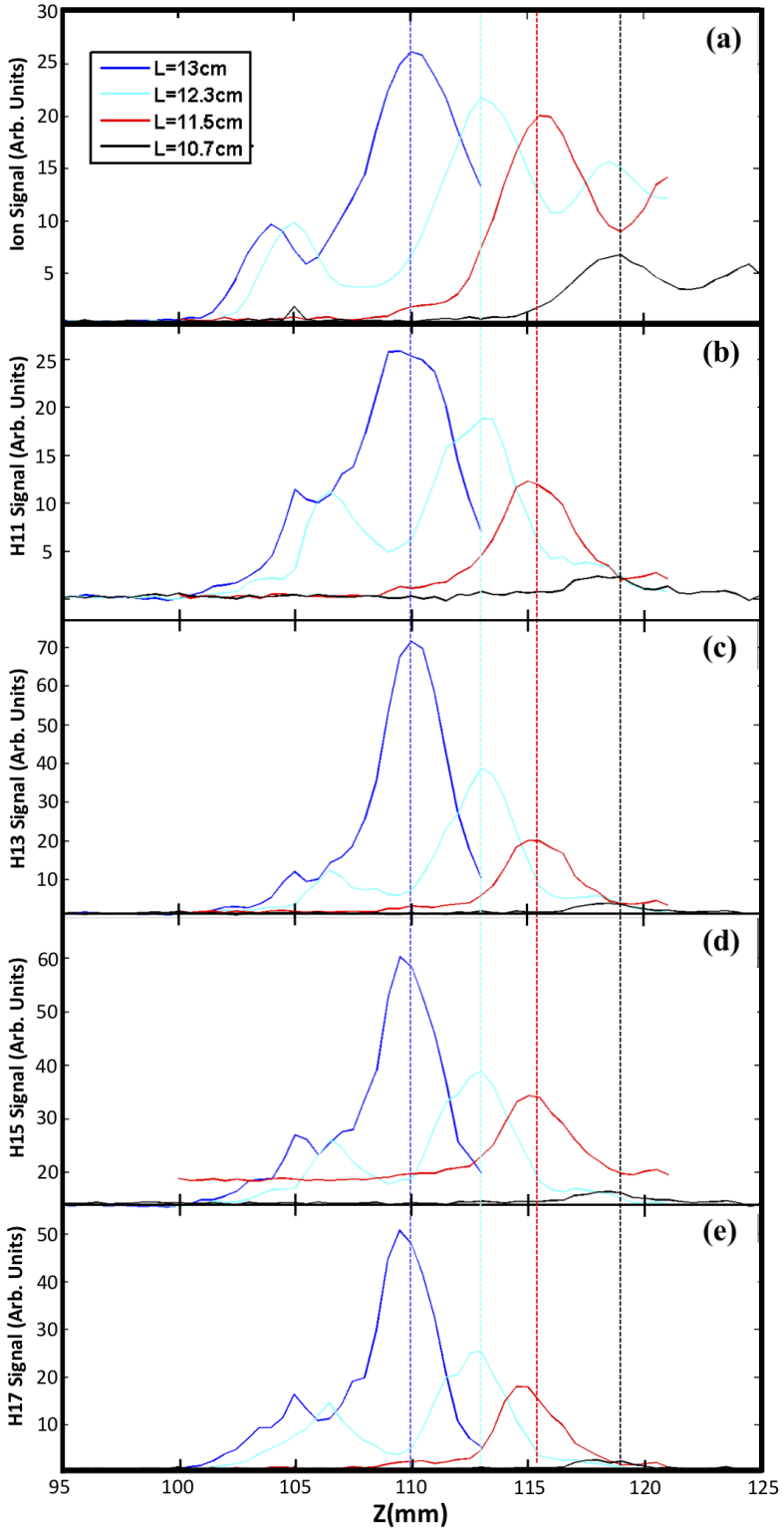

Figure 5.14: *Ionization yield along with the accompanying HHG yields as a function of position within the Bessel profile for four different values of L. Vertical dashed lines mark the position of peak ionization yield for each case. The axicon is at z=0.*

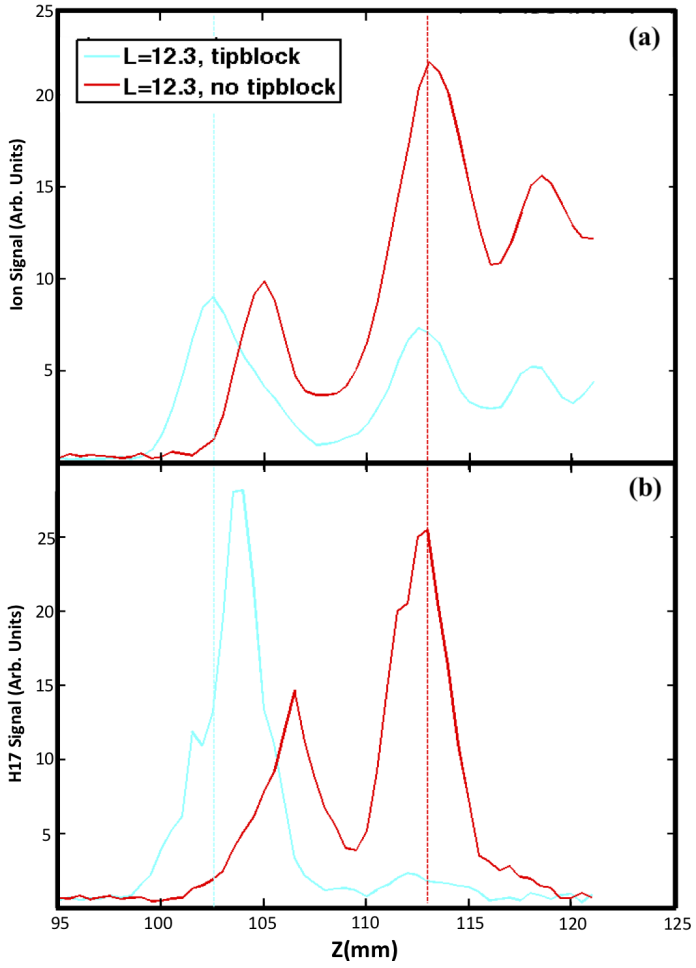

Figure 5.15: *(a) Ionization yields for L=12.3mm with and without the tipblock. (b) HHG yields for harmonic 17 corresponding to the ionization yields. The axicon is at z=0.*

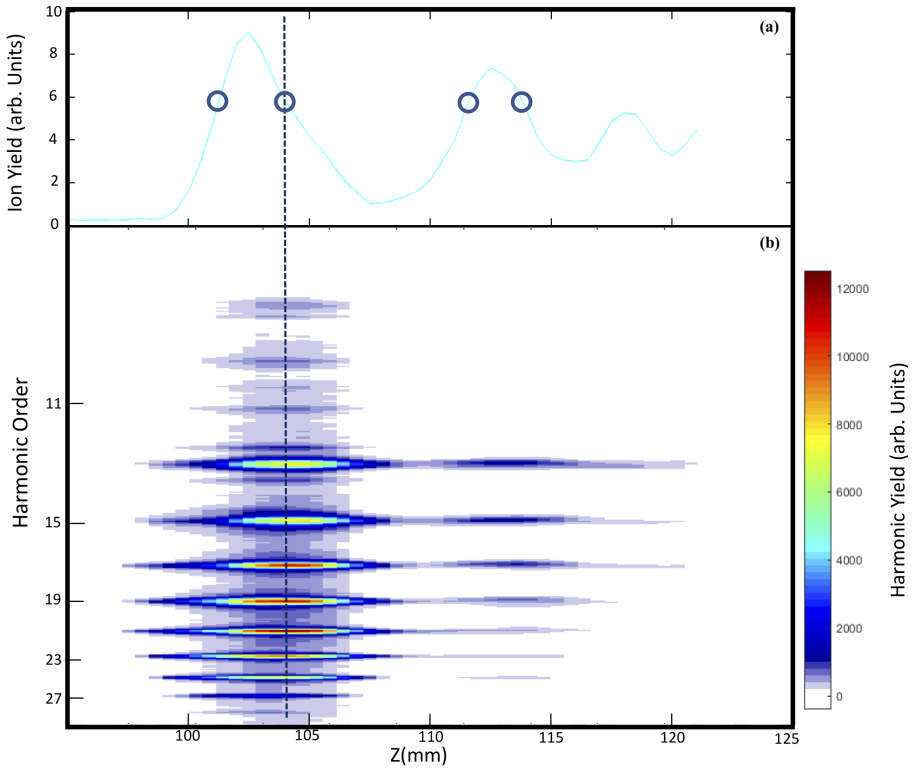

Figure 5.16: *Ionization trace (a) plotted with the 2D map of HHG yield (b) for L=12.3mm and the tipblock inserted. Vertical blue dashed line marks the position of peak HHG yield. Open blue circles mark all the points in the ionization trace where the ion yield is the same as the value for peak HHG yield. The axicon is at z=0.*

increased output flux.

Figure 5.16 shows the results just for L = 12.3mm with the tip block inserted. The 2D map of the harmonic spectra is plotted as a function of gas jet position along with the ionization yield. Harmonics from the 9th through the 29th are present. The same shift in peak ionization yield and harmonic yield is even more evident. What is also clear is that harmonics are preferentially generated on the "falling edge" of the first intensity fringe. The position of peak harmonic yield is marked by the blue dashed line. Also marked by open blue circles are the four areas of ionization yield equal to that were harmonic generation originates from. The fact that the HHG yield is dramatically lower at each of these positions elucidates the very complicated relation phase matching plays. Evidently, the "real world" conditions are much more complicated than the theoretical calculations show (imagine that). Figure 5.17 - 5.19 shows the 2D HHG spectra for the full gas jet scan for the other various

geometries.

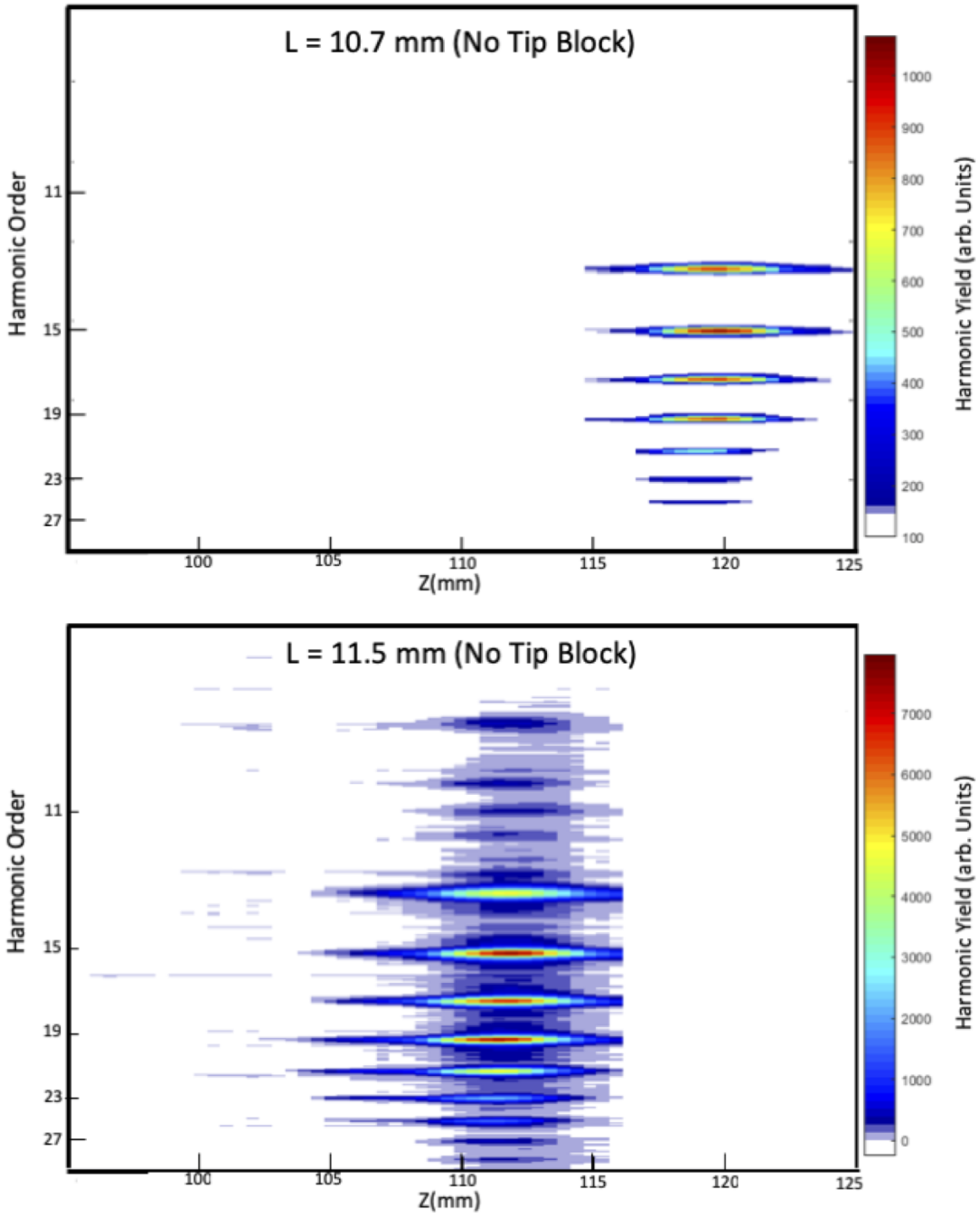

Figure 5.17: *2D map of HHG yield spectrum as function of distance from the axicon tip.*

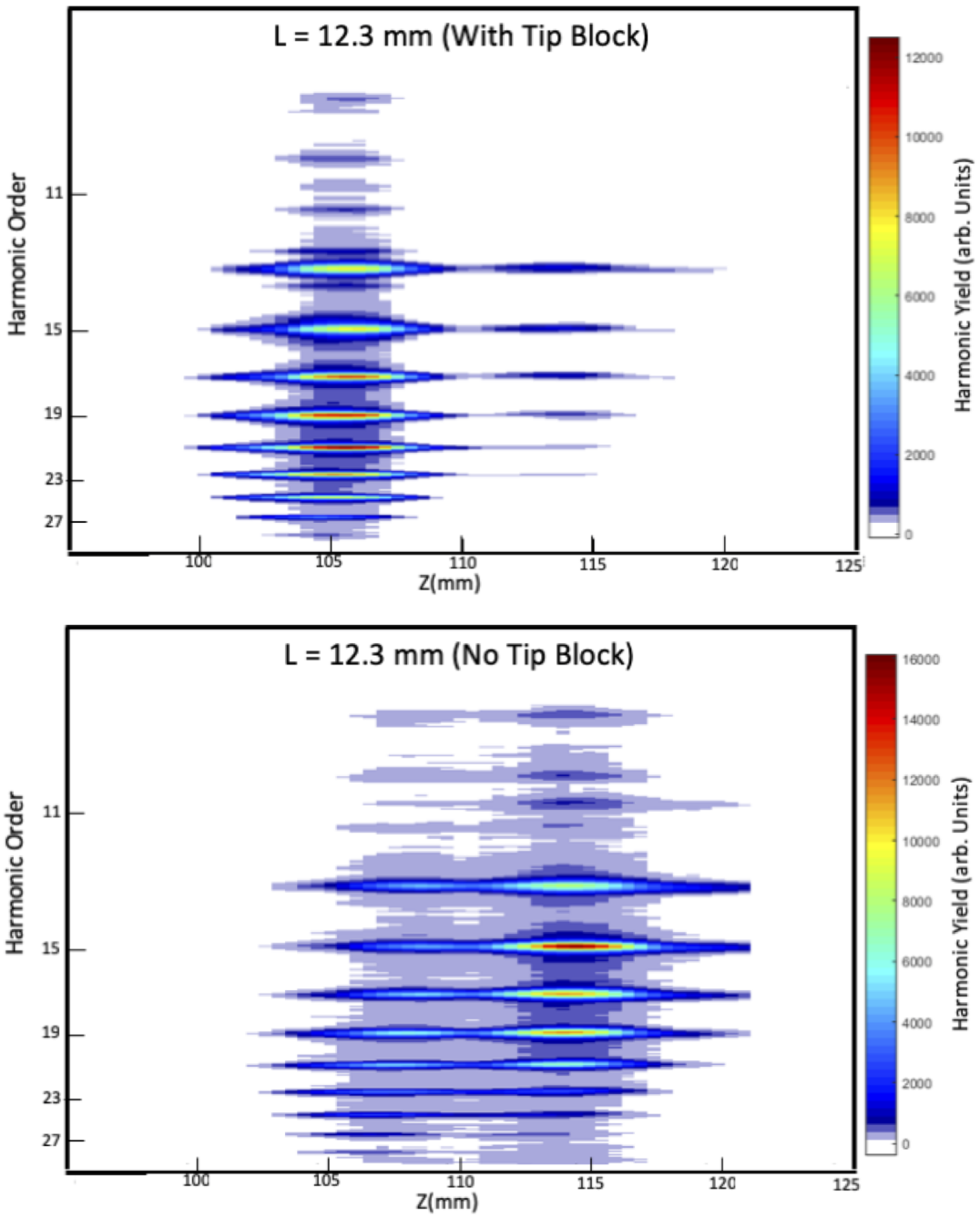

Figure 5.18: *2D map of HHG yield spectrum as function of distance from the axicon tip.*

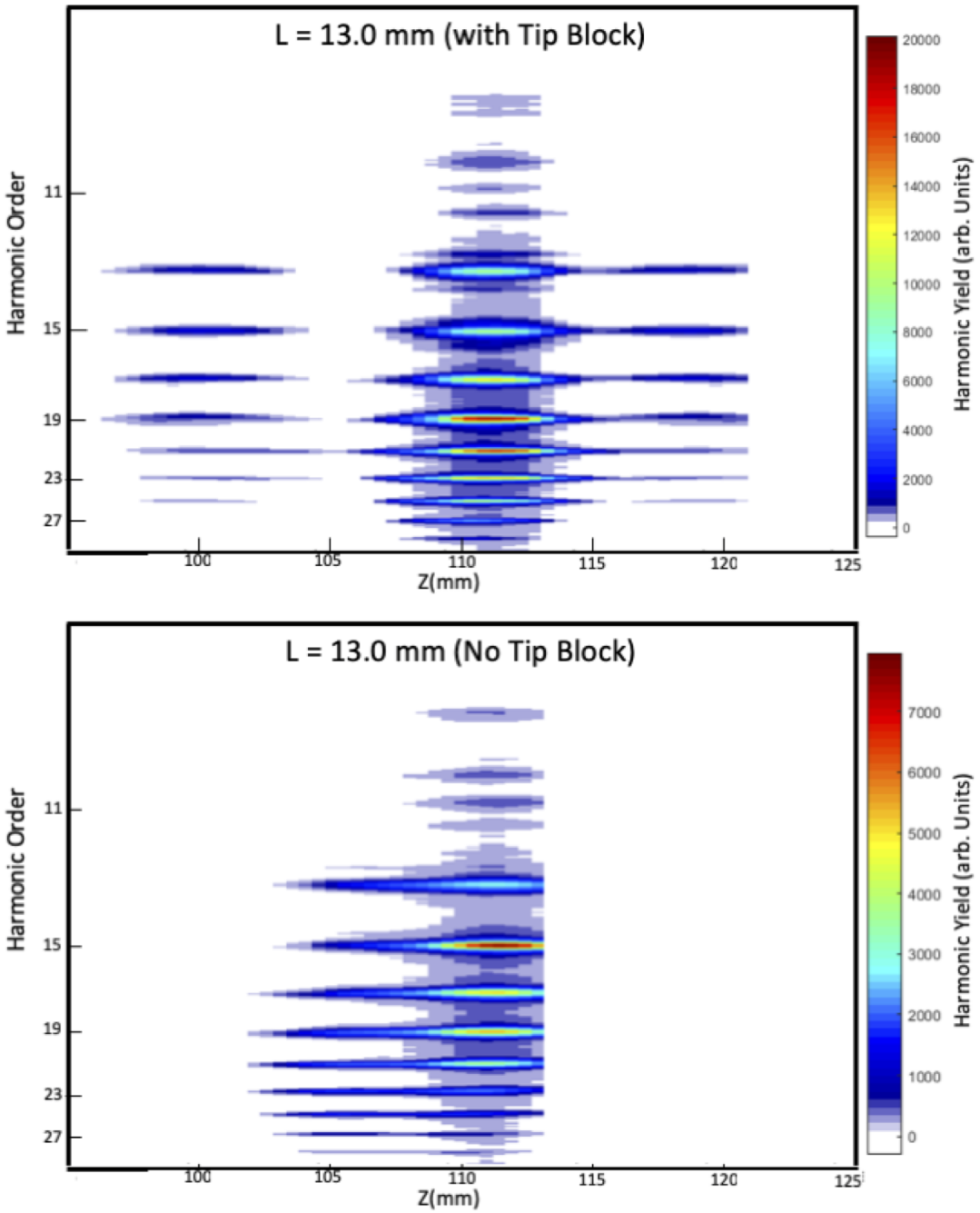

Figure 5.19: *2D map of HHG yield spectrum as function of distance from the axicon tip.*

5.4 Conclusions and Future Work

We have shown that by using a positive focusing lens in combination with a shallow-angle axicon it is possible to produce a femtosecond Bessel beam with parameters suitable for strong-field studies. The combination of optics allows for a degree of tunablity while also allowing for the generation of high-peak intensities with a reasonably long working distance. This setup was successfully used to drive and study high harmonic generation.

The local focal profile conditions for high harmonic generation were sampled by measuring both the HHG spectrum as well as the corresponding ionization rate as a function of gas jet position in the focus. Ionization yields were found to correspond well with the all-optical, HDR, beam characterizations with the total length of ionization far exceeding what is possible with Gaussian focal profiles of similar working distances. The ionization yields oscillate through several local maxima and contain a global maximum at working distances also in line with what was found in the optical characterizations.

The generated harmonic flux also oscillates through the focal profile but does not always directly follow the ionization yield. This indicates that different positions along the focus have more favorable or less favorable phase matching conditions. Inserting the circular tip-block, to eliminate the effects of the blunted axicon tip, has a large effect on both the ionization yields as well as the HHG flux. With no other conditions changed, inserting the tip-block both significantly reduces and shifts the position of peak ionization. However, even with the reduced ionization, the peak of the HHG flux is increased with the tip block inserted, showcasing the strong differences in not just ionization but also HHG phase matching. Varying the distance between the focusing lens and the axicon significatnly alters the high harmonic generation spatial profile showing the ability to tune for a desired output just by adjusting this relatively simple parameter. While a number of experimental difficulties still exist, this points to promising ability to create a compact XUV source.

Future measurements will focus on measuring the absolute difference in flux from a Gaussian focus relative to a Bessel focus. Additionally, other experimental factors can be varied to get a better handle on the respective phase matching terms. This includes varying

the optical input power, the target gas and the target pressure over a wide range. Finally, full gas cell geometries could be explored in order to fully exploit the long axial intensity range to produce high flux harmonics. The complicated behavior unearthed in this study shows that a full parameter space will need to be explored to arrive a full working knowledge. However, despite the difficulties, Bessel beams remain an enticing option for use in HHG sources. This is particularly true in situations where a compact geometry or where working below the critical ionization threshold is desired.

Chapter 6

Strong-Field Interactions in Nanosystems

Nanoelectronics, nanophotonics and nanoplasmonics have been fields of growing interest in the last several years [154–158]. These areas bring more conventional and explored fields in optics and electronics into the nanoscale regime where many new phenomena occur and macroscopic descriptions break down or have to be strongly modified. Research into ultrafast nanoscale physics has great potential to both increase the fundamental understanding as well as lead to groundbreaking new technologies and applications. Among one of the most exciting technologies are opticially diven nanoelectronics with the potential to take electronic devices into the petahertz regime by driving the electronic response of the nanosystem with optical frequencies [154; 159]. Micro and nano-arrays have been used to dramatically enhance the strength of a driving optical field leading to other possible revolutionary breakthroughts involving ultrafast nanoelectronics including tabletop free electron lasers [160; 161] and novel high harmonic generation sources [162; 163].

All of these applications require exquisite control and knowledge of the interaction of nano-matter with ultrafast laser pulses. This chapter presents work that aims to add to this pursuit through two separate studies. The first looks into the thermal response and damage of gold nanowires under exposure to intense, femtosecond pulses. The second study examines

strong-field ionization and photoelectron rescattering in nanoparticles. Both of these studies add to the overall understanding of ultrafast light matter interaction at the nanoscale and lead to the ability to perform more targeted and precise future studies.

6.1 Thermal Dynamics in Nanowires Exposed to Intense, Ultrafast Pulses

One particularly exciting area of nanophotonics is light-driven, nano-circuitry. Ultrafast nanoscale circuitry relies on the ability to utilize the non-linear interaction of light with nanoscale materials in order to control (collective) electron motion on a sub-optical-cycle timescale. These non-linear regimes are reached for strong laser pulses with intensities typically just below the damage threshold of the materials. Such interactions give rise to (sub-optical- cycle) electron emission and acceleration from isolated nanotips [89; 164], nanospheres [165], and nanostructured surfaces [166; 167]. In all of these cases, the highest laser intensity that can be applied to the material depends on the material composition and the pulse duration. The exact reasons for damage of nanoscale materials are therefore often not well understood.

This section presents work to better understand the damage mechanisms and thermodynamics that occur within gold nanowires after exposure to intense, femtosecond pulses. This is broken into two parts, the experimental measurement of the optical damage threshold and the development of a model to simulate the full thermal response in the nanowire from heating from an intense laser pulse. This model is then extended to simulate the effects of multi-pulse heating when the system is exposed to a train of laser pulses.

6.1.1 Measurement of the Optical Damage Threshold of Gold Nanowires

Here, we study the melting of single-crystalline nanowires under the illumination of femtosecond light fields with different intensities and pulse durations. Two types of nanowire arrangements are studied: (1) free-standing Au nanowires that are grown on tungsten needle electrodes and (2) Au nanowires attached to fused silica slides. Both sample types are single-crystalline nanowires that were grown via the directed electrochemical nanowire assembly (DENA) process [168]. The relatively low repetition rate of the laser used in our studies, with 500 μs between individual pulses, prevents heat from accumulating over many laser shots.

Experimental Setup

Our experiments make use of the Kansas Light Source (KLS), a chirped pulse amplification (CPA) Ti:Sapphire laser system. This laser provides pulses of 32 ± 3 fs in duration (FWHM of the intensity), with 1.8 mJ of energy and a central wavelength of 790 nm at a repetition rate of 2 kHz. The shot-to-shot variation in pulse energy was approximately 5%. The pulses are attenuated to $100 \pm 10\,\mu$J before entering the experimental set-up shown in figure 6.1 A half-wave plate and a polarizing beam cube are used to attenuate the peak power of the pulses while keeping the focusing conditions constant. The beam is focused onto the sample through ambient air, using a plano-convex 60 mm lens (L3), to spot-size of 9 μm. A manual three-dimensional translation stage is used to position the sample in the focus. A halogen lamp is used as a microscope backlight for visualization and alignment. Lenses L1 and L2 function as a condenser for the halogen lamp light as shown in figure 6.1. The halogen light is collimated by placing L2 at $f_{L2} + f_{L3}$ (the respective focal lengths) in front of L3, allowing for illumination of the entire sample. Both the halogen and the laser radiation are imaged using a 20× microscope objective (O) attached to a camera. In order to find the optical damage threshold, the samples are initially exposed to laser intensities significantly below the damage regime and the intensity is stepped up gradually. To ensure that no optical damage

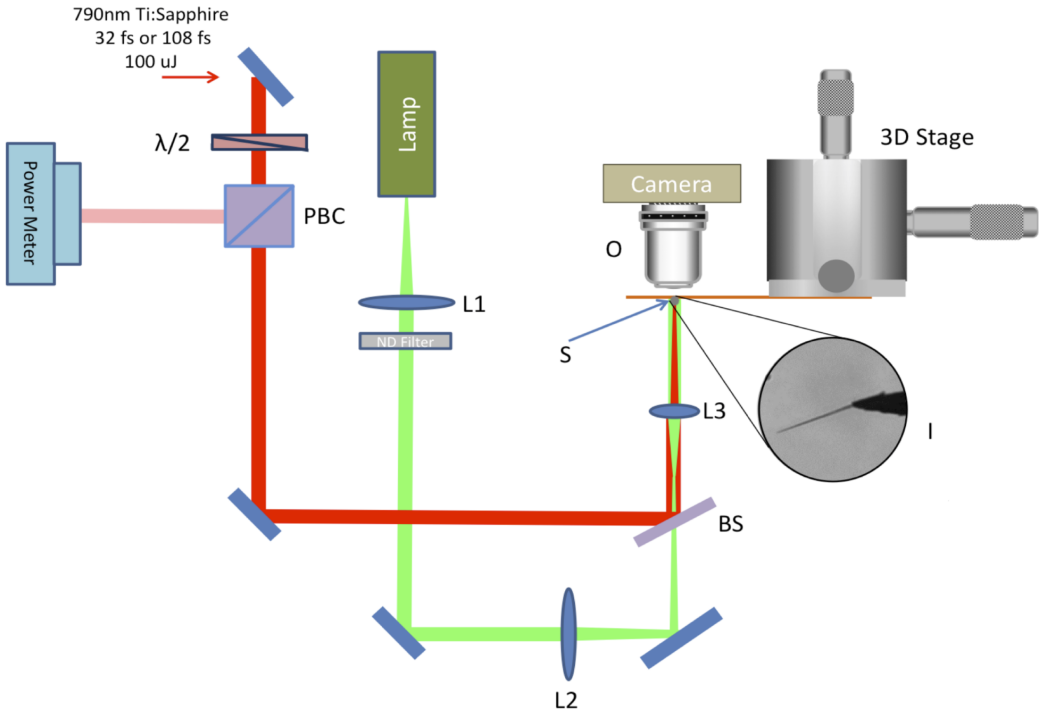

Figure 6.1: *Experimental setup for measuring the optical damage threshold of single-crystalline gold nanowires. λ/2, half-wave plate; PBC, polarizing beam cube; L1, 100 mm biconvex lens; L2, 100 mm biconvex lens; BS 50/50 beam splitter; L3, 60 mm plano-convex lens; S, sample mounting point; O, 20× long working distance objective; I, image of typical sample.*

was sustained, the sample is exposed to approximately 20,000 laser pulses (10 seconds) before moving to the next intensity step. The energy of the pulses is increased in 2.5 nJ steps until the first signs of damage are observed. Damage signatures take the form of bending, curling, melting, or balling up by the free-standing nanowires, whereas the slide-mounted wires either melted or completely ablated. All initial signs of damage are observed at the center of the laser focus. Using the KLS grating-pair-based compressor, we are able to compensate for the frequency dispersion of all elements in the optical path. The pulse duration measurements are performed with all the optical elements in place using a Frequency Resolved Optical Gating (FROG) device. In addition to the transform limited measurements, we also perform experiments with 108 fs, positively chirped pulses. These pulses are created by adjusting the grating distance in the amplifier compressor. The relation between the laser polarization and the nanowire orientation is random.

Sample Preparation and Characterization

The Au nanowires are fabricated by a technique called directed electrochemical nanowire assembly (DENA) [168; 169]. This technique, based on dendritic solidification [170], permits relatively straight-forward fabrication of metallic nanowires. The crystal structure of these wires is invariant along their lengths; hence they are single-crystalline [168; 171]. We employ two different electrode types to prepare Au nanowire samples. The first set consists of nanowires fabricated at the tip of movable tungsten electrodes [172]. The setup consists of two electro-etched tungsten electrodes immersed in $HAuCl_4$ solution. After mounting the tungsten electrodes on two different 3D stages and positioning them $\sim 1\,\mu$m above a microscope slide, a $20\,\mu$l aliquot of aqueous solution containing 20.0 mM $HAuCl_4$ (Sigma Aldrich) is deposited across a $\sim 30\,\mu$m inter-electrode gap. A function generator (Hewlett Packard, 8116A) is used to apply a square wave voltage signal of $\pm$ 4.0 V, 20.0 MHz to the tungsten electrodes to induce growth of the Au nanowire from the biased electrode towards the grounded electrode [173]. The voltage signal is turned off once the Au nanowire reached the desired length. The wire is removed from the growth solution by translation of the microscope stage and allowed to dry. The second mounting configuration consists of Au nanowires that are grown at the tips of electrodes that are fabricated on a fused silica slide by evaporative deposition. A $\sim 5\,\mu$m layer of gold is deposited on the glass slide using a vacuum evaporator (Varian VE10). After growing the Au nanowire from the tip a of gold electrode by the method described above, it is twice cleaned by depositing a $\sim 10\,\mu$l aliquot of deionized water on the wire, then wicking away the excess solution with a Kimwipe. Thus, the Au nanowires grown in this way lay in direct contact with the silica substrate.

Figure 6.2 shows four images of typical nanowires used in this experiment. Figure 6.2 (a) shows a Scanning Electron Microscope (SEM) image taken before the sample was damaged. The Au nanowire pictured is approximately 250 nm wide and $25\,\mu$m long, giving an aspect ratio of 100. It was prepared using the DENA technique described above. Figure 6.2 (b) shows an optical microscope image of the same nanowire, also prior to experimental damage, taken using the setup shown in figure 6.1. The objective used was a 20$\times$ long-working-

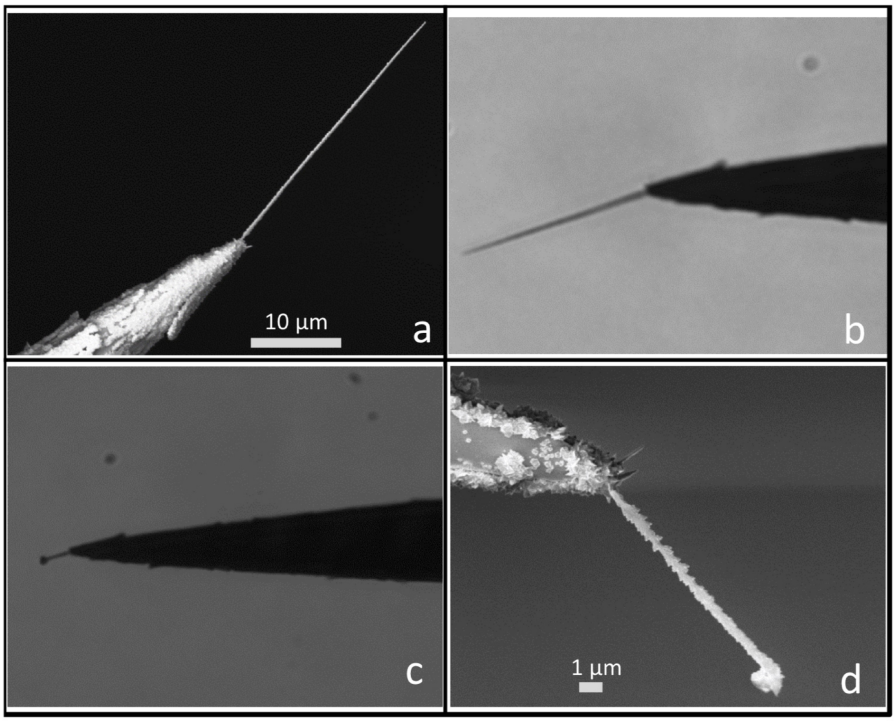

Figure 6.2: *Freestanding Au nanowire grown from a tungsten electrode: (a) SEM image of a 25 µm long undamaged wire. (b) Optical micrograph of the same nanowire as imaged in the experimental setup; (c) Optical micrograph of same nanowire shown in panel (a) post damage; (d) SEM image of typical nanowire post damage.*

distance microscope objective. A Complementary Metal Oxide Semiconductor (CMOS) camera sensor with 2.2 µm pixels collected the image. Figure 6.2 (c) shows an image of the same nanowire, also taken with the setup shown in figure 6.1, after 5 seconds of exposure to pulsed laser intensity of $8.8 \times 10^{12} W/cm^2$. Figure 6.2 (d) displays an SEM image of a typical nanowire post experimental damage under similar experimental conditions as for the sample depicted in figure 6.2 (c). Damaged wires all melted in a very localized region located at the center of the laser focus. In total, we investigated 63 nanowire samples, of which 18 were free-standing on W electrodes and 45 were grown from evaporated gold electrodes on fused silica. All samples were exposed to either 32 fs or 108 fs intense laser pulses.

Experimental results

Our main experimental results are shown in figure 6.3. The figure shows the number of samples that were damaged at a given peak laser intensity. Figures 6.3(a) and 6.3(b) show the

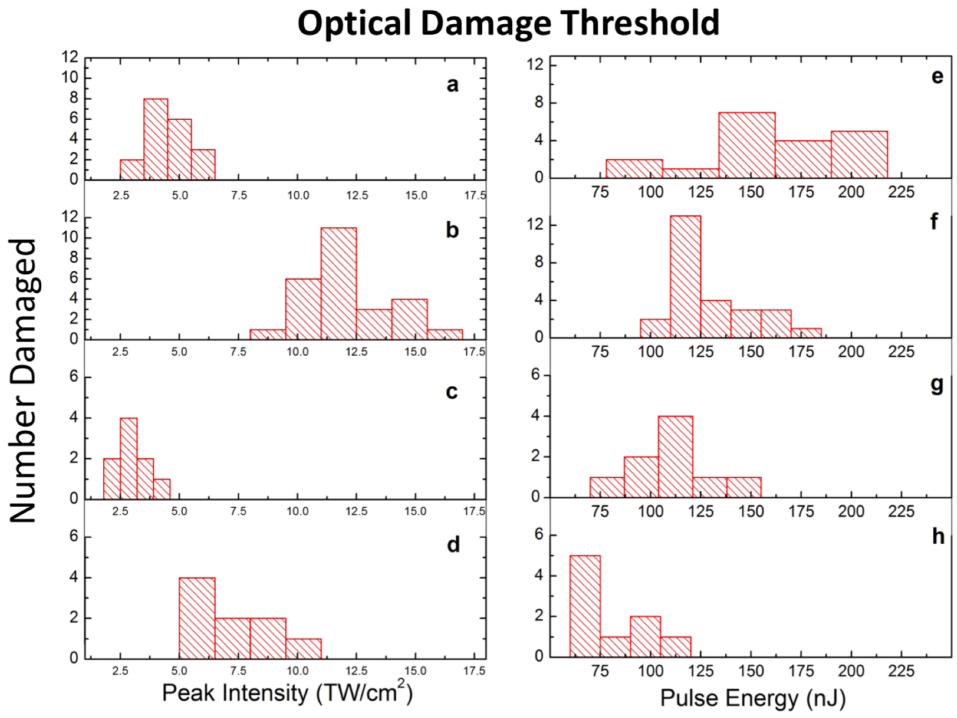

Figure 6.3: *Measured optical damage threshold distribution as a function of intensity for (a) 108 fs pulses and nanowires on fused silica slides, (b) 32 fs pulses and nanowires on fused silica slides, (c) 108 fs pulses and free-standing nanowires on tungsten electrodes, and (d) 32 fs pulses and free standing nanowires on tungsten electrodes. Measured optical damage threshold distribution as a function of pulse energy for (e) 108 fs pulses and nanowires on fused silica slides, (f) 32 fs pulses and nanowires on fused silica slides, (g) 108 fs pulses and free standing nanowires on tungsten electrodes, and (h) 32 fs pulses and free standing nanowires on tungsten electrodes.*

distribution of damaged wires when these are on a fused silica substrate for pulse durations of 108 fs and 32 fs, respectively. Figures 6.3(c) and 6.3(d) show the distribution of damaged wires when these are free-standing on a tungsten electrode for pulse durations of 108 fs and 32 fs, respectively. The influence of pulse duration becomes evident by comparison of figures 6.3(a) and 6.3(b) or figures 6.3(c) and 6.3(d). The influence of the growth process and heat conduction between the wires and the environment can be extracted from comparison of figures 6.3(a) and 6.3(c) for damage at 108 fs and figures 6.3(b) and 6.3(d) for damage at 32 fs. While the horizontal axis in figures 6.3(a)- 6.3(d) is the peak intensity of the laser, it is also useful to compare when damage occurs as a function of pulse energy. Figures 6.3(e) and 6.3(h) show the damage threshold as a function of energy.

Perhaps the most dramatic aspect of these measurements is the very high intensities at which the nanowires are found to survive. With average damage thresholds ranging from a few $\mathrm{TW/cm^2}$ to above $10\,\mathrm{TW/cm^2}$ for the respective cases, it is suspected that Au nanowires survive well into the optical strong-field regime. In addition to this result, a clear distinction in optical damage threshold between the 32 fs and 108 fs cases can be seen for both wires grown on tungsten needles and on gold coated silica slides. The damage threshold for both cases was higher for 32 fs pulses than for 108 fs pulses. This corresponds to a factor of 2.4 ± 0.7 for free-standing nanowires and a factor of 2.7 ± 0.6 for the wires attached to fused silica substrates, where the uncertainty is due to the spread in the measured damage threshold. In contrast to this peak intensity picture the energy per pulse at which damage occurs varies only modestly between all four cases. The average pulse energy at which the free-standing nanowires damaged was 80 nJ for 32 fs pulses and 112 nJ for 108 fs pulses. The wires attached to fused silica exhibited average damage pulse energies of 132 nJ and 169 nJ for the 32 fs pulses and 108 fs pulses, respectively.

The decreased damage threshold, with respect to intensity for the longer pulses, points to the fact that fluence (with units of energy per area) is actually the more relevant quantity in determining thermal damage thresholds. For a fixed intensity, the pulse with a longer duration will have a larger overall fluence as it requires more pulse energy to reach the same intensity as the shorter pulse. This increase in pulse energy will increase the amount of energy coupled into the nanosystem by a proportionate amount. To better explain the mechanisms underlying this process the next section presents a phenological model that links the optical pulse to the thermal response of the nanosystem.

6.2 Numerical Simulation of Ultrafast Laser Heating in Gold Nanowires

The Two-Temperature-Model (TTM) is an established phenomenological model based on a coupling between the temperature of the free electrons in the metal and the metal lattice.

The TTM is well documented for describing the thermal effects of an ultrafast laser pulse interacting with a metal [174–179]. This interaction and subsequent heating can be described as a three-step process.

The first step (1), electronic absorption, is the ballistic heating of the free electrons in the metal by the driving laser. This occurs while the laser pulse is present and thus naturally occurs with a timescale equal to the pulse duration. For ultrafast laser pulses, this results in a state where the electronic temperature has been dramatically increased while the temperature of the lattice has remained unchanged. In the second step (2), electron-phonon thermalization, the gold lattice heats up through electron-phonon collisions. The characteristic time scale for this process ranges from single picoseconds to a few hundreds of picoseconds depending on the system. Finally, the third step (3), external heat diffusion, is heat diffusion through and eventually out of the nanowire. This step follows the standard diffusion equation, solved for the particular geometry of the system. The third step often takes several orders of magnitude longer than the electron-phonon thermalization. Additionally, the time scale for heat dissipation is highly dependent on both the geometry and boundary conditions of the system. All three of these steps are modeled by the following set of coupled differential equations [174; 175; 178; 179]

$$C_l \left(\frac{\partial T_l}{\partial t} \right) = C_l \kappa_l \nabla^2 (T_l) + G(T_e - T_l) - S_{la}(\mathbf{r}, t), \tag{6.1}$$

$$C_e(T_e) \left(\frac{\partial T_e}{\partial t} \right) = C_e \kappa_e \nabla^2 (T_e) - G(T_e - T_l) + S(\mathbf{r}, t), \tag{6.2}$$

where $T_l = T_l(\mathbf{r}, t)$ is the lattice temperature profile, $T_e = T_e(\mathbf{r}, t)$ is the electron temperature profile, C_l and C_e are the respective lattice and electron heat capacities, κ_l and κ_e are the respective thermal diffusivities, G is the electron-phonon coupling constant, $S_{la}(\mathbf{r}, t)$ is the heat loss from the lattice to the surrounding air and $S(\mathbf{r}, t)$ is the absorbed power density from the laser pulse and has the functional form of [175]

$$S(t, x, z) = (1 - R)\alpha \; exp(-\alpha z) I_0(x, t), \tag{6.3}$$

with R being the reflectivity of gold (0.974 at 800 nm [180]), α is the absorption coefficient ($8.038 \times 10^5 cm^{-1}$ at 800 nm [180]) and z is defined to be in the direction of the laser propagation. I_0 is the spatial temporal peak intensity function.

6.2.1 Thermal Response of Gold Nanowires to a Single Femosecond Laser Pulse

Equations 6.1 and 6.2, along with the laser source term 6.3 can be solved computationally to simulate the thermal dynamics in a metallic nanowire interacting with an ultrafast pulse. Solving these equations fully, for all time scales, however, presents a significant computational challenge. Fortunately, a series of approximations can be made, with a high degree of accuracy, that greatly reduce the computational complexity. Physical insights about the different time-scales of the respective processes allow for decoupling into a set of more manageable equations.

As the ultrafast laser pulse interacts with the nanowire, the electric field rapidly heats the free electrons in the metal. This temperature can be driven to multi-thousands of Kelvin depending on the pulse intensity. The large difference in the electron temperature and lattice temperature gives rise to a strong coupling between the electrons and lattice which results in fast thermalization between the two. As mentioned above, this thermalization is much faster than the heat diffusion of the system. Due to the large time difference between the laser-heating, electron-phonon thermalization and the external heat diffusion, these dynamics can be decoupled for computational proposes without significant effect on the accuracy of the computation. Only a very small amount of heat diffusion occurs during the time it takes the electronic and lattice temperatures to equilibrate. All dynamics involving the electronic temperature can be computed prior to calculating the heat diffusion in the system. After the electronic and lattice temperature have reached the equilibrium point, the diffusion can be "unfrozen" and calculated using the standard diffusion equation. That is, the initial energy deposition into the electronic degrees of freedom and subsequent electron-phonon thermalization can be solved to serve as the initial condition of the heat-diffusion solution.

Additionally, energy lost to radiative effects is negligible and is not included in the simulation. These simplifications reduce and separate Equations 6.1, 6.2 and 6.3 into the following

$$C_l \left(\frac{\partial T_l}{\partial t} \right) = G(T_e - T_l), \tag{6.4}$$

$$C_e(T_e) \left(\frac{\partial T_e}{\partial t} \right) = -G(T_e - T_l) + (1 - R)\alpha \, exp(-\alpha z) I_0(x, t), \tag{6.5}$$

$$\frac{\partial T_l(x,t)}{\partial t} = \kappa_l \nabla^2 (T_l(x,t)), \tag{6.6}$$

where x is defined to run along the length of the nanowire, z is defined as into the nanowire (and in the direction of laser propagation), the other parameters remain the same as in equations 6.1 and 6.2 and $\kappa_l = 127 \times 10^{-6} m^2/\text{s}$ [181].

Equations 6.5 and 6.4 describe the absorption of optical energy by the free electrons and the transfer of that energy to the lattice and are solved over fast time scales (femtoseconds to tens of picoseconds).

Solving these equations numerically, using a variable step fourth-and fifth-order Runge-Kutta method (Matlab ODE45), gives the electronic and lattice temperatures as a function of time after being illuminated with a femtosecond laser pulse. The results of these simulations are shown in figure 6.4 for various peak intensities of an 800 nm, 32 fs pulse and at a depth of 25 nm into the nanowire (z=25 nm in equation 6.5).

Figure 6.4(a) shows the electron temperature (given in units of mean electron energy) as a function of time along with the instantaneous intensity of the pulse for four separate peak laser intensities, 7.5 TW/cm^2, 2.5 TW/cm^2, 0.75 TW/cm^2, and 0.25 TW/cm^2. These plots show that the heating happens on a time scale defined by the laser pulse duration, since the peak electron temperature is reached very shortly after the peak of the laser pulse. Figure 6.4(b) shows the lattice and electron temperature over a longer timescale. The figure shows that the electron cooling time is dependent on the laser intensity and that the peak lattice temperature is only a fraction of the peak electron temperature. Looking at both the

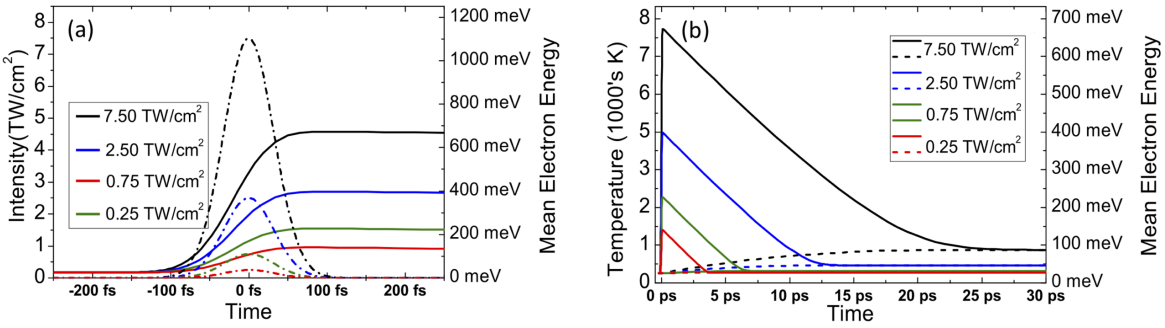

Figure 6.4: *a) Fast timescale electron energies (solid lines) are shown for (b) 32fs pulses, along with the respective laser intensity temporal profiles (dot-dash lines). (b)Temporal profile of both lattice temperature (dashed lines) and mean electron energy (solid lines) after interaction with 7.5 TW/cm^2, 2.5 TW/cm^2, 0.75 TW/cm^2 and 0.25 TW/cm^2 32fs laser pulse.*

electron and lattice temperatures as a function of time shows two very distinct time scales, thus confirming the above three-step model.

Figure 6.4 shows the electronic and lattice temperature as a function of time, at the peak of the laser focus, and for fixed depth into the nanowire (25 nm). To get the full response to the laser pulse and thus the full amount of optical energy coupled into the nanowire, equations 6.5 and 6.4 must be solved for all positions along the laser focus and for the full depth of the nanowire.

The intensity of the laser pulse at the surface of the nanowire is given by:

$$I(x,t) = I_0 exp\Big[-2\Big(\frac{x}{\omega_0}\Big)^2\Big] exp\Big[-4ln2\Big(\frac{t}{\tau}\Big)^2\Big], \tag{6.7}$$

where I_0 is peak intensity ω_0 is the focal spot size and τ is the pulse duration.

Equations 6.5 and 6.4 are solved individually for each position along the length of the nanowire (x-axis) illuminated by the focus. The intensity used for each of these positions is the local intensity, given by equation 6.7. Also, due to the z dependence in the source term the solution must be calculated for all depths (z-axis) for every x-position. Numerically, this is done by breaking the system into a two-dimensional grid along the length and depth of the nanowire. In each grid, equations 6.5 and 6.4 are propagated for a time sufficiently long to allow for complete thermalization of the electronic and lattice temperature. For all relevant laser intensities this occurs in less than 50 ps and for most intensities, in less than

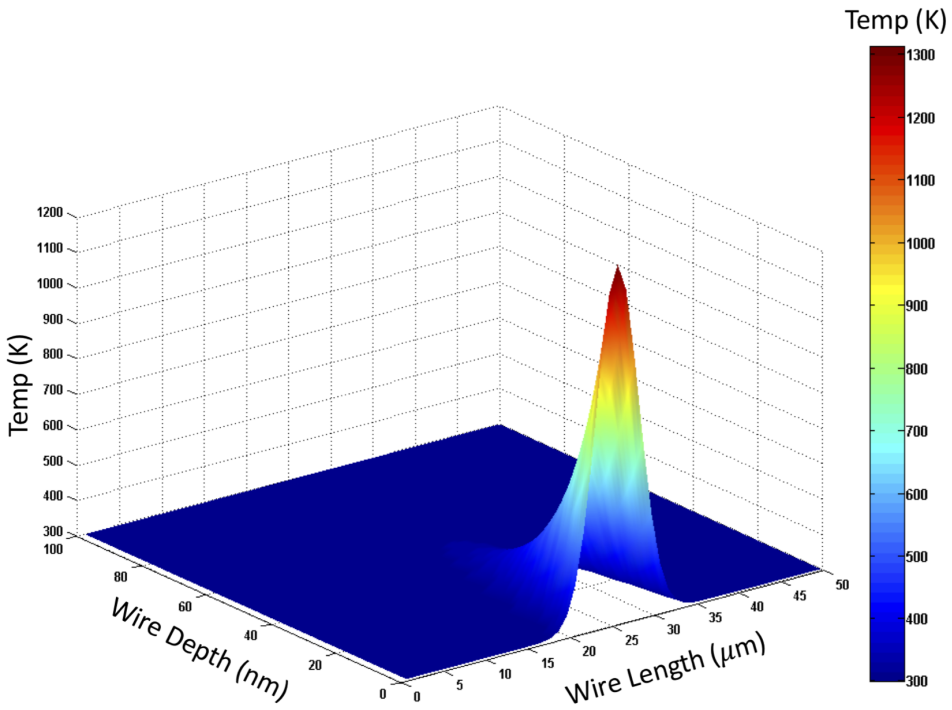

Figure 6.5: *Initial heat profile of the lattice temperature in a 100 nm thick nanowire after exposure to a 25 fs, 800 nm laser pulse with a peak intensity of* $1 \times 10^{12} W/cm^2$. *The base temperature is 300 Kelvin (room temperature). The peak temperature occurs at the surface of the nanowire located at the center a laser focus with a 10 μm spot size.*

20 ps. For all calculations shown here, 1,000 points were used along the length of the wire and 100 points were used into the depth of the wire.

Figure 6.5 shows the results of this calculation for a 25 fs, 800 nm pulse with a peak intensity of 1 TW/cm^2. The nanowire has a thickness (depth) of 100 nm and the laser focus has a spot size of 10 μm. The initial temperature distribution in the z-axis, at a given position along the wire, is a decaying exponential with the hottest point at the surface. This is simply due to the free electron screening of the electric field with increasing depth (which produces the optical skin depth). Along the length of the nanowire, the initial temperature at the surface of the nanowire is greatest at the center of the focus and decreases towards the wings of the focus. The temperature scale is Kelvin so the base temperature is taken to be room temperature at 300 degrees Kelvin. This distribution is then the initial temperature profile in the nanowire after electron-phonon thermalization and prior to heat diffusion.

At this point, both steps one and two from the TTM are competed and the only dynamics

left are due to heat diffusion. To solve this, we first consider the fact that the system has two characteristic dimensions, the length and depth of the nanowire. For a nanowire with a diameter (depth) of 100 nm and a length of 100 μm this gives an aspect ratio of 1000. This large difference in length scales leads to an additional approximation, that the diffusion in the z-dimension can be considered separate and prior to diffusion along the length (x-dimensions). This approximation is further bolstered by the shape of the initial heat distribution. The flow of heat is proportional to the gradient of temperature in the system. As can be seen in figure 6.5 the gradient along the z-direction is much larger than the x-direction. Notice, that the z-axis is plotted in nanometers while the x-axis is in micrometers. Thus, the flow of heat will be much more rapid in the z-direction than in the x-direction.

So, the diffusion in the z-direction (depth into the wire) can be calculated prior to "unfreezing" diffusion in the x-direction (along the length of the wire) with little effect on the overall accuracy of the solutions. This decouples the two, two-dimensional, second-order differential equation into two, subsequent one-dimensional, second-order differential equations. This separation dramatically speeds up the computation time and will be seen to be very important in section 6.2.2.

The computational strategy is to propagate the initial temperature distribution, according the heat diffusion equation until the temperature reaches equilibrium (constant temperature as a function of z). This is numerically performed using a time-forward finite-difference scheme with insulating boundary conditions at each surface (front and back) to account for the fixed "walls" of the nanowire.

Figure 6.6 (a) shows the same initial temperature distribution as figure 6.5. Figure 6.6(b)-(f) show the temperature distribution for a series of time steps up to 5 ns. It is clear that by this time the system has reached equilibrium. Figure 6.7(a)-(f) shows the same but for a laser pulse with a peak intensity of 10 TWcm^2. While the dynamics appear to be almost identical, a large difference can be seen in the actual value of the temperature. For both figure 6.6and figure 6.7 the color scale for each plot is scaled individually for each plot but the z-axis is kept fixed across all frames.

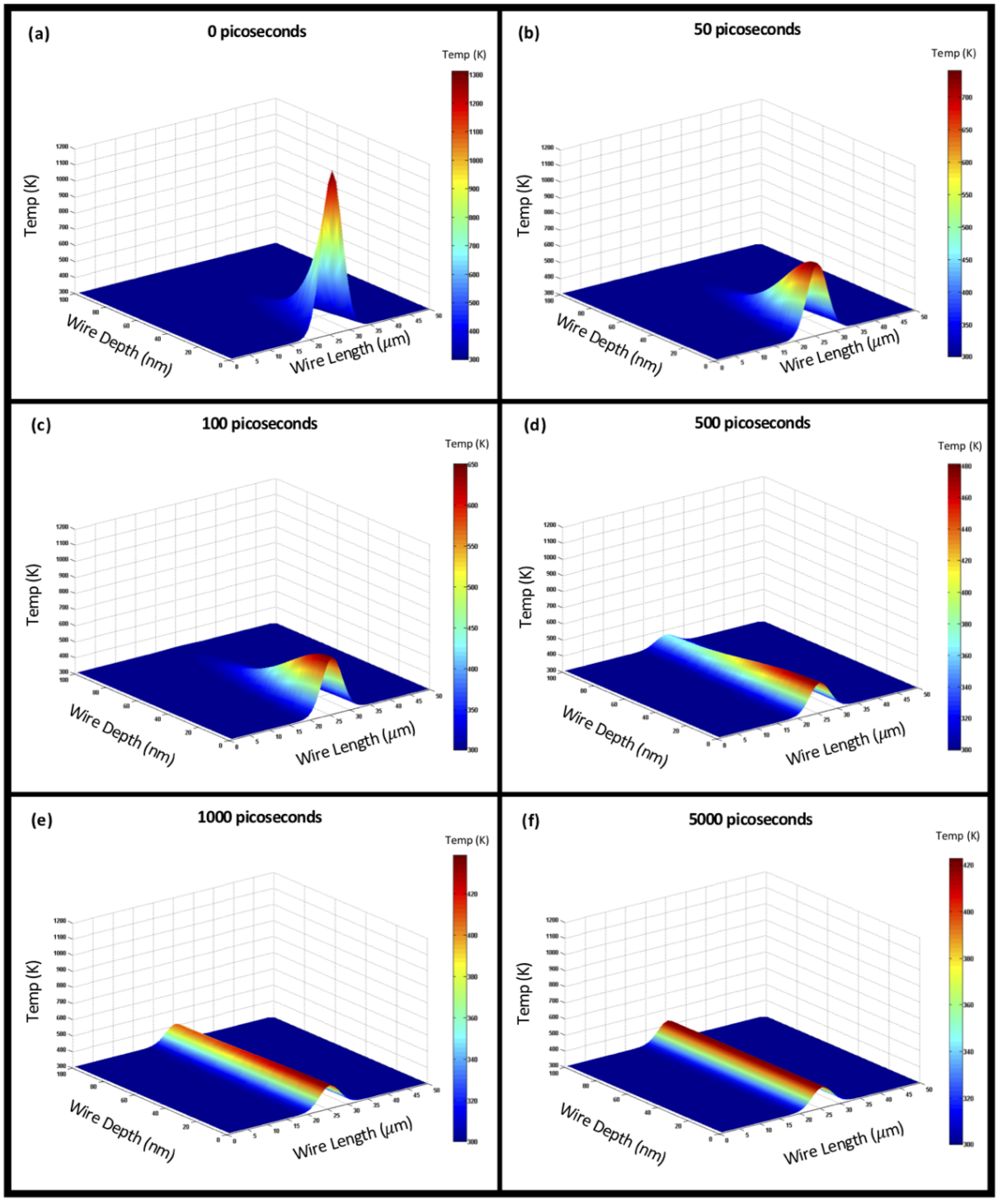

Figure 6.6: *Heat diffusion through the depth of a nanowire after exposure to a 25fs, 800nm laser pulse with a peak intensity of* $1 \times 10^{12} W/cm^2$ *and a focal spot size of* $10\mu m$*. Lateral heat diffusion (along the length of the wire) is frozen out. Color scale is renormalized for each time frame while the z-axis is kept fixed.*

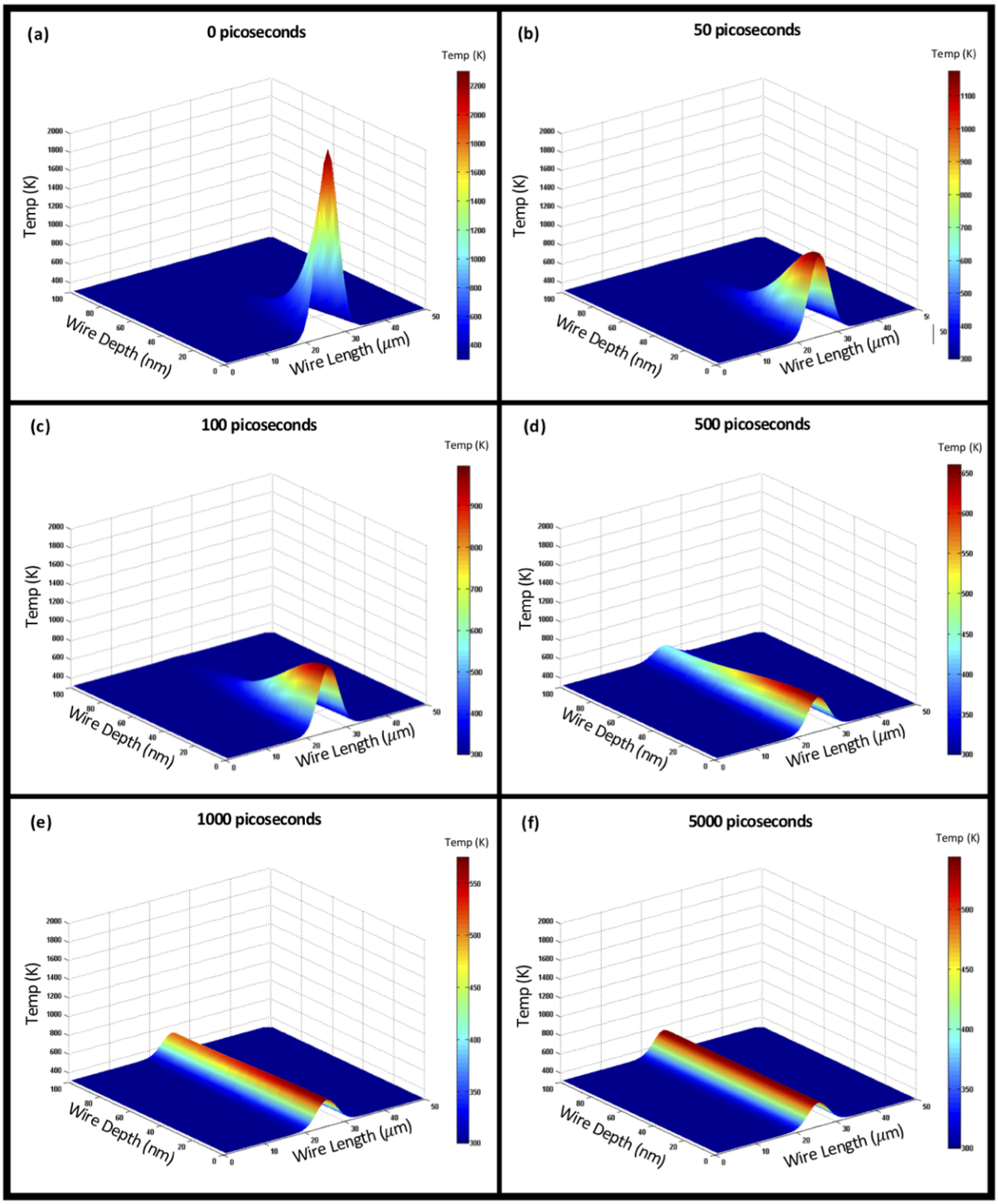

Figure 6.7: *Heat diffusion through the depth of a nanowire after exposure to a 25fs, 800nm laser pulse with a peak intensity of* $1 \times 10^{13} W/cm^2$ *and a focal spot size of* $10\mu m$*. Lateral heat diffusion (along the length of the wire) is frozen out. Color scale is renormalized for each time frame while the z-axis is kept fixed.*

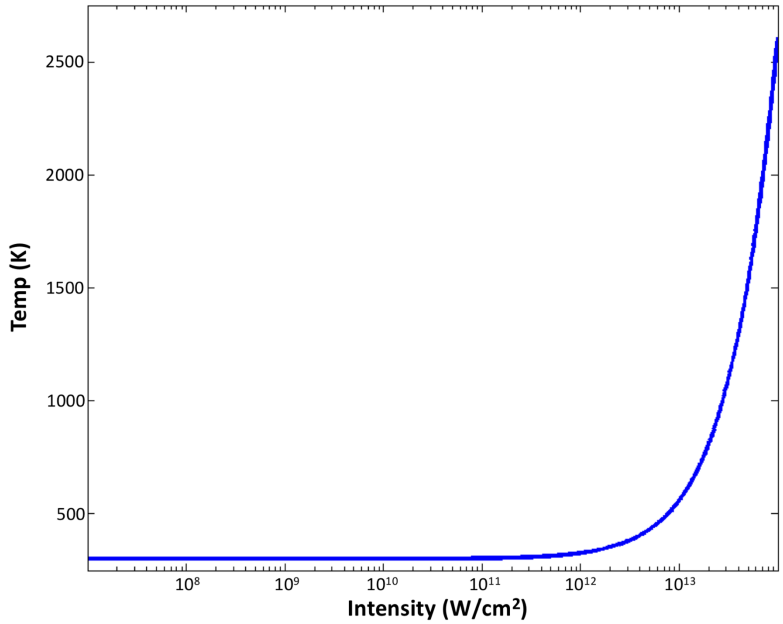

Figure 6.8: *Peak temperature of the nanowire after heat diffusion in the z-dimension (depth) has completed plotted as a function of intensity. The temperature crosses the melting point of gold (1337K) at an intensity of* $\sim 4 \times 10^{13} W/cm^2$

Figure 6.8 plots the final, peak temperature of the nanowire after propagation in the z-direction as a function of intensity. This plot can be linked to understanding the damage threshold date presented in figure 6.3. Figure 6.8 shows the temperature crossing the melting point of gold (1337 K) at intensities in the mid $10^{13} W/cm^2$ range. As described in section 6.1.1 the damage observed was a complete morphology change (bending, curling, balling up, etc.) of the nanowire. It is probably accurate to assume that for this to happen the temperature through the full depth of the wire would be equal to or exceed the melting point. The damage measurements give a damage threshold in the mid to high $10^{12} W/cm^2$ depending on the sample, for 32 fs pulses. This shows that the thermal modeling somewhat over estimates the damage point as a function of intensity but is overall qualitatively consistent with the measurements.

The final step to complete the simulation of the thermal response of a nanowire to a single ultrafast pulse is the remaining diffusion in the x-direction. For numerical stability and scalability purposes this diffusion is calculated using a Crank-Nicolson method. To accurately reflect the geometry of the system, one side of the nanowire is given an insulating

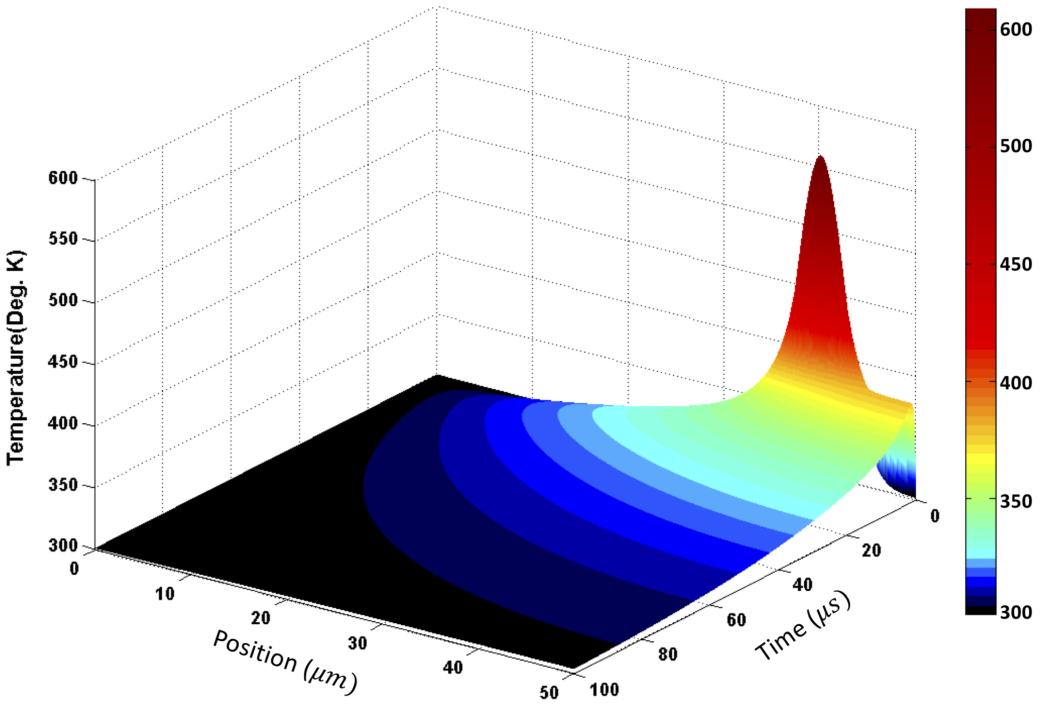

Figure 6.9: *Gold nanowire cooling profile from an initial heat distribution after exposure to a 25fs, 800nm laser pulse with a peak intensity of* $1 \times 10^{12} W/cm^2$ *and a focal spot size of* $10\mu m$*. The laser focus is simulated to be near the free tip of the nanowire. The boundary at* $50\mu m$ *has insulating boundary conditions applied while the boundary at* $0\mu m$ *is kept at a constant 300 degrees Kelvin to enforce conducting boundary conditions.*

(Neumann) boundary condition while the other is given constant temperature (Dirichlet) boundary condition. Figure 6.9 shows the temperature distribution profile along the length of the nanowire, as a function of time, for the same laser conditions as shown in figures 6.5 and 6.6. The pulse is also placed near the insulating tip. The profile starts out as Gaussian, from the profile of the laser focus. The heat initially spreads symmetrically in both the positive and negative x-directions with the center of the focus staying the hottest. However, when the diffusion reaches the insulating boundary (nanowire tip) the heat is reflected. This point quickly becomes the hottest point of the wire as heat can only leave the system though the other boundary at the base of the nanowire. Within $20\,\mu$s the wire has cooled to a few tens of degrees above room temperature and by $100\,\mu$s the temperature at the tip is only slightly elevated above room temperature.

The full thermal response and dynamics take on four distinct time-scales. The first is

femtosecond heating of the electronic degrees of freedom which occurs on the same time scale as the pulse. The second set of dynamics is electron-phonon thermalization which takes a few picoseconds to several tens of picoseconds. The third timescale is the heat diffusion though the depth of the nanowire which is completed after a few nanoseconds. The fourth and final timescale is the diffusion along the length of and out of the nanowire, which happens in tens of microseconds. This last step is quite sensitive to the exact conditions. For example, if both boundaries are set to a constant temperature to conduct heat out of the nanowire, as opposed to just one edge, then cooling will occur much faster

6.2.2 Thermal Response and Effects of Gold Nanowires to a Train of Femtosecond Pulses

Figure 6.9 shows that it can take on the order of 50-100 microseconds for the heat to diffuse out of the nanowire. The wire cools rapidly at first but then as the heat spreads out and thermal gradient is reduced, the diffusion rate slows. This often results in a small residual amount of heat left in the system after exposure to an ultrafast laser pulse. For most cases, the effect of this residual heat is completely negligible. However, for systems exposed to a train of pulses, this residual heat can build up pulse-to-pulse, resulting in significant effects after a number of laser pulses.

For the damage threshold measurements presented in section 6.1.1 the laser had a repetition rate of 2 kHz with pulses separated by 500 μs. This gives ample time for heat to leave the system before the next pulse. However, if sources with higher repetition rate, and thus less time in between pulses, are used then the system may not completely cool before the arrival of the next pulse. This is compounded for laser intensities near (but below) the single shot damage threshold, as they can couple a large amount of heat into the system, making complete cooling more difficult.

This multi-shot heating effect is important to consider when working with very high repetition rate ultrafast sources such as Ti:Sapphire oscillators or mode-locked fiber lasers. The repetition rate in these systems can approach or even exceed 100 MHz, giving less than 10

ns for cooling. Applications such as field-enhanced high harmonic generation from nanotips [162; 163] or nanosystems exposed to femtosecond radiation as an ultrafast photoelectron source [89; 160; 161; 164] are particularly sensitive to multi-shot heating as they operate at relatively high intensities and high repetition rates.

This section extends the above thermal modeling to a train of pulses. Ultimately the goal of these simulations is to determine if the nanowire will be melted by a single, intense, pulse or if heat will build up in the system as a function of the number of laser pulses, leading to damage. Here we explore the multi-pulse thermal effects in gold nanowires irradiated by a train of 25 fs pulses centered at 800 nm using a the two temperature model developed in section 6.2.1.

Extending the TTM to multiple pulses is fairly simple conceptually, if not exactly simple computationally. All three steps, electron heating, electron-phonon thermalization and heat diffusion (in both the z-dimension and x-dimension) are modeled fully for each pulse. Then the final heat profile in the nanowire is used as the initial profile to calculate the response to the next pulse. An important note is that the electronic heat capacity is a function of temperature so equation 6.5 is dependent on the initial temperature of the system. So it is necessary to use the full heat distribution along the length of the wire when solving equations 6.4 and 6.5. Figures 6.10 (a) and (b) show, schematically, how this is done. All temperatures are plotted in degrees above room temperature (ART). The peak temperature of the wire after the focus is 1,000 degrees C above room temperature which is just below melting temperature and corresponds to an optical intensity of approximately $3 \times 10^{13} W/cm^2$. The time between shots is 500 μs.

Figure 6.10 (c) shows the heat profile in the wire for, three subsequent laser pulses, one time instant before the next laser pulse for the same conditions as Figures 6.10 (a) and (b). As can be seen, the temperature rises after each shot but the absolute difference decreases. This is due to the fact that as heat builds up in the system, pulse by pulse, the thermal gradient between the temperature of the system and the temperature of the outside environment grows, resulting in a larger thermal conductance. This eventually leads to a steady state where the amount of thermal energy absorbed by the system from the n^{th} pulse

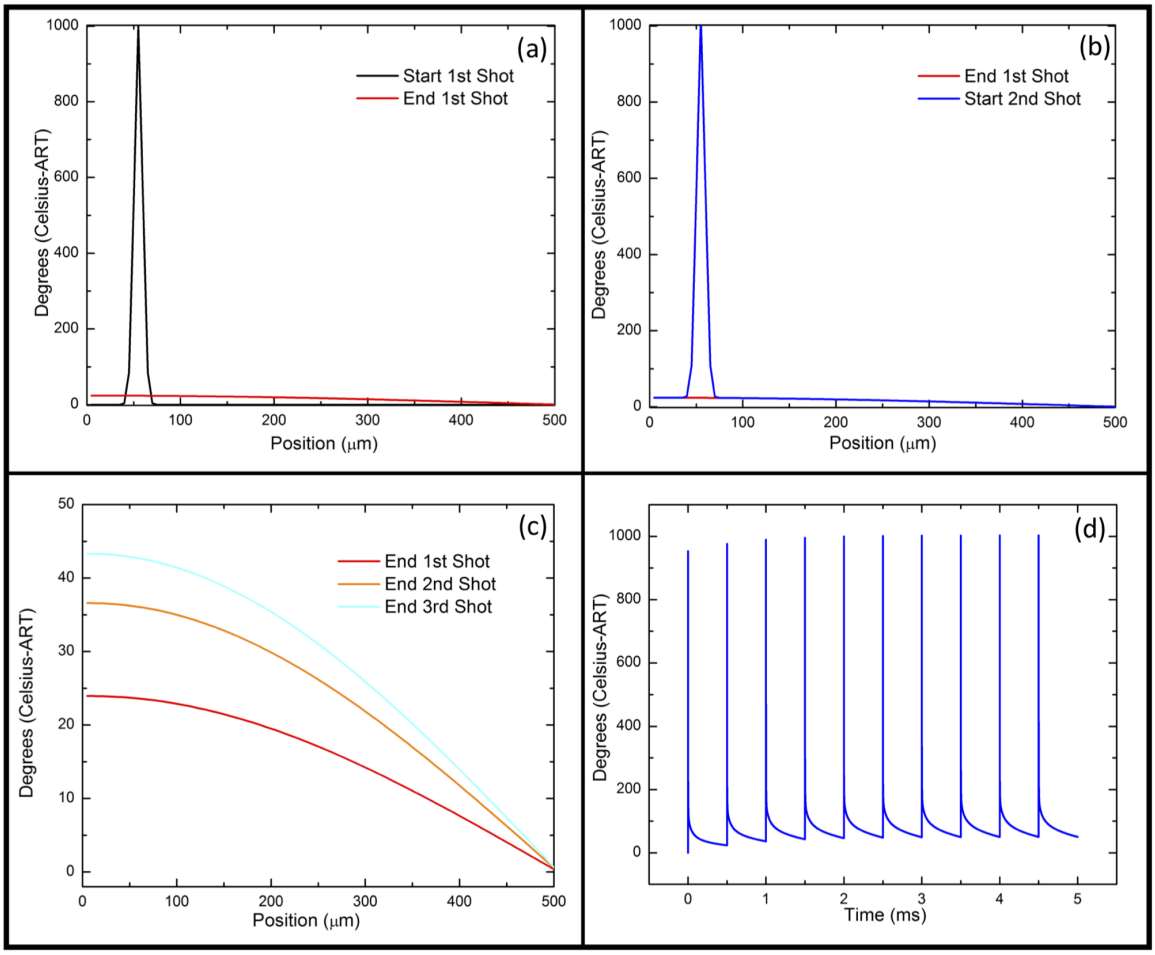

Figure 6.10: *Schematic of how multi-pulse heating simulations are carried out. The laser focus is simulated to be near the wire tip and the boundary at 0μm is treated as insulating while the boundary at 500μm is conducting. (a) Temperature profile along the wire directly after the first laser shot (black) and after cooling for 500μs (red). (b) Temperature profile from the second laser shot (blue) calculated using the final profile form the previous laser pulse (red). (c) Temperature profile of the first three subsequent laser pules. (d) Temperature of the wire at the focal position as a function of time for the first 10 lasers pulses.*

is completely dissipated just before the n^{th+1} pulse arrives. The temperature of the system still changes after every pulse, but it relaxes to the same value before the next pulse. This is depicted by figure 6.10 (d), which follows the wire temperature at the center of the laser focus as a function of time. The temperature profile rises after the first few shots but then comes to a steady state.

The question then becomes, what effect this steady state residual heat has on the measurements being performed. The most dramatic effect obviously occurs when this residual

heat raises the base temperature to a value such that the nanowire melts in regimes where single-shot temperatures are far below the melting temperature.

To answer this question, we performed this multi-pulse simulation for a wide range of pulse intensities and repetition rates. For damage, the quantity of relevance is the peak temperature. So, for each individual condition (repetition rate and intensity) the simulation was run until the peak temperature rose to its steady state value. This is defined as an increase of less the 1-degree K from one pulse to the next.

For some conditions, this happens within relatively few pulses (as depicted in 6.10 (d)). However, for other conditions, this steady state condition can take many thousands of pulses to reach. This leads to a significant computational challenge. It is very computationally expense to solve the full systems of equations over the full parameter range for the required number of pulses.

To speed this up, we break the computation into two separate parts. In the first part, the electron heating by the laser pulse, followed by the electron-phonon thermalization and the diffusion in the z-direction are calculated. The dynamics in these steps will always be faster than the pulse-to-pulse spacing for all relevant repetition rates. This calculation is performed for intensities ranging from $1 \times 10^7 W/cm^2$ to $1 \times 10^{15} W/cm^2$. Also, since the electronic heat capacity is a function of temperature, the calculation is performed with a complete range of starting temperatures from room temperature to melting temperature. Calculating this full range of parameters took several weeks to complete, even when parallelized to a machine running a 12 core Xeon E5 2.5 GHz chip. All calculations were done in Matlab. However, once completed, the results can then be saved into a lookup table that can be referenced for the next step which factors in the multi-pulse effect. This eliminates the need to do the full calculation for each pulse. The ability to do this is a significant advantage, in terms of computational time, of splitting the diffusion into two subsequent steps as described in section 6.2.1.

Figures 6.11 and 6.12 show the results of the full multi-pulse heating simulation for the same system described in section 6.2.1 and shown in Figure 6.9. Like in these calculations, the pulse is placed near the tip of the nanowire and the heat is confined to only leave the

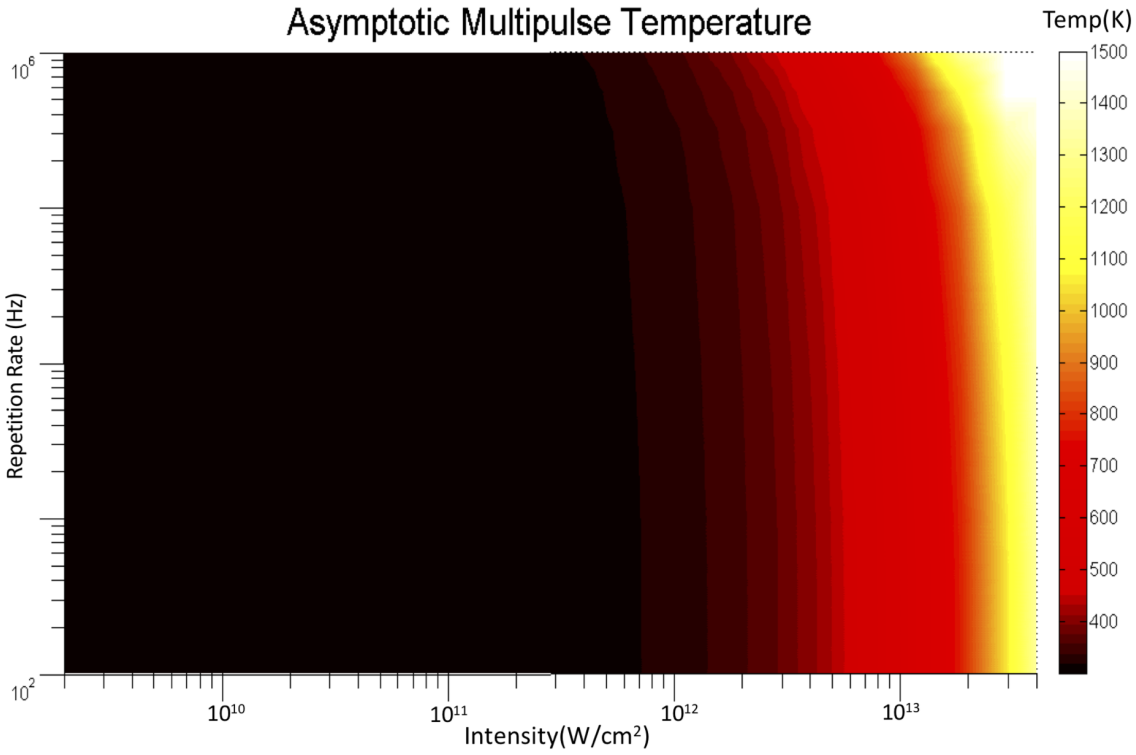

Figure 6.11: *Asymptotic final peak temperature of a 100 nm gold nanowire as a function of laser intensity and repetition rate*

system from the other end. Figure 6.11 plots the steady-state, peak temperature as a function of repetition rate and pulse intensity and figure 6.12 shows several key temperature contour lines for the same. The curvature of these contour lines show how multi-pulse effects develop at higher intensities and repetition rates. The increase in curvature towards the horizontal indicates the amount of multi-pulse heating. For parameters where no multi-pulse heating is present these lines are vertical as the final temperature of the nanowire does not greatly depend of the number of laser shots incident on it. For repetition rates up to around 10 kHz, corresponding to a time in between pulses of 100 μs, the heat accumulated pulse-to-pulse is negligible. In this regime, the simulations predict that the nanowire will only damage if a single pulse is intense enough to heat it above melting. This occurs at intensities around $3 \times 10^{13} W/cm^2$ for 25 fs pulses. As the repetition rate increases past 10 kHz, multi-heat effects become significant as the heat does not have time to diffuse out of the system before the next pulse arrives.

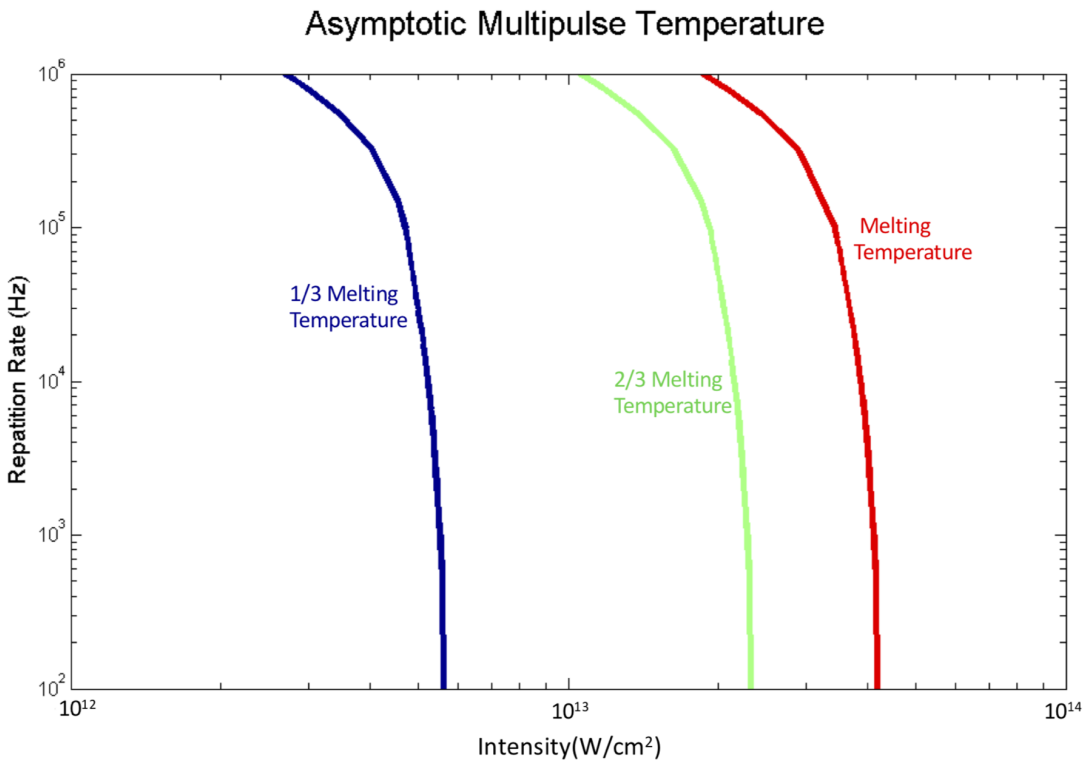

Figure 6.12: *Three temperature profiles showing the asymptotic final peak temperature of a 100nm gold nanowire as a function of laser intensity and repetition rate.*

These results show that when working with very low-dimensional nanosystems it is important to consider the multi-pulse heating effects of higher repetition rate systems. These effects are also very geometry dependent. In a sense, the simulations shown here represent the "worst case scenario" as the heat has a limited volume to spread into and can only leave though one end of the system. If the boundary conditions allowed heat to leave through both ends of the wire or the wire was a larger diameter then the multi-pulse effects would be reduced. Future work in this area could expand these simulations to include different geometries, wavelengths and pulse durations as well as perform experiments to validate the numerical models.

6.3 Wavelength Scaling of Photoionization of Dielectric Nanoparticles

Colloidal nanoparticles can be an ideal test system for studies of light-matter interactions with increasing levels of complexity. The ability to precisely synthesize these systems, with a high-degree of control on size and composition [182; 183], allows for the systematic investigation of many-body interactions and their various aspects in response to an intense external optical field [158; 184]. Photoelectron emission represents one of the most fundamental responses of matter to a strong optical field. Recently, considerable effort has been spent to understand the electron dynamics in individual nanoparticles photoionized by intense, femtosecond pulses [165; 185–189], largely motivated by the vision of nanoscopic, ultrafast electronic control. One of the resultant properties at the nanoscale is the concentration of highly localized near-fields with dimensions far below the diffraction limit. Driving this enhanced near-field with an ultrafast laser provides the potential for controlling electronic motion at the nanoscale [86; 87; 164–166]. This section details our work to understand strong-field photoionization in dielectric nanoparticles. In particular, emphasis is placed on extending the driving wavelength into the mid-infrared (MIR). Over the preceding decade a number of studies have been performed to investigate strong-field ionization in dielectric

nanoparticles with visible or near-infrared (NIR) fields. However, to the best of our knowledge, no work has been performed using mid-infrared driving pulses in gas-phase dielectric nanoparticles. The quadratic scaling of the ponderomotive potential with wavelength, and the established subsequent effects on photoelectron rescattering dynamics for atomic targets, presents a strong motivation for investigating strong-field ionization of nanoparticles with mid-infrared wavelengths.

6.3.1 Size Dependent Electron Emission from Laser-Driven SiO_2 Nanoparicles

Analogous to the atomic case, photoelectrons emitted from nanoparticles can be driven back by the oscillating laser field to interact with the particle surface. However, the photoelectron rescattering process and resulting electron energy spectra is strongly influenced by the unique bulk properties of the system. In particular, these spectra carry signatures of laser-induced near-field enhancements [165] and dynamical many-particle charge interactions [87], processes not present in atomic or molecular systems. Figure 6.13 shows the photoelectron momentum distribution (PMD) for atomic xenon and 120nm SiO_2 nanopartices from both 800 nm and 1800 nm pulses, for similar peak intensities. Figure 6.13 (a) and figure 6.13 (b) show the PMD for strong-field ionization of Xe for 800 nm an 1800 nm with intensities of 16 TW/cm^2 and 17 TW/cm^2 respectively. Figure 6.13 (c) and Figure 6.13 (d) show the PMD for 120 nm SiO_2 nanoparticles with intensities of 18 TW/cm^2 and 19 TW/cm^2 respectively. As a note, all four PMDs were taken with different VMI repeller voltages and thus span different maximum electron energy range. White circles in each plot denote the position of the labeled momentum values in atomic units for better comparison.

Several differences are readily apparent. The intricate fringe and interference ATI patterns seen in xenon are nonexistent in the nanoparticle photoelectron momentum distribution. This can primarily be attributed to many-body effects, space charge and trapping potentials that destroy the coherence between the photoelectrons. More strikingly, the maximum photoelectron energy from nanoparticles is many times higher than those from xenon

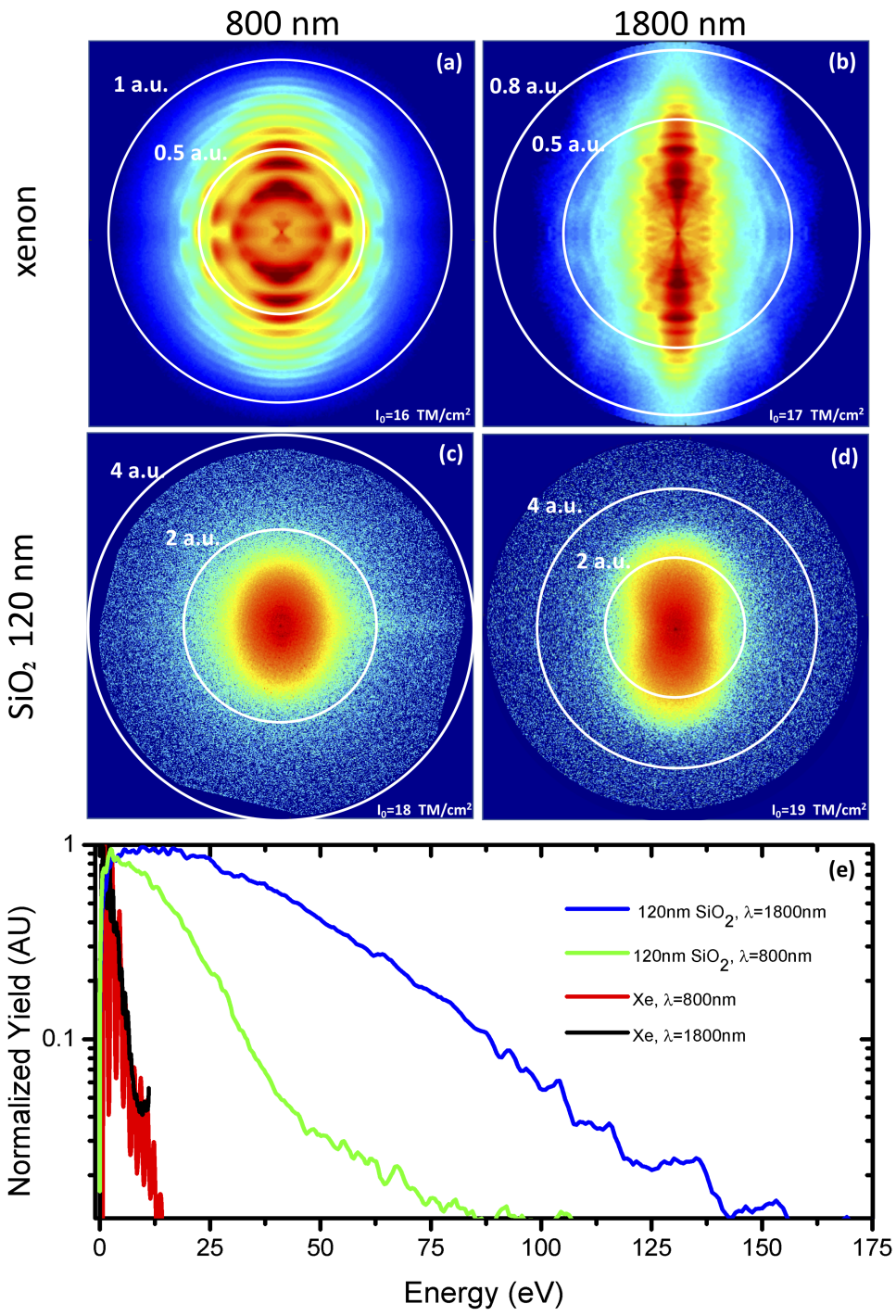

Figure 6.13: *Photoelectron momentum distribution for Xe and 120nm SiO_2. (a) Xe, 800 nm, 1.6×10^{13} W/cm^2, VMI repeller voltage: -500 V, (b) Xe, 1800nm, 1.7×10^{13} W/cm^2, VMI repeller voltage: -250 V, (c) 120nm SiO_2 NP, 800nm, 1.6×10^{13} W/cm^2, VMI repeller voltage: -4,000 V, (c) 120nm SiO_2 NP, 1800nm, 1.6×10^{13} W/cm^2, VMI repeller voltage: -8,000 V. All images are non-inverted. (e) Normalized energy spectra along polarization direction for (a)-(d).*

at the same peak intensity. This fact is most clearly seen in figure 6.13 (e) which plots the energy distribution of panels (a)-(d) along the polarization direction. The nanoparticle photoelectron maximum energies are significantly higher than the $10\,U_p$ rescattering limit in strong-field ionization of atoms. Thus, the photoelectron emission properties, especially the maximum electron energy ("photoelectron cutoff"), can be expected to sensitively depend on both nanoparticle properties (composition, shape, size) and laser pulse characteristics (wavelength, peak intensity, pulse duration).

The energies of the photoelectrons are determined by their quiver motion in the continuum under the influence of the optical field. In the atomic case, discussed in section 3.2.3, the final electron energy is determined almost entirely by the specific trajectory and the action acquired during this propagation, with direct backscattering producing the maximum photoelectron energy. This is also the case for nanoparticle photoelectron rescattering events where the most energetic elections reach maximum energy after backscattering from the surface at an optimal phase of the field. However, as opposed to atomic systems, the local field in which the electron propagates depends on the optical response of the nanoparticle to the driving field. The classical electrodynamic interaction of the laser field with the nanoparticle results in the generation of well-defined near-fields, whose linear response structure is accurately described by the Mie solution [190] These near-fields can lead to local electric field enhancements several times that of the particle-free laser field. This correspondingly increases the local ponderomotive potential and maximum rescattered photoelectron energies. The spatial distribution of the induced near-field also depends strongly on the size of the system, described by a dimensionless Mie size parameter $\rho = \pi d/\lambda$ (where d is the particle diameter and λ is the incident wavelength).

As a result of the thousands to millions of atoms in the nanoparticle, a single interaction with the intense laser field can easily produce hundreds to thousands of photoelectrons even at relatively low peak intensities. This has a dramatic effect to the final photoelectron energy spectra. The presence of a large number of continuum electrons in a tightly confined space leads to a repulsive interaction often termed the space charge effect. In addition, as each electron is stripped off, a resulting positive charge is built up on the surface of the

nanoparticle. This positive surface charge forms a potential that suppresses further ionization [165; 191]. Subsequent electrons must acquire sufficient energy from the laser field not just to overcome the binding potential but also this Coulombic trapping potential. The presence of this potential has been linked to the observation that the number of detected photoelectrons scales linearly with nanoparticle size [191]. Both the repulsive space charge and trapping potential modify the continuum electron trajectories and can result in a significant increase in the maximum electron energy for some trajectories [191].

A number of experimental and theoretical studies [87; 192] have been performed in the near-infrared looking into the photoelectron cutoff as a function of nanoparticle size and peak driving intensity. For these wavelengths, the cutoff energy was found to increase nearly linearly with both size of the nanoparticle and intensity. The increase as a function of intensity can be understood as the linear increase of the ponderomotive potential and enhanced near-field. This produces a proportional increase in the rescattering energies.

Several different mechanisms contribute to the scaling of the cutoff energy as a function of nanoparticle diameter. First, the maximum near-field increases with size. This in turn increases the energy the electron gains while being accelerated in the continuum before undergoing backscattering. A second important effect is the increased photoelectron yield. As the particle diameter increases, the total amount of ionization grows resulting in an increased space charge and cutoff energy. The overall effect from the increased near-field, ponderomotive potential and the space charge gives that the cutoff energy grows nearly linearly with particle size. This fact has been verified both experimentally [87; 192] as well as with a full theoretical treatment [191].

Given the complexity of the dynamics involved in the photoelectron trajectories, and in particular the trajectories that lead to cutoff electrons, the scaling laws with wavelength are difficult to predict a priori. The rest of this section presents our experiment and results of strong-field ionization of SiO_2 nanoparticles as a function of both particle size and intensity with 1800 nm driving pulses.

6.3.2 Experimental Setup

This study uses the same optical and velocity map imaging (VMI) setup detailed in section 3.3. Briefly, a high-energy optical parametric amplifier (OPA) is pumped with 18 mJ, 25 fs 800 nm pulses at a repetition rate of 1 kHz. The OPA is then tuned to generate the desired MIR pulses. In this experiment 1400 nm and 1800 nm pulses are used with pulse duration of 60 fs and 80 fs respectively. The signal and idler output beams are separated in the far-field by inducing a slight non-colinear overlap in the final amplification crystal of the OPA. The beam is then coupled into an optical setup to attenuate the pulse energy to the desired level before being focused into the VMI with a positive lens. The intensity in the interaction region is calibrated in the same manner explained in section 3.3.

Instead of the effusive gas jet shown in figure 3.2, nanoparticles are coupled into the VMI, in gas-phase, using an aerosolization system and aerodynamic lens. This is shown in figure 6.14. A suspension of silica (SiO_2) nanoparticles in water is aerosolized and a solid-state membrane drier selectively removes the solvent (water) from the carrier gas (N_2). An aerodynamic lens is used to focus the gas-phase nanoparticles to increase the beam density while a three-stage differential pumping system removes excess carrier gas to preserve the high vacuum at the interaction region [64; 193; 194]. Spherical silica nanoparticle samples (nanoComposix, Inc.) ranging from 20 nm to 750 nm (silanol surface coating) were custom ordered specifically for their narrow size distribution ($< 10\%$), solvent choice and overall purity. The initial number concentration of each sample was experimentally determined to minimize the probability of more than one nanoparticle per aerosol droplet while also ensuring less than one particle in the interaction volume per laser shot.

A single-shot-camera, alongside a real-time hit finding routine, is used to record the photoelectron spectra for each laser shot. When the gas-phase nanoparticle passes through the intense laser focus a large number of photoelectrons are produced, much more than would be seen from ionization of the background gas alone. To suppress background, a minimum number of detected electrons sorting condition is applied. Detailed information about this technique can be found in [64]. For each experimental condition (wavelength, intensity and

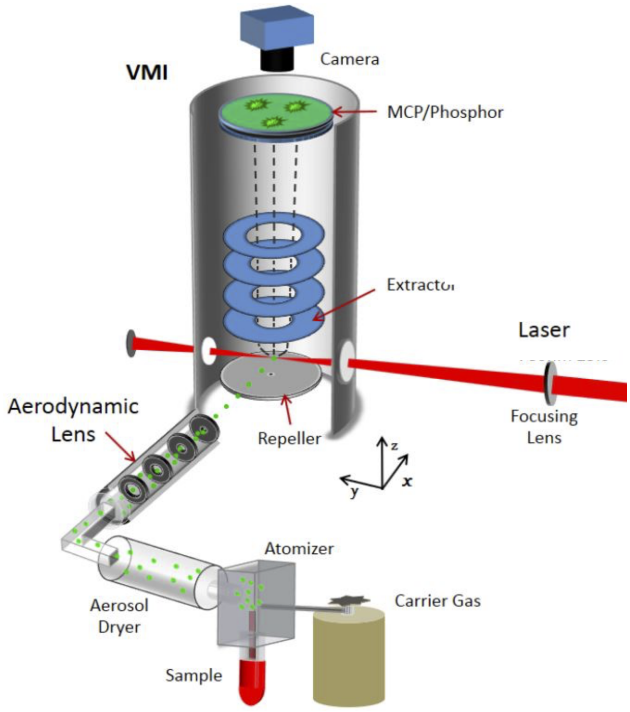

Figure 6.14: *High energy velocity map imaging (VMI) spectrometer coupled to nanoparticle source. Single, isolated gas-phase nanoparticles are focused and injected into vacuum to interact with focused ultrafast pulses. Emitted electrons are focused onto the MCP/phosphor assembly where a single-shot camera records the electron spectra for each laser shot. A continuous nanoparticle source guarantees a fresh sample for each interaction while a narrow size distribution of the nanoparticles ensures identical particles shot-to-shot. Adapted from [64].*

nanoparticle diameter) the total photoelectron momentum distribution is constructed from laser shots that produce more than this number of electrons. A line-out along the polarization direction is extracted from this PMD and converted to energy to select the cutoff value. The cutoff energy is determined from this line-out as the point where the signal is reduced to the background level. The cutoff photoelectron energy is then used to investigate size, intensity, and wavelength scaling effects.

6.3.3 Results and Discussion

Figure 6.15 shows the cutoff energy as a function of size for a series of peak intensities at both 800 nm and 1800 nm. The 800 nm data was originally taken and reported in [64].

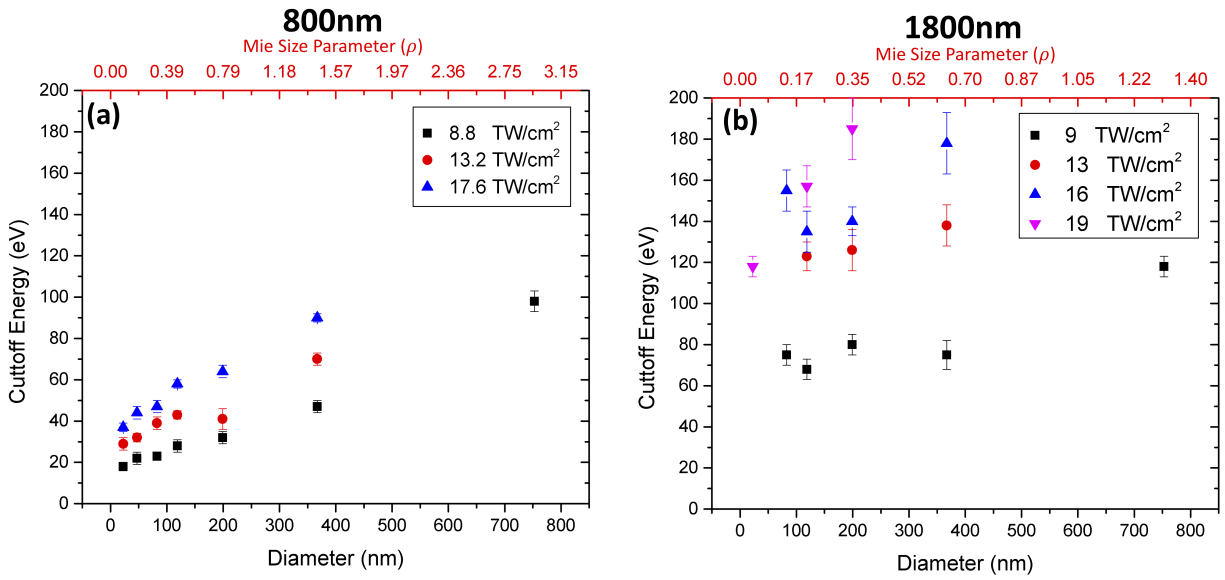

Figure 6.15: *Photoelectron cutoff energies as a function of nanoparticle diameter for (a) 800 nm driving wavelength and (b) 1800 nm driving wavelength. The corresponding Mie parameter ρ is given by the top axis.*

Several different behaviors are immediately apparent. First, as expected, increasing the driving intensity results in an increase in the cutoff energy for both 800 nm and 1800 nm wavelengths. The 800 nm data also shows a clear increase of absolute cutoff energy as a function of nanoparticle size. This effect is quite dramatic. The largest nanoparticle (750 nm) emits electrons almost six times more energetic than the smallest (20 nm) nanoparticle, given the exact same incident laser intensity. This follows the near linear increase as explained above and understood in terms of the ponderomotive potential, near-field enhancements and space charge scaling.

However, while the 1800 nm cutoff energies are higher than the 800 nm case, as expected by the quadratic scaling of the ponderomotive potential with wavelength, they do not show a linear or even monotonic increase as a function of nanoparicle diameter. The intensities covered for both the 800 nm and 1800 nm span a similar range.

To attempt to understand this deviation in behavior, as compared to the 800 nm data, we separate out the various individual effects that scale with wavelength. The first and most obvious is the ponderomotive energy. Recall that for the atomic case, in the tunnel ionization regime, the photoelectron cutoff scales directly with U_p. Figure 6.16 shows the same cutoff

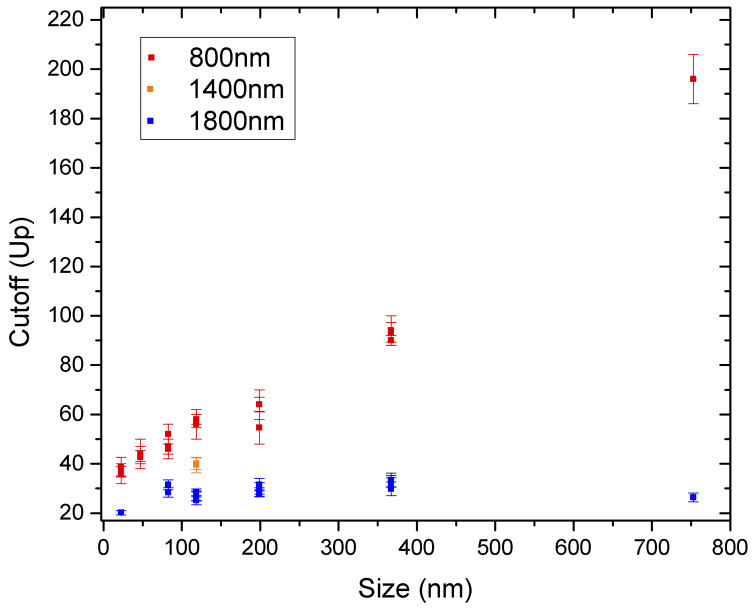

Figure 6.16: *Size dependent photoelectron cutoff energy values in units of ponderomotive potential from SiO_2 nanoparticles at 800 nm, 1400 nm and 1800 nm driving wavelengths.*

energies for both 800 nm and 1800 nm, plotted in terms of the ponderomotive energy instead of electron volts. These are now plotted on the same graph and all intensities for each size are included. Also, a single data point taken with 1400 nm for 120 nm diameter nanoparticles has also been included. The ponderomotive energy used here for scaling corresponds to the particle-free value for the calibrated intensity.

Looking at the plot, we see that scaling by the ponderomotive potential brings cutoff values at a given size and wavelength on top of each other or close to on top of each other. This shows that for all wavelengths, the cutoff energy does indeed scale with U_p or in other words, linearly with intensity. The 800 nm data still shows the clear linear increase with size but the 1800nm very obviously does not. In fact, after scaling by U_p, the 1800 nm photoelectron cutoff values show a slight decrease with size. While only one data point was measured at 1400 nm, and thus the trend with nanoparticle size is impossible to determine, it does fall nicely between the 800 nm and 1800 nm points indicating a systematic functionality in the underlying physics with driving wavelength.

The flat, or slightly decreasing, trend with size at 1800 nm represents a large departure from the mostly understood physics that explain the scaling when strong-field ionization

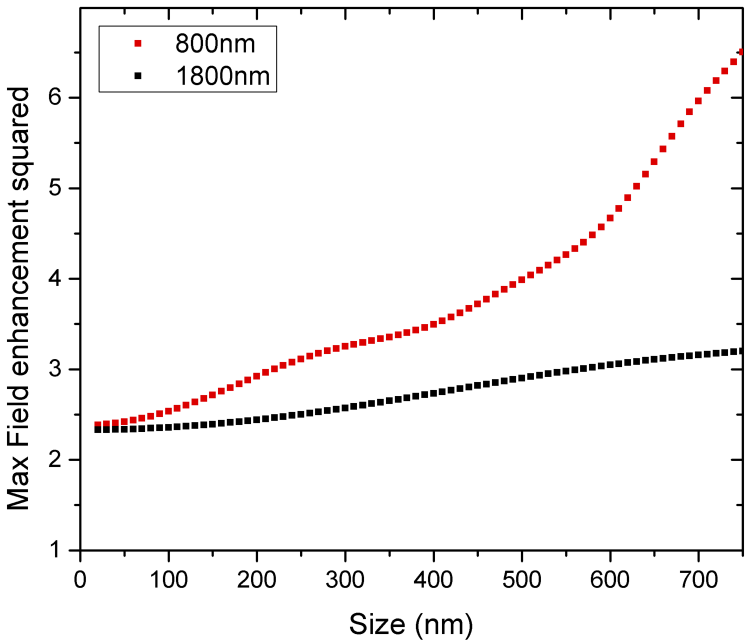

Figure 6.17: *Squared maximum field enhancement as a function of nanoparticle diameter for 800 nm (red) and 1800 nm (black).*

is driven with 800 nm pulses. Part of this effect can be attributed to the slower increase as a function of size in near-field enhancement for 1800 nm versus 800 nm (for the range of nanoparticle sizes studied here). Figure 6.17 plots the square of the maximum field enhancement (α) as a function of size for both 800 nm and 1800 nm, calculated by numerically solving for the Mie field [195]. Since optical intensity is proportional to the square of the electric field, the squared field enhancement (α^2) represents the maximum increase in local intensity from the induced near-field.

To see if this difference in near-field scaling explains the photoelectron cutoff trend for 1800 nm strong-field ionization, the (ponderomotive) scaled cutoff energies shown in figure 6.18 are further scaled by α^2. Physically, this corresponds to scaling the cutoff energies by the 'maximum local ponderomotive potential'. A note to this method is that it is not completely apparent that scaling by the maximum is the only (or correct) method to account for the near-field. For example, it may be more relevant to scale by the field enhancement along the polarization axis, at the pole of the sphere. However, due to the highly non-linear response of strong-field ionization to the field strength this method seems most appropriate without

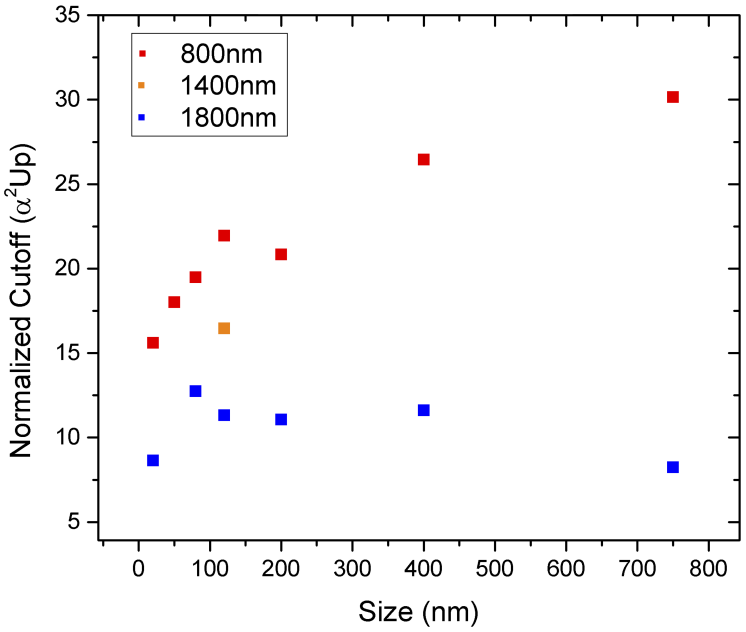

Figure 6.18: *Size dependent photoelectron cutoff energy values scaled by ponderomotive potential and squared field enhancement (α^2) from SiO_2 nanoparticles at 800 nm, 1400 nm and 1800 nm driving wavelengths.*

more detailed modeling of the entire nanoparticle response. Prior to scaling by α^2 the data points from multiple intensities are averaged, which is possible since the normalization by U_p already accounted for the intensity scaling.

This normalization does bring the 1800 nm and 800 nm cutoff energies closer inline, but a large discrepancy is obviously still present. The 800 nm cutoffs still continue to increase with size while 1800 nm cutoffs remain flat.

Considering the electron excursion distance during the rescattering process brings an additional possible explanation for the reduced energies at 1800 nm. The classical electron excursion distance (l_e) scales quadratically with wavelength (inverse square with frequency)

$$l_e = \frac{eE_0}{m\omega^2}, \tag{6.8}$$

where e is the electron charge, E_0 is the field strength, m is the electron mass and ω is the angular frequency.

Scaling the cutoff energy by $\alpha^2 U_p$ implicitly assumes that enhanced near-field the electron

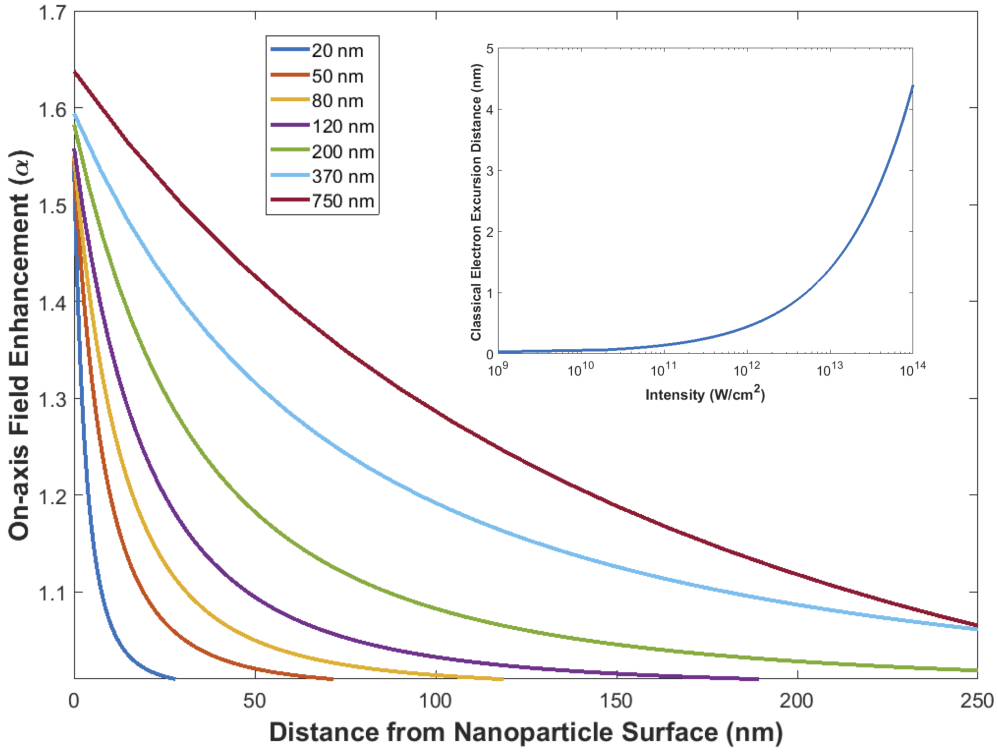

Figure 6.19: *SiO_2 field enhancement along the polarization axis as a function of distance from the nanoparticle surface for 1800 nm incident light. Inset: classical electron excursion distance as a function of intensity for 1800 nm driving wavelength.*

trajectory samples stays constant. However, this comes into question for longer excursion distances where the near-field could decay over distances shorter than the quiver amplitude. This effect has been experimentally observed for photoemission from sharp nanotips [164].

To check if this could be the case for our samples, we calculate the full near-field for all nanoparticle sizes used in this study at 1800 nm. Figure 6.19 shows the field enhancement along the polarization direction as a function of distance from the nanoparticle surface.

The inset in figure 6.19 shows the classical electron excursion distance as a function of intensity for 1800 nm. Even at a relatively high intensity of 10^{14} W/cm^2 the electron does not move travel than 5 nm. Comparing this to the decay of the near-field shows that for all but the smallest nanoparticle size (20 nm), to a good approximation, the field is constant over the electron trajectory. So a decaying near-field over the electron trajectory is unlikely to contribute to the overall trend shown in figures 6.15, 6.16, and 6.18, for 1800 nm driving wavelengths, except for the 20 nm case. This could be the explanation for the lower

photoelectron cutoff with 20 nm nanoparticles.

The final possibility for explaining why 800 nm cutoff electron energies scale linearly with nanoparticle size, while the cutoff energies for 1800 nm remain flat, is the contribution from space charge. Our measurements at 800 nm do show an approximately linear increase in the number of cutoff electrons as a function of size while the number of cutoff electrons decreases slightly with size for 1800 nm. This fact points to the explanation that space charge effects are reduced proportionally at 1800 nm. However, the total number of photoelectrons is perhaps the more relevant quantity. Unfortunately, due to detector saturation for lower electron energies we are unable to comment effectively on the total electron yield. Additionally, the full spatial distribution of free electrons at the time of ionization of a cutoff electron is needed to state with certainty the exact contribution of space charge. This is a much more difficult quantity to ascertain the effects of without a full theoretical treatment of the strong-field ionization process.

6.3.4 Conclusion and Future Work

We show here, to the best of our knowledge, the first size dependent measurement of strong-field ionization of gas-phase dielectric nanoparticles with mid-infrared wavelengths. The photoelectron cutoff energies are extracted from the full angular distribution and compared to results with 800nm pulses for a similar intensity range. The increased ponderomotive energy at longer wavelengths does result in an overall increase to the absolute cutoff energy. However, a large difference in the scaling as a function of nanoparticle size between the 800nm wavelengths and 1800nm wavelengths is observed. This represents a deviation from current understanding. While some of this difference can be attributed to relative decreased near-field enhancements other, not yet fully understood, physical processes, such as decreased space charge effects are needed to completely explain our observations.

Establishing the true wavelength scaling laws for strong-field ionization of gas phase nanoparticles is an important step in the overall quest to precisely control electron dynamics on the nanoscale with ultrafast pulses. Future experiments are planned for a larger range of

driving wavelengths to better establish the full functionally. Additionally, various theoretical approaches are being considered to gain more insight into the exact nature of the space charge effects on the ionization dynamics as a function of wavelength.

Chapter 7

Conclusion

A number of different topics were explored in this thesis. In chapter 3 the study of strong-field ionization in xenon, as a function of both wavelength and intensity, gave a dataset that systematically contains information on the strong-field ionization process, where several different mechanisms are involved. Signatures of direct above threshold ionization, Freeman resonances, direct backscattering, and the interference between direct electrons and low-energy rescattered electrons were tracked from the near-infrared regime through the mid-infrared regime. The transition from multiphoton ionization to tunnel ionization, due to both increasing wavelength and intensity, is also shown along with a method for calibrating intensity from the ponderomotive shifting of photoelectrons. These measurements help to create more comprehensive and consistent picture of strong-field ionization and the scaling dynamics with intensity and wavelength. Chapter 4 presented both the locking and tagging of the carrier-envelope phase. The long-term carrier-envelope phase stabilization of amplified, high-energy pulses was demonstrated. Additionally, a single-shot, all optical method of carrier-envelope phase tagging was developed and shown to provide comparable accuracy as the above threshold ionization carrier envelope phase meter. In chapter 5 the production, characterization and use of Bessel beams for strong-field applications was shown. Femtosecond Bessel beams were then used to drive high harmonic generation and showed the potential for use in a compact, high-flux XUV source. The interaction of ultrafast and strong-field

pulses with both nanowires and nanoparticles was studied in chapter 6. The damage threshold of gold nanowires was found experientially while the full thermal response was modeled numerically. This model was extended to calculate the multi-pulse heat buildup in nanowires irradiated from a train of pulses. Also, the first investigation of strong-field photoionization of dielectric nanoparticles with mid-infrared wavelengths was presented. This showed a deviation from current understanding for the scaling of photoelectron cutoff energies as a function of nanoparticle size.

Final Comments

As I mentioned in the introduction, during the course of my Ph.D. I have had the opportunity to work on a large range of projects and experiments. The research presented in the preceding pages represents the results of much of that work. All of these individual studies are aimed, in some way or another, at better understanding intense, ultrafast light-matter interactions. So, what have I learned during all of this? What would I say actually happens when an optical pulse that generates an electric field stronger than atomic binding potential slams into an atom, or molecule, or nanoparticle? Well, to the zeroth order the phrase 'all hell breaks loose' comes to mind. Almost any response pathway possible can and does occur. However, as evidenced by all of the results presented here, when you look a little deeper and attempt to understand the interaction to first-order, or second-order, or whatever order it may take, you find that these complicated interactions are far from random. In many cases, such as photoelectron rescattering, relatively simple classical models can be quite powerful. In other cases, semi-classical descriptions that at first glance seem to have no hope of accuracy, such as the strong-field approximation, can produce quantitative results. Concepts from atomic ionization, such as the ponderomotive scaling of the energy of backscattered photoelectrons, also hold deep importance for systems containing millions of atoms. That is not to say that predicting strong-field interactions is easy, far from it. It has taken the combined work of thousands of researchers and more than 50 years of intensive investigation to build up the current understanding. Technological innovations in strong-field light sources and

ultrafast measurement techniques have and will continue to play a major role in pushing this understanding even deeper. This thesis represents my contributions to this continued pursuit.

As humans we are largely incapable of comprehending the unimaginably fast dynamics that play out during the basic interactions that make up our universe. However, we are capable of building machines and making measurements of these fundamental, dynamic building blocks. We are capable of developing theories and models that describe underlying physical laws and we are capable of using this understanding to make predictions about new and yet to be investigated phenomena. Science provides the framework for investigating nature and the big question ultrafast science seeks to answer is: how does our world work at its fastest timescales?

> ***"Equipped with his five senses, man explores the universe around him and calls the adventure Science."*** **- Edwin Powell Hubble**

Bibliography

[1] T.H. Maiman. Stimulated Optical Radiation in Ruby. *Nature*, 187:493–494, 1960.

[2] F.J. McClung and R.W. Hellwarth. Giant optical pulsation from ruby. *Journal of Applied Physics*, 33:828–829, 1962.

[3] Todd Ditmire. High-power Lasers. *American Scientist*, 98(5):394–401, 2010.

[4] E. K. Damon and R. G. Tomlinson. Observation of Ionization of Gases by a Ruby Laser. *Applied Optics*, 2(5):546–547, 1963.

[5] R. G. Meyerand and A. F. Haught. Gas breakdown at optical frequencies. *Physical Review Letters*, 11(9):401–403, 1963.

[6] P. B. Corkum and Ferenc Krausz. Attosecond science. *Nature Physics*, 3:381–387, 2007.

[7] Philip H. Bucksbaum. Attophysics: Ultrafast control. *Nature*, 421(6923):593–594, 2003.

[8] Ahmed H. Zewail. Femtochemistry: Atomic-Scale Dynamics of the Chemical Bond . *The Journal of Physical Chemistry A*, 104(24):5660–5694, 2000.

[9] M. Meckel, D. Comtois, D. Zeidler, A. Staudte, D. Pavicic, H. C. Bandulet, H. Pepin, J. C. Kieffer, R. Dörner, D. M. Villeneuve, P. B. Corkum, V. Pervak, F. Krausz, and E. Goulielmakis. Laser-Induced Electron Tunneling and Diffraction. *Science*, 320 (5882):1478–1482, 2008.

[10] B Wolter, M G Pullen, A.-T Le, M Baudisch, K Doblhoff-Dier, A Senftleben, M Hemmer, C D Schröter, J Ullrich, T Pfeifer, R Moshammer, S Gräfe, O Vendrell, C D Lin,

and J Biegert. Ultrafast electron diffraction imaging of bond breaking in di-ionized acetylene. *Science*, 354(6310), 2016.

[11] A Sellitto, VA Cimmeelli, and D Jou. *Mesoscopic theories of heat transport in nanosystems*. Springer, Berlin, Germany, 2016.

[12] Adam M. Summers, Adam S. Ramm, Govind Paneru, Matthias F. Kling, Bret N. Flanders, and Carlos A. Trallero-Herrero. Optical damage threshold of Au nanowires in strong femtosecond laser fields. *Optics Express*, 22(4):4235, 2014.

[13] Anthony E. Siegman. *Lasers*. Palo Alto, 1986.

[14] Derrek Joseph Wilson. *The scaling of strong field interactions with wavelength*. PhD thesis, Kansas State University, 2018.

[15] Donna Strickland and Mourou Gerard. Compression of Amplified Chirped Optical Pulses. *Optics Communications*, 56(3):219–221, 1985.

[16] E. B. Treacy. Optical pulse compression with diffraction gratings. *J. Quantum Electron.*, 5(9):454–458, 1969.

[17] Referred to by some as the Légaré limit.

[18] Robert W Boyd. *Nonlinear Optics*. 3rd edition, 2008.

[19] Thomas Brabec and Ferenc Krausz. Intense few-cycle laser fields: Frontiers of nonlinear optics. *Reviews of Modern Physics*, 72(2):545–591, 2000.

[20] Nora G. Kling. *Controlling the Dynamics of Electrons and Nuclei in Ultrafast Strong Laser Fields*. PhD thesis, Kanas State University, 2013.

[21] Dimitar Popmintchev, Benjamin R Galloway, Ming-chang Chen, Franklin Dollar, Christopher A Mancuso, Amelia Hankla, Luis Miaja-avila, Galen O Neil, Justin M Shaw, Guangyu Fan, Skirmantas Ali, Giedrius Andriukaitis, Tadas Bal, Oliver D Mücke, Audrius Pugzlys, Andrius Baltu, Henry C Kapteyn, Tenio Popmintchev, and

Margaret M Murnane. Near- and Extended-Edge X-Ray-Absorption Fine-Structure Spectroscopy Using Ultrafast Coherent High-Order Harmonic Supercontinua. *Physical Review Letters*, 120(9), 2018.

[22] P. B. Corkum. Plasma perspective on strong field multiphoton ionization. *Physical Review Letters*, 71(13):1994–1997, 1993.

[23] Katsumi Midorikawa. Ultrafast dynamic imaging. *Nature Photonics*, 5(11):640–641, 2011.

[24] M Hentschel, R Kienberger, Ch. Spielmann, G A Reider, N Milošević, T Brabec, P Corkum, U Heinzmann, M Drescher, and F Krausz. Attosecond metrology. *Nature*, 414:509, 2001.

[25] Seth L. Cousin, Nicola Di Palo, Bárbara Buades, Stephan M. Teichmann, M. Reduzzi, M. Devetta, A. Kheifets, G. Sansone, and Jens Biegert. Attosecond streaking in the water window: A new regime of attosecond pulse characterization. *Physical Review X*, 7(4):1–14, 2017.

[26] Thomas Gaumnitz, Arohi Jain, Yoann Pertot, Martin Huppert, Inga Jordan, Fernando Ardana-Lamas, and Hans Jakob Wörner. Streaking of 43-attosecond soft-X-ray pulses generated by a passively CEP-stable mid-infrared driver. *Optics Express*, 25(22):27506, 2017.

[27] Daniel D. Hickstein, Predrag Ranitovic, Stefan Witte, Xiao Min Tong, Ymkje Huismans, Paul Arpin, Xibin Zhou, K. Ellen Keister, Craig W. Hogle, Bosheng Zhang, Chengyuan Ding, Per Johnsson, N. Toshima, Marc J J Vrakking, Margaret M. Murnane, and Henry C. Kapteyn. Direct visualization of laser-driven electron multiple scattering and tunneling distance in strong-field ionization. *Physical Review Letters*, 109(7):1–5, 2012.

[28] T Marchenko, H G Muller, K J Schafer, and M J J Vrakking. Electron angular

distributions in near-threshold atomic ionization. *Journal of Physics B*, 43(9):095601, 2010.

[29] T Marchenko, H G Muller, K J Schafer, and M J J Vrakking. Wavelength dependence of photoelectron spectra in above-threshold ionization. *Journal of Physics B*, 43(18): 125001, 2010.

[30] A. Einstein. Über einen die Erzeugung und Verwandlung des Lichtes betreffenden heuristischen Gesichtspunkt. *Ann. Phys*, 14:132–148, 1905.

[31] H. Hertz. *Electric Waves*. Dover, New York, 1962.

[32] Pierre Agostini and Louis F. DiMauro. *Atomic and Molecular Ionization Dynamics in Strong Laser Fields: From Optical to X-rays*, volume 61. Elsevier Inc., 2012.

[33] L.V. Keldysh. Ionization in the Field of a Strong Electromagnetic Wave. *JETP, Soviet Physics*, 20(5):1307–1314, 1965.

[34] R. Kopold, W. Becker, M. Kleber, and G. G. Paulus. Channel-closing effects in high-order above-threshold ionization and high-order harmonic generation. *Journal of Physics B*, 35(2):217–232, 2002.

[35] P. Agostini, F. Fabre, G. Mainfray, G. Petite, and N. K. Rahman. Free-Free Transitions Following Six-Photon Ionization of Xenon Atoms. *Physical Review Letters*, 42(17): 1127–1130, 1979.

[36] G G Paulus, F Grasbon, and H Walther. Interference effects in above-threshold ionization. *Journal of Modern Optics*, 50(3/4):343–352, 2003.

[37] L. D. Landau and E. M. Lifshitz. *Quantum Mechanics (Non-relativistic Theory)*. Butterworth-Heinemann, Burlingon, 3rd edition, 1997.

[38] A. M. Perelomov, V. S. Popov, and M. V. Terent'ev. Ionization of atoms in an alternating electrical field. *Sov. Phys. JETP*, 23(5):924, 1966.

[39] Christer Z. Bisgaard and Lars Bojer Madsen. Tunneling ionization of atoms. *American Journal of Physics*, 72(2):249–254, 2004.

[40] C. D. Lin, Anh-Thu Le, Cheng Jin, and Hui Wei. *Attosecond and Strong-Field Physics*. Cambridge University Press, Cambridge, 2018.

[41] X M Tong, Z X Zhao, and C D Lin. Theory of molecular tunneling ionization. *Physical Review A*, 66(3):033402, 2002.

[42] Misha Yu Ivanov, Michael Spanner, and Olga Smirnova. Anatomy of strong field ionization. *Journal of Modern Optics*, 52(2-3):165–184, 2005.

[43] M V Ammosov, N 8 Delone, and V P Krainov. Tunnel ionization of complex atoms and of atomic ions in an alternating electromagnetic field. *Sov. Phys. JETP*, 64(1191), 1986.

[44] Gennady L. Yudin and Misha Yu Ivanov. Nonadiabatic tunnel ionization: Looking inside a laser cycle. *Physical Review A*, 64(1):4, 2001.

[45] A. Becker and F. H.M. Faisal. Intense-field many-body S-matrix theory. *Journal of Physics B*, 38(3), 2005.

[46] A. L'Huillier, L. A. Lompre, G. Mainfray, and C. Manus. Multiply Charged Ions Formed by Multiphoton Absorption Processes in the Continuum. *Physical Review Letters*, 48(26):1814–1818, 1982.

[47] W Becker, S P Goreslavski, D B Milošević, and G G Paulus. The plateau in above-threshold ionization : the keystone of rescattering physics. *Journal of Physics B*, 51 (16), 2018.

[48] S V Popruzhenko. Keldysh theory of strong field ionization : history, applications, difficulties and perspectives. *Journal of Physics B*, 47(20), 2014.

[49] Howard R Reiss. Absorption of Light by Light. *Journal of Mathematical Physics*, 3 (1), 1962.

[50] F H M Faisal. Multiple absorption of laser photons by atoms. *Journal of Physics B*, 6(4), 1973.

[51] Howard R Reiss. Effect of an intense electromagnetic field on a weakly bound system. *Physical Review A*, 22(5), 1980.

[52] P. Salières, B. Carré, L. Le Deroff, F. Grasbon, G. G. Paulus, H. Walther, R. Kopold, W. Becker, D. B. Milošević, A. Sanpera, and M. Lewenstein. Feynman's Path-Integral Approach for Intense-LaserAtom Interactions. *Science*, 292(May):902–906, 2001.

[53] V. S. Popov. Imaginary-Time Method in Quantum Mechanics and Field Theory. *Physics of Atomic Nuclei*, 68(4):686, 2005.

[54] Yu Hang Lai, Junliang Xu, Urszula B Szafruga, Bradford K Talbert, Xiaowei Gong, Harald Fuest, Matthias F Kling, Cosmin I Blaga, Pierre Agostini, and Louis F Dimauro. Experimental investigation of strong field ionization theories from visible to mid-infrared. *Physical Review A*, 96(4), 2017.

[55] A. Lohr, M. Kleber, R. Kopold, and W. Becker. Above-threshold ionization in the tunneling regime. *Physical Review A*, 55(6):R4003–R4006, 1997.

[56] W Becker, F Grasbon, R Kopold, D B Milošević, G G Paulus, and H Walther. *Above-threshold ionization: fron classical features to quantum effects*, volume 48. 2002.

[57] S. V. Popruzhenko and D. Bauer. Strong field approximation for systems with Coulomb interaction. *Journal of Modern Optics*, 55(16):2573–2589, 2008.

[58] Min Li, Ji Wei Geng, Hong Liu, Yongkai Deng, Chengyin Wu, Liang You Peng, Qihuang Gong, and Yunquan Liu. Classical-quantum correspondence for above-threshold ionization. *Physical Review Letters*, 112(11):1–5, 2014.

[59] Tian Min Yan, S. V. Popruzhenko, M. J J Vrakking, and D. Bauer. Low-energy structures in strong field ionization revealed by quantum orbits. *Physical Review Letters*, 105(25):10–13, 2010.

[60] Y. Huismans, A. Rouzée, A. Gijsbertsen, J. H. Jungmann, A. S Smolkowska, P. S W M Logman, F. Lépine, C. Cauchy, S. Zamith, T. Marchenko, J. M. Bakker, G. Berden, B. Redlich, A. F. G. van der Meer, H. G. Muller, W. Vermin, K. J. Schafer, M. Spanner, M. Yu. Ivanov, O. Smirnova, D. Bauer, S. V. Popruzhenko, and M. J.J. Vrakking. Time-Resolved Holography with Photoelectrons. *Science*, 331(6013):61–64, 2011.

[61] R R Freeman, P. H. Bucksbaum, H. Michelberg, S. Darack, D. Schumacher, and M. E. Geusic. Above-Threshold Ionization with Subpicosecond Laser Pulses. *Physical Review Letters*, 59(10), 1987.

[62] Benjamin Langdon, Jonathan Garlick, Xiaoming Ren, Derrek J. Wilson, Adam M. Summers, Stefan Zigo, Matthias F. Kling, Shuting Lei, Christopher G. Elles, Eric Wells, Erwin D. Poliakoff, Kevin D. Carnes, Vinod Kumarappan, Itzik Ben-Itzhak, and Carlos A. Trallero-Herrero. Carrier-envelope-phase stabilized terawatt class laser at 1 kHz with a wavelength tunable option. *Optics Express*, 23(4):4563, 2015.

[63] N G Kling, D Paul, A Gura, G Laurent, S De, H Li, Z Wang, B Ahn, C H Kim, T K Kim, I V Litvinyuk, C L Cocke, I Ben-Itzhak, D Kim, and M F Kling. Thick-lens velocity-map imaging spectrometer with high resolution for high-energy charged particles. *Journal of Instrumentation*, 9(05):P05005–P05005, 2014.

[64] Jeffrey Powell. *Strong-field driven dynamics of metal and dielectric nanoparticles*. PhD thesis, Kansas State University, 2017.

[65] M. J J Vrakking. An iterative procedure for the inversion of two-dimensional ion/photoelectron imaging experiments. *Review of Scientific Instruments*, 72(11):4084, 2001.

[66] Benjain Whitaker. *Imaging in Molecular Dynamics Technology and Applications*. Cambridge University Press, 2003.

[67] F. Grasbon, G. G. Paulus, H. Walther, P. Villoresi, G. Sansone, S. Stagira, M. Nisoli,

and S. De Silvestri. Above-threshold ionization at the few-cycle limit. *Physical Review Letters*, 91(17):1–4, 2003.

[68] C. I. Blaga, F. Catoire, P. Colosimo, G. G. Paulus, H. G. Muller, P. Agostini, and L. F. DiMauro. Strong-field photoionization revisited. *Nature Physics*, 5(5):335–338, 2009.

[69] Ph A. Korneev, S. V. Popruzhenko, S. P. Goreslavski, T. M. Yan, D. Bauer, W. Becker, M. Kübel, M. F. Kling, C. Rödel, M. Wünsche, and G. G. Paulus. Interference carpets in above-threshold ionization: From the coulomb-free to the coulomb-dominated regime. *Physical Review Letters*, 108(22):1–5, 2012.

[70] S. Agust, D. Strickland, D. D. Meyerhofer, S. L. Chint, and J. H. Eberly. Tunneling Ionization of Noble Gasses in a High-Intensity Laser Field. *Physical Review Letters*, 36(5):705–716, 2013.

[71] A. E. Kaplan, I. Marzoli, W. E. Lamb, and W. P. Schleich. Multimode interference: Highly regular pattern formation in quantum wave-packet evolution. *Physical Review A*, 61(3):6, 2000.

[72] Rolf Wiehle, Bernd Witzel, Hanspeter Helm, and Eric Cormier. Dynamics of strong-field above-threshold ionization of argon: Comparison between experiment and theory. *Physical Review A*, 67(6):7, 2003.

[73] V. Schyja, T. Lang, and H. Helm. Channel switching in above-threshold ionization of xenon. *Physical Review A*, 57(5):3692–3697, 1998.

[74] W Becker, S P Goreslavski, and G G Paulus. Low-energy electron rescattering in laser-induced ionization. *Journal of Physics B*, 47:2040, 2014.

[75] Ferenc Krausz and Misha Ivanov. Attosecond physics. *Reviews of Modern Physics*, 81 (1):163–234, 2009.

[76] M. Nisoli, S. De Silvestri, and O. Svelto. Generation of high energy 10 fs pulses by a new pulse compression technique. *Applied Physics Letters*, 68(20):2793–2795, 1996.

[77] V. Pervak, A.V. Tikhonravov, M.K. Trubetskov, S. Naumov, F. Krausz, and A. Apolonski. 1.5-octave chirped mirror for pulse compression down to sub-3 fs. *Applied Physics B*, 87(1):5–12, 2007.

[78] A. Wirth, M. Th. Hassan, I. Grguras, J. Gagnon, A. Moulet, T. T. Luu, S. Pabst, R. Santra, Z. A. Alahmed, A. M. Azzeer, V. S. Yakovlev, V. Pervak, F. Krausz, and E. Goulielmakis. Synthesized Light Transients. *Science*, 334(September):195–200, 2011.

[79] G. G. Paulus, F. Grasbon, H. Walther, P. Villoresi, M. Nisoli, S. Stagira, E. Priori, and S. De Silvestri. Absolute-phase phenomena in photoionization with few-cycle laser pulses. *Nature*, 414(6860):182–184, 2001.

[80] D. B. Milošević, G. G. Paulus, D. Bauer, and W. Becker. Above-threshold ionization by few-cycle pulses. *Journal of Physics B: Atomic, Molecular and Optical Physics*, 39 (14), 2006.

[81] D Zille, D Adolph, M Möller, A M Sayler, and G G Paulus. Chirp and carrier-envelope-phase effects in the multiphoton regime: measurements and analytical modeling of strong-field ionization of sodium. *New Journal of Physics*, 20(6):063018, 2018.

[82] N I Shvetsov-Shilovski, A M Sayler, T Rathje, and G G Paulus. Carrier-envelope phase effect in the yield of sequential ionization by an intense few-cycle laser pulse. *New Journal of Physics*, 13(12):123015, 2011.

[83] Nora G. Johnson, O. Herrwerth, A. Wirth, S. De, I. Ben-Itzhak, M. Lezius, B. Bergues, M. F. Kling, A. Senftleben, C. D. Schröter, R. Moshammer, J. Ullrich, K. J. Betsch, R. R. Jones, A. M. Sayler, T. Rathje, K. Rühle, W. Müller, and G. G. Paulus. Single-shot carrier-envelope-phase-tagged ion-momentum imaging of nonsequential double ionization of argon in intense 4-fs laser fields. *Physical Review A*, 83(1):013412, 2011.

[84] M. Kübel, R. Siemering, C. Burger, Nora G. Kling, H. Li, A. S. Alnaser, B. Bergues, S. Zherebtsov, A. M. Azzeer, I. Ben-Itzhak, R. Moshammer, R. de Vivie-Riedle, and M. F. Kling. Steering Proton Migration in Hydrocarbons Using Intense Few-Cycle Laser Fields. *Physical Review Letters*, 116(19):193001, 2016.

[85] Nora G. Kling, K. J. Betsch, M. Zohrabi, S. Zeng, F. Anis, U. Ablikim, Bethany Jochim, Z. Wang, M. Kübel, M. F. Kling, K. D. Carnes, B. D. Esry, and I. Ben-Itzhak. Carrier-Envelope Phase Control over Pathway Interference in Strong-Field Dissociation of H 2 +. *Physical Review Letters*, 111(16):163004, 2013.

[86] S. Zherebtsov, F. Süßmann, C. Peltz, J. Plenge, K. J. Betsch, I. Znakovskaya, A. S. Alnaser, N. G. Johnson, M. Kübel, A. Horn, V. Mondes, C. Graf, S. A. Trushin, A. Azzeer, M. J.J. Vrakking, G. G. Paulus, F. Krausz, E. Rühl, T. Fennel, and M. F. Kling. Carrier-envelope phase-tagged imaging of the controlled electron acceleration from SiO2nanospheres in intense few-cycle laser fields. *New Journal of Physics*, 14, 2012.

[87] F. Süßmann, L. Seiffert, S. Zherebtsov, V. Mondes, J. Stierle, M. Arbeiter, J. Plenge, P. Rupp, C. Peltz, A. Kessel, S. A. Trushin, B. Ahn, D. Kim, C. Graf, E. Rühl, M. F. Kling, and T. Fennel. Field propagation-induced directionality of carrier-envelope phase-controlled photoemission from nanospheres. *Nature Communications*, 6(1):7944, 2015.

[88] H. Li, B. Mignolet, G. Wachter, S. Skruszewicz, S. Zherebtsov, F. Süßmann, A. Kessel, S. A. Trushin, Nora G. Kling, M. Kübel, B. Ahn, D. Kim, I. Ben-Itzhak, C. L. Cocke, T. Fennel, J. Tiggesbäumker, K.-H. Meiwes-Broer, C. Lemell, J. Burgdörfer, R. D. Levine, F. Remacle, and M. F. Kling. Coherent Electronic Wave Packet Motion in C 60 Controlled by the Waveform and Polarization of Few-Cycle Laser Fields. *Physical Review Letters*, 114(12):123004, 2015.

[89] Michael Krüger, Markus Schenk, and Peter Hommelhoff. Attosecond control of electrons emitted from a nanoscale metal tip. *Nature*, 475(7354):78–81, 2011.

[90] T. Hanke, G. Krauss, D. Träutlein, B. Wild, R. Bratschitsch, and A. Leitenstorfer. Efficient Nonlinear Light Emission of Single Gold Optical Antennas Driven by Few-Cycle Near-Infrared Pulses. *Physical Review Letters*, 103(25):257404, 2009.

[91] Agustin Schiffrin, Tim Paasch-Colberg, Nicholas Karpowicz, Vadym Apalkov, Daniel Gerster, Sascha Mühlbrandt, Michael Korbman, Joachim Reichert, Martin Schultze, Simon Holzner, Johannes V. Barth, Reinhard Kienberger, Ralph Ernstorfer, Vladislav S. Yakovlev, Mark I. Stockman, and Ferenc Krausz. Optical-field-induced current in dielectrics. *Nature*, 493(7430):70–74, 2012.

[92] T. M. Fortier, P. A. Roos, D. J. Jones, S. T. Cundiff, R. D. R. Bhat, and J. E. Sipe. Carrier-Envelope Phase-Controlled Quantum Interference of Injected Photocurrents in Semiconductors. *Physical Review Letters*, 92(14):147403, 2004.

[93] C. Van Vlack and S. Hughes. Carrier-Envelope-Offset Phase Control of Ultrafast Optical Rectification in Resonantly Excited Semiconductors. *Physical Review Letters*, 98(16):167404, 2007.

[94] Tim Paasch-Colberg, Agustin Schiffrin, Nicholas Karpowicz, Stanislav Kruchinin, Özge Salam, Sabine Keiber, Olga Razskazovskaya, Sascha Mühlbrandt, Ali Alnaser, Matthias Kübel, Vadym Apalkov, Daniel Gerster, Joachim Reichert, Tibor Wittmann, Johannes V. Barth, Mark I. Stockman, Ralph Ernstorfer, Vladislav S. Yakovlev, Reinhard Kienberger, and Ferenc Krausz. Solid-state light-phase detector. *Nature Photonics*, 8(3):214–218, 2014.

[95] Zenghu Chang. *Fundamentals of Attosecond Optics*. Taylor & Francis, Boca Raton, FL, 2011.

[96] Eric Wayne Moon. *Carrier-Envelope Phase Stabilization of Grating-Based Chirped-Pulse Amplifiers*. PhD thesis, Kansas State University, 2009.

[97] Steven T. Cundiff and Jun Ye. Colloquium : Femtosecond optical frequency combs. *Reviews of Modern Physics*, 75(1):325–342, 2003.

[98] D J Jones, S A Diddams, J K Ranka, A Stentz, R S Windeler, J L Hall, and S T Cundiff. Carrier-Envelope Phase Control of Femtosecond Mode-Locked Lasers and Direct Optical Frequency Synthesis. *Science*, 288(April):635, 2000.

[99] Andrius Baltuška, Matthias Uiberacker, Eleftherios Goulielmakis, Reinhard Kienberger, Vladislav S Yakovlev, Thomas Udem, Theodor W Hänsch, Ferenc Krausz, A Baltuška, M Uiberacker, E Goulielmakis, R Kienberger, V S Yakovlev,) T Udem, and T W Hänsch. Phase-Controlled Amplification of Few-Cycle Laser Pulses. *IEEE Journal of Selected Topics in Quantum Electronics*, 9(4), 2003.

[100] Masayuki Kakehata, Hideyuki Takada, Yohei Kobayashi, Kenji Torizuka, Hiroaki Takamiya, Kazuki Nishijima, Tetsuya Homma, Hideo Takahashi, Katsuaki Okubo, Shinki Nakamura, and Yahei Koyamada. Carrier-envelope-phase stabilized chirped-pulse amplification system scalable to higher pulse energies. *Optics Express*, 12(10): 2070, 2004.

[101] R. Holzwarth, Th. Udem, T. W. Hänsch, J. C. Knight, W. J. Wadsworth, and P. St. J. Russell. Optical Frequency Synthesizer for Precision Spectroscopy. *Physical Review Letters*, 85(11):2264–2267, 2000.

[102] G Sansone, E. Benedetti, F. Calagari, C. Vozzi, L. Avaldi, R. Flammini, L. Poletto, P. Villoresi, C. Altucci, R. Velotta, S Stagira, and S. De Silvestri. Isolated single-cycle attosecond pulses. *Science*, 314:443–6, 2006.

[103] Shu-Wei Huang, Giovanni Cirmi, Jeffrey Moses, Kyung-Han Hong, Siddharth Bhardwaj, Jonathan R. Birge, Li-Jin Chen, Enbang Li, Benjamin J. Eggleton, Giulio Cerullo, and Franz X. Kärtner. High-energy pulse synthesis with sub-cycle waveform control for strong-field physics. *Nature Photonics*, 5(8):475–479, 2011.

[104] Etienne Gagnon, Isabell Thomann, Ariel Paul, Amy L. Lytle, Sterling Backus, Margaret M. Murnane, Henry C. Kapteyn, and Arvinder S. Sandhu. Long-term carrier-

envelope phase stability from a grating-based, chirped pulse amplifier. *Optics Letters*, 31(12):1866, 2006.

[105] Zenghu Chang. Carrier-envelope phase shift caused by grating-based stretchers and compressors. *Applied Optics*, 45(32):8350, 2006.

[106] Fabian Lücking, Vincent Crozatier, Nicolas Forget, Andreas Assion, and Ferenc Krausz. Approaching the limits of carrier-envelope phase stability in a millijoule-class amplifier. *Optics Letters*, 39(13):3884, 2014.

[107] D. Adolph, A. M. Sayler, T. Rathje, K. Rühle, and G. G. Paulus. Improved carrier-envelope phase locking of intense few-cycle laser pulses using above-threshold ionization. *Optics Letters*, 36(18):3639, 2011.

[108] Sebastian Koke, Christian Grebing, Harald Frei, Alexandria Anderson, Andreas Assion, and Günter Steinmeyer. Direct frequency comb synthesis with arbitrary offset and shot-noise-limited phase noise. *Nature Photonics*, 4(7):462–465, 2010.

[109] T. Wittmann, B. Horvath, W. Helml, M. G. Schätzel, X. Gu, A. L. Cavalieri, G. G. Paulus, and R. Kienberger. Single-shot carrierenvelope phase measurement of few-cycle laser pulses. *Nature Physics*, 5(5):357–362, 2009.

[110] A. M. Sayler, Tim Rathje, Walter Müller, Klaus Rühle, R. Kienberger, and G. G. Paulus. Precise, real-time, every-single-shot, carrier-envelope phase measurement of ultrashort laser pulses. *Optics Letters*, 36(1):1, 2011.

[111] T Rathje, Nora G Johnson, M Möller, F Süßmann, D Adolph, M Kübel, R Kienberger, M F Kling, G G Paulus, and A M Sayler. Review of attosecond resolved measurement and control via carrierenvelope phase tagging with above-threshold ionization. *Journal of Physics B*, 45(7):074003, 2012.

[112] M Kübel, K J Betsch, Nora G Johnson, U Kleineberg, R Moshammer, J Ullrich, G G Paulus, M F Kling, and B Bergues. Carrier-envelope-phase tagging in measurements with long acquisition times. *New Journal of Physics*, 14(9):093027, 2012.

[113] Masayuki Kakehata, Hideyuki Takada, Yohei Kobayashi, Kenji Torizuka, Yoshihiko Fujihira, Tetsuya Homma, and Hideo Takahashi. Single-shot measurement of carrier-envelope phase changes by spectral interferometry. *Optics Letters*, 26(18):1436, 2001.

[114] Chengquan Li, Eric Moon, He Wang, Hiroki Mashiko, Christopher M. Nakamura, Jason Tackett, and Zenghu Chang. Determining the phase-energy coupling coefficient in carrier-envelope phase measurements. *Optics Letters*, 32(7):796, 2007.

[115] He Wang, Michael Chini, Eric Moon, Hiroki Mashiko, Chengquan Li, and Zenghu Chang. Coupling between energy and phase in hollow-core fiber based f-to-2f interferometers. *Optics Express*, 17(14):12082, 2009.

[116] Sebastian Koke, Christian Grebing, Bastian Manschwetus, and Günter Steinmeyer. Fast f-to-2f interferometer for a direct measurement of the carrier-envelope phase drift of ultrashort amplified laser pulses. *Optics Letters*, 33(21):2545, 2008.

[117] Reginald A Fessenden. Wireless signaling. *US Patent*, US706740A(706), 1902.

[118] Alexander Apolonski, Boris Povazay, Angelika Unterhuber, Wolfgang Drexler, William J. Wadsworth, Jonathan C. Knight, and Phillip St. J. Russell. Spectral shaping of supercontinuum in a cobweb photonic-crystal fiber with sub-20-fs pulses. *Journal of the Optical Society of America B*, 19(9):2165, 2002.

[119] G. G. Paulus. A meter of the "absolute" phase of few-cycle laser pulses. *Laser Physics*, 15(6):843854, 2005.

[120] Yinyu Zhang, Philipp Kellner, Daniel Adolph, Danilo Zille, Philipp Wustelt, Daniel Würzler, Slawomir Skruszewicz, Max Möller, A. Max Sayler, and Gerhard G. Paulus. Single-shot, real-time carrier-envelope phase measurement and tagging based on stereographic above-threshold ionization at short-wave infrared wavelengths. *Optics Letters*, 42(24):5150, 2017.

[121] http://www.menlosystems.com/products/cep-stable-lasers-and-cep-phase-stabilization/.

[122] Stefan John Zigo. *Photoionization of isomeric molecules: From the weak-field to the strong-field limit*. PhD thesis, Kansas State University, 2017.

[123] M. Nisoli, S. Stagira, S. De Silvestri, O. Svelto, S. Sartania, Z. Cheng, M. Lenzner, C. Spielmann, and F. Krausz. A novel-high energy pulse compression system: generation of multigigawatt sub-5-fs pulses. *Applied Physics B*, 65(2):189–196, 1997.

[124] A. M. Sayler, Tim Rathje, W. Müller, Ch. Kürbis, Klaus Rühle, Gero Stibenz, and G. G. Paulus. Real-time pulse length measurement of few-cycle laser pulses using above-threshold ionization. *Optics Express*, 19(5):4464, 2011.

[125] M. Möller, A. M. Sayler, T. Rathje, M. Chini, Zenghu Chang, and G. G. Paulus. Precise, real-time, single-shot carrier-envelope phase measurement in the multi-cycle regime. *Applied Physics Letters*, 99(12):121108, 2011.

[126] Claude Marceau, Guillaume Gingras, Steven Thomas, Yacine Kassimi, and Bernd Witzel. Energy-phase coupling inside sapphire-based f-2f nonlinear interferometers from 800 to 1940 nm. *Applied Optics*, 53(5):898, 2014.

[127] Selcuk Akturk. Tailored-Beam Ultrashort Laser Pulses. *Quantum Physics Letters*, 112 (3):97–112, 2012.

[128] D McGloin and K Dholakia. Bessel beams: Diffraction in a new light. *Contemporary Physics*, 46(1):15–28, 2005.

[129] V. Jarutis, R. Paškauskas, and A. Stabinis. Focusing of Laguerre-Gaussian beams by axicon. *Optics Communications*, 184(1):105–112, 2000.

[130] R Grunwald, M Bock, V Kebbel, S Huferath, U Neumann, G Steinmeyer, G Stibenz, J-L Néron, and M Piché. Ultrashort-pulsed truncated polychromatic Bessel-Gauss beams. *Optics express*, 16(2):1077–1089, 2008.

[131] Adam M. Summers, Xiaoming Yu, Xinya Wang, Maxime Raoul, Josh Nelson, Daniel

Todd, Stefan Zigo, Shuting Lei, and Carlos A. Trallero-Herrero. Spatial characterization of Bessel-like beams for strong-field physics. *Optics Express*, 25(3):1646, 2017.

[132] R M Herman and T A Wiggins. Production and uses of diffractionless beams. *Journal of the Optical Society of America A*, 8(6):932–942, 1991.

[133] J. Durnin. Exact solutions for nondiffracting beams I The scalar theory. *Journal of the Optical Society of America A*, 4(4):651, 1987.

[134] J. Durnin, J. Miceli, and J. H. Eberly. Diffraction-free beams. *Physical Review Letters*, 58(15):1499–1501, 1987.

[135] Arash Sabatyan and Bahar Meshginqalam. Generation of annular beam by a novel class of Fresnel zone plate. *Applied Optics*, 53(26):5995, 2014.

[136] Pierre-Andre Belanger and Marc Rioux. Ring pattern of a lens-axicon doublet illuminated by a Gaussian beam. *Applied Optics*, 17(7):1080–1086, 1978.

[137] Narupon Chattrapiban, Elizabeth A. Rogers, David Cofield, Wendell T. Hill, III, and Rajarshi Roy. Generation of nondiffracting Bessel beams by use of a spatial light modulator. *Optics Letters*, 28(22):2183, 2003.

[138] John H. McLeod. The Axicon: A New Type of Optical Element. *Journal of the Optical Society of America*, 44(8):592, 1954.

[139] C.J.R. Sheppard and T. Wilson. Gaussian-beam theory of lenses with annular aperture. *IEE Journal on Microwaves, Optics and Acoustics*, 2(4):105, 1978.

[140] F. Gori, C. Guattari, and C Padovani. Bessel-Gauss beams. *Optics Communications*, 64(6):491–495, 1987.

[141] T. Auguste, O. Gobert, and B. Carré. Numerical study on high-order harmonic generation by a Bessel-Gauss laser beam. *Physical Review A*, 78(3):1–11, 2008.

[142] Alexandre April. Bessel-Gauss beams as rigorous solutions of the Helmholtz equation. *Journal of the Optical Society of America A*, 28(10):2100, 2011.

[143] Vladimir Belyi, Andrew Forbes, Nikolai Kazak, Nikolai Khilo, and P. Ropot. Bessel like beams with zdependent cone angles. *Optics Express*, 18(3):1966, 2010.

[144] Pamela R. Bowlan, Madis Lõhmus, Peeter Piksarv, Heli Valtna-Lukner, Peeter Saari, and Rick Trebino. Measuring the Spatio-Temporal Field of Diffracting Ultrashort Pulses. *Optics Letters*, 34(15):2276–2278, 2009.

[145] C Vinegoni, C Leon Swisher, P Fumene Feruglio, R J Giedt, D L Rousso, S Stapleton, and R Weissleder. Real-time high dynamic range laser scanning microscopy. *Nature Communications*, 7:11077, 2016.

[146] Selcuk Akturk, Bing Zhou, Benjamin Pasquiou, Michel Franco, and Andre Mysyrowicz. Intensity distribution around the focal regions of real axicons. *Optics Communications*, 281(17):4240–4244, 2008.

[147] T. Pfeifer, C. Spielmann, and G. Gerber. Femtosecond x-ray science. *Reports on Progress in Physics*, 69(2):443–505, 2006.

[148] Alessandro Averchi, Daniele Faccio, Ricardo Berlasso, Miroslav Kolesik, Jerome V. Moloney, Arnaud Couairon, and Paolo Di Trapani. Phase matching with pulsed Bessel beams for high-order harmonic generation. *Physical Review A*, 77(2):4–7, 2008.

[149] A. D. Shiner, C. Trallero-Herrero, N. Kajumba, H. C. Bandulet, D. Comtois, F. Légaré, M. Giguère, J. C. Kieffer, P. B. Corkum, and D. M. Villeneuve. Wavelength scaling of high harmonic generation efficiency. *Physical Review Letters*, 103(7):1–4, 2009.

[150] Philippe Balcou, Pascal Salieres, Anne L'Huillier, and Maciej Lewenstein. Generalized phase-matching conditions for high harmonics: The role of field-gradient forces. *Physical Review A*, 55(4):3204–3210, 1997.

[151] Carlo Altucci, Riccardo Bruzzese, Domenico D'Antuoni, Corrado de Lisio, and Salvatore Solimeno. Harmonic generation in gases by use of BesselGauss laser beams. *Journal of the Optical Society of America B*, 17(1):34, 2000.

[152] Charles G. Durfee, Andy R. Rundquist, Sterling Backus, Catherine Herne, Margaret M. Murnane, and Henry C. Kapteyn. Phase matching of high-order harmonics in hollow waveguides. *Physical Review Letters*, 83(11):2187–2190, 1999.

[153] Ba Khuong Dinh. *Phase-Matched High Order Harmonic Generation and Applications*. PhD thesis, Swineburne University of Technology, 2012.

[154] Ekmel Ozbay. Plasmonics: Merging Photonics and Electronics at Nanoscale Dimensions. *Science*, 311(5758):189–193, 2006.

[155] A. V. Akimov, A. Mukherjee, C. L. Yu, D. E. Chang, A. S. Zibrov, P. R. Hemmer, H. Park, and M. D. Lukin. Generation of single optical plasmons in metallic nanowires coupled to quantum dots. *Nature*, 450(7168):402–406, 2007.

[156] M. S. Tame, K. R. McEnery, . K. Özdemir, J. Lee, S. A. Maier, and M. S. Kim. Quantum plasmonics. *Nature Physics*, 9(6):329–340, 2013.

[157] Kevin J Savage, Matthew M Hawkeye, Rubén Esteban, Andrei G Borisov, Javier Aizpurua, and Jeremy J Baumberg. Revealing the quantum regime in tunnelling plasmonics. *Nature*, 491(7425):574–7, 2012.

[158] Mark I. Stockman. Nanoplasmonics: past, present, and glimpse into future. *Optics Express*, 19(22), 2011.

[159] J. Leuthold, C. Hoessbacher, S. Muehlbrandt, A. Melikyan, M. Kohl, C. Koos, W. Freude, V. Dolores-Calzadilla, M. Smit, I. Suarez, J. Martínez-Pastor, E.P. Fitrakis, and I. Tomkos. Plasmonic Communications: Light on a Wire. *Optics and Photonics News*, 24(5):28, 2013.

[160] Johannes Passig, Sergey Zherebtsov, Robert Irsig, Mathias Arbeiter, Christian Peltz, Sebastian Göde, Slawomir Skruszewicz, Karl-Heinz Meiwes-Broer, Josef Tiggesbäumker, Matthias F. Kling, and Thomas Fennel. Nanoplasmonic electron acceleration by attosecond-controlled forward rescattering in silver clusters. *Nature Communications*, 8(1):1181, 2017.

[161] E. A. Peralta, K. Soong, R. J. England, E. R. Colby, Z. Wu, B. Montazeri, C. McGuinness, J. McNeur, K. J. Leedle, D. Walz, E. B. Sozer, B. Cowan, B. Schwartz, G. Travish, and R. L. Byer. Demonstration of electron acceleration in a laser-driven dielectric microstructure. *Nature*, 503(7474):91–94, 2013.

[162] M. F. Ciappina, Srdjan S. Aćimović, T. Shaaran, J. Biegert, R. Quidant, and M. Lewenstein. Enhancement of high harmonic generation by confining electron motion in plasmonic nanostrutures. *Optics Express*, 20(24):26261, 2012.

[163] T. Shaaran, M. F. Ciappina, R. Guichard, J. A. Pérez-Hernández, L. Roso, M. Arnold, T. Siegel, A. Zaïr, and M. Lewenstein. High-order-harmonic generation by enhanced plasmonic near-fields in metal nanoparticles. *Physical Review A*, 87(4):041402, 2013.

[164] G. Herink, D. R. Solli, M. Gulde, and C. Ropers. Field-driven photoemission from nanostructures quenches the quiver motion. *Nature*, 483(7388):190–193, 2012.

[165] S. Zherebtsov, Th Fennel, J. Plenge, E. Antonsson, I. Znakovskaya, A. Wirth, O. Herrwerth, F. Süßmann, C. Peltz, I. Ahmad, S. Trushin, V. Pervak, S. Karsch, M. J.J. Vrakking, B. Langer, C. Graf, M. I. Stockman, F. Krausz, E. Rühl, and M. F. Kling. Controlled near-field enhanced electron acceleration from dielectric nanospheres with intense few-cycle laser fields. *Nature Physics*, 7:656–662, 2011.

[166] Peter Dombi, Anton Horl, Peter Racz, Marton Istvan, Andreas Trugler, Joachim R Krenn, and Ulrich Hohenester. Ultrafast Strong-Field Photoemission from Plasmonic Nanoparticles. *Nano Lett*, 13:25, 2013.

[167] Phillip M. Nagel, Joseph S. Robinson, Bruce D. Harteneck, Thomas Pfeifer, Mark J. Abel, James S. Prell, Daniel M. Neumark, Robert A. Kaindl, and Stephen R. Leone. Surface plasmon assisted electron acceleration in photoemission from gold nanopillars. *Chemical Physics*, 414:106–111, 2013.

[168] Birol Ozturk, Bret N Flanders, Daniel R Grischkowsky, and Tetsuya D Mishima. Single-step growth and low resistance interconnecting of gold nanowires. *Nanotechnology*, 18(17):175707, 2007.

[169] Bret N Flanders. Directed Electrochemical Nanowire Assembly: Precise Nanostructure Assembly via Dendritic Solidification. *Modern Physics Letters B*, 26(01):1130001, 2012.

[170] David A. Kessler, Joel Koplik, and Herbert Levine. Pattern selection in fingered growth phenomena. *Advances in Physics*, 37(3):255–339, 1988.

[171] Ishan Talukdar, Birol Ozturk, Bret N. Flanders, and Tetsuya D. Mishima. Directed growth of single-crystal indium wires. *Applied Physics Letters*, 88(22):221907, 2006.

[172] Govind Paneru and Bret N. Flanders. Complete reconfiguration of dendritic gold. *Nanoscale*, 6(2):833–841, 2014.

[173] Prem S Thapa, Bruce J Ackerson, Daniel R Grischkowsky, and Bret N Flanders. Directional growth of metallic and polymeric nanowires. *Nanotechnology*, 20(23):235307, 2009.

[174] Hideyuki Inouye, Koichiro Tanaka, Ichiro Tanahashi, and Kazuyuki Hirao. Ultrafast dynamics of nonequilibrium electrons in a gold nanoparticle system. *Physical Review B*, 57(18):11334–11340, 1998.

[175] G. L. Eesley. Generation of nonequilibrium electron and lattice temperatures in copper by picosecond laser pulses. *Physical Review B*, 33(4):2144–2151, 1986.

[176] S. Nolte, C. Momma, H. Jacobs, A. Tünnermann, B. N. Chichkov, B. Wellegehausen,

and H. Welling. Ablation of metals by ultrashort laser pulses. *Journal of the Optical Society of America B*, 14(10):2716, 1997.

[177] M.I. Kaganov, I.M. Lifshitz, and L.V. Tanatarov. Relaxation between Electrons and the Crystalline Lattice. *JETP, Soviet Physics*, 4(2):173, 1957.

[178] S I Anisimov, B.L. Kapeliovich, and T.L. Perel'man. Electron emission from metal surfaces exposed to ultrashort laser pulses. *JETP, Soviet Physics*, 39(2):376, 1974.

[179] Zhibin Lin, Leonid V. Zhigilei, and Vittorio Celli. Electron-phonon coupling and electron heat capacity of metals under conditions of strong electron-phonon nonequilibrium. *Physical Review B*, 77(7):075133, 2008.

[180] E.D Palik. *Handbook of Optical Constants of Solids*. Academic Press, 74th edition, 1985.

[181] W. Benenson. *Handbook of Physics*. Springer, 2000.

[182] Xianmao Lu, Matthew Rycenga, Sara E. Skrabalak, Benjamin Wiley, and Younan Xia. Chemical Synthesis of Novel Plasmonic Nanoparticles. *Annual Review of Physical Chemistry*, 60(1):167–192, 2009.

[183] Marek Grzelczak, Jorge Pérez-Juste, Paul Mulvaney, and Luis M. Liz-Marzán. Shape control in gold nanoparticle synthesis. *Chemical Society Reviews*, 37(9):1783, 2008.

[184] Peter Hommelhoff and Matthias F. Kling. *Attosecond Nanophysics: From Basic Science to Applications*. Wiley, 2015.

[185] Mark I. Stockman, Matthias F. Kling, Ulf Kleineberg, and Ferenc Krausz. Attosecond nanoplasmonic-field microscope. *Nature Photonics*, 1:539–544, 2007.

[186] M. F. Ciappina, J A Pérez-Hernández, A S Landsman, W A Okell, S Zherebtsov, B Förg, J Schötz, L Seiffert, T Fennel, T Shaaran, T Zimmermann, A Chacón, R Guichard, A Zaïr, J W G Tisch, J P Marangos, T Witting, A Braun, S A Maier, L Roso,

M Krüger, P Hommelhoff, M F Kling, F Krausz, and M Lewenstein. Attosecond physics at the nanoscale. *Reports on Progress in Physics*, 80(5), 2017.

[187] Maxim Durach, Anastasia Rusina, Matthias F. Kling, and Mark I. Stockman. Predicted Ultrafast Dynamic Metallization of Dielectric Nanofilms by Strong Single-Cycle Optical Fields. *Physical Review Letters*, 107(8):2–6, 2011.

[188] Mark I Stockman, Katrin Kneipp, Sergey I Bozhevolnyi, Soham Saha, Aveek Dutta, Justus Ndukaife, Nathaniel Kinsey, Harsha Reddy, Urcan Guler, Vladimir M Shalaev, Alexandra Boltasseva, Behrad Gholipour, Harish N S Krishnamoorthy, Kevin F MacDonald, Cesare Soci, Nikolay I Zheludev, Vassili Savinov, Ranjan Singh, Petra Groß, Christoph Lienau, Michal Vadai, Michelle L Solomon, David R Barton, Mark Lawrence, Jennifer A Dionne, Svetlana V Boriskina, Ruben Esteban, Javier Aizpurua, Xiang Zhang, Sui Yang, Danqing Wang, Weijia Wang, Teri W Odom, Nicolò Accanto, Pablo M de Roque, Ion M Hancu, Lukasz Piatkowski, Niek F van Hulst, and Matthias F Kling. Roadmap on plasmonics. *Journal of Optics*, 20(4):043001, 2018.

[189] Jianxiong Li, Erfan Saydanzad, and Uwe Thumm. Imaging Plasmonic Fields with Atomic Spatiotemporal Resolution. *Physical Review Letters*, 120:223903, 2018.

[190] Mie Gusrav. Beiträge zur Optik trüber Medien, speziell kolloidaler Metallösungen. *Annalen der Physik*, 330(3):377–445, 1908.

[191] L. Seiffert, F. Süßmann, S. Zherebtsov, P. Rupp, C. Peltz, E. Rühl, M. F. Kling, and T. Fennel. Competition of single and double rescattering in the strong-field photoemission from dielectric nanospheres. *Applied Physics B*, 122(4):101, 2016.

[192] Jeffrey A. Powell, Adam M. Summers, Seyyed Javad Robatjazi, Philipp Rupp, Johannes Stierle, Qingcao Liu, Matthias F. Kling, and Artem Rudenko. Size dependent electron emission from laser-driven SiO2 nanospheres. *Optics Express*, ((To Be Submitted)).

[193] Peng Liu, Paul J. Ziemann, David B. Kittelson, and Peter H. McMurry. Generating Particle Beams of Controlled Dimensions and Divergence: I. Theory of Particle Motion in Aerodynamic Lenses and Nozzle Expansions. *Aerosol Science and Technology*, 22 (3):293–313, 1995.

[194] Peter S. K. Liu, Rensheng Deng, Kenneth A. Smith, Leah R. Williams, John T. Jayne, Manjula R. Canagaratna, Kori Moore, Timothy B. Onasch, Douglas R. Worsnop, and Terry Deshler. Transmission Efficiency of an Aerodynamic Focusing Lens System: Comparison of Model Calculations and Laboratory Measurements for the Aerodyne Aerosol Mass Spectrometer. *Aerosol Science and Technology*, 41(8):721–733, 2007.

[195] E. C. Le Ru and P. G. Etchegion. *Principles of Surface-Enhanced Raman Spectroscopy and Related Plasmonic Effects*. Elsevier, Amsterdam, 2009.